UNIVERSITÉ DE STRASBOURG

ÉCOLE DOCTORALE de PHYSIQUE et CHIMIE-PHYSIQUE

IPCMS, Strasbourg

THÈSE en co-tutelle présentée par :

Lukáš Ondič

soutenue le 14 Février 2014

pour obtenir le grade de : **Docteur de l'université de Strasbourg**

Discipline/ Spécialité : Physique/ Nanophysique

Silicon nanocrystals, photonic structures and optical gain

THÈSE dirigée par :
  Bernd Honerlage   Prof., Université de Strasbourg, France

THÈSE co-dirigée par :
  Kateřina Herynková   Dr., Institute of Physics, ASCR, Czech Republic

RAPPORTEURS :
  Jean-Sébastien Lauret   Prof., École normale supérieure de Cachan, Orsay, France
  Jiří Oswald   Ing., Institute of Physics, ASCR, Czech Republic

---

AUTRES MEMBRES DU JURY :
  Jaromír Plášek   Prof., Charles University in Prague, Czech Republic
  Petr Němec   Dr., Charles University in Prague, Czech Republic
  Thomas Heiser   Prof., Université de Strasbourg, France
  Pierre Gilliot   Dr., IPCMS, Strasbourg; Université de Strasbourg, France
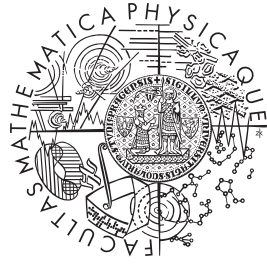
Charles University in Prague
Faculty of Mathematics and Physics
Czech Republic

Université de Strasbourg
IPCMS – DON Strasbourg
France

Doctoral Thesis

"thése en cotutelle"

Silicon nanocrystals, photonic structures and optical gain

by

RNDr. Lukáš Ondič

2013

Silicon nanocrystals, photonic structures and optical gain

Department of Chemical Physics and Optics, Faculty of Mathematics and Physics, Charles University in Prague

Department of Ultrafast Optics and Nanophotonics, The Institute of Physics and Chemistry of Materials of Strasbourg & University of Strasbourg

Supervisors:

RNDr. Kateřina Herynková, PhD.
Institute of Physics, Academy of Sciences of the Czech Republic, Prague, Czech Republic
Prof. Dr. Bernd Hönerlage
Institute de Physique et Chimie des Matériaux de Strasbourg; Université de Strasbourg, Strasbourg, France

Consultant:

Prof. RNDr. Ivan Pelant, DrSc.
Institute of Physics, Academy of Sciences of the Czech Republic, Prague, Czech Republic

Referees:

Ing. Jiří Oswald, CSc.
Institute of Physics, Academy of Sciences of the Czech Republic, Prague, Czech Republic
Prof. Jean-Sébastien Lauret
École normale supérieure de Cachan; Laboratoire Aimé Cotton, Orsay, France

Members of the jury:

Prof. RNDr. Jaromír Plášek, CSc.
Institute of Physics of Charles University, Prague, Czech Republic
Doc. RNDr. Petr Němec, PhD.
Department of Chemical Physics and Optics, Charles University, Prague, Czech Republic
Prof. Thomas Heiser
Laboratoire des Sciences de l'Ingénieur, de l'Informatique et de l'Imagerie, Université de Strasbourg, Strasbourg, France
Dr. Pierre Gilliot
Institute de Physique et Chimie des Matériaux de Strasbourg; Université de Strasbourg, Strasbourg, France
RNDr. Kateřina Herynková, PhD.
Prof. Dr. Bernd Hönerlage
Ing. Jiří Oswald, CSc.
Prof. Jean-Sébastien Lauret

I declare that I carried out this doctoral thesis independently, and only with the cited sources, literature and other professional sources.

In Prague & Strasbourg, November 2013   Signature of the author:

Abstract

Silicon nanocrystals (SiNCs) of sizes below approximately 5 nm are a material with an efficient room-temperature photoluminescence (PL) and optical gain. Optical gain is a prerequisite for obtaining stimulated emission from a pumped material, and the achievement of stimulated emission (and lasing) from Si-based nanostructures is of particular interest of the field of silicon photonics. The aim of this work was (i) to investigate fundamental optical properties of SiNCs, (ii) to design and prepare a photonic crystal with enhanced light extraction efficiency and (iii) to explore a possibility of enhancing optical gain of light-emitting SiNCs by combining them with a two-dimensional photonic crystal. First, free-standing oxide (SiO_x/SiO_2)-passivated SiNCs were prepared by electrochemical etching of a Si wafer. Their optical properties were studied by employing time-resolved spectroscopy, also at cryogenic temperatures. The fast blue-green emission band of these SiNCs was linked with the quasi-direct recombination of hot electrons and holes in the vicinity of the Γ-point. Furthermore, the spectral shift of the slow orange-red band (of these SiNCs) as a function of temperature was explained on the basis of an interplay between tensile strain and bulk Si temperature-induced indirect bandgap shift. The optical gain coefficient was measured using the standard "Variable stripe length" (VSL) method supplemented with the "Shifting excitation spot" (SES) technique. It was shown that SiNCs (prepared by etching) embedded in a SiO_2-solgel derived matrix possess optical gain of the order of tens of cm^{-1} at both emission bands. The presence of ultrafast gain was investigated in the oxide-passivated SiNCs dispersed in ethanol. However, no optical gain was observed on the ultrafast component of luminescence due to the insufficient power of excitation pulses. Also other types of SiNCs, methyl-capped ($-CH_3$) free-standing SiNCs and $SiNCs/SiO_2$-multilayers, were experimentally studied. In the former, zero net optical gain coefficient was measured most probably due to the very low concentration of SiNCs in the sample. In the latter, free carrier absorption (FCA) losses prevented the onset of stimulated emission and thus no positive net optical gain was observed. Optical gain can be enhanced by employing periodic dielectric structures, photonic crystals. By employing Finite-difference time-domain computer simulations, it was shown that stimulated emission from a low-gain medium can be achieved by embedding it into a two-dimensional photonic crystal with well-designed dimensions. With this keeping in mind, a two-dimensional photonic crystal was fabricated on the top of a silica layer with embedded SiNCs. It was shown that such a structure allows, compared to a plane layer, an effective enhancement of extraction efficiency of light (emitted from SiNCs) into air. Up to 7-fold increase of intensity was achieved for modes propagating in the direction normal to the sample plane. This effect was attributed to the Bragg-diffraction of guided modes on the surface periodicity. However, the onset of stimulated emission was not observed most probably due to high FCA losses present in this sample. Up to 6-fold enhancement of extraction efficiency was also measured for nanocrystalline diamond (NCD) layers with a two-dimensional photonic crystal etched on their surface compared to plane NCD layers. The sources of light were in the case of the NCD layers various defects (not SiNCs) introduced during the fabrication process. The oxide-passivated SiNCs (prepared by etching) drop-casted on such periodically patterned NCD layers exhibited the modification of their PL spectrum. We proposed some further steps for future sample improvement.

Résumé

Les nanocristaux de Silicium (SiNCs) de taille inférieure à 5 nm sont des matériaux qui présentent une intense photoluminescence (PL) et capables d'amplification optique. Cette dernière propriété est un pré-requis à l'obtention d'émission stimulée sous pompage optique. Atteindre l'émission stimulé (et l'effet laser) à partir de nanostructures basées sur Si est d'un intérêt particulier dans le domaine de la photonique à base de silicium. Le but de ce travail était (i) d'étudier les propriétés optiques fondamentales de SiNCs, (ii) de concevoir et de réaliser un cristal photonique présentant une efficacité d'extraction augmentée et (iii) d'explorer la possibilité d'améliorer le gain optique des émetteurs de lumière à base de SiNCs en les combinant avec un cristal photonique à deux dimensions. D'abord, des SiNCs isolés, passivés par oxydation (SiO_x/SiO_2), ont été préparés par attaque électrochimique d'un wafer de Si. Leurs propriétés optiques ont été étudiées par spectroscopie résolue en temps à des températures cryogéniques. La bande d'émission bleue-verte de recombinaison rapide a été attribuée à la recombinaison quasi-directe des électrons et trous chauds autour du point Γ. Le déplacement spectral en fonction de la température de la bande orange-rouge lente a été expliqué par l'effet combiné de la contrainte en tension et du déplacement intrinsèque de la bande indirecte du Si massif avec la température. Le coefficient d'amplification optique a été mesuré par la technique de "Variable stripe length" (VSL) renforcée par la méthode de "Shifting excitation spot" (SES). Nous avons démontré que les SiNCs préparés par attaque chimique et contenus dans des matrices sol-gel de SiO_2 présentaient pour les deux bandes d'émission une amplification optique de l'ordre de quelques dizaines de cm^{-1}. La présence de gain optique ultrarapide a été étudiée dans des SiNCs passivés par oxydation dispersés dans l'éthanol. Elle n'a pas pu être observée pour cette composante de la luminescence à cause d'une puissance insuffisante des impulsions excitatrices. D'autres types de SiNCs, des SiNCs isolés méthyle-capsulés ($-CH_3$) et des multicouches de $SiNCs/SiO_2$, ont aussi été étudiés expérimentalement. Dans les premiers, aucune amplification optique n'a pu être détectée, très probablement à cause de la concentration très faible de SiNCs dans cet échantillon alors que dans les deuxièmes, des pertes par absorption dues aux porteurs libres (FCA) ont empêché l'émission stimulée et, par conséquent, l'observation du gain optique. L'amplification optique peut cependant être augmentée en utilisant des structures diélectriques périodiques : des cristaux photoniques. Des simulations numériques par "Finite-difference time-domain computer simulation technique" ont montré qu'une émission stimulée pouvait être obtenue dans un milieu à faible gain si celui-ci est incorporé dans un cristal photonique à deux dimensions spécialement conçu. Dans cet esprit, un cristal photonique à deux dimensions a été fabriqué sur une couche de silice contenant des SiNCs. La structure a montré une augmentation de l'efficacité d'extraction de la lumière émise par les SiNCs par rapport à une couche simple. Une augmentation de l'intensité d'un facteur 7 a été obtenue pour des modes se propageant verticalement dans la couche. Cet effet a été attribué à une diffraction de Bragg des modes guidés due à la périodicité. Par contre, aucun début d'émission stimulée n'a été observée, probablement à cause de pertes par FCA caractéristiques de cet échantillon. Nous avons également montré que des couches de diamant nanocristallin (NCD) préparées avec un cristal photonique à deux dimensions sur leur surface présentaient une efficacité d'extraction jusqu'à un facteur 6 supérieure à celles de couches de NCD simples. Dans le cas des couches de NCD, les sources de lumière n'étaient pas des nanocristaux mais des défauts de différentes natures introduits pendant le processus de fabrication. Les SiNCs passivés par oxydation, préparés par attaque chimique et "drop-castés" sur de telles couches de NCD périodiquement structurées voient leur spectre de PL modifié.

Abstrakt

Křemíkové nanokrystaly (SiNCs) menší než cca 5 nm jsou materiálem s účinnou foto-luminiscencí (PL) za pokojové teploty, která vykazuje i optický zisk. Optický zisk je nutná podmínka k dosažení stimulované emise z vybuzeného materiálu a právě dosažení stimulované emise (a laserování) z nanostruktur na bázi Si je důležité z pohledu křemíkové fotoniky. Cílem této práce bylo (i) studovat fundamentální optické vlastnosti SiNCs, (ii) navrhnout a připravit fotonický krystal se zvýšenou extrakcí světla a (iii) prostudovat možnost zvýšení optického zisku SiNCs jejich zabudováním do dvoudimenzionálního fotonického krystalu. Nejdříve byly pomocí elektrochemického leptání Si desky připraveny oxidem (SiO_x/SiO_2) pasivované SiNCs. Jejich optické vlastnosti byly prostudovány použitím časově rozlišené spektroskopie, a to i za nízkých teplot. Rychlý modrozelený emisní pás SiNCs byl interpretován jako kvazipřímá rekombinace horkých elektronů s dírami v blízkosti bodu Γ. Dále bylo ukázáno, že spektrální posuv pomalého oranžověčerveného pásu SiNCs s teplotou je důsledkem souhry tlakové a teplotní změny zakázaného pásu objemového Si. Koeficient optického zisku byl měřen metodou "Proužku s proměnnou délkou" (VSL) doplněnou technikou "Posouvajícího se ex-citačního bodu" (SES). Ukázali jsme, že SiNCs (připravené leptáním) zabudované do SiO_2-solgel matrice vykazují optický zisk v řádu desítek cm^{-1} na obou luminiscenčních pásech. Existence ultrarychlého zisku byla studována v oxidem pasivovaných SiNCs rozptýlených v etanolu, avšak důsledkem nedostačujícího výkonu excitačních pulzů nebyl ultrarychlý zisk po-zorován. Taktéž byly studovány další typy SiNCs, a to metylem ($-CH_3$) pasivované SiNCs a multivrstvy SiNCs/SiO_2. V prvním typu vzorku byl naměřený nulový čistý optický zisk inter-pretován jako důsledek nízké koncentrace SiNCs. V multivrstvách SiNCs/SiO_2 zase vysoké ztráty absorpcí na volných nosičích zabránily vzniku stimulované emise. Optický zisk se však dá zvýšit použitím periodických dielektrických struktur, fotonických krystalů. Použitím počítačové simulace založené na metodě "Finite-difference time-domain" jsme ukázali, že stimulované emise z aktivního média s nízkým optickým ziskem je možné dosáhnout jeho zabudováním do dvou-dimenzionálního fotonického krystalu. Na základě těchto výsledku byl na povrchu křemenné destičky se zabudovanými SiNCs vyroben dvoudimenzionální foton-ický krystal. Ukázali jsme, že tato struktura umožňuje, oproti planární vrstvě, efektivní zvýšení extrakce světla (emitovaného SiNCs) do vzduchu. Bylo dosaženo až sedminásobného zvýšení intenzity světla extrahované ve směru kolmém k povrchu vrstvy jako důsledek Brag-govské difrakce vedených modů na povrchové periodicitě. Nástup stimulované emise jsme však nepozorovali, což je s největší pravděpodobností důsledek vysokých ztrát absorpcí na volných nosičích ve studovaném vzorku. Až šestinásobné zvýšení efektivity extrakce světla bylo změřeno pro nanokrystalické diamantové (NCD) vrstvy s dvoudimenzionálním foton-ickým krystalem na jejich povrchu v porovnání s planárními NCD vrstvami. Zdrojem světla byly v případě NCD vrstev různé defekty, vznikající během výrobního procesu. Dále jsme ukázali, že PL spektrum SiNCs je možné modifikovat nakápnutím jejich roztoku na periodicky strukturovanou NCD vrstvu. Navrhli jsme, jakým směrem lze v tomto výzkumu pokračovat dále.

Acknowledgements

First of all, I would like to thank both my supervisors, Dr. Kateřina Herynková and Prof. Bernd Hönerlage, for their guidance and support during the research and writing of this thesis. The major part of this work was done at the IPCMS-DON, CNRS in Strasbourg (France) and at the Department of Thin Films at the Institute of Physics, ASCR in Prague (Czech Republic). This concerns the experimental work as well as the theoretical simulations.

I would like to express my sincere gratitude to Prof. Ivan Pelant for his support and great help with experimental and theoretical issues that I had to deal with during my doctoral studies. I would like to thank him for a patience during our discussions on different scientific topics and during writing manuscripts and this thesis.

I would also like to express my great appreciation to Prof. Jiří Čtyroký for sharing invaluable knowledge about waveguide and photonic crystal physics with me and for providing me an access to his computational software.

Furthermore, I owe my thanks to all the members of the Department of Thin Films and Nanostructures in Prague for creating helpful and friendly atmosphere. Namely, I would like to mention two Katka's that I had the pleasure to work with, Dr. Kateřina Dohnalová and Dr. Kateřina Kůsová.

I cannot forget to thank all the members of the Department of Ultrafast Optics and Nanophotonics in Strasbourg, Dr. Pierre Gilliot, Dr. Mathieu Gallart, Ing. Marc Ziegler and Ing. Olivier Crégut. I want to express my thanks to my friends Dr. Jean Besbas, Dr. Bertrand Yuma and MSc. Déborah Persuy for making my stay in Strasbourg very joyful and pleasant.

I would also like to acknowledge and thank scientists, who took care about the fabrication of samples investigated in this thesis. Photonic crystal samples were fabricated by Dr. Marián Varga, Dr. Oleg Babchenko and Dr. Alexander Kromka from the Institute of Physics, ASCR. Silicon nanocrystals-rich/SiO_2 multilayers were fabricated by the group of prof. M. Zacharias from the Albert Ludwigs University in Freiburg (Germany). Samples fabricated by the implantation of Si^+ into silica matrix were provided by Dr. S. Cheylan from the University of Canberra (Australia).

Last but not least, my personal thanks belong to all members of my family. Without discussion, the greatest thanks belong to my wife Ing. Maja Ondičová and my little daughter Sofia Lili for making my every day beautiful and full of surprises.

Contents

List of Abbreviations and Symbols

Abbreviation	Description
0/1/2/3D	One/two/three dimensional
C480	Coumarin 480
CMOS	Complementary metal-oxide-semiconductor
cw	Continuous wave
DFB	Distributed feedback
DOS	Density of states
FCA	Free carrier absorption
FDTD	Finite-difference time-domain
H_2O_2	Hydrogen peroxide
HF	Hydrofluoric acid
HRTEM	High resolution transmission electron microscopy
(i)CCD	(Intensified) charge-coupled device
InP	Indium phosphide
(int)SES	(Integrated) shifting excitation spot
LED	Light-emitting diode
MEEP	MIT electromagnetic equation propagation
MIT	Massachusetts Institute of Technology
MPB	MIT photonic-bands
MQW	Multi-quantum well
NA	Numerical aperture
NC(s)	Nanocrystal(s)
NCD	Nanocrystalline diamond
OPA/O	Optical parametric amplifier/oscillator
PECVD	Plasma-enhanced chemical vapor deposition
PL	Photoluminescence
QD(s)	Quantum dot(s)
RCWA	Rigorous coupled-wave analysis
Si	Silicon
SiNCs	Silicon nanocrystals
SiO_2	Silicon dioxide
TE	Transverse-electric
TM	Transverse-magnetic
UV	Ultraviolet
VSL	Variable stripe length

Symbol	Description
α	Coefficient of band-to-band absorption
α_{FCA}	Coefficient of FCA losses
η	Internal quantum efficiency
θ	Angle of incidence (with respect to the sample normal)
λ	Wavelength of light in vacuum (air)
ξ	Filling factor
σ_{FCA}	FCA cross-section
τ_{nr}	Non-radiative lifetime
τ_r	Radiative lifetime
ω	Frequency of light
$E(\mathbf{k})$	Electronic band diagram
E_{exc}	Excitation energy
E_{gap}	Optical bandgap energy
g	Optical gain coefficient
G	Net optical gain coefficient
I_x	Intensity of the signal
K	Coefficient of scattering
$\mathbf{k}$	Wavector
n	refractive index
n_{NC}	Volume density of NCs
m	mode number

Institutes

AVČR	Akademie věd České republiky, v.v.i.
ASCR	Academy of Sciences of the Czech Republic, v.v.i.
FZÚ	Fyzikální ústav
IoP	Institute of Physics
IPCMS	Institute de Physique et Chimie des Matériaux de Strasbourg
CNRS	Centre national de la recherche scientifique

Introduction

Introduction

Nowadays, the fastest supercomputers reach 10^{15} (peta) floating-point operations per second (flop/s) performance. For comparison, ordinary calculator performs only several flop/s. These supercomputers consist of several thousands of nodes, one of the best—IBM Sequoia, USA— has more than 98 thousand of servers covering area of about 420 m^2 [1]. However, the power consumption of such a system is immense reaching about 8 MW. Most of it is used on moving an enormous amount of data by electrical interconnects between the nodes which inevitably generates a great amount of heat. The future goal is even to increase the performance speed to exaflop/s (exabyte = 10^{18} byte), however for such computers, the power consumption and heat generation issues must be addressed. A possible solution might be moving data using light, the so-called photonics.

So far light has been mainly used to send information over long distances because it provides very fast and almost lossless connections. Nevertheless, also the idea of using optical interconnects on shorter distance levels, either for connecting servers or inter or even intra-chip connections already exists for some time, however, it is limited mostly by high cost and several technological issues. In order to make this approach cost-effective, a technology based on silicon (i.e. silicon photonics) should be used [2, 3, 4]. Silicon, the second most abundant element in Earth's crust compatible with well-developed CMOS technology, when used as an optical medium may provide the economies of scale, ease of manufacture and low costs.

The basic principle of a silicon-based optical circuits is the following: at the input, light emitted by a coherent light source (laser) is sent through an optical waveguide. During its propagation, an electronic information is encoded onto light by modulators. At the output, light is detected and decoded into electrical signal. Nowadays, producing silicon waveguides, high speed photodetectors and even silicon-based modulators [5, 6] is possible. However, even though the optically-pumped Raman silicon laser was already demonstrated [7, 8], the main drawback still remains the absence of an electrically-pumped silicon-based laser.

Presently, silicon is the most important semiconductor in the electronic and photovoltaic industries, which follows from a combination of its excellent properties: wide-abundance and thus low-cost, non-toxicity and high-purity, well-developed processing technology, tunable electrical properties and existence of an insulating natural oxide (SiO$_2$). Unfortunately, silicon is an indirect semiconductor with very poor luminescence (quantum efficiency as low as 10^{-6}). Therefore, alternative solutions must be used. The most popular approach is based on a combination of III-V lasers directly attached to the silicon chip, the so-called hybrid silicon lasers [9], in which light generated by the III-V laser is coupled to the silicon waveguide. Devices based on this approach are already available on the market (see, e.g. Luxtera [10]). However, more cost-effective would be to have a true silicon-based laser, which would allow

smaller size and true integration.

Various ways are studied to obtain efficient luminescence and lasing from silicon, mainly taking advantage from the quantum confinement of excitons in a nanometer-scale crystalline structures. Silicon nanostructures, such as porous silicon [11, 12, 13, 14], silicon quantum dots or nanocrystals [15], silicon-on-insulator superlattices [16, 17] and silicon nanopillars [18], offer a potential for being an efficient light-emitter that may be used in silicon photonics. Silicon nanocrystals with sizes below 5 nm are a material with relatively high luminescence quantum yield [19, 20]. However, achieving lasing from silicon nanocrystals remains a challenge due to their low optical gain [21, 22], which is a parameter describing a single-pass amplification of light propagating through an excited medium. Except the positive optical gain, which is an essential prerequisite for lasing, also the optical quality of a material is very important in order to avoid losses caused by light scattering.

However, even in devices with low optical gain, the lasing action can be achieved via combining them with a photonic crystal. The photonic crystal is a periodically modulated material possessing a periodicity in the refractive index in one-, two- or three-dimensions that can control photons, much as semiconductors control electrons. It was shown theoretically [23] and also experimentally [24] that two-dimensional photonic crystals with optical gain can be used to achieve stimulated emission. In addition, stimulated emission at low temperature was already demonstrated for periodically surface-patterned bulk silicon [25]. The photonic crystal provides an optical feedback for the radiation caused by multiple reflections on the periodicity. Due to many passages of light through the active material, laser action can build-up even with low optical gain. Moreover, photonic crystals can serve also as passive devices which increase light extraction efficiency from layers doped with a luminescent material. Light propagating in a material with periodically patterned surface can interact with the periodicity and be Bragg-diffracted into surrounding air.

Aim of this thesis

This work was conducted within the doctoral program "en-cotutelle" realized between Charles University in Prague (represented by the Institute of Physics (IoP), Academy of Sciences of the Czech Republic in Prague) and the University of Strasbourg (represented by the Institute of Physics and Chemistry of Materials of Strasbourg (IPCMS), French National Centre for Scientific Research).

The aim of this thesis is to investigate a possibility of enhancing the optical gain of light-emitting silicon nanocrystals by combining them with a two-dimensional photonic crystal. To achieve this goal, first, the recombination and relaxation processes of photo-excited carriers in silicon nanocrystals must be understood and an optical gain coefficient must be evaluated. Then, information from these measurements will be employed during the theoretical design of photonic crystals. Two-dimensional photonic crystals will be used to increase the extraction efficiency and optical gain of embedded light-emitting medium. Dimensions of these photonic structures will be chosen so that an overlap between the emission spectrum of a light source and the leaky modes of the photonic crystal is achieved. First, the optical properties of two-dimensional photonic crystals prepared on a nanocrystalline diamond layer such as a photonic band diagram, absorption and extraction efficiency will be studied. This will allow us to understand the physics of light propagation in photonic crystals. The acquired knowledge will be then applied to design and fabricate a two-dimensional photonic crystal on a silica layer embedded with silicon nanocrystals. The possibility of enhancing optical gain of silicon nanocrystals combined with a photonic crystal will be studied both experimentally

and theoretically.

The text of this thesis is organized into an introduction, seven chapters and an appendix. The chapters (3–6) comprising the original results of this work are build on the articles authored or co-authored by the author of this thesis. In these chapters, always a short summary of the main results is given, which is then followed by the enclosed publications.

Chapter 1 of this thesis explains the physics of efficient luminescence in silicon nanocrystals compared to very poor emission from a bulk silicon. It summarizes results from the literature concerning the optical properties of silicon nanocrystals which will be relevant in the following parts. It also gives a list of the properties of an ideal sample that should possess high optical gain.

Chapter 2 presents the mechanism of light propagation in photonic crystals; mostly in the structures with a two-dimensional periodicity. The concept of a photonic band diagram is thoroughly explained in order to allow the reader fully understand the results of this thesis. Further, the principle of light extraction from photonic crystal slabs is described and a practical example of this effect is given. Finally, the principle of the optical gain enhancement phenomenon together with its experimental realization is presented.

Chapter 3 focuses on the fundamental optical properties of our oxide-passivated silicon nanocrystals. First, a preparation method of such nanocrystals is briefly explained. Then, experimental setups employed for the characterization of recombination processes in the studied samples are presented. Finally, the results of experiments uncovering temporally, spectrally and temperature-resolved information about luminescence in silicon nanocrystals are discussed.

Chapter 4 describes the principle of a method used for the evaluation of an optical gain coefficient. The results of this method applied to different types of samples based on silicon nanocrystals are presented. Finally, the computer-simulation-based verification of the optical gain enhancement phenomenon in photonic crystals with low optical gain is given.

Chapter 5 explains theoretical and experimental approaches employed to design and characterize the two-dimensional photonic crystals studied in this thesis. It also comprises the results of enhanced light extraction efficiency from nanocrystalline diamond photonic crystals.

Chapter 6 summarizes experimental results, which evidence the influence of photonic crystals (fabricated on the top of two different materials) on the emission properties of silicon nanocrystals.

Chapter 7 concludes the experimental and theoretical findings of this work. It also presents ideas how to continue in order to achieve the goal of enhanced optical gain in silicon nanocrystals.

The appendix comprises a commentary to videos which are attached to this thesis. These videos aim to show methods used for the evaluation of an optical gain coefficient and to illustratively explain the phenomenon of light extraction (coupling) from (into) photonic crystals.

For easy orientation in the pdf text of this thesis, references to chapters, sections, figures, tables and citations are done in an interactive form, so that clicking on the reference number will bring the reader directly to the particular reference. Figures, tables and equations are numbered sequentially, separately for every chapter. Numbers in square brackets are used for citations, which are all placed at the end of the text.

At the very end of the text, a curriculum vitae of the author, with a complete list of his publications, is attached.

Chapter 1

Silicon nanocrystals

1.1 Silicon

A crystal is an arrangement of atoms or molecules ordered in a periodically repeating pattern called the Bravais crystal lattice. Silicon is a semiconductor with a diamond crystal lattice. The crystal introduces a periodic potential to electrons which are delocalized in it. For certain energies and directions of propagation of electrons, described by dispersion relations (band diagram), electrons can propagate (in the perfect crystal without defects) like a diffuse gas of free particles. On the other hand, the propagation through the crystal is forbidden for certain intervals of electrons' energies, the so-called bandgaps. Wavefunction of the electron is a Bloch-mode [26, 27], which basically comprises a plane wave modulated by a periodical function dictated by the crystal periodicity. As a consequence of the periodicity, all physically relevant electronic modes are included in the first irreducible Brillouin zone of the crystal lattice. As already mentioned, the band diagram is a relation of the electron energy with respect to its propagation vector characterized by the electron wavevector **k** (momentum). Values of the wavevector are chosen such that they follow significant directions in the momentum (reciprocal) space up to the points of high symmetry of the Brillouin zone since band extrema occur most often at these points.

Figure 1.1 shows the simplified sketch of the electronic band diagrams of Indium phosphide (InP) and Silicon (Si). At equilibrium (and at low temperature), the highest occupied energy band is a valence band and the lowest unoccupied is a conduction band, separated by the energy gap E_{gap}. Under high energy (exceeding the bandgap) external excitation, electrons
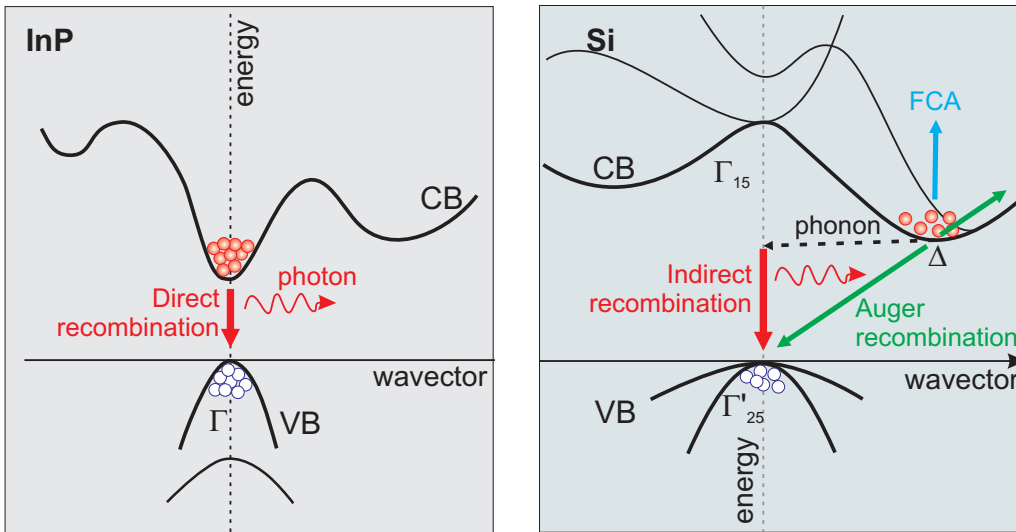

Figure 1.1: Simplified plot of electronic band diagrams of InP (left) and Si (right). Indium phosphide is a direct bandgap semiconductor, in which the radiative recombination of the excited electrons (red dots) in the conduction band (CB) with holes (white dots) in the valence band (VB) is a two particle process, which takes place at the Γ-point of the Brillouin zone. On contrary, Si is an indirect semiconductor in which the recombination of electron with hole happens via a phonon-assisted transition. Two main processess which hamper luminescence of Si, Auger recombination and free-carrier absorption (FCA), are also depicted.

are excited from the valence band to the higher states within the conduction band leaving empty states, holes, in the valence band. Afterwards, by emission of phonons, the electrons quickly relax to lower energy states and finally reach the minimum of the conduction band (in Si it happens on the time scale of the order of $10^{-11} - 10^{-13}$ s). Similarly, the holes thermalize

reaching the very top of the valence band. Finally, either radiative (emission of photons) or non-radiative (emission of phonons) recombination of electron-hole pairs takes place in the material. Indium phosphide is a direct bandgap semiconductor, i.e. maximum of the valence band and minimum of the conduction band line up vertically on the wavevector axis, or in other words, they share the same crystal momentum. Consequently, the radiative direct recombination occurs rapidly (on the nanosecond time scale) and efficiently via a two-particle (electron and hole) process. On the other hand, Si is an indirect bandgap semiconductor, in which the minimum of the conduction band at Δ-valley is not aligned with the maximum of the valence band at the Γ-point of the Brillouin zone. Therefore, the radiative recombination of the electron and hole must involve a third particle—phonon—which carries away the excess momentum. This results in very low optical transition rates with an energy of the emitted photon close to that of the indirect bandgap $E_{gap} = 1.12$ eV (at room temperature). The efficiency of this radiative transition is very low due to the existence of faster non-radiative processes. One of the major non-radiative processes is the Auger recombination, during which the recombining electron transfers the released energy to another electron in the conduction band. Another non-radiative process may be mediated by a free-carrier absorption (FCA) mechanism wherein the emitted photon is absorbed by an excited electron in the conduction. In both aforementioned non-radiative processes (Fig. 1.1), electrons absorb the energy, jump to the higher energetic level in the conduction band and then release the excess energy in the form of phonons, i.e. transfer the energy to the crystal lattice in the form of heat.

The probability of non-radiative processes in Si is much higher than the probability of the indirect-radiative recombination. Therefore, lifetimes (inversely proportional to the probability of the process) of non-radiative processes τ_{nr} are much shorter than those of radiative processes τ_r in Si. This results in a very low internal quantum efficiency η of light emission (luminescence), which is defined as a ratio of radiative to overall recombination probability [28]:

$$\eta = \frac{1/\tau_r}{1/\tau_r + 1/\tau_{nr}}. \tag{1.1}$$

Its value is generally of the order of 10^{-6} in Si. Therefore it naturally follows that Si is a very poor light emitter. As already presented in Introduction, even though optical devices such as modulators, waveguides, detectors were already manufactured from crystalline Si, the inability to prepare electrically-pumped coherent light sources based on Si hinders silicon photonics. The problem of low luminescence efficiency of bulk Si can be overcome by moving from bulk to structures with dimensions on the nanometre length scale (nano-scale), as explained in the next section.

1.2 Silicon nanocrystals

1.2.1 Origin of photoluminescence

In this section, interesting physical phenomena, which arise when dimensions of Si are decreased to the nano-scale, are described. Depending on the degree of freedom of the electron movement in nanostructures, nanomaterials can be divided into three main categories: two-dimensional (2D) quantum wells, one-dimensional (1D) nanowires and zero-dimensional (0D) quantum dots (QDs) or nanocrystals (NCs). In the direction of the spatial confinement, the energy of electrons becomes quantizied, i.e. forms discrete atomic-like energy levels, due to the more rigid boundary conditions imposed on the charge carriers' wavefunctions in the material.

As a consequence, density of states (DOS) in nanostructures becomes lower compared to that of the bulk, which is schematically depicted in Fig. 1.2(a).

A simplified model of a silicon nanocrystal (SiNC) based on the model of a particle in a QD explains qualitatively the well-known shift (splitting) of the energetic levels with the NC size. As the QD gets smaller, energy intervals between its electronic levels increase. Similarly, with decreasing the diameter of the NC, its bandgap opens, i.e. the conduction and valence bands move further apart from each other. This phenomenon, which arises from spatial localization of carriers in a nanometre-sized volume, is known as quantum confinement effect. More specifically, it occurs when the dimensions of a nanostructure are comparable to the Bohr-radius of an exciton in the bulk material, which is in the case of Si around 5 nm.
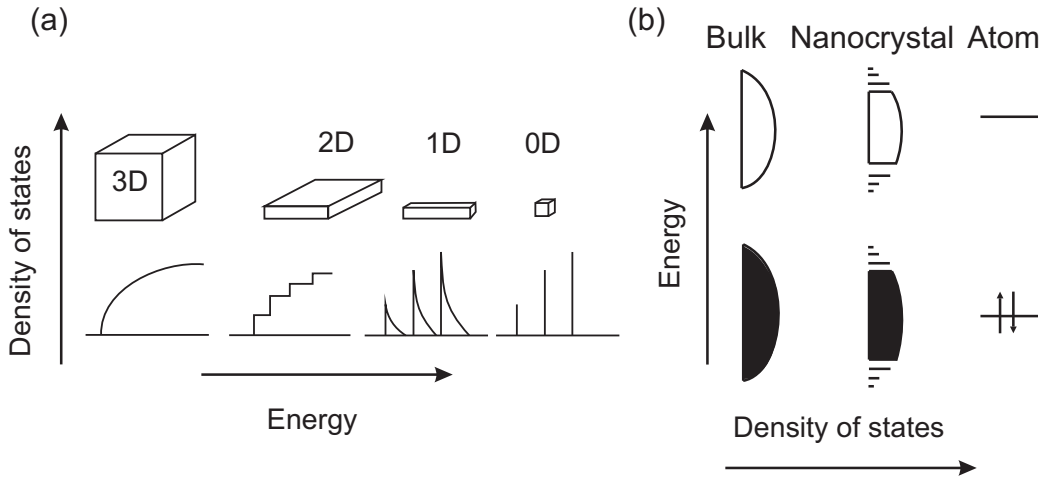

Figure 1.2: (a) Schematic illustration of the density of states in semiconducter clusters. (b) Density of states in one band of a semiconductor as a function of dimension. Adapted from Ref. [29]

However, more realistic picture of what happens with the energy bands when moving from bulk to a nanocrystal and to a single atom is depicted in Fig. 1.2(b) [29]. In the nanocrystal, discrete levels are formed at the former band edges, where the DOS is rather low, however, these levels overlap in the former center of the band due to high DOS and due to a broad homogeneous linewidth.

For a particle in a periodic potential of the bulk solid, the energy and momentum can be both precisely defined, whereas its position cannot. This follows from Heisenberg's uncertainty principle. On the contrary, quantum confinement of the particle in a small volume (nanocrystal) induces that uncertainty of the particle's position decreases due to its localization, which results in non-zero uncertainty of the particle's momentum. Therefore, even though the energy of the particle is well-defined, the concept of the band diagram E($\mathbf{k}$) seems to have no more sense for NCs. However, this is not entirely true as was shown recently by Hapala et al. [30]. Figure 1.3 shows the $\mathbf{k}$-space densities of the electronic states in the Γ-X direction for the $-$H passivated SiNCs with different sizes computed by the authors of Ref. [30]. For all studied sizes of NCs, the effect of state delocalization in momentum space and the formation of discrete levels preferentially close to the band edges ($\rightarrow$ minigaps) is evident. Interestingly, dispersion of the blurred electronic bands, which copy the shape of the Si bulk band structure, can be distinguished for sizes of 2 and 2.5 nm (compare Figs. 1.3(b,c) with (d)). Consequently, according to the simulation, $-$H passivated SiNCs bigger than 2 nm in diameter preserve their indirect bandgap character. Finally, the effect of the bandgap widening with decrease of the NC size is also verified by the computation in Fig. 1.3.
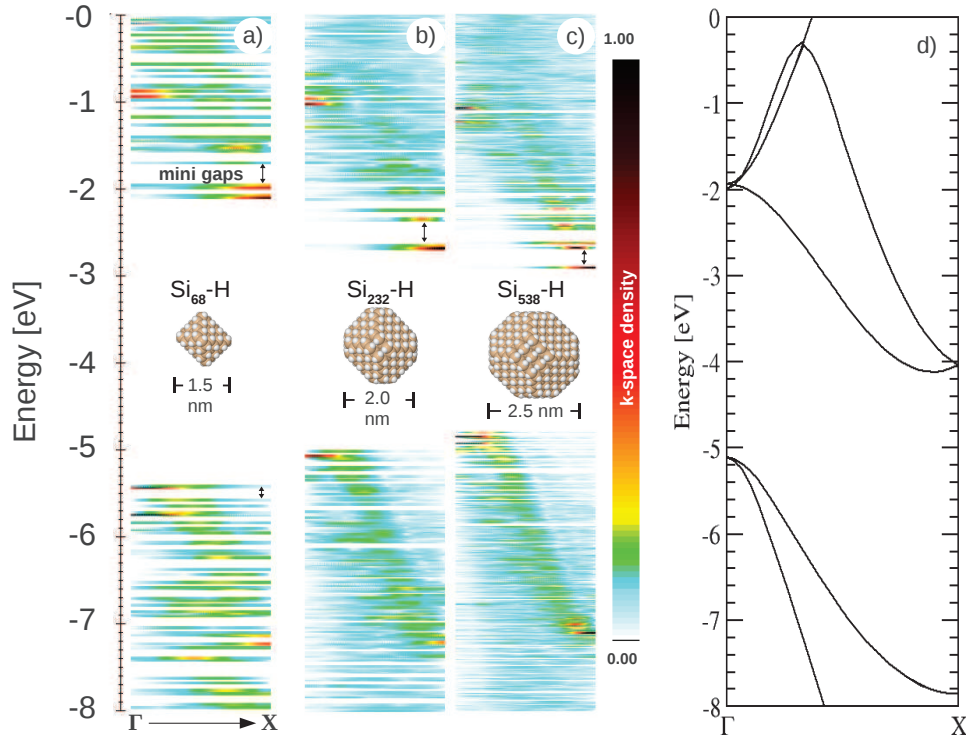
Figure 1.3: 1D cross sections of the projected k-space density of electronic states in the −H passivated SiNCs of different sizes: (a) 1.5 nm, (b) 2.0 nm and (c) 2.5 nm. Gradual emergence of energy bands which qualitatively resemble the bulk Si band structure plotted in (d) can be seen with increasing NC size. The color scale is normalized by the maximal density independently for each NC size. Taken from Ref. [30]

Despite the fact that −H passivated SiNCs are an interesting material from the point of view of theoretical studies, other types of passivation, which are stable in air, are needed from the perspective of the practical application of SiNCs. Air-stable passivation of SiNCs is realized by covering their surface either by silicon oxide or by various organic species. The type of surface passivation has then important influence on their optical properties due to the large surface-to-volume ratio. The passivation causes that electronic states are often more localized in real space compared to those of −H passivated NCs of a similar size [30], which implies higher delocalization in **k**-space causing relaxation of **k**-conservation restriction and selection rules of optical transitions and increasing the probability of radiative recombination. Electronic wavefunctions of some electronic states can be also partially localized at the surface of the NC ("surface states"), however, these states are still core-related states as the core has the major influence on their properties.

Experimentally, efficient photoluminescence (PL) from Si nanostructures, namely porous Si, was firstly demonstrated by Canham in 1990 [11]. Light-emitting porous Si is basically a network of interconnected small SiNCs. Since then the interest in light emission from SiNCs arose and a large effort was made to understand the mechanism underlaying the origin of the PL. Two main emission bands are usually observed in the PL spectra of SiNCs, one (slowly decaying in time) located in the red-orange and the other one (fast decaying) in the blue-green spectral range. However, a lack of consensus regarding their microscopic origin persists even after more than 20 years from their discovery.

Two main models have been widely discussed with respect to the origin of the red-orange band. First, a quantum confinement model based on an assumption of a strong relaxation of **k**-conservation rule, which should lead to an efficient and fast quasi-direct phonon-less recombination in the core of NC. The second (quite opposite) model attributes the red-orange PL of SiNCs to strongly localized oxygen-related surface states (as defined above) located in the bandgap and resulting in slowly decaying PL. However, a different model was suggested recently by Hannah et al.[31], which may finally explain the true origin of the slow-decaying PL band in SiNCs. Authors proved via pressure-dependent measurements of the PL of organically passivated SiNCs of sizes down to 2.6 nm, that the long-lived (on the microsecond time scale) efficient red-orange PL originates from the core-states with indirect-gap character [31] (although the corresponding wavefunction might be real-space partially localized at and thus sensitive also to the surface [30, 32]). Simulations regarding the SiNCs with $Si-O-Si$ defect on the surface show similar results of pressure-dependent PL, which means that the long-lived PL in oxygen (silicon oxide) passivated SiNCs may also originate in the indirect (from the Δ-valley to the Γ-point) radiative recombination [31].

On the other hand, the origin of fast-decaying (typically on the nanosecond time scale) blue-green PL band is still under debate. In the case of small (2.2 ± 0.5 nm) alkyl-passivated SiNCs, it was recently shown that the core-related quasi-direct recombination is the major radiative channel [33]. In the case of larger, oxide-passivated SiNCs, as those investigated in this thesis, the situation is not such straightforward and there exist again at least two possible explanations. One group of authors [34, 35] claim that oxide-defects present in the SiO_x surface capping layer are responsible for the fast (F) blue-green PL, sometimes also called the F-band. A second group of authors [36, 37, 38, 39] identify the F-band with PL originating in the core of very small nanocrystals. In addition, it was recently experimentally shown that a direct $\Gamma - \Gamma$ recombination at the Γ-point of the Brillouin zone can be achieved in SiNCs under specific excitation conditions [40], which may be another way to explain the F-band origin. As it follows from the above discussion, more scientific work needs to be done to understand the origin of the F-band, which was also partially aim of this thesis.

To summarize, quantum confinement effect and suitable surface passivation makes SiNCs a material with interesting physical properties such as efficient quantum yield of PL up to 80%, tunable size of the bandgap $\rightarrow$ tunable color of emission and absorption energy, multi-exciton generation [41, 42], blinking effects [43] and positive optical gain [44]. The latter is discussed in detail in the next paragraph.

1.2.2 Optical gain

As already briefly explained in Introduction, optical gain is a parameter of the material which describes its ability to amplify light via the process of stimulated emission. Positive value of the optical gain coefficient is an essential prerequisite for lasing. However, in order to obtain laser action, positive optical gain must outweigh the losses of the system caused mainly by the non-radiative processes, by light scattering and re-absorption. Finally, a well-tuned optical resonator providing feedback is needed to realize a true light generator (not a mere amplifier).

First demonstration of very high positive optical gain of around 100 cm^{-1} obtained in SiNCs dispersed in SiO$_2$-matrix was published by Pavesi et al. in 2000 [44]. However, since then such a high value of the optical gain was neither reproduced nor confirmed by applying similar experimental conditions. Rather lower values, of the order of tens of cm^{-1}, were measured by several groups, mostly on the red-orange slowly decaying band [16, 45, 46, 47, 48, 49, 50] but also on the fast-decaying blue-green band [51, 52].

Recently, also ultra-fast (subpicosecond) stimulated emission was obtained in solution

of oxide-passivated SiNCs under special excitation conditions achieved by using high power femtosecond laser pulses [53]. Authors reported very high values of the optical gain up to 600 cm^{-1} for highly concentrated samples.

Optical gain can be experimentally evaluated by several techniques. The two ones, usually used with SiNCs, are Pump & probe and Variable stripe length (VSL) techniques. The latter will be in detail described in Chapter 4.

Finally, following results from literature, the properties of a sample containing SiNCs, that is expected to be an ideal candidate possessing high optical gain, are summarized in the following list.

1. Small diameter of NCs.
   In order to avoid FCA losses, which decrease quadratically with decreasing wavelength of the absorbed photon [54], the bandgap of SiNCs should be as large as it can be reached by the preparation technique. From this point of view, organically-capped SiNCs with PL band located in the blue-green [33] or yellow [55] spectral range are more suitable for obtaining stimulated emission than oxide-passivated SiNCs emitting either in the orange-red [56] or even infrared [44] spectral range. In particular, SiNCs embedded in a solid SiO$_2$ matrix seem not to be a good choice.

2. High concentration of SiNCs.
   Indeed, the more NCs are present in the excited area, the more of them can participate in the stimulated emission. Certain minimum filling factor of SiNCs must be achieved [28]. However, the optical quality must be preserved or some ideal balance between the concentration and the optical quality has to be found.

3. High optical quality.
   Agglomeration of SiNCs into large clusters (hundreds of nanometers or a micron in diameter) enhances scattering losses of visible light which also compete with the optical gain. The effect of agglomeration is passivation-dependent and occurs mostly for oxide-passivated SiNCs prepared by electrochemical etching of Si wafer [56]. In the case of samples prepared by thermal annealing of Si-enriched SiO$_2$ subtrate, a very good optical quality can be achieved up to a certain concentrations after which the agglomerates may appear. However, the best results are usually obtained for organically-capped SiNCs dispersed in a liquid solution [55] (colloidal dispersion). This is related to the fact that properly organically-capped SiNCs do not agglomerate and therefore do not scatter light of visible wavelengths.

4. Narrow distribution of sizes of NCs.
   PL spectrum of an ensemble of SiNCs with different diameters is inhomogeneously broadened. Therefore, when the lasing, which normally occurs at a single wavelength, is achieved, only a part of NCs emitting at this particular wavelength will contribute to the stimulated emission signal.

5. High PL quantum yield (proper surface engineering).
   In order to suppress most of the non-radiative processes that can occur in SiNCs, in particular, non-radiative recombination due to unsaturated dangling bonds on the NC's surface and Auger recombination, a suitable chemistry of the capping layer must be found. The inhibition of Auger recombination was recently achieved in II-VI nanocrystals [57, 58].

Chapter 2

Photonic crystals

2.1   Theory

A crystalline solid or crystal is composed of periodically arranged atoms or molecules in three dimensions which create a periodic electronic potential for moving electrons. Analogously, in optics, a photonic crystal is created by a periodic patterning of a dielectric material, i.e. by introducing a periodicity in the dielectric function or, equivalently, in the refractive index. In this case, control over propagation of photons rather than electrons is of interest. The simplest example of a photonic crystal is a quater-wave stack of alternating layers of two different materials which works as a reflector for a certain interval of light wavelengths. By definition, the quater-wave stack is a 1D photonic crystal due to its periodicity spanning in one dimension perpendicular to the layers. The interval of completely reflected wavelengths is called a photonic bandgap. As it will be shown later, similarly as behavior of electrons in a crystal is described by an electronic energy band diagram, propagation of photons in a photonic crystal is described by a photonic band diagram. Depending on the energy and direction of propagation, photons can either move without losses in a photonic crystal or their propagation may be completely forbidden. In other words, photonic bandgaps are introduced for certain colors of light, which can be used for controlling the light propagation. More complicated 1D photonic crystals together with 2D and 3D photonic crystals are shown in Fig. 2.1. Figure 2.1 depicts an optical circuit based on different types of photonic crystals where for example a nano-cavity is created by omitting one hole in the middle of a photonic crystal waveguide (red-colored), i.e. by creating a defect in the periodic sequence of the holes [59]. Light of wavelengths falling within the photonic bandgap of this structure and fulfilling a boundary condition can be trapped as a resonant cavity mode. The main advantage of such a cavity is that the optical mode is confined in a very small space of several hundreds of nanometers long ($\rightarrow$ small modal volume). Cavities with high Q-factors can be achieved by proper engineering of the photonic crystal dimensions, which allow to enhance spontaneous emission rates of light sources (e.g. QDs) embedded inside of them due to the Purcell effect [60]. Next, Fig. 2.1 also depicts a 90° bent waveguide made by cutting out one row of the dielectric rods in the green-colored 2D photonic crystal, i.e. by creating a line-defect. Due to the existence of a 2D photonic bandgap, the propagation of light with wavelengths from the bandgap is within the photonic crystal forbidden and light is guided along the line-defect only. Obviously, confinement in the z-direction (out-of-plane direction) would have to be accomplished, for example, by immersing the waveguide into a dielectric material of a lower refractive index then the rods.

In the following text, a brief theoretical description of light behavior in photonic crystals is given. The more detailed explanation can be found, e.g. in a book written by J. D. Joannopoulos et al. [61], which can also serve as a clearly written introduction to the physics of photonic crystals.

As always in electromagnetism, Maxwell's equations are the starting point, completed with certain assumptions. A dielectric medium under study will be composed of homogeneous regions of dielectric material not changing in time. It will be transparent (lossless) isotropic with no sources of light or electric current. Then the material can be described by a scalar dielectric function $\varepsilon(\mathbf{r},\omega)$. In order to further simplify the computation, material dispersion, i.e. frequency dependence of the dielectric constant, will be ignored ($\varepsilon(\mathbf{r})$) keeping in mind that the solution is valid only in a restricted interval of frequencies for which the value of dielectric constant is correct. Then the index of refraction n is simply a square root of ε ($n = \sqrt{\varepsilon}$). Next, only a linear regime (weak fields) will be considered. Then, for displacement field $\mathbf{D}$ it holds that $\mathbf{D}(\mathbf{r}) = \varepsilon_0 \varepsilon(\mathbf{r}) \mathbf{E}(\mathbf{r})$, where $\mathbf{E}$ is an electric field vector and ε_0 is the
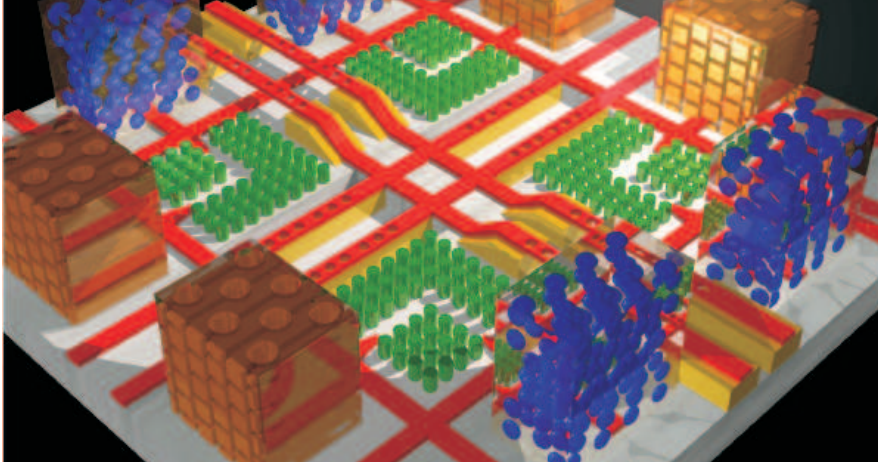
Figure 2.1: Optical circuit based on photonic crystals with different symmetries. Taken from Ref. [61].

vacuum permittivity. Similarly, magnetic induction $\mathbf{B}$ is related to the magnetic field $\mathbf{H}$ by equation $\mathbf{B}(\mathbf{r}) = \mu_0 \mu(\mathbf{r}) \, \mathbf{H}(\mathbf{r})$, where μ_0 is the vacuum permeability and $\mu(\mathbf{r})$ is the relative magnetic permeability of material which, however, is approximately unity for most dielectrics of interest.

All the above mentioned assumptions lead to the following Maxwell's equations (in SI units)

$$\nabla \cdot \mathbf{H}(\mathbf{r}, t) = 0 \tag{2.1}$$

$$\nabla \cdot [\varepsilon(\mathbf{r}) \, \mathbf{E}(\mathbf{r}, t)] = 0 \tag{2.2}$$

$$\nabla \times \mathbf{E}(\mathbf{r}, t) + \mu_0 \frac{\partial \mathbf{H}(\mathbf{r}, t)}{\partial t} = 0 \tag{2.3}$$

$$\nabla \times \mathbf{H}(\mathbf{r}, t) - \varepsilon_0 \varepsilon(\mathbf{r}) \frac{\partial \mathbf{E}(\mathbf{r}, t)}{\partial t} = 0. \tag{2.4}$$

Linearity of Maxwell's equations allows to separate temporal from spatial dependence in $\mathbf{E}$ and $\mathbf{H}$. Taken together with an assumption that the electric and magnetic field patterns will vary harmonically (sinusoidally[1]) with time, field vectors can be expressed in the following form[2]

$$\mathbf{H}(\mathbf{r}, t) = \mathbf{H}(\mathbf{r}) \, e^{-i\omega t} \tag{2.5}$$

$$\mathbf{E}(\mathbf{r}, t) = \mathbf{E}(\mathbf{r}) \, e^{-i\omega t}. \tag{2.6}$$

By inserting the above equations into Eqs.(2.1) and (2.2) we get conditions for transverse character of electromagnetic waves, i.e. electric and magnetic fields are perpendicular to the direction of their propagation. By inserting the equations for $\mathbf{E}$ and $\mathbf{H}$ into Eqs.(2.3) and (2.4) and then by combining them with the goal to obtain an equation only for $\mathbf{H}$ one gets

$$\nabla \times \left(\frac{1}{\varepsilon(\mathbf{r})} \nabla \times \mathbf{H}(\mathbf{r}) \right) = \left(\frac{\omega}{c} \right)^2 \mathbf{H}(\mathbf{r}). \tag{2.7}$$

Solutions to this equation together with the transversality condition yields a set of photonic modes having the spatial pattern $\mathbf{H}(\mathbf{r})$ and corresponding allowed frequencies ω supported by

---

[1]From Fourier analysis it follows that any solution can be build up using an appropriate combination of such harmonic modes.

[2]In order to obtain physical fields, the real part of the complex-valued fields must extracted.

the photonic crystal with given $\varepsilon(\mathbf{r})$. The frequency range of a photonic crystal can be either a continuous or discrete set or combination of both depending on the spatial boundaries of the system.

The equation above can be looked upon as an eigenvalue problem: The result of the operator acting on a function $\mathbf{H}(\mathbf{r})$ (an eigenvector or eigenmode) is a constant (an eigenvalue) times the original function $\mathbf{H}(\mathbf{r})$. This operator is Hermitian[3] meaning that it is linear, its eigenvalues are real numbers and the corresponding eigenvectors with different frequencies are orthogonal to each other. The above equation is scale invariant [61], which means that if the photonic crystal material configuration (lattice constant) is changed by compression or expansion, i.e. $\varepsilon(\mathbf{r}) \rightarrow \varepsilon(\mathbf{r}/s)$ for some scale parameter s, then the new mode profile and its corresponding frequency ω' can be obtained only by rescaling the old mode profile and its frequency ω. It holds that $\omega' = \omega/s$.

After finding modes $\mathbf{H}(\mathbf{r})$, the electric field spatial profile $\mathbf{E}(\mathbf{r})$ can be recovered by using Eqs. (2.3) and (2.4):

$$\mathbf{E}(\mathbf{r}) = \frac{i}{\omega \varepsilon_0 \varepsilon(\mathbf{r})} \nabla \times \mathbf{H}(\mathbf{r}) \,. \tag{2.8}$$

In the next section, the solutions of this equation for photonic crystals with a 2D periodicity is discussed. This type of photonic crystals will be of our interest in this thesis because it can be successfully employed to enhance either extraction efficiency of light from a thin layer or for enhancing optical gain.

---

[3] Proof can be found in Ref. [61].

2.2 Two-dimensional photonic crystals

A two-dimensional photonic crystal is a structure periodic in the two dimensions and homogenous in the third one. It can be composed for example of infinitely long dielectric columns ordered into a square lattice. Sketch of this structure having the lattice constant a and the radius of columns r is shown in Fig. 2.2. Because of its discrete translational symmetry in the xy-plane, $\varepsilon(\mathbf{r}) = \varepsilon(\mathbf{r} \pm \mathbf{R})$ holds for any $\mathbf{R}$ being a linear combination of the primitive lattice vectors $\mathbf{a}_1 = a\mathbf{x}$ and $\mathbf{a}_2 = a\mathbf{y}$.

Figure 2.2: 2D photonic crystal composed of infinitely tall dielectric columns with radius r ordered into a square lattice with lattice constant a. The right top inset shows the square lattice from above. The right bottom inset shows the Brillouin zone corresponding to this structure, with the irreducible zone shaded light blue.
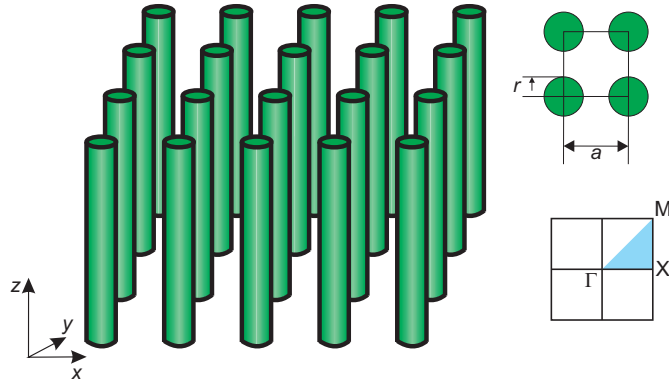
Experimentally, the above described structure can be prepared by using very tall columns such that the incident light would not "see" edges of the sample and its wavefront would not affected by the finite height of the sample [62].

Now, the question arises: How will light propagate in a 2D photonic crystal? For this to be answered, Eq. (2.7) must be solved using the appropriate structural parameters. To simplify the computation, a character of the solution can be "guessed" or, in other words, an ansatz for electromagnetic modes $\mathbf{H}(\mathbf{r})$ can be found. This also allows to obtain some physical insight into the problem. As a consequence of the in-plane periodicity of the dielectric constant, Bloch's theorem, mostly known from the theory of solid-state physics where it is used for describing propagation of conducting electrons in crystals or metals, can be applied. Here, it describes propagation of an electro-magnetic mode as a movement of a plane wave modulated by a periodic envelope function through the periodic lattice:

$$\mathbf{H}_{m,k_z,\mathbf{k}_{||}}(\mathbf{r}) = e^{i\mathbf{k}_{||}\cdot\boldsymbol{\rho}}e^{ik_z z}\mathbf{u}_{m,k_z,\mathbf{k}_{||}}(\boldsymbol{\rho}). \tag{2.9}$$

The modulating function $\mathbf{u}_{m,k_z,\mathbf{k}_{||}}(\boldsymbol{\rho})$ is periodic in the xy-plane, ρ being a position vector $\mathbf{r}$ projected on the xy-plane.[4] The electromagnetic mode is labeled or indexed by an integer number m and by the values of the wavevector $\mathbf{k} = (\mathbf{k}_{||}, k_z)$, where $\mathbf{k}_{||}$ is a planar wavevector characterizing mode propagation in the xy-plane.

Due to the translational symmetry in the x- and y-directions, $\mathbf{k}_{||}$ is conserved. Next, from Bloch's theorem it follows that $\mathbf{k}_{||}$ and $\mathbf{k}_{||} + \mathbf{C}$ ($\mathbf{C}$ being an integer multiple of a primitive vector of reciprocal space[5]) index similar eigenmodes, i.e. $\mathbf{H}_{m,k_z,\mathbf{k}_{||}+\mathbf{C}} = \mathbf{H}_{m,k_z,\mathbf{k}_{||}}$. Therefore it is sufficient to consider only the planar wavevectors from an irreducible Brillouin zone, which covers all the possible physical solutions of Eq. (2.7). The irreducible Brillouin zone of

---

[4]$\mathbf{u}(\boldsymbol{\rho} + \mathbf{R}) = \mathbf{u}(\boldsymbol{\rho})$

[5]Reciprocal space is defined by a reciprocal lattice with primitive reciprocal vectors $(\mathbf{b}_1, \mathbf{b}_2)$ defined so that $\mathbf{a}_i \cdot \mathbf{b}_j = 2\pi\delta_{ij}$, where $(\mathbf{a}_1, \mathbf{a}_2)$ are the primitive lattice vectors of the square lattice. For a given square lattice, the corresponding reciprocal lattice is also a square lattice with spacing $2\pi/a$ instead of a.
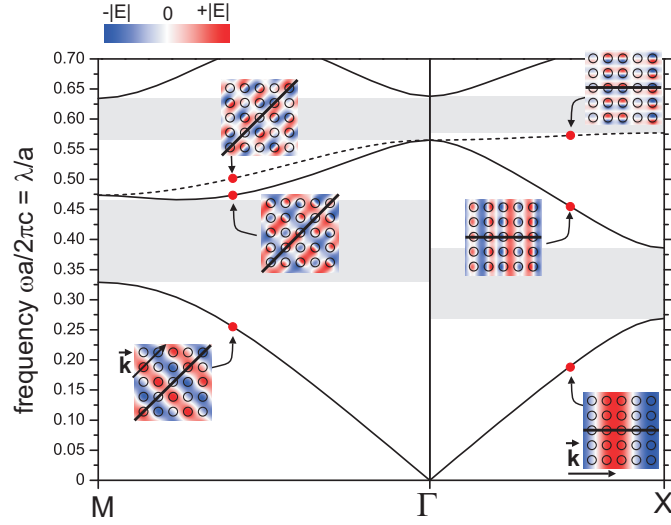
Figure 2.3: The TM band structure along the Γ-M and Γ-X directions of a 2D photonic crystal consisting of diamond (refractive index 2.4) columns with radius $r = 0.3a$ ordered into a square lattice with the lattice constant a and surrounded by air. Modes plotted by the solid (dashed) lines are symmetric (asymmetric) with respect to the mirror plane depicted by the thick black line in the insets. The insets show the electric field (parallel to the columns) patterns of the modes at the states marked by the red spots. The contour of each column is depicted with an open black circle. The gray regions depicts photonic bandgaps between the symmetric modes. Adapted from [63].

the reciprocal space of a square lattice is delimited by the points of high symmetry Γ, X and M as shown in Fig. 2.2 by a blue triangle.

The out-of-plane wavevector k_z is, due to the continuous symmetry in the z-direction, also conserved but unlike $\mathbf{k}_{||}$, it can possess arbitrary values. However, in order to demonstrate the formation of photonic bandgaps, only the modes propagating strictly parallel to the xy-plane ($k_z = 0$) will be considered.[6]

Solving Eq. (2.7) with the ansatz (2.9) lead to the solution, for each $\mathbf{k}_{||}$, comprised of an infinite set of modes with discretely spaced frequencies $\omega_m(\mathbf{k}_{||})$ labeled (starting from the lowest one) by the so-called (integer) band index m. Plot of ω_m as a function of $\mathbf{k}_{||}$ (taken along the significant directions of the Brillouin zone) forms a photonic band structure or band diagram.

Figure 2.3 plots the band structure of a 2D photonic crystal consisting of diamond columns with the radius $r = 0.3a$ and the refractive index of 2.4 in the visible range, surrounded by air. For simplicity, only the modes propagating along the Γ-X and Γ-M directions with $\mathbf{H}$ lying in the xy-plane and $\mathbf{E}$ perpendicular to it, the so-called transverse-magnetic (TM) modes, are plotted. The electric field patterns of the TM modes $\mathbf{H}_{m,\mathbf{k}_{||}}$ (the insets of Fig. 2.3) depicted for the lowest three bands at the wavevectors marked by the red spots allow to further divide these modes into symmetric (solid lines) or asymmetric (dashed lines) with respect to the mirror plane that is: perpendicular to the xy-plane, parallel with the direction of the mode propagation and at the same time goes through the middle of the columns (the thick black lines). Furthermore, the wave fronts of the propagating light waves can be clearly recognized in the insets. It should be noted that the symmetric modes can be excited from outside by a plane wave light source tuned at the proper allowed frequency and incident on the photonic crystal from the side.

---

[6]No bandgaps are present in the case of the out-of-plane propagation.

In Fig. 2.3 and also further in the text, the mode frequency ω is expressed in the units of $2\pi c/a$, where c is the velocity of light in vacuum. In other words, it holds that a number on the vertical axis $X = \omega a/2\pi c = \lambda/a$, where λ is the vacuum wavelength of a mode. Besides the fact that this gives a quick idea about the mode wavelength, it also allows to apply the computed band diagram to other 2D photonic crystals possessing different lattice constants (keeping the other parameters unchanged). The latter follows from the scale invariance of Maxwell's equations discussed in the previous section.

The photonic bandgaps between the symmetric modes (in the sense defined above), i.e. frequency intervals with no photonic modes, are depicted by the gray rectangles in Fig. 2.3. It is also important to notice that modes with a zero group velocity $v_g = \partial\omega/\partial k_{||}$ are formed at the points of high symmetry. The band diagram and the electric fields were calculated by the author using a conjugate gradient plane wave expansion method [64] implemented in a Photonic-Bands (MPB) package developed at the Massachusetts Institute of Technology (for details see Chapter 5, Section 5.1).

2.3 Photonic crystal slabs

Photonic crystal slabs differ from the above-described 2D photonic crystals only by having a finite thickness in the vertical, z-direction.[7] This, however, brings important new features such as vertical light confinement due to the refractive index difference between a photonic crystal slab and surrounding air. Together with the existence of a 2D photonic bandgap, preventing light propagation in the horizontal plane, waveguides and nano-cavities can be realized by creating structural defects in these periodic structures. An example of a photonic crystal-based waveguide created by omitting one row of periodically ordered holes "drilled" in a thin GaAs slab is shown in Fig. 2.4(a). Next, Fig. 2.4(b) shows an example of a cavity positioned in the middle of a photonic crystal slab. Two other important applications, contrary to the previous ones, do not require the existence of a photonic bandgap and thus are less demanding on the material properties such as high refractive index. First, light extraction efficiency from a thin layer can be increased by patterning its surface into the form of 2D photonic crystal. And second, the enhancement of optical gain of active material can be obtained by taking the advantage of existence of modes with low group velocity, the so-called slow modes, present in photonic crystals. Both will be discussed in detail further.
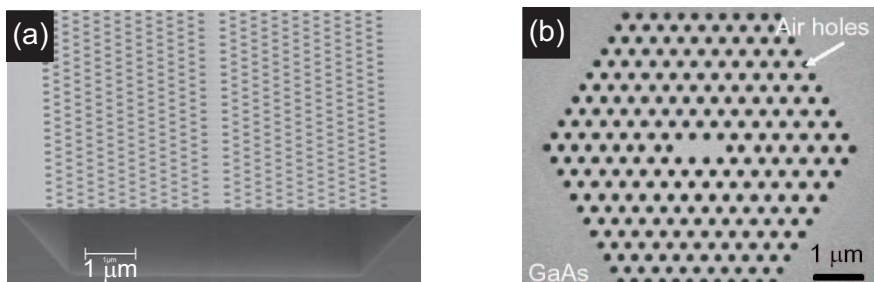

Figure 2.4: SEM images of photonic crystal slab examples. (a) A 2D photonic crystal waveguide prepared on a GaAs membrane. Light is guided along the line defect created by omitting one row of the hexagonally ordered holes. Picture taken from [65]. (b) A nano-cavity prepared in the middle of a GaAs 2D photonic crystal slab [66].

---

[7]However, a statement that a 2D photonic crystal was prepared on the top of a dielectric layer is used when referring to the structure which is periodic in two dimensions and possesses a finite height, i.e. it is equivalent to the term "photonic crystal slab".
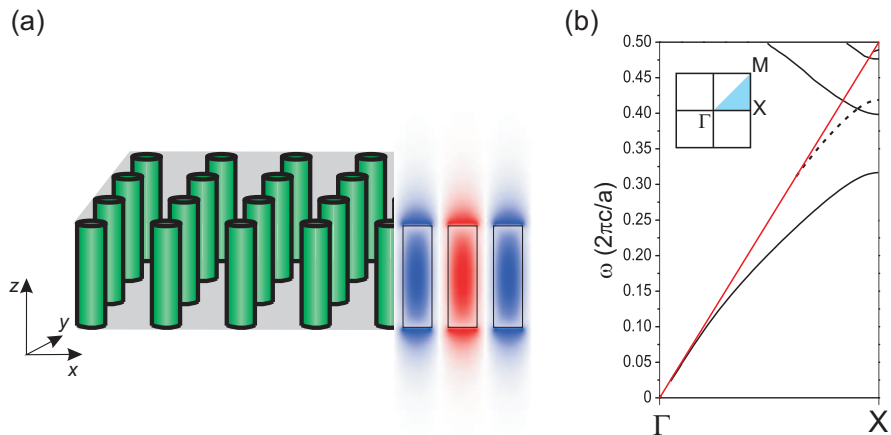
(a)

(b)

Figure 2.5: (a) A photonic crystal slab composed of periodically ordered columns with the height of $h = 2a$ possessing a square symmetry with the lattice constant a. The electric field pattern of the vertical component E_z of the fundamental TM mode at the X-point taken in the plane cutting vertically the columns is shown at the right. This mode is clearly confined in the photonic crystal slab. (b) The TM modes along the $\Gamma-X$ direction of the structrure shown in (a). Modes plotted by the solid (dashed) lines are symmetric (asymmetric) with respect to the mirror plane that is for modes propagatin in x-direction parallel with the xz-plane. Unlike in Fig. 2.3, an air lightline (red straight line), which meaning is discussed in the text, can be defined here. The left inset shows the points of high symmetry at the corners of the irreducible Brillouin zone depicted by the light blue triangle.

Let us now, however, return to the description of light propagation in a photonic crystal slab surrounded by air as the one sketched in Fig. 2.5(a). It is basically the same structure as was discussed in the previous section with only one difference: the height of the columns is not infinite. Specifically, the height of $h = 2a$ (where a is again the lattice constant of a square lattice) was chosen to demonstrate the formation of a photonic bandgap. Due to the discrete translational symmetry of the structure in the xy-plane, the planar wavevector $\mathbf{k}_{||}$ is conserved as it was in the case of the 2D photonic crystal. On the other hand, the vertical wavevector component k_z is not conserved and can vary with the position vector $\mathbf{r}$ such as it is, for example, when light propagates through an interface of two dielectrics (except for the case of normal incidence).[8] A photonic band diagram is thus again (as in the case of the 2D photonic crystal) a dispersion of ω versus $\mathbf{k}_{||}$ in the irreducible Brillouin zone of the square lattice.

Figure 2.5(b) shows the photonic band diagram for the TM-modes propagating in the $\Gamma-X$ direction of the above-described photonic crystal slab. It was computed by the author employing the MPB package.[9] Even though the result of simulation is valid for a structure, which is infinite in the xy-plane, it very well resembles the photonic properties of real structures with finite width and length. The finite height of the structure is indeed included in the simulation. The dispersion of a fundamental mode going from the point $(\omega, \mathbf{k}_{||}) = (0, 0)$ to the X-point and also the dispersion curves of higher order modes are present in the band diagram. The band diagram looks, at least for the fundamental mode, very similar to that

---

[8]Furthermore, as opposed to the case of the 2D photonic crystal, here the value of k_z cannot have an arbitrary value but is fixed by the values of both, $\mathbf{k}_{||}$ and ω. For example in free space, i.e. above and below the photonic crystal, the value of k_z can be directly evaluated from the knowledge of $\mathbf{k}_{||}$ and ω as will be presented further.

[9]There are some peculiarities connected with using the MPB for computing the modes above the air lightline $\omega = c|\mathbf{k}_{||}|$, which are discussed in Chapter 5, Section 5.1.

of the infinite 2D photonic crystal shown in Fig. 2.3. It again consists of modes that are symmetric (solid lines) and asymmetric (dashed lines) with respect to the mirror plane that is perpendicular to the xy-plane, parallel with the direction of the mode propagation and cuts the column through its middle. The key difference is, however, that an air lightline given by the relation $\omega = c\mathbf{k}_{||}$ (a red line in Fig. 2.5) can be defined for the structure of finite height.[10] Its physical meaning, explained in detail further below, is following. Modes below the lightline are confined in the slab (i.e. decay exponentially in the z-direction) as shown for the fundamental mode at the X-point in Fig. 2.5 by plotting the distribution of its vertical electric field E_z.[11] Because it is a mode on the band edge, it has zero group velocity and thus it forms standing waves, in this case, with the intensity maxima located in the material with higher ε and nodes in the material with lower ε. Modes below the lightline are guided within the photonic crystal slab with no losses (basically thanks to the total internal reflection phenomenon). On the other hand, modes above the air lightline are Bragg-diffracted into air during their propagation in the slab and slowly leak into the surroundings. Therefore, they are called "leaky modes" or guided resonances [67]. This concept can be applied to increase the light extraction efficiency from planar layers (e.g. LEDs) and will be discussed in detail in the next section.

2.4 Light extraction enhancement

The light extraction is an important issue to be faced when developing LEDs. Light-emitting diodes are typically based on a PN junction or quantum well implemented in a thin dielectric layer and therefore a phenomenon of total internal reflection needs to be minimized. Only a small part of light emitted in the layer radiates to air depending on the material refractive index n. The extraction efficiency C_{ex} of light from a thin dielectric planar layer is given by the relation[12] $C_{ex} = 1/n^2$[68]. Several approaches are available for enhancing the extraction efficiency. The most typical two are based on either creating a rough surface on a thin-film LED [69] or using flip-chip LEDs [70]. The next one that will be discussed here is based on creating a 2D periodic pattern on the top of a thin light-emitting layer, thus creating the so-called photonic crystal LEDs. Very thorough reviews on this topic are Refs. [71, 72].

The photonic crystal LEDs can be divided into the following two categories.

First, *strongly coupled photonic crystal LEDs*, in which a photonic crystal structure penetrates the entire device and its photonic bandgap is tuned near the emission spectrum of a light source. This was theoretically studied, for example, by Fan et al. in Ref. [73] and experimentally by Fujita et al. in Ref. [74].

Second, *weakly coupled photonic crystal LEDs*, in which a 2D photonic crystal is etched only on the top of a waveguiding layer and acts as a diffraction grating that allows outcoupling of guided modes from the layer [75, 76]. The angular pattern of emission can be controlled by tuning the characteristics of the photonic crystal.

In this section, the second alternative is presented in detail. First, an explanation of the principle of light extraction from a weakly coupled photonic crystal is given, based on our computational results. Specifically, in line with this thesis, properties of a shallow photonic crystal on a diamond-based planar waveguide are described. Experimental results of mea-

---

[10]Lightline can be defined also for the infinitely high 2D photonic crystal, but with no physical meaning as there is no free space above or below the crystal.

[11]Note the discontinuity of E_z at the air-rod horizontal interfaces.

[12]It can be derived simply by integrating the emitted radiation over a spatial angle going from zero to the angle of total internal reflection, thus the not-totally-reflected part of emission only.
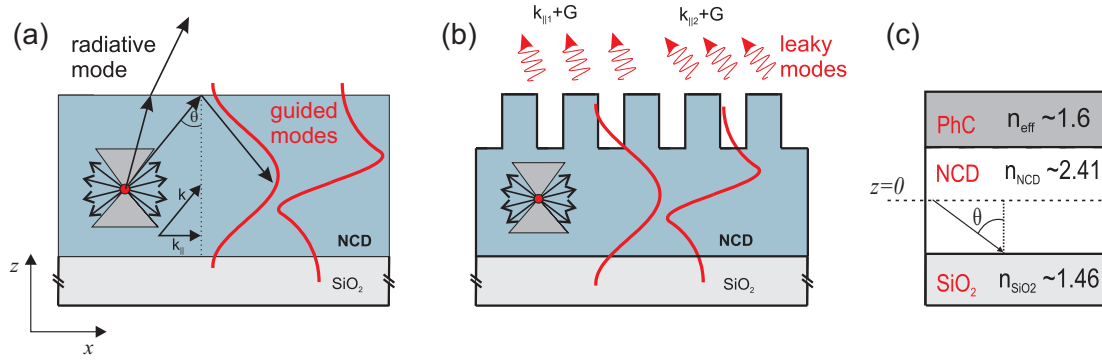
Figure 2.6: (a) A sketch of a planar waveguide based on an approximately 400 nm thick diamond layer deposited on a silica substrate. The red dot represents a light source and the black arrows are light rays with the angle of incidence θ. The upper (lower) gray cone is an extraction lightcone defined by the critical angle of the total reflection on the air (silica)-diamond interface. The red curves are the electric field profiles of a fundamental and higher-order guided mode. (b) A cross-section of a photonic crystal slab composed of the square array of columns etched into the planar waveguide shown in (a). The red arrows are photons that were Bragg-diffracted on the surface periodicity. (c) A sketch of the structure shown in (b), in which the photonic crystal is approximated by the effective medium theory.

surements conducted on this sample will be presented in Chapter 5, Section 5.3. Second, a practical example from the literature of a photonic crystal LED based on GaN showing an enhanced extraction efficiency is given.

The principle of light extraction

In this paragraph, the principle of light extraction enhancement induced by creating a weakly coupled photonic crystal on the top of a diamond layer deposited on a silica substrate is explained. First, light coupling into the optical modes of a thin non-corrugated planar diamond layer is described. Then, a theoretical study shows how the light propagation is altered after a shallow photonic crystal is implemented on the top of the layer. The dimensions and refractive index of the studied structure reflect the parameters of a real sample that was prepared with the goal to enhance the extraction efficiency of light emitted by the nanocrystalline diamond defects (for details see Chapter 5).

Figure 2.6(a) shows a schematic illustration of the cross-section of the planar diamond waveguide. A light source emitting into all directions is depicted by the red dot. Depending on the angle of incidence θ, light emitted towards the air-diamond interface is either reflected (due to the phenomenon of total internal reflection) on that interface or transmitted through it. Taking into account the diamond refractive index of ~ 2.4 in the visible spectral range, the critical angle of the total reflection on the air-diamond interface is $\theta_c \sim 24°$. The same logic works also for the diamond-silica (SiO_2) interface. Light emitted within the upper gray cone (defined by the critical angle) is transmitted to air and belong to the group of waveguide modes called "radiative modes" having the field profile extended to air. Light emitted within the lower lightcone is either coupled to "substrate modes" (light reflected on the silica-air interface) or also radiates to air ($\rightarrow$ radiative modes). On the other hand, light totally reflected on the both diamond interfaces will be "trapped" in the diamond layer. In case it fulfills requested boundary conditions, it couples to "guided modes" having the field profile localized within the core and evanescent in air and the substrate.

All types of waveguide modes are characterized by the in-plane wavevector $|\mathbf{k}_{||}| = |\mathbf{k}| \sin \theta$, θ being the angle of mode propagation within the core, and by the mode frequency ω which
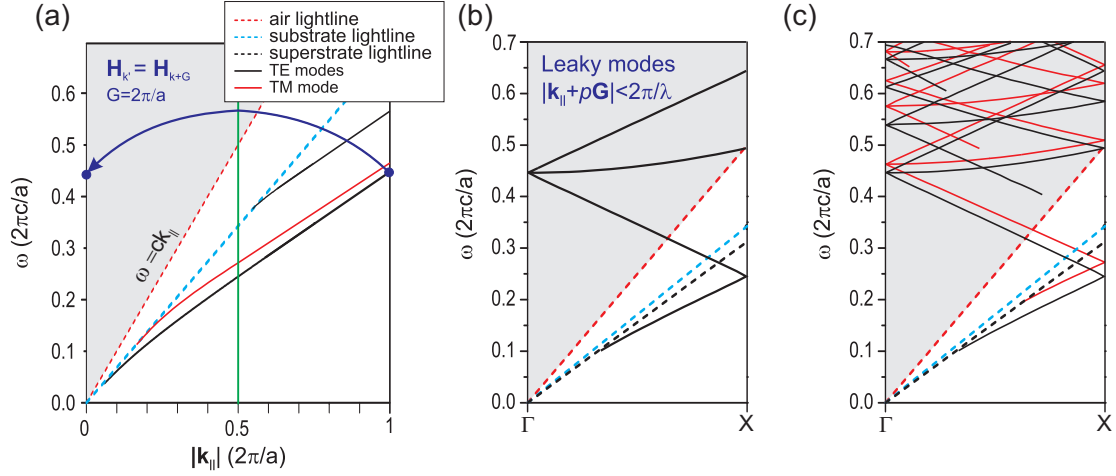
Figure 2.7: (a) The band diagram of a planar waveguide sketched in Fig. 2.6(a). The units of ω and $|\mathbf{k}_{||}|$ are expressed with respect to the lattice constant parameter a. (b,c) The band diagrams in the $\Gamma{-}X$ direction of a photonic crystal slab sketched in Fig. 2.6(b) computed by FDTD simulation in which the photonic crystal was substituted with an effective medium (as illustrated in Fig. 2.6(c)). In (b), periodicity induced folding only of the TE fundamental mode is depicted, whereas in (c) all the modes supported by the photonic crystal are included. See the text for details.

are related through the dispersion relation (photonic band diagram) $\omega(|\mathbf{k}_{||}|)$ of the waveguide. Both quantities, ω and $\mathbf{k}_{||}$, are conserved, therefore a photonic band diagram is a suitable way of describing light behavior both in waveguides and in photonic crystals.

The photonic band diagram of the planar diamond waveguide (Fig. 2.6(a)), computed from the transverse resonance condition, is shown in Fig. 2.7(a). The units of ω and $\mathbf{k}_{||}$ are expressed with respect to the lattice constant a of a photonic crystal, which will be fabricated on the top of the planar layer. Even though a has no physical meaning in the case of the homogeneous layer and works only as a scaling parameter, it is useful for the explanation of formation of the photonic crystal band diagram (as will become clear soon). Modes above the air lightline (red dashed line) are the radiative modes, i.e. states that radiate to air, and because there is an infinite number of these states they form a continuum in a band diagram (the gray shaded area in the plotted band diagram in Fig. 2.7(a)). Modes between the air lightline and the substrate lightline (blue dashed line, defined by relation $\omega = v_s|\mathbf{k}_{||}|$, v_s being the speed of light in the substrate) are the substrate modes. The guided modes of the studied structure, on the other hand, form discrete bands underneath the substrate lightline. Thus, they can be characterized by the in-plane wavevector $\mathbf{k}_{||\mathbf{m}}$, where m is a mode number which basically identifies the electromagnetic field profile within the core.

In general, guided modes can be divided, based on their symmetry, into transverse-electric (TE) and transverse-magnetic (TM) modes. In the sketch in Fig. 2.6(a), the electric field profiles of a fundamental TE (Gaussian) and higher order TE mode are depicted by the red curves. As mentioned above, light guiding is (from the point of view of the ray-optics model) based on the total internal reflection phenomenon. However, the wave-optics model (and Maxwell's equations) need to be used (and solved) when looking for modes with wavelengths comparable to the dimensions of a waveguide. Videos demonstrating (by means of a computer simulation) light coupling to a planar waveguide (without substrate) is attached to this thesis (see Appendix).

In this paragraph, the importance of the air lightline in the photonic band diagram description of light behavior in waveguides and in photonic crystal slabs is explained using the

symmetry-based concept and the wave-character of light. As mentioned above, the air light-line divides a band diagram into two regions. Modes above the air lightline radiate to air. Modes below it are totally reflected on the waveguide-air interface. For the magnitude of the planar wavector the relation $k_{||} = |\mathbf{k}| \sin \theta$ holds. It is, due to in-plane translational symmetry, a conserved quantity and thus identical in diamond and air. Far away from the waveguide, every radiative mode can be expressed as superposition of plane waves in air. The magnitude of $\mathbf{k}$ of plane waves in air is $|\mathbf{k}| = \omega/c$, ω being a conserved quantity. Combining these two relations and expressing the vertical component of the wavector in air k_z yields the following relation

$$k_z = \sqrt{\frac{\omega^2}{c^2} - k_{||}^2}. \tag{2.10}$$

If $\omega > ck_{||}$, then k_z is real in air. This means that the mode possessing such k_z will have non-zero vertical component of the wavector and thus will radiate out from the waveguide. In a band diagram, modes with $\omega > ck_{||}$ fill the region above the air lightline. On the contrary, if $\omega < ck_{||}$, then k_z is purely imaginary in air. This implies that k_z exponentially decreases in air, which is the definition of guided modes. Thus, guided modes must lie below the air lightline.

Next, introducing a 2D periodicity in the form of periodically ordered columns on the surface of the above discussed diamond planar layer allows to express guided modes in the form of Bloch modes. The cross-section taken through the middle of the columns of this structure is sketched in Fig. 2.6(b). The fundamental guided modes $\mathbf{k}_{||\mathbf{m}}$ are now coupled to other harmonics $\mathbf{k}_{||\mathbf{m}} + p\mathbf{G}$ by the reciprocal vector $|\mathbf{G}| = 2\pi/a$, where p is an integer identifying the harmonic. It means that $\mathbf{H}_{\mathbf{k}_{||m}} = \mathbf{H}_{\mathbf{k}_{||m}+\mathbf{G}}$ and thus the irreducible Brillouin zone of the crystal lattice includes all the possible (physically different) light modes supported by the device. This, the so-called "band folding", is plotted by the dark blue arrow in Fig. 2.7(a)—a state at the right edge of the band diagram (blue dot) is basically flipped back on the beginning of the band diagram as a consequence of the periodicity introduced into the layer. Now the reason for introducing the parameter a into the band diagram of the planar waveguide should be clear. Therefore, merely by folding the bands of the planar waveguide at the edges of the irreducible Brillouin zone (defined by the photonic crystal symmetry), a qualitative picture of the photonic crystal slab band diagram can be derived. One of the edges of the Brillouin zone of the studied photonic crystal with the square symmetry, corresponding to the X-point, is depicted by the green vertical line. Folding of the fundamental TE mode at the Brillouin zone edge leads to a photonic diagram shown in Fig. 2.7(b). It is evident that some modes that were in the case of the planar waveguide guided in the core, now occur above the air lightline. Therefore they must possess a real k_z and thus radiate out to air, i.e. they become leaky modes. These harmonics satisfy a diffraction condition[13] $|\mathbf{k}_{||\mathbf{m}} + p\mathbf{G}| < 2\pi/\lambda$ and are Bragg-diffracted by the photonic structure into surrounding air during their propagation in the core. Diffraction efficiency, described by the Q-factor of a mode (characterizing how quickly is the mode extracted), depends strongly on the spatial overlap of a leaky mode with a photonic crystal [71].

The photonic band diagram containing all the folded TE and TM modes is shown in Fig. 2.7(c). It was computed using an effective medium theory to describe the photonic crystal (see the illustration in Fig. 2.6(c)) and Finite-difference time-domain (FDTD) method using the MIT Electromagnetic Equation Propagation (MEEP) package [77]. It should be noted that the effective medium (which substitutes the photonic crystal) with the refractive index lower than the diamond core behaves as a superstrate and thus all the guided modes are

---

[13]It says, basically, that only modes that have non-zero real k_z in air can be diffracted.

now positioned below the superstrate lightline—details can be found in Ref. [78]. In addition to the continuum of radiative modes above the air lightline, the air lightcone is filled with the photonic bands of leaky modes which work as an efficient radiative channel and allow to increase the extraction efficiency of light from the layer. The qualitatively very similar band diagram can be computed for the $\Gamma-M$ crystal direction (or any other azimuthal direction) which means that the leaky modes propagating in all azimuthal directions are diffracted out from the structure under specific angles defined by the photonic band diagram. Videos showing the effect of light out-coupling to air via interaction with a photonic crystal are attached to this thesis (see Appendix).

An example of a photonic crystal LED

In this paragraph, one example of the enhanced light extraction efficiency by employing a photonic crystal taken from the literature is presented. Authors of Ref. [75] studied the emission patterns of a light-emitting InGaN−GaN multi-quantum well (MQW) buried in a GaN slab with different types of 2D photonic crystals on the top. The emission maximum of the MQW was tuned at around 450 nm. Figure 2.8 shows one example of the studied devices based on a 2D photonic crystal with the triangular lattice of holes with a lattice constant $a = 250$ nm. The properties of the photonic structure were tuned such that the spectral overlap of the MQW emission spectrum and the photonic crystal leaky modes was obtained. The thickness of the GaN slab, the depth and radius of holes were chosen in order to obtain the spatial overlap of the mode profiles with the photonic crystal and thus to ensure high efficiency of the extraction phenomenon. Very bright blue emission was obtained from the patterned part of the device as shown in the top-view optical image of the biased photonic crystal LED (Fig. 2.8(c)).

Figure 2.8: Design of a photonic crystal LED studied in Ref. [75]. (a) Cross-section of the device. (b) Top-view of the device measured by atomic force microscopy. (c) Top-view of the biased device. Adapted from Ref. [75]
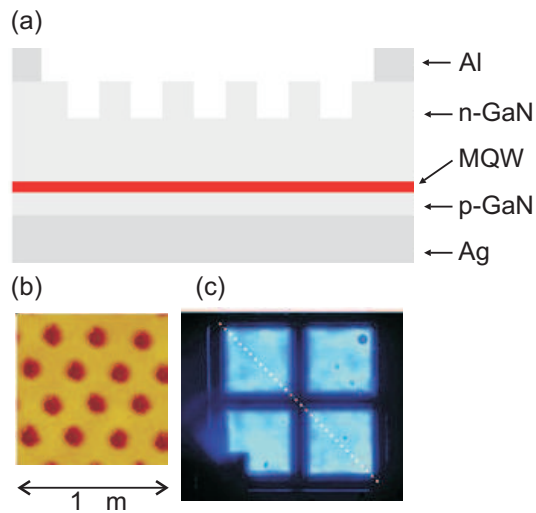
As explained earlier, in the case of a planar LED, light emitted by a MQW either couples to the guided modes of the slab or, in case it lies in the lightcone of the structure, it radiates to air. The electroluminescence radiation pattern of the planar LED measured in the far-field[14] with a polarizer transmitting only the TM polarization is shown in Fig. 2.9(a). As a consequence of the Fabry-Pérot resonances within the GaN cavity, the luminescence spectrum of the MQW as a function of the detection angle has the shape of a broad lobe (see also the

---

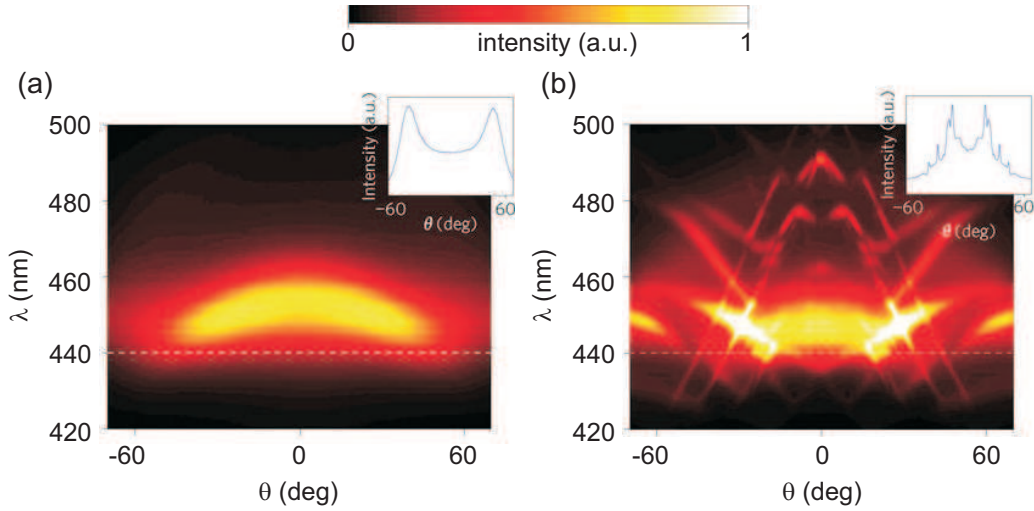[14] An optical fiber on a rotational arm was rotated above the device along the chosen azimuthal direction.

Figure 2.9: The TM-polarized far-field emission patterns of a InGaN-GaN LED. (a) The measured far-field pattern of electroluminescence intensity as a function of detection angle (0° corresponding to vertical (normal) emission) and wavelength for a planar LED. (b) The measured far-field pattern for a photonic crystal LED in the $\Gamma-K$ direction of a triangular lattice. Insets show emission patterns as a function of detection angle at a specific wavelength, marked by dashed white lines. Adapted from Ref. [75]

monochromatic inset at 440 nm). Figure 2.9(b) shows the far-field diffraction pattern of the photonic crystal LED measured along the $\Gamma-K$ direction. Sharp peaks corresponding to the out-coupled leaky modes being superimposed on the Fabry-Pérot resonances are clearly visible. The diffraction angles of these modes shift with wavelength forming basically the photonic band diagram of the structure as $\mathbf{k}_{||}$ and angle θ are directly related. The high intensity of the extracted modes indicates the high efficiency of the extraction mechanism. The photonic crystal LED exhibits qualitatively very similar diffraction patterns in all azimuthal (in-plane) directions. By integrating their intensity over all azimuthal angles and wavelengths gives the value of the overall extraction efficiency of the device.

Authors of Ref. [75] also experimentally evaluated the extraction efficiency of different samples and for the best-performing device[15] they obtained $C_{ex} = 68 - 78\%$ compared to the extraction efficiency of 27% derived for the planar LED. This result is comparable to the efficiency of unencapsulated[16] rough-surface thin-film LEDs with $C_{ex} \sim 65\%$, which are based on light scattering on the rough-surface. The main advantage of photonic crystal LEDs is that the emission is concentrated in a relatively narrow angle around the normal to the device surface whereas in the case of rough-surface LEDs it is distributed almost equally in space.

---

[15]Device parameters: a 700 nm thick GaN layer, an Archimedean A13 lattice with the lattice constant of 455 nm, the filling factor of 0.3 and the depth of holes of 250 nm.

[16]Al top contact is not covered with any protection. In the case of encapsulated LEDs, the protection layer is typically a dielectric material.

Results of other authors

Let us now briefly comment on results of other authors on the extraction efficiency enhancement by employing 2D photonic crystals, which are summarized in Table 2.1. In the experiments, vertically-emitted radiation was collected by using either an optical objective or optical fiber placed above the device. An enhancement factor is defined as a ratio between the intensity of radiation coming from a photonic crystal and an unpatterned reference taken at the wavelength on which the photonic crystal shows the best performance. Besides the enhancement factor, it is also important to compare the semi-angle of a detection cone defined by the numerical aperture of the objective. The effect of the detection angle on the extraction enhancement factor is manifested by the results of Kim et al. [79] who measured larger enhancement for the lower detection angle. This results from the directionality of radiation out-coupled by the photonic structure. All the presented devices are designed such that the majority of light out-coupled by the photonic crystal propagates in the directions close to the sample normal. Modes diffracted exactly in the direction perpendicular to the device surface (the modes at the Γ-point) are most efficiently enhanced due to the symmetry degeneracy at the Γ-point. This effect is evidenced by the results of Cluzel et al. [80], who measured 122-fold extraction efficiency enhancement. The authors employed an optical fiber (placed in a reasonable distance from their sample) for the detection of the sample PL, which provided high angular resolution, i.e. the very low numerical aperture. Therefore, they detected basically only the most efficiently extracted Γ-mode. The above discussion is here to notify the reader that not only the value of the enhancement factor but also the experimental conditions under which it was obtained should be considered when comparing the results of different authors.

Authors	Enhancement factor	detection semi-angle
Cluzel et al. [80]	122	optical fiber
Ryu et al. [81]	30	25°
Erchak et al. [82]	6	15°
Kim et al. [79]	4.6 (5.6)	70°(30°)
Presti et al. [83]	4	4°

Table 2.1: Summary of the extraction enhancement factors with respect to the semi-angles of the detection cones. Numerical aperture of the optical fiber was not specified in Ref. [80].

The efficiency of light extraction from devices with photonic crystals depends on many factors. Probably the most important are the height of a photonic crystal, the width of the unpatterned core layer underneath it and the lattice constant. Furthermore, it is the material optical quality, which should provide low optical losses. The optical quality can be controlled by choosing a material with low absorption losses at the operating wavelength and by employing fabrication methods that allow to prepare samples with minimum structural defects. More on this topic can be found in Refs. [71, 72].

It should be finally noted that a similar concept can be used to increase the efficiency of light-trapping into layers with photonic crystals which is an important factor from the point of view of solar cells or waveguide couplers. It holds that light can be in the same manner as it is out-coupled from a photonic crystal slab, also coupled-into the photonic structure from outside, following the photonic band diagram.

2.5   Optical gain enhancement

The principle of optical gain enhancement

One of the important characteristics of materials used as active regions in lasers is an optical gain parameter g. Optical gain defines how efficiently is the intensity of light propagating through a material with population inversion (achieved by pumping) amplified. The typical values of the optical gain coefficient of materials used in lasers vary from several hundreds to tens[17] of cm^{-1}. In order to obtain lasing from the pumped material, an optical feedback must be provided by introducing an optical resonator. Conventional semiconductor lasers are Fabry-Pérot lasers, in which a Fabry-Pérot resonator is formed between two opposite reflective parallel facets of an active material or simply between two parallel mirrors. However, the more sophisticated way of achieving an optical feedback leading to a stable single-mode laser output is provided by DFB lasers [84]. Distributed feedback lasers are relatively low-cost and reliable optical sources capable of high-speed modulation used in optical communications. The design of these lasers is such that the surface of a planar active region is periodically shaped into the form of a diffraction grating that operates as a Bragg reflector. The Bragg diffraction phenomenon causes formation of standing waves in the material at specific wavelengths and thus provides the feedback.

In conventional DFB lasers, the feedback is realized by a 1D grating, i.e. a 1D photonic crystal whose photonic bandgap spectrally overlap with the spontaneous emission spectrum of an active material. However, with the improvement of fabrication methods, also DFB lasers with 2D gratings, called "2D photonic crystal lasers", were developed. The grating can operate either as a first-order or second-order grating. First-order gratings, having typically the period of one-half of the operating wavelength, feeds the guided radiation back into the waveguide. On the other hand, second-order gratings diffract the amplified radiation out of the waveguide in the direction normal to the grating, the so-called "surface" or "vertically-emitting" lasers.

The effect of light amplification in DFB lasers can be described by using the photonic band diagram approach. Dowling et al. [85] pointed out that the group velocity v_g of modes at the edges of photonic bands (the band edge states) approaches zero. This makes a very good sense when we realize that $v_g = \partial\omega/\partial k$ strongly depends on the curvature of photonic bands (see, e.g Fig. 2.3). At the points of the high symmetry of a Brillouin zone, bands flatten due to boundary conditions and thus v_g decreases and equals zero directly at the band edge. However, as a consequence of the finite dimensions of real devices, the group velocity of band edge states will never be exactly zero.[18] Nevertheless, the value of v_g will be very low making the efficient optical feedback possible. The physical interpretation of this effect is that photons propagating through a photonic crystal undergo many multiple reflections on the interfaces of different materials and thus only very slowly percolate through the structure (see a sketch in Fig. 2.10). If one of the materials is an active material with population inversion, this phenomenon can lead to a considerable intensity enhancement of light going from one end of the device to the other one. The intensified light is then out-coupled either at the very end of the structure in the case of first-order gratings or in the vertical (normal) direction in the case of second-order gratings. Authors of Ref. [85] call this effect the enhancement of optical gain. Or in other words, a photonic crystal laser behaves as it had effective optical gain g_{eff}

---

[17]Some lasers can have an active medium with very low optical gain, for example, ruby, which possesses optical gain of 0.2 cm^{-1} only.

[18]Recall that a photonic band diagram is always computed for a photonic crystal spanning over the whole planar space.

Figure 2.10: Schematic illustrations of light propagation (a) in a homogeneous layer and (b) in a 1D photonic crystal (only a small part of the structure is shown).
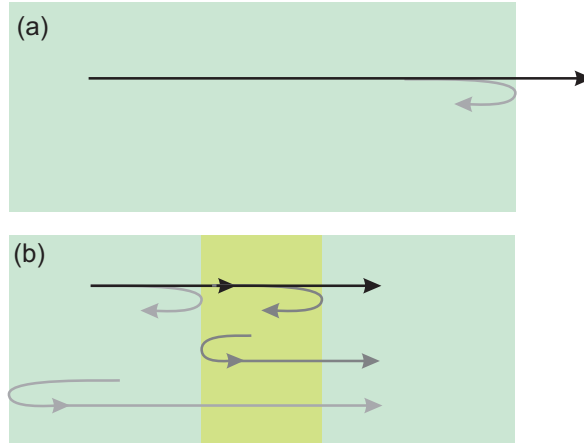
which is much higher than the intrinsic optical gain g of an active material. In the case of the approximation of the small value of v_g (as a consequence of the increased optical path of the multiply reflected photon) it can be derived that

$$g_{eff} = \frac{cn}{v_g} g, \qquad (2.11)$$

n being the refractive index of the active region. The authors of Ref. [85] also calculated temporal evolution of a Gaussian wave packet incident on a 1D photonic crystal and showed that the enhancement of optical gain occurs at the photonic band edges.

Sakoda in Ref. [23] showed that also the effect of the group velocity anomaly can lead to the high enhancement of optical gain in 2D photonic crystals. This phenomenon arises when a photonic band is flat within a broad interval of wavevectors, i.e. the group velocity of modes in the given wavevector's region is low. Such a region can be clearly recognized in the computed band diagram of a 2D diamond photonic crystal shown in Fig. 2.3, note the second TM mode in the $\Gamma-$M direction. The effect of gain enhancement in this structure is evidenced by means of a computer simulation performed by the author in Chapter 4, Section 4.3. This simulation extends works published by Sakoda or others, in particular by considering a material with the low optical gain values. The output of the simulations show that even when only the relatively small number of the periods of an active material is considered, the optical gain enhancement can be achieved in both, 2D photonic crystals and 2D photonic crystal slabs [63].

An example of a vertically-emitting 2D photonic crystal laser

In practice, photonic crystal band edge lasers, either vertically or horizontally-emitting, operating in the visible, infra-red or terahertz range [66, 24, 86, 87, 88, 89, 90, 91], were developed. In this paragraph, one example of a cw photonic crystal laser (optically pumped) emitting in the infra-red region in the direction normal to the sample plane is presented[24]. A schematic cross-section of the device is depicted in Fig. 2.11(a). It contains a photonic crystal slab based on holes possessing a square symmetry (the lattice constant $a = 600$ nm and the air-hole radius $r = 0.2a$), etched in an InGaAsP thin layer[19] with a bounded MQW. Diamond is employed to enhance spreading and dissipation of heat generated during the lasing in order to increase the operational time of the device.

The computed band diagram of the fabricate photonic crystal slab bonded to a MgF_2 layer is shown in Fig. 2.11(b). It is expected that the device will operate at one of the states at the Γ-point because its characteristic dimensions were designed such that the MQW emission spectrum overlap with these states. And as it was already explained in the previous section, as a result of the fact that the modes are positioned above the air lightline, they will be out-coupled into air, which makes it possible to detect them by an optical fiber as sketched in Fig. 2.11(a). Because they are exactly at $|\mathbf{k}_{||}| = 0$, the extracted (and amplified) light will propagate in the normal direction, thus the name vertically-emitting laser.[20]

The structure was pumped by a cw laser operating at 980 nm from the output of the optical fiber (Fig. 2.11(a)). Through the same fiber, the output power of the device as a function of the pump laser power was detected. The result of this measurement is plotted in Fig. 2.11(c). The abrupt change of the slope suggests that the laser threshold was achieved and lasing started at about 15 mW of excitation power. Very high output powers up to 200 μW were reached, which is, according to the authors of Ref. [24], the highest reported cw output from any type of the photonic crystal laser. The emission spectrum below (blue arrow) and above (red arrow) the lasing threshold are also plotted in Fig. 2.11(c). Below the threshold, three peaks originating from the out-coupled Γ-point modes superpositioned on a broad emission band are visible. On the other hand, above the threshold only a single laser line originating from the Γ_1-mode becomes dominant. The authors achieved more than one-hour cw operational time.

To summarize, photonic crystal band edge lasers provide higher operational power than cavity-based photonic crystal lasers [92, 93, 94, 95] due to large mode volumes arising from their open cavity nature. On the other hand, cavity lasers provide very low mode volumes and thus high efficiency of the Purcell effect [60].

---

[19]Authors do not specify the thickness of the photonic crystal layer. However, in order to obtain light confinement, it must be at least several hundreds of nanometers thick. MgF_2 layer then provides a buffer layer with the refractive index lower than that of the InGaAsP and allows the vertical confinement of band edge modes in the photonic crystal.

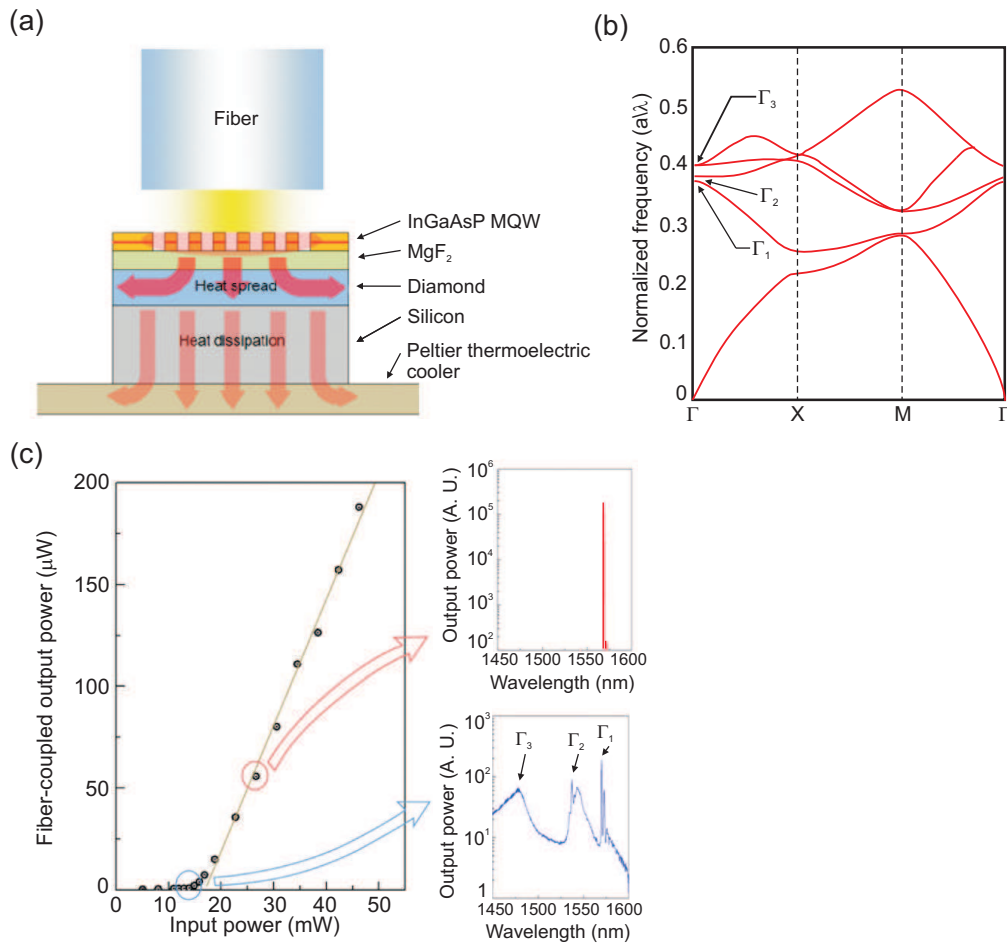[20]Sometimes also called surface-emitting lasers or second-order DFB lasers.

Figure 2.11: A photonic crystal vertically-emitting band edge laser. (a) A schematic cross-section of the device. A photonic crystal etched on the top of the device consisted of holes possessing a square symmetry. (b) The photonic band diagram of the photonic structure. (c) Dependence of the out-coupled versus input power manifesting laser threshold. The emission spectra below and above the threshold are also plotted. Above the threshold, a single very efficient laser peak occurs. Adapted from Ref. [24].

Photoluminescence characteristics of silicon nanocrystals

In this chapter, the most popular fabrication methods of SiNCs are described along with the experimental techniques employed to measure optical properties of SiNCs. Finally, results concerning the time-integrated and time-resolved PL of the SiNCs samples are presented.

3.1 Experimentals

3.1.1 Fabrication methods of Si nanocrystals

Silicon nanocrystals can be prepared via numerous fabrication methods, comprising either bottom-up or top-down approaches [2]. The most frequently used bottom-up technique is based on thermal annealing of a Si-rich silicon oxide, which leads to the formation of SiNCs embedded in a SiO_2-matrix. Non-stochiometric environment in the silicon oxide can be created for example by chemical vapor deposition, sputtering or ion implantation. The latter was applied to fabricate samples studied in Chapter 6. The samples composed of the regularly repeating bilayers of SiNCs embedded in SiO_2 and a pure stoichometric SiO_2 [96] are investigated in Chapter 4, Section 4.2.2. Other bottom-up methods are based on wet-chemical approaches [97] or on the plasma dissociation of silane gas [31], which typically leads to narrow-sized SiNCs with organic capping.

The most popular top-down techniques, which are based on the size reduction of bulk Si until nanoscopic dimensions are reached, are laser ablation and an electrochemical etching method. The former method applies high-power laser pulses to extract small nano-sized clusters from a Si target [98]. The latter is based on the electrochemical etching (anodic oxidation) of a Si wafer and leads to the formation of a sponge-like porous structure consisting of Si crystallites. This method was used to prepare the majority of the SiNCs samples studied in this thesis and therefore it is briefly described below.

Figures 3.1(a,b) schematically illustrate the setup used for the electrochemical etching of a Si wafer, which is in our case a boron-doped p-type $\langle 100 \rangle$ oriented thin Si plate. The wafer is placed in a teflon chamber between an Al bottom plate-electrode and a top electrode made from a Pt stripe placed on the rim of the chamber. By assuring continuous stirring of the etch bath, which comprises hydrofluoric acid, ethanol and hydrogen peroxide, during the process of low-current electrolysis ($1.6 - 2.5$ mA/cm^2), the homogeneous distribution of an electric field is achieved. The holes (in p-type silicon) then enable a chemical reaction which etches the Si wafer (Fig. 3.1(b)) and forms the net of pores with lateral dimensions below ~ 3 nm. After the etching process, the sample is left on air and gradually oxidizes, i.e. is covered by a SiO_x/SiO_2 shell. As a result of the quantum confinement of carriers in the pores of a crystalline Si capped with surface oxide, the sample exhibits efficient PL under external UV irradiation (Fig. 3.1(d)). Finally, the porous layer (several μm thick) is pulverized from the wafer and a powder containing the clusters of SiNCs is obtained. Afterwards, the powder is either embedded into a SiO_2 sol-gel matrix (for details see Chapter 4) or dispersed in an ethanol-based solution. Large agglomerates of SiNCs can be partially broken by ultrasonic treatment. Details of this method and also HRTEM images evidencing the crystalline nature of the prepared SiNCs can be found in Ref. [49]. Several types of the SiNC-powders which differ in optical properties can be fabricated by modifying the etch bath components, for example by adding H_2O_2 post-treatment as demonstrated in detail in Ref. [56] (attached as Enclosure 3.4).
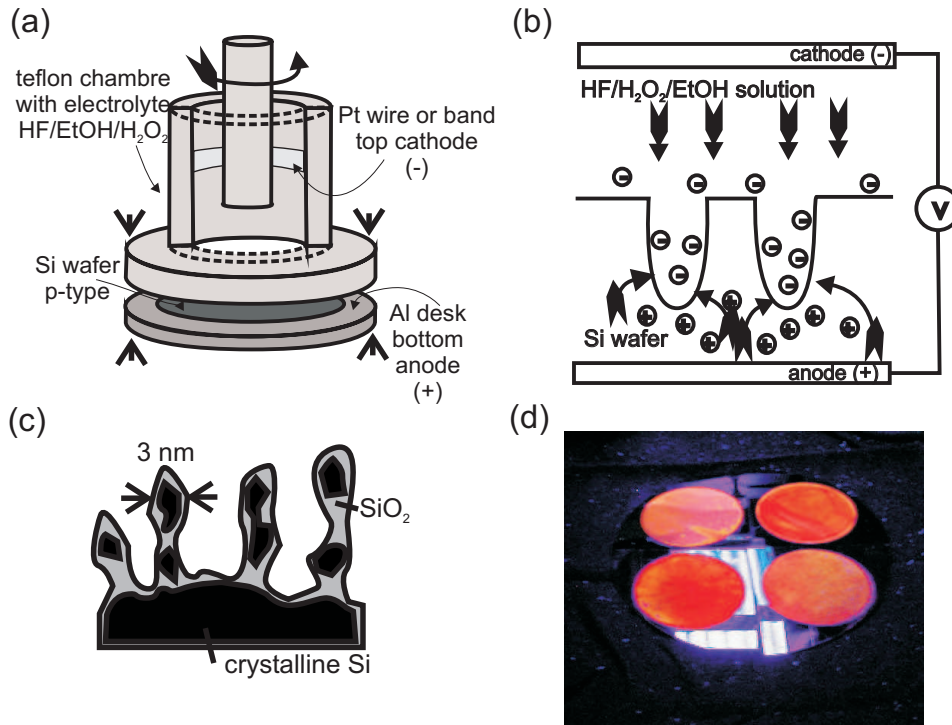
Figure 3.1: A sketch of the electrochemical etching of a Si wafer employed to fabricate SiNCs. (a) An etching chamber. (b) A sketch of the chemical process involved in the reaction. (c) A schematic illustration of the surface of the etched wafer. (d) The light-emitting porous surface of the etched Si wafers under the UV-lamp excitation.

3.1.2   Time-integrated photoluminescence

The steady-state characterization of the studied samples was performed to acquire basic information about their PL. For excitation of a sample, a cw HeCd laser emitting at 325 nm with the maximal output power of ~ 10 mW was employed. Photoluminescence emission was then collected under a specific detection angle from the excited area of the sample using either two concave lenses or an optical fiber. In order to spectrally resolve the PL, the signal was collected in a spectrograph (the range of 300–900 nm) and then projected either onto a Peltier-cooled charge coupled device (CCD) (Prague, ASCR) or onto a Nitrogen-cooled CCD detector (Strasbourg, IPCMS). An edge-filter prevented the entry of the excitation wavelength into the spectrographs. The measured spectra were corrected for the spectral response of the detection system.

For temperature-dependent measurements, samples were placed into an optical He-flow cryostat (Oxford Instruments) enabling to cover the temperature range from 4K to room temperature (Strasbourg, IPCMS).
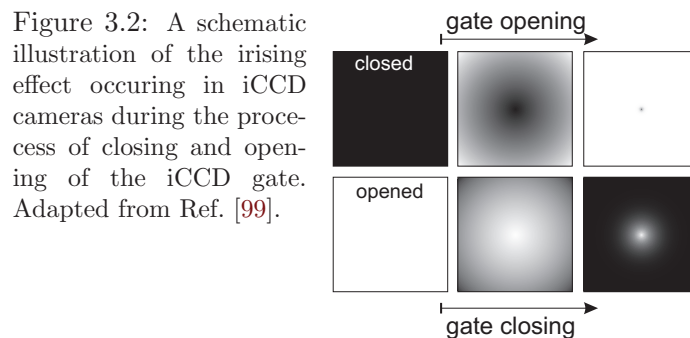
3.1.3   Time-resolved photoluminescence

Time-resolved measurements discussed in this thesis were performed using either excitation pulses with length of the order of nanoseconds (Prague, ASCR) or femtoseconds (Strasbourg, IPCMS). Details of each experimental setup are described below.

Nanosecond laboratory − Prague, ASCR

The output of a pulsed Nd:YAG laser (the repetition rate of 10 Hz, the pulse length of ~ 8 ns) was used as a source for the nanosecond excitation. The fundamental wavelength of 1064 nm was converted to the third harmonic at 355 nm. The generated high-energy (~ 170 mJ/pulse) pulses were either sent through several optical elements (filters, lenses, etc.) onto a sample or were directed towards the input of an optical parametric oscillator (OPO). By means of a non-linear crystal, the OPO enabled to cover the spectrally broad excitation range of $\lambda_{exc} = 420 - 2000$ nm.

The PL emission signal was then collected by an optical fiber with a coupler enhancing the collection efficiency, positioned under a specific angle with respect to the sample plane. The fiber output was attached to an Andor Shamrock SR163i spectrograph imaging the signal onto a Peltier-cooled intensified CCD camera (iCCD, Andor, irising time of ~ 4 ns—see below for the explanation). The iCCD enabled to detect simultaneously both spectrally and time-resolved signal, by means of fast gating of a photocatode. By setting a particular length of a detection time window sometimes called a gate (down to 12 ns) and then changing the detection window time delay with respect to the excitation event (detection is pre-triggered to cover also the onset of the signal), the signal can be stored at the different time instants. Consequently, the signal temporal decay or its spectral evolution in time can be reconstructed.

The iCCD detection can be used to well characterize dynamics on the microsecond time scale. Measuring the nanosecond time evolution with the above described experimental setup has some peculiarities. First, if the length of the detection time window is comparable to the duration of the excitation pulse, the onset of the PL signal will basically copy the time evolution of the pulse. Second, the opening of the gate is achieved by applying high variable voltage (up to 200 V) from the edges to the middle of the photocatode. On the contrary, the voltage of opposite polarity is used to close the gate, which may be visualized as closing of an iris gate (see Fig. 3.2). Therefore, it is called an irising effect. Time needed to fully open

Figure 3.2: A schematic illustration of the irising effect occuring in iCCD cameras during the process of closing and opening of the iCCD gate. Adapted from Ref. [99].

the gate is referred to as an irising time. As a consequence, when the length of the detection window is comparable to the irising time, the detected signal can be seriously distorted, which may lead to the false interpretation of the measured data. The irising effect is described in detail in Ref. [99], attached as Enclosure 3.3. A software procedure that can be used to correct the distorted data is also presented in Ref. [99]. However, in order to acquire the more reliable

results of the PL decays on the nanosecond time scale, another detection technique should be employed. This method is described in the following paragraph.

**Femtosecond laboratory – Strasbourg, IPCMS**

Two types of excitation sources were employed for the time-resolved PL measurements with femtosecond pulses: RegA Coherent and Tangerine lasers. The first one is based on a Ti-sapphire laser and a Ti-sapphire amplifier both pumped by a green solid-state laser. Femtosecond pulses from the laser are coupled to the amplifier which then provides excitation pulses at the wavelength of ~ 800 nm with the duration of about 100 fs and a repetition rate of 200 kHz. The second harmonic at ~ 400 nm of the amplifier output is then used for the excitation of a sample. The energy of the pulse is of the order of several millijoules. The second system (Tangerine) is based on a photonic crystal fiber laser (the material of the fiber is Yb:KYW). The fundamental wavelength of the laser is at 1030 nm with more than 100 μJ per pulse. Third-harmonic generation via non-linear crystals provides the excitation wavelength $\lambda_{exc} = 343$ nm with the maximal energy in the pulse equal to ~ 20 μJ. The pulse duration is ~ 350 fs and the repetition rate is tunable up to 2 MHz. The great advantage of this laser is an exceptional spatial beam quality due to the guiding of the beam in the fiber core. Therefore it was employed for the optical gain measurements using the VSL and SES methods, which are in detail described in Chapter 4. Different excitation wavelengths are obtained via non-linear processes in optical parametric amplifiers placed at the output of both systems. The laser beam is then either directed immediately onto the sample for the measurements of the PL decay or it passes through the setup built for the optical gain measurements.

The PL emission signal of the excited sample is recorded by a streak camera Hamamatsu coupled with a spectrograph. The streak camera allows to obtain spectral and temporal information about the PL in one shot, which is stored as a 2D matrix. This matrix comprises information on the intensity of the PL signal (in number of photons) as a function of time (rows) and wavelength (columns). The different lengths of the streak camera detection time windows can be set to cover the desired temporal range, while the lowest accessible time window is 1 ns long with the resolution of about 30 ps. The detected spectra were corrected for the spectral response of the detection system evaluated with a calibrated quartz tungsten lamp (Newport).

3.2 Results and Discussion

In this section, the main results of an experimental study conducted on oxide-passivated SiNCs fabricated by the electrochemical etching of a Si wafer are presented. The oxide-passivated free-standing Si nanoparticles with different dimensions (from 2 to 3.5 nm [56]) were prepared by the author and his colleagues at the Institute of Physics, ASCR in Prague. Under external (cw and pulsed) UV excitation, two distinct emission bands—blue and red—occur simultaneously in the PL spectra of the studied SiNCs as opposed to the usual PL spectra of SiNCs fabricated by different methods, which typically show only one type of the emission band. The physical properties of these two bands, a slowly decaying (on the microsecond time scale) red-orange S-band and a fast decaying (on the nanosecond time scale) blue-green F-band, have been introduced already in Chapter 1. When the dimensions of the fabricated SiNCs decrease, the spectral maximum of their S-band blueshifts from 680 nm down to 590 nm in agreement with quantum confinement effect (see Ref. [56], attached as Enclosure 3.4).

Figure 3.3: A simplified sketch of the Si band diagram depicting the effect of temperature and tensile strain on the valence band. The F-band and S-band in SiNCs are also depicted by the blue and red long arrows. Adapted from Ref. [100].
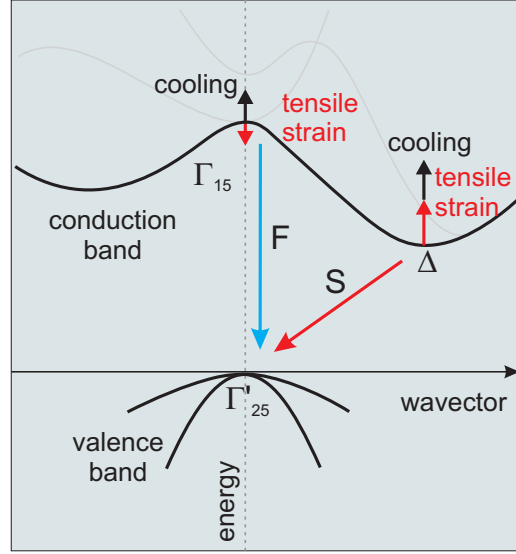
Further decrease of size of the studied SiNCs leads to the PL spectrum comprising only the F-band, whereas the S-band is not detected anymore. This effect originates most probably from the fact that the number of small NCs in an ensemble of SiNCs exceeds the number of bigger ones. The small ones emit preferentially via the quasi-direct (due to the high space localization of carriers and subsequent relaxation of the wavector conservation rule) and/or via the $\Gamma - \Gamma$ direct recombination, both being fast radiative channels. The slow S-band is attributed, in line with the latest important results of another research group [31], to the indirect phonon-assisted recombination between the core-states in cooperation with surface passivation species, i.e. the surface-influenced core-states [30].

SiNCs samples with the S-band located at around 600 nm and the F-band at around 430 nm (both detected under 325 nm cw excitation) were used in most of our measurements (with free-standing oxide-passivated SiNCs) presented from now on in this and the following chapters. These samples (SiNCs powder) appear white-colored under daylight (in some our publications therefore labeled as "white" SiNCs).

The decay characteristics and temperature dependence of the F-band in the oxide-passivated free-standing SiNCs were investigated by means of ultrafast spectroscopy (see the previous section for details on the experimental setup). A sample was prepared by drop-casting a SiNCs/ethanol colloidal dispersion on a Si wafer. After drying, the layer of SiNCs was formed and the sample was placed into the He-flow cryostat. The results of these novel and original measurements (employed in the femtosecond laboratory at IPCMS, Strasbourg) are summarized in a submitted manuscript, attached as Enclosure 3.6. The main output of this manuscript is the interpretation of the F-band as originating mainly from the quasi-direct phonon-less core-related recombination between the electronic states positioned in the close vicinity of the Γ-point of the Brillouin zone (Fig. 3.3—blue arrow). This statement is evidenced by a qualitative model, which explains a striking contrast between the F-band and S-band spectral shifts as a function of temperature. Specifically, the observed spectral red-shift of the S-band ($\Delta_S \sim 200$ meV) was almost 6-times larger than the red-shift of the F-band ($\Delta_F \sim 35$ meV) with temperature varying from 4K to room temperature (see Enc. 3.6). These spectral shifts were interpreted as due to the interplay between the bulk-related and strain-induced effect on the Si band structure (Fig. 3.3).

Furthermore, the character of the F-band's decay curves is composed of two components:

(i) a fast picosecond one fitted by a single-exponential function and (ii) a slower nanosecond one fitted by a stretched exponential function. This result agree very well with the theoretical model of carriers' relaxation dynamics in SiNCs presented recently by Moskalenko et al. [101]. Based on their simulation, the core-related electron-hole recombination in an ensemble of NCs with a broad size distribution (as are also the NCs used in this study) is governed by the multiphonon relaxation of carriers, specifically holes, in-between the discrete energetic levels at the edge of the Si valence band [101]. This again points at the core-related origin of the F-band.

The effect of strain and temperature on the spectral position of the S-band in SiNCs is in detail investigated in Ref. [102], attached as Enclosure 3.5. The large amount of data concerning the spectral position of the S-band with respect to the size of a NC in the different types of oxide-passivated SiNCs were collected and compared, yielding an interesting result: the S-band of matrix-embedded SiNCs (typically in SiO_2) is always red-shifted compared to free-standing SiNCs of the same size (in the form of powder or colloidal suspension) by about 200 meV. This was attributed to the effect of compressive strain generated by the surrounding environment during the thermal annealing and gradual growth of the matrix-embedded SiNCs whereas the free-standing SiNCs are relaxed and under no strain.

3.3 Enclosure

Data processing correction of the irising effect of a fast-gating intensified charge-coupled device on laser-pulse-excited luminescence spectra

L. Ondič, K. Dohnalová, I. Pelant, K. Žídek and W. D. A. M. de Boer

Review of Scientific Instruments, 81: 063104, 2010

Data processing correction of the irising effect of a fast-gating intensified charge-coupled device on laser-pulse-excited luminescence spectra

L. Ondič,[1,2,a)] K. Dohnalová,[1,3] I. Pelant,[1] K. Žídek,[2] and W. D. A. M. de Boer[3]

[1]*Institute of Physics, Academy of Sciences of the Czech Republic,*
v.v.i., Cukrovarnická 10, CZ-162 53 Prague 6, Czech Republic
[2]*Department of Chemical Physics and Optics, Faculty of Mathematics and Physics, Charles University,*
Ke Karlovu 3, 121 16 Prague 2, Czech Republic
[3]*Van der Waals-Zeeman Institute, University of Amsterdam, Valckenierstraat 65, NL-1018 XE Amsterdam,*
The Netherlands

Intensified charge-coupled devices (ICCDs) comprise the advantages of both fast gating detectors and spectrally broad CCDs into one device that enables temporally and spectrally resolved measurements with a few nanosecond resolution. Gating of the measured signal occurs in the image intensifier tube, where a high voltage is applied between the detector photocathode and a microchannel plate electron multiplier. An issue arises in time-resolved luminescence spectroscopy when signal onset characterization is required. In this case, the transient gate closing process that causes the detected signal always arises in the middle of the ICCD chip regardless of the spectral detection window—the so-called irising effect. We demonstrate that in case when the detection gate width is comparable to the opening/closing time and the gate is pretriggered with respect to the signal onset, the irising effect causes the obtained data to be strongly distorted. At the same time, we propose a software procedure that leads to the spectral correction of the irising effect and demonstrate its validity on the distorted data. © *2010 American Institute of Physics.*
[doi:10.1063/1.3431536]

I. INTRODUCTION

Intensified charge-coupled devices (ICCDs) are widely applied in fluorescence studies to realize the so-called time-resolved emission spectroscopy. The investigated solution of luminescent species or the sample of a solid phosphor is excited by, as a rule, a pulsed laser and the generated luminescence response is optically led to a spectrograph equipped at the exit port with an ICCD detector. In this way, the spectrally decomposed luminescence radiation can be captured at a given instant, driven by the temporal gate position with respect to the excitation event.[1] Measurements of this kind usually need short detection gate window, able to open and close very quickly.

The gated imaging is achieved by the image intensifier incorporated in front of the charge-coupled sensor. The most commonly used image intensifier for such purpose is a proximity-focused unit combining a photocathode, a microchannel plate electron multiplier, and a phosphor screen arranged in series.[2] These can be gated either by pulsing the voltage between the light-sensitive photocathode and the front face of the microchannel plate, or alternatively, the voltage across the microchannel plate can be switched. In the first case, the composition of the cathode determines the conductivity, which limits the speed of the high voltage pulse propagation. In the most common construction of the ICCD detectors, opening voltage proceeds from the photocathode edges toward its center. This reveals itself as a "blind" cir-

cular spot, diminishing gradually with time toward the center [Fig. 1(a)].[3] After the due time period, given by the gate width, the intensifier is set to close through the application of an opposite voltage. Similarly as for opening, the voltage proceeds from the edges to the center, leading to a gradual reduction in the active region from the edges, similar to shutting the iris [Fig. 1(b)], therefore the term "irising effect." The closing process takes place more quickly than the opening due to a different absolute value of the applied voltage.[3] According to the irising time value, ICCD cameras used nowadays can be divided into two main groups: slow gating ("Gen I") and fast gating ("Gen II" and "Gen III").

It is often tacitly supposed that the gate opening/closing times may be neglected in comparison with the intensifier gate width. If this is not the case, the registered spectra might be seriously distorted and incorrectly interpreted. This effect has been exploited by Shaddix and Williams in Ref. 3 using slow-gating ICCD system. The present communication demonstrates similar risk also for fast-gating ICCD detectors. We also show how this adverse effect can be rectified.

II. EXPERIMENTAL: SIGNAL ONSET AND PRETRIGGERED GATING

The manufacturer defines for this particular fast-gating ICCD model the minimum optical gate width as that for which the peak signal level exceeds 20% of the signal level, recorded with the same source and a 100 ns gate. It is supposed to be a parameter that characterizes the size of the detection gate from which the camera gives correct results.
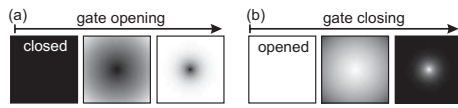
a)Electronic mail: ondic@fzu.cz.

FIG. 1. ICCD gate (a) opening and (b) closing process.

According to our particular camera specification, the minimum optical gate width is 12 ns with the irising time less than 4 ns. The influence of the irising effect on the detected photoluminescence (PL) emission was measured using the minimum gate width of 12 ns, shifted by a step of 0.1 ns around the position of the PL emission rise time (by the use of a pretriggering of the ICCD camera by the laser system). This is schematically sketched in Figs. 2(a) and 2(b) for the middle area of the detector chip at the gate delay of 0 and 20 ns, respectively. Owing to the pretriggering, the ICCD photocathode begins the closing process before the temporal onset of the luminescence signal at the edge regions of the detector chip is reached. As we mentioned above, due to the applied closing voltage, the center of the chip is closed, immediately after the first photons impinge on the photocathode. It becomes thus clear that for a spectrally broad signal, the detected spectrum develops always from the center of the chip, irrespective of the true spectral shape of the signal. Due to the fact that the irising time is not negligible in compari-
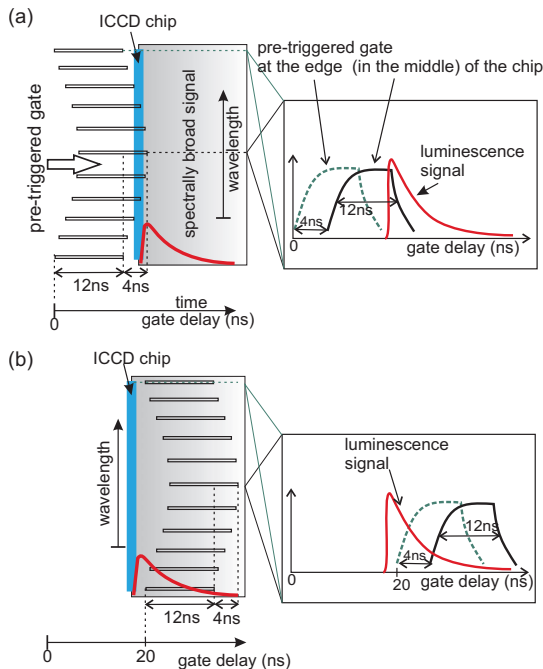

FIG. 2. (Color online) Sketch of the detection gate (narrow stripes at the left panel) penetration into a spectrally broad luminescence signal with ultra-fast rising time (gradient filled area). Gate is gradually delayed from center to the edges of the detector chip (solid vertical stripe at the left panel). Situation is plotted for gate delay of (a) 0 ns and (b) 20 ns. The right panels depict the situation for a single wavelength, positioned in the middle (solid curve) and at the edge (dashed curve) of the detector chip.
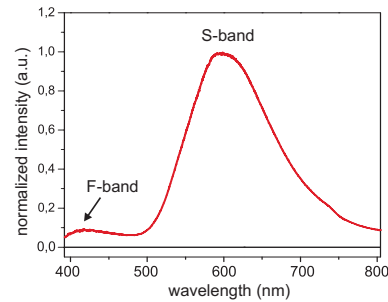

FIG. 3. (Color online) Steady-state room-temperature PL spectrum of SiNCs/SiO$_2$. It reveals two spectrally broad bands, an F band around 430 nm with nanosecond decay time and an S band around 600 nm with microsecond decay time.

son with the applied minimum gate width, the impact on the experimentally acquired spectra is significant, as will be demonstrated in the following section.

III. RESULTS AND CORRECTION

We illustrate the irising effect for room-temperature time-resolved PL measurements of a sample consisting of high density ($\sim$15 vol %) oxygen passivated silicon nanocrystals with diameter of 2–3 nm embedded into a SiO$_2$-based matrix (sample fabrication details can be found in Ref. 4). Steady-state PL spectra were obtained using a continuous-flow HeCd laser excitation (325 nm) and detected using an Andor CCD detector coupled to an imaging spectrograph. A typical steady-state PL emission spectrum of our sample is plotted in Fig. 3. Two spectrally broad bands are observed: (i) a fast band (F band) at 430 nm with a nanosecond decay time[5] and (ii) a slow band (S band) at 600 nm with a microsecond decay time ($\sim$10 μs).[6] Time-resolved PL spectra were excited with a Nd:YAG (yttrium aluminum garnet) laser (355 nm, 8 ns pulse duration, 10 Hz repetition rate, excitation density $\sim$kW/cm^2). In this case, the sample exhibits relatively broad PL signal in the blue-green region with nanosecond dynamics. It is shown in the Appendix that the luminescence rise time itself is very short. The fast signal rise time as driven by the laser pulse, sufficiently long decay time, and considerable spectral width of the studied spectra make our sample suitable for the demonstration of the irising effect. The signal, measured at room temperature, was collected by an optical fiber coupled to a detection system consisting of an Andor Shamrock SR163i imaging spectrometer equipped with an Andor ICCD camera (model DH720–18H-13). All presented PL emission spectra were corrected for the steady-state spectral response of the detection system.

In order to demonstrate the aforementioned effects, identical time-resolved PL emission spectra were measured in two detection spectral windows of the spectrograph, always on the same sample. The first detection window spans from 369 to 702 nm [Figs. 4(a) and 4(b)] and the second one from 435 to 772 nm [Figs. 4(c) and 4(d)]. It is obvious that the signal onset appears in the middle of the chip, regardless of the spectral detection window position, indicating that we
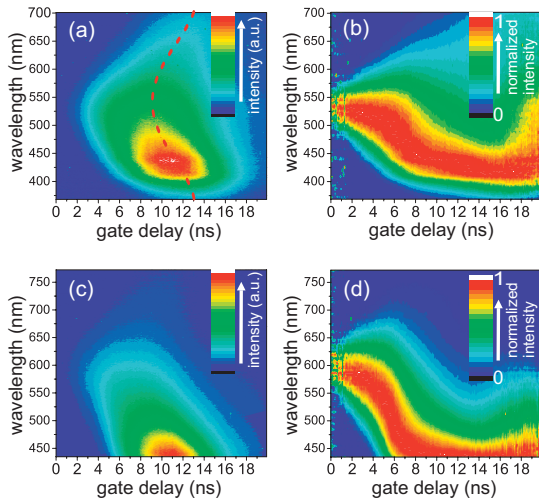
FIG. 4. (Color) Time-resolved PL spectra (gate width of 12 ns shifted by the step of 0.1 ns; signal is pretriggered) of a SiNCs/SiO$_2$ sample measured with the ICCD detector with relatively long irising time (~4 ns) in two spectral detection windows: (a) and (b) 369–702 nm and (c) and (d) 435–772 nm. (b) and (d) show normalized time-resolved PL spectra from (a) and (c). Dashed line in (a) marks signal maxima for each wavelength through different gate delays.
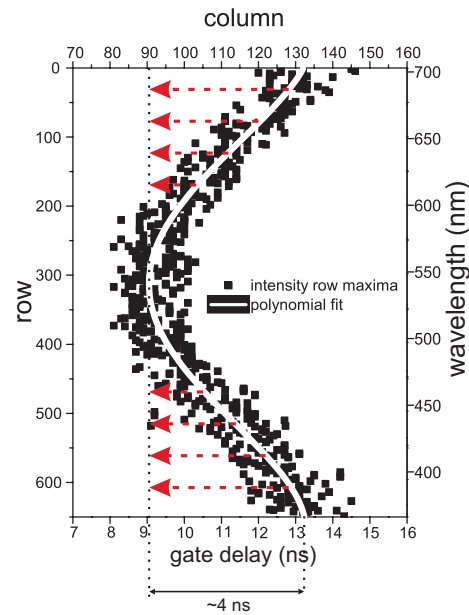

FIG. 5. (Color online) Highlighted position of the signal maxima for each row (wavelength) in the matrix, which consists of ordered measured data (rows are wavelengths and columns are different gate delays). Polynomial fit (white curve) of the column-on-row dependence and the basic concept of the irising correction (dashed arrows) are shown, consisting in reordering the data within the matrix.

obtain different spectral development in time in different detection windows, even if the signal input is identical.

Clearly, this effect does not reflect any real processes in the investigated sample but rather represents a detection artifact, in this particular case, the irising effect. This is indeed confirmed by the photon-counting measurements (Fig. 7). Therefore we conclude that the measurements depicted in Fig. 4 do not provide us with relevant physical information about the samples. Since the irising effect is expected to be an intrinsic property of each particular ICCD detector due to its internal construction, it should neither vary with the experimental conditions nor drift markedly with time. Hence its correction ought to be feasible through a simple data processing algorithm and should be implemented as a routine calibration process. This we are going to propose. The process will be demonstrated using the data from Fig. 4(a). First, the acquired data are ordered in a matrix in which each row represents specific detected wavelength and each column is connected with a certain gate delay. In our particular case, the delay increases from 0 to 20 ns by a step of 0.1 ns and we have data for 649 pixels (wavelengths) between 369 and 702 nm, i.e., our matrix contains 649 rows and 200 columns. Subsequently, in each row of the matrix (for each wavelength) we find a maximum of the intensity that, obviously, is connected with a specific matrix column (gate delay) (Fig. 5). The intensity maximum occurs at a given wavelength when two conditions are satisfied: first, the whole detection window covers the signal and, second, the detection window position is in the vicinity of the signal peak. In other words, it happens for those gate delays for which the signal at a specific wavelength is falling onto the ICCD chip during the whole detection time. Due to the irising effect and the pretriggering, this occurs earlier in the middle of the chip and

later at the edges (Fig. 2). Mathematically rigorous approach is through a functional dependence of columns on rows, which was fitted with a polynomial function of the fourth order (Fig. 5). This function characterizes the irising effect behavior of the specific ICCD quite accurately. We note here that the mathematical description of the fitting function was chosen according to the shape of the obtained column-on-row dependence and therefore is characteristic for a particular device. The correction is based on the physical assumption that for all detected wavelengths, the rise of the signal is "instantaneous," in other words, the maximum of the time-resolved PL signal should occur for each wavelength at the same time (gate delay). This assumption is validated by the verification measurements on the same sample on a different PL setup, using a single-photon-counting technique with 17 ps resolution (see Appendix). Moreover, in Sec. IV, we demonstrate the validity of this assumption using a reference detector.

In such case, one expects to observe the signal onset in a single column of the data matrix. Therefore, using the polynomial fit, the correction shifts all data in each row (except a few ones in the middle) in time according to their relative position to the shortest gate delay as is schematically indicated by dashed arrows in Fig. 5. After applying this correction, the row maxima will all occur at the same gate delay.

The aforementioned correction has been applied to the time-resolved PL spectra shown in Fig. 4(a). Corrected spectra are plotted in Fig. 6(a) and reveal very different time evolution, compared to the as-measured ones in Fig. 4(a).
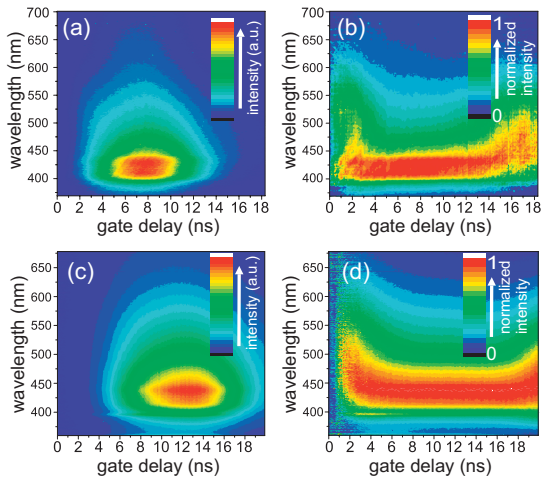
FIG. 6. (Color) (a) Time-resolved PL spectra from Fig. 4(a), corrected for the irising effect. (b) Normalized (a). (c) Time-resolved PL spectra obtained with "reference" ICCD with short irising time of ~0.2 ns. Detection parameters are similar to that used in Fig. 4(a). (d) Normalized (c).

For a more precise correction, a white-light source with instantaneous rise time and spectrally stable shape would be required. Once the irising effect is evaluated using a proper light source, the correction can be applied to other measurements of any light source to reduce the irising effect to possible minimum. However, we should consider that the irising effect might slightly change due to the aging of the ICCD detector and therefore repeating the evaluation of the correction function after a reasonably long time period seems appropriate. We note that in order to obtain reasonable correction, it is also important to use short gate delay step.

IV. REFERENCE MEASUREMENTS AND CONCLUSIONS

Finally we exploited an opportunity to realize similar measurements on a faster reference ICCD Andor camera (model DH720–18F-03) with minimum optical gate width of 3.81 ns and irising time of only 0.20 ns. Two-dimensional map of time-resolved PL spectra obtained with a similar experimental setup, detection parameters, and sample as above is displayed in Fig. 6(c), normalized in Fig. 6(d). The irising time of this demo ICCD is negligible compared to the applied detection gate window (12 ns); therefore the experimental results are negligibly affected by the finite opening and closing time of the photocathode and should bear a correct physical information about the sample. These reference measurements verify the validity of the software correction for the irising effect. The comparison of corrected spectra in Figs. 6(a) and 6(b) with the as-measured spectra (not corrected for the irising effect) using the faster reference ICCD detector in Figs. 6(c) and 6(d) shows significant similarities. The signal slowly shifts with time from the blue-green region (400–550 nm) to the blue (430 nm) one and then backward. Although the normalized spectra show the similarity in spectral shift, apparent differences can be seen in onset time. Possible explanations for this are the following. First, it is

hardly possible to set the pretriggering time on different ICCD cameras such that the signal onset would occur for the same gate delay on both of them and therefore the onsets might be slightly shifted. Second, the relatively long irising time might cause that the 12 ns wide detection window appears to be effectively longer. That is the case with our ICCD model but not in the case of the faster reference one, even though the data corrected for the irising effect [Figs. 6(a) and 6(b)], using the proposed data processing procedure, show a significantly better match with the as-measured data using faster reference detector [Figs. 6(c) and 6(d)] than that plotted without the correction in Figs. 4(a) and 4(b).

We can conclude that the aforementioned procedure represents an important step when measuring PL temporal evolution with ICCD detectors and can offer relatively simple "software" solution instead of pushing the "hardware" limits of fast gating further.

APPENDIX: LUMINESCENCE RISE TIME MEASUREMENTS

Optical signal that is to be used to supply data for correction of the irising effect should have—among other things—sufficiently fast rise time, much shorter than the irising time itself. Here we would like to confirm that the sample type of SiNCs, employed for nanosecond experiments through the main text, complies with this requirement. To do this, we excited the sample with 2 ps pulses from a frequency-doubled Ar⁺ pumped dye laser (323 nm, repetition rate of 3.8 MHz) and the spectrally resolved signal was detected with an ultrafast multichannel photomultiplier Hamamatsu R-3809 working in a single photon counting
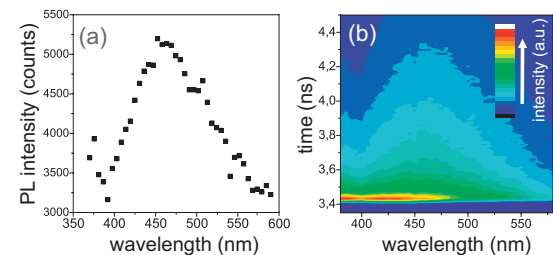

FIG. 7. (Color) (a) Time-integrated (detection window of 50 ns) PL emission spectrum of a SiNCs sample excited by 323 nm short laser pulses (2 ps) and detected with an ultrafast multichannel photomultiplier in a single photon counting mode. (b) Temporal evolution of the spectrum from (a). Fast rise time over whole detected spectrum is present.

mode (instrumental response of 17 ps). Figure 7(a) displays room-temperature emission spectrum of the sample under the above excitation conditions, integrated over 50 ns after excitation. The emission band peaks at ~450 nm and extends beyond ~550 nm, in good agreement with the nanosecond-pumped spectra shown in Figs. 6(a) and 6(c). The crucial information is contained in Fig. 7(b), which represents temporal evolution of the whole PL spectrum. It can be clearly seen that the initial signal rise is extremely fast (<30 ps). Accordingly, when excited with 8 ns Nd:YAG laser pulses, the leading edge of the PL signal that hits the ICCD photocathode (Sec. II) is limited exclusively by the excitation

pulse temporal shape but not by luminescent rise time itself.

[1] *Luminiscence of Solids*, edited by D. R. Vij (Plenum, New York, 1998).
[2] G. Holst and T. Lomheim, *CMOS/CCD Sensors and Camera Systems* (JCD, Bellingham/SPIE, Washington, 2007).
[3] C. R. Shaddix and T. C. Williams, Rev. Sci. Instrum. **80**, 033702 (2009).
[4] K. Dohnalová, I. Pelant, K. Kůsová, P. Gilliot, M. Galart, O. Crégut, J.-L. Rehspringer, B. Hőnerlage, T. Ostatnický, and S. Bakardjieva, New J. Phys. **10**, 063014 (2008).
[5] L. Tsybeskov, J. V. Vandyshev, and P. M. Fauchet, Phys. Rev. B **49**, 7821 (1994).
[6] K. Dohnalová, L. Ondič, K. Kůsová, I. Pelant, J. L. Rehspringer, and R.-R. Mafouana, J. Appl. Phys. **107**, 053102 (2010).

3.4   Enclosure

White-emitting oxidized silicon nanocrystals: Discontinuity in spectral development with reducing size

K. Dohnalová, **L. Ondič**, K. Kůsová, I. Pelant, J. L. Rehspringer and R.-R. Mafouna

White-emitting oxidized silicon nanocrystals: Discontinuity in spectral development with reducing size

K. Dohnalová,[1,a] L. Ondič,[1] K. Kůsová,[1] I. Pelant,[1] J. L. Rehspringer,[2] and R.-R. Mafouana[2]

[1]*Institute of Physics, Academy of Sciences of the Czech Republic, v.v.i., Cukrovarnická 10, CZ-162 53 Prague 6, Czech Republic*
[2]*IPCMS, Unité mixte CNRS-ULP (UMR7504), 23, rue du Loess-BP 43, F 670 34 Strasbourg Cedex 2, France*

Small oxidized silicon nanocrystals of average sizes below 3.5 nm are prepared using modified electrochemical etching of a silicon wafer. Modifications introduced in the etching procedure together with postetching treatment in H_2O_2 lead to a decrease in the nanocrystalline core size and also, to some extent, to changes in the surface oxide. The interplay between these two factors allows us to blueshift the photoluminescence (PL) spectrum from 680 down to 590 nm, which is accompanied by changes in PL dynamics. This continual development, however, stops at about 590 nm, below which abrupt switching to fast decaying blue emission band at about 430 nm was observed. Discontinuity of the spectral shift and possible relation between both bands are discussed. © *2010 American Institute of Physics*. [doi:10.1063/1.3289719]

I. INTRODUCTION

Oxidized silicon nanostructures have been of the high interest since the first observation of efficient room-temperature visible photoluminescence (PL) in 1990 by Canham[1] from porous silicon (por-Si) prepared by electrochemical etching.[2] The impact of the oxidized surface of small silicon nanocrystals (SiNCs) (diameter 1–5 nm) on PL spectra and origin of two usually observed emission bands—a fast blue "F-band" and a slow red "S-band"—has been discussed ever since the pioneering works of Kanemitsu *et al.*[3–6] Nevertheless, vast majority of published papers on the luminescence properties of por-Si or light-emitting SiNCs deals separately with either the F- or the S-band. Consequently, no clear concept as whether there is some firm relationship between these two emission processes has been established up to now. For instance, the F-band was studied mostly in por-Si prepared using the thermal oxidation process,[7,8] which exhibits only this fast blue emission, any slow red luminescence was not reported here. Similarly, ultrasmall Si nanoclusters fabricated by enhanced lateral electrochemical etching[9] emit solely in the blue region, similarly to many kinds of organically capped Si nanocrystals.[10–12] On the contrary, the famous paper by Wolkin *et al.*[13] on the pinning of the S-band spectral position owing to silicon-oxygen surface bonds does not mention the F-band at all. Similar deficiency in any information on the F-band can be met in most publications devoted to luminescence of SiNCs prepared by Si-ion implantation,[14,15] co-sputtering,[16] plasma-enhanced chemical vapor deposition[17] or reactive Si deposition method.[18] All the cited papers focus their attention exclusively on the S-band. Both the F- and S-band were simultaneously observed and discussed in Ref. 6 however, only under pulsed laser excitation. And yet, both the F- and

S-bands can be in general observed under cw excitation in one and the same type of samples, as demonstrated recently, e.g., in Refs. 19 and 20. Simultaneous observation of both emission bands in steady-state PL, if properly weighted, can lead to white emission, which may be interesting for applications.

The present paper is aimed at a systematic investigation, via the time-resolved PL technique, of both emission bands occurring in SiNCs fabricated by various modifications of Si-wafer electrochemical etching. The obtained results enable us to speculate about various proposed models of radiative recombination channels in SiNCs.

II. EXPERIMENTAL

Steady-state PL spectra were excited using a continuous laser at 325 nm (HeCd, 2.5 mW) and detected by an Andor charge coupled device (CCD) camera.

Time-resolved PL spectra were excited using a pulsed laser [neodymium doped yttrium aluminum garnet (Nd:YAG)], 355 nm, 10 Hz repetition rate, 7 ns pulse duration, $\sim kW/cm^2$) and detected using an Andor intensified CCD (iCCD) camera (minimal gate width 8 ns, irising effect ~ 4 ns, cooled to $-20\ ^{\circ}C$) coupled to an Andor Shamrock imaging spectrograph. Detection system was pretriggered. Spectra were measured at room temperature and corrected for the spectral response of the detection system by a calibrated 45 W Oriel tungsten halogen lamp.

III. SAMPLE PREPARATION

Preparation technique of the SiNCs is based on a combination of electrochemical etching, catalyzed by the addition of H_2O_2 and a H_2O_2 postetching treatment. Generally, we prepare several types of samples called "standard," "yellow," "white," and "blue" [see Table I, Fig. 1(a)] with different optical properties.

---

a)Electronic addresses: dohnalova@fzu.cz and k.dohnalova@uva.nl.

107, 053102-1

TABLE I. Preparation parameters of various types of SiNCs powders; *p*-type wafers (B-doped, 0.075–0.100 Ω cm, $\langle 100 \rangle$-oriented, etched area $\sim$10 cm^2), and 2 h etching time are used. Etching takes place in a teflon chamber under stirring for all samples. Platinum is used as the top electrode.

| Sample | Preparation | | S-band | |
	Etching bath, current density	Postetching treatment	Position (nm)	Full width at half maximum (meV)
"Standard"	13 ml 50% HF+37 ml 99% EtOH; 1.6 mA cm^{-2}	none	680	500
"Yellow"	13 ml 50% HF+7 ml 3% H$_2$O$_2$+32 ml 99% EtOH; 2.5 mA cm^{-2}	5 min 3% H$_2$O$_2$ treatment	645	485
"White" "Blue"	13 ml 50% HF+2 ml 30% H$_2$O$_2$+37 ml 99% EtOH; 2.5 mA cm^{-2}	30% H$_2$O$_2$ treatment for 10–20 min, maturing at higher-humidity environment (several days, 50%–70%)	590–600 560 (very weak)	450

First, the preparation of a "standard" sample starts with electrochemical etching of *p*-type wafers [B-doped, 0.075–0.100 Ω cm, (100)-oriented, etched area $\sim$10 cm^2], platinum is used as the top electrode and the bath is stirred. The etching bath consists of HF(50%):EtOH($>$99.9%) =1:2.85 (without the addition of H$_2$O$_2$) at a constant current density of 1.6 mA cm^{-2} for 2 h. After intense rinsing in pure ethanol (EtOH) and slow drying in air, the resulting nanocrystalline layer is mechanically scraped-off the substrate and undergoes 30–60 min ultrasonic treatment in EtOH. PL of the SiNC layers can be observed with the naked eye under UV lamp excitation [Fig. 1(a)]. It is well worth mentioning that the naked-eye-observed PL immediately after the etching procedure, when the SiNCs are hydrogen-terminated, is green [Fig. 1(a)], turning red only after oxidation.[21] This "intrinsic" PL is green for all the types of SiNC layers described here (before application of H$_2$O$_2$ postetching treatment). Dried SiNCs powder prepared using the above-described way is labeled as "standard" and exhibits orange-red PL.

If we dip such a "standard" por-Si layer (before scraping

it into a form of powder) for several minutes into H$_2$O$_2$ (3%), we find that steady-state PL further blueshifts and, at the same time, a new blue emission component arises, whose intensity ratio to the red band increases with further prolongation of the H$_2$O$_2$ treatment [Fig. 1(b)]. After several tests, we managed to prepare three discrete types of por-Si layers, which are reproducible and show stable bright PL— "yellow," "white," and "blue" [Table I, Fig. 1(a)].

The "yellow" nanocrystalline layer is etched in modified bath HF(50%):EtOH($>$99.9%):H$_2$O$_2$(3%)=1:2.46:0.54 at 2.3 mA cm^{-2} for 2 h. The freshly prepared nanocrystalline layer is then rinsed with pure EtOH and immediately dipped into H$_2$O$_2$ (3%) for 5 min (postetching procedure), in order to further decrease the SiNCs crystalline core. Afterwards, the nanocrystalline layer is intensely rinsed with pure EtOH in order to remove all chemical left overs, dried slowly in air and mechanically scraped-off the substrate. The resulting fine powder appears yellowish under daylight (different absorption) and also emits yellowish, compared to the "standard" SiNCs powder [Fig. 1(a)].

Finally, the "white" and "blue" nanocrystalline layers are etched in HF(50%):EtOH($>$99.9%):H$_2$O$_2$(30%) =1:2.85:0.15 at 2.3 mA cm^{-2} for 2 h and then postetched in H$_2$O$_2$ (30%) for 10–20 min, which leads to enhanced decrease in the size of the SiNC core. Afterwards, the SiNCs layer is rinsed with pure EtOH. Contrary to the "yellow" nanocrystalline layer (etched and postetched in low-concentrated H$_2$O$_2$), the "white" one shows strong dependence of the final PL spectrum on air humidity and length of the slow drying procedure in air. Since the reaction of the crystalline silicon with H$_2$O$_2$ follows the equation:

$$2Si + 4H_2O_2 \rightarrow 2Si(OH)_4 \leftrightarrow$$
$$\leftrightarrow Si(OH)_3 - O - Si(OH)_3 + H_2O, \quad (1)$$
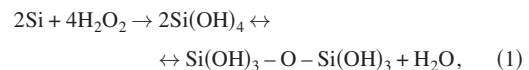
it is obvious that air humidity plays a crucial role in the efficiency of this treatment. Therefore the "white" nanocrystalline layer was dried slowly (usually for tens of hours or several days) in normal atmosphere in a chamber with stabilized humidity (50%–70%) and temperature (25–30 °C). During this time, a small amount of the 30% H$_2$O$_2$ probably persists in the netlike structure of the nanocrystalline layer and, depending on the air humidity conditions, the postetching procedure slowly continues. During this "maturing" pro-
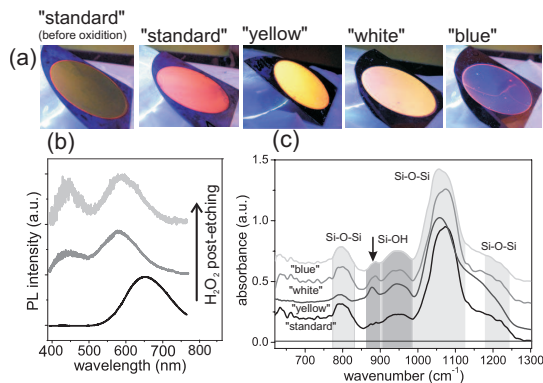

FIG. 1. (Color) (a) Photo of room-temperature steady-state PL of SiNCs layers (por-Si) as seen by naked eye under UV lamp. From left to right: freshly prepared (hydrogen-terminated) nonoxidized "standard" por-Si (as in Ref. 21) and oxidized "standard," "yellow," "white," and "blue" por-Si. (b) Steady-state room-temperature PL spectra excited by cw laser at 325 nm of "standard" por-Si as a function of duration of dipping into H$_2$O$_2$ (time increases from bottom up, while the lowest was not dipped at all). (c) FTIR absorption spectra of the "standard," "yellow," "white," and "blue" SiNCs powders.

cedure the PL of the SiNCs layer blueshifts, going through the "white" stage (PL under UV excitation peaks at 590 nm), and is followed directly by the "blue" stage (PL under UV excitation peaks at 430 nm) [Fig. 1(a)]. Duration of these stages is sample and humidity dependent. The mechanical scraping off of the SiNCs layer during the "white" stage leads to production of the "white" SiNCs powder, while scraping-off later, during the "blue" stage leads to production of the "blue" SiNCs powder. Optical properties of resulting SiNC powders, which can be stored in air at ambient conditions, remain stable after scraping off from the substrate and both types of powders appear white under daylight.

IV. EXPERIMENTAL RESULTS

A. Sample characterization

The differences in the PL emission [Fig. 1(b)] may be due to two effects, namely, core size decrease and/or surface passivation modifications. Consistent size characterization of this particular powder SiNCs samples is a bit difficult since SiNCs in this range of sizes are expected to undergo several core restructuralizations. First, one can expect a transition from crystalline to largely disordered system somewhere between 1 and 2 nm (Ref. 22) and further structural changes occur between 1 and 1.5 nm.[23] Therefore a single technique as high resolution transmission electron microscopy (HR-TEM) or Raman spectroscopy, depending on the crystallinity of the core, cannot be used for the whole set of powders. Therefore we present results from several characterization techniques which give consistent image of the studied samples.

The mean core diameter of the "standard" and "yellow" SiNCs was characterized in Ref. 24 using HRTEM and Raman spectroscopy, yielding 3.5 nm and 2.5–2.7 nm in the case of the "yellow" SiNCs. The "white" SiNCs diameter (core+oxide shell) was characterized in Ref. 25 by atomic force microscopy (AFM) to be between 1 and 2 nm. We believe that the AFM measurements might have somewhat underestimated the real size since in our other AFM measurements we actually observed that the nanocrystals on the surface, deposited from a mixture with a solvent, are embedded in a layer of molecules deposited with the solvent, which effectively decrease the measured size. Nevertheless, this series of measurements serves as a convincing argument that the fact that the size of the nanocrystalline core decreases when modifications of the etching procedure are applied, i.e., from the "standard" through the "yellow" to the "white" sample. Unfortunately we did not succeed in measuring the size of the "blue" SiNCs since it appears to be below the resolution of the used techniques.

The surface passivation of the SiNCs powders was studied with Fourier transform infrared spectroscopy (FTIR) in Ref. 24 and comparison of spectra for all types of SiNCs powders is given in Fig. 1(c). All show similar peaks: Si—O—Si cage, stretching and bending modes at 1160, 1050, and 800 cm^{-1},[26] and peaks at ~870 and 945 cm^{-1}, related to Si—OH modes.[26] The peak at 1160–1200 cm^{-1} might be also related to Si=O stretching mode,[27] however, Si=O bond is rather not stable (transforming into Si—OH)
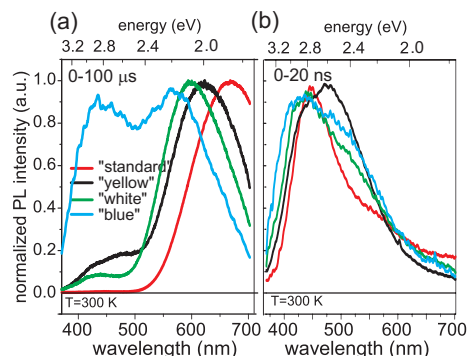

FIG. 2. (Color) Time-integrated [(a) 0–100 μs, (b) 0–20 ns] room-temperature PL spectra of various types of SiNCs powders excited by pulsed laser Nd:YAG at 355 nm (10 Hz, 7 ns). Signal was detected by pretriggered iCCD camera (times $t=0$ μs and $t=0$ ns are coincident with excitation pulse onset).

when in contact with polar reagents as H_2O_2, EtOH or water.[27] The only significant difference appears between the group of H_2O_2-treated SiNCs and the "standard" ones, when the former group shows an increase in the Si—OH signal at 870 cm^{-1}.

To sum up the characterization of SiNCs powders, we believe that the samples "standard," "yellow," "white," and "blue" can be considered a series (in the given order) with the most significant parameter being the decreasing size of their nanocrystalline core. The surface passivation also slightly differs, however, the FTIR spectra clearly show the main difference to occur between H_2O_2-treated and non-treated samples, while only minor changes appear among the group of H_2O_2-treated samples.

B. PL spectra and dynamics

In Fig. 2(a) we show PL spectra excited under pulsed excitation and detected within a gate width of 100 μs (detection gate is coincident with excitation pulse, i.e., t $=0$ μs is coincident with the excitation pulse onset). PL spectra of the SiNCs powders consist generally of two main broad bands: a blue spectral band at ~430 nm (F-band) decaying on the approximately nanosecond scale[25] and a red slow spectral band at ~590–850 nm (S-band) decaying in approximately microseconds.[28] Therefore we can separately measure the fast F-band by shortening the detection gate width to 20 ns [Fig. 2(b)].

The dynamics of the S-band is in more detail studied in Fig. 3. The first column in Figs. 3(a1–d1) shows comparison of normalized PL spectra integrated over different gate widths and delays: 0–20 ns, 0–1 μs, 49–50 μs and 0–100 μs. The second and third columns in Figs. 3(a2)–3(d2) and 3(a3)–3(d3) show the spectral development in the as-measured S-band component with delay time in 0–50 μs (separately for 0–5 and 5–50 μs in different intensity scales to clearly illustrate both the early development and a weak slow component); except for the "blue" SiNCs, where nearly no S-band appears, therefore the gate shifts only from 0 up to 22 μs. The spectra in Figs. 3(a2)–3(d2) and 3(a3)–3(d3) are
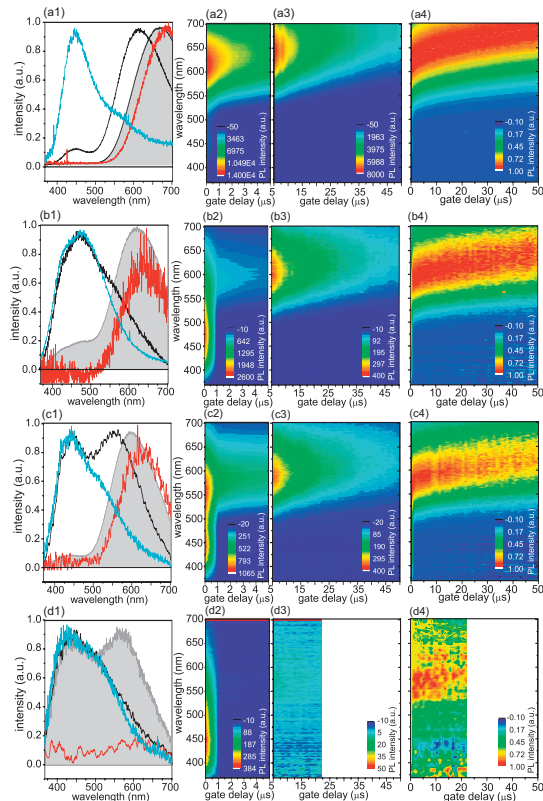
FIG. 3. (Color) Time-resolved spectroscopy of the PL spectra of the (a) "standard," (b) "yellow," (c) "white," and (d) "blue" SiNCs powders. First column (a1–d1) shows comparison of F-band (blue line) taken in 0–20 ns window, time-integrated PL (gray area) taken in 0–100 μs and PL taken in 0–1 μs (black line) and 49–50 μs (red line). Second and third columns (a2–d2; a3–d3) show the S-band kinetic series on microsecond timescales (gate width and step of 1 μs) separately for 0–5 μs and 5–50 μs (note different intensity scales). Last column (a4–d4) shows normalized spectra from (a2–d2;a3–d3).

comparable in intensity (the number of excited SiNCs was very similar). The normalized S-band PL spectra for different time delays after excitation are shown in the fourth column in Figs. 3(a4)–3(d4), to emphasize the S-band narrowing and shift with size and delay time.

The relaxation time of the S-band at 550–660 nm [data taken from measurement depicted in Figs. 3(a2)–3(d2) and 3(a3)–3(d3)] was fitted with a stretched-exponential dependence $I(t) = I_0 e^{-(t/\tau)^{\beta}}$, characteristic for disordered and amorphous materials, where τ is the decay time and the coefficient β has to fulfill $0 \le \beta \le 1$. In more detail, the coefficient β was fitted from linear dependence $\log\{-\ln[I(t)/I_0]\} = \beta \log t - \beta \log \tau$, with slope β,[29] and then used for fitting decay time τ from the exponential equation. This procedure was applied to emphasize the importance of measurements at shorter time delays in contrast to standard nonlinear least square fitting and yielded a better fit. In Figs. 4(a) and 4(b) we show the coefficient β and the decay time τ as a function of the sample type and emission wavelength. In Fig. 4(c) we illustrate the shift of the S-band peak on the delay time.
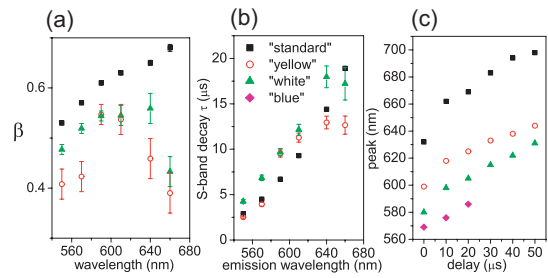

FIG. 4. (Color) (a) Coefficient β and (b) decay time τ fitted with stretched-exponential law at various emission wavelengths. (c) Spectral shift in the S-band peak.

V. DISCUSSION

In our series of samples, two phenomena can be observed: (i) the S-band spectrally blueshifts and (ii) fades away (the relative contribution of the F-band increases) with the enhancement in the H_2O_2 treatment, i.e., with decreasing size of the nanocrystalline core. This behavior is obvious from Fig. 2(a), in which the time-integrated PL spectra of different powders are shown. In the "standard" SiNCs the S-band dominates, in the "yellow" and "white" samples the F-band starts to be more important and in the case of the "blue" sample the F-band is equal in intensity to the S-band. Besides, one can see continual spectral shift in the S-band and a slight narrowing of its spectral width [Figs. 3(a4)–3(d4), Table I].

The observation of the discontinuity in the spectral blueshift, which seems to be a consequence of switching between S- and F-band emission, is interesting. In this context, it is interesting to note that some, though very faint S-band component persists even in the "blue" sample [see Figs. 3(d1)–3(d4)], while being spectrally blueshifted down to 560 nm. This signal can most probably be attributed to the lower end of the size distribution of SiNCs, which give rise to the inhomogeneously broadened S-band. A similar discontinuity in the spectral blueshift was observed, e.g., by Sato and Swihart[30] who prepared colloidal dispersions of SiNCs by etching of SiO_x powder in an HF:HNO$_3$ mixture, followed by a subsequent exchange of resulting H-termination with capping by organic molecules. The authors[30] observed that the blueshift of PL with increasing etching time never yielded blue-emitting SiNCs, stopping at about 500 nm, even if particle sizes as low as 1.5 nm were achieved (the smallest particles could not be imaged with HRTEM). Instead, blue PL of the dispersion appeared after prolonged sonication and was attributed to (partial) oxidation of SiNCs. Although it appears that the "blue" PL stage cannot be reached through this kind of etching, it is important to point out that PL can be shifted further if SiNCs are organically capped: e.g., $\lambda_{max}^{em} = 440$ nm for $\lambda^{exc} = 320$ nm as reported in Ref. 10 (SiNCs were prepared by milling), $\lambda_{max}^{em} = 440$ nm for $\lambda^{exc} = 320$ nm, or $\lambda_{max}^{em} = 350$ nm for $\lambda^{exc} = 300$ nm as reported in Ref. 12 (SiNCs were synthesized in reverse micelles) and $\lambda_{max}^{em} = 335$ nm for $\lambda^{exc} = 290$ nm as reported in Ref. 11 (SiNCs were synthetized in reverse micelles).

This suggests that, for very small sizes of SiNCs, a

qualitative change occurs, i.e., the particles are no longer crystalline but amorphouslike, as is also indicated by theoretical calculations.[23] This qualitative change from a nanocrystal to an amorphous nanoparticle would certainly have dramatic impact on optical properties. Another hypothetical reason for this discontinuous spectral shift may lie in some kind of "collective behavior" of a large ensemble of SiNCs (diffusion of excitons to larger nanocrystals when the larger nanocrystals are in close vicinity, e.g., in agglomerates), which leads to their overall red emission,[31,32] while small individual SiNCs crumbled off the ensembles keep their own blue PL, driven mainly by the quantum confinement effect.

PL dynamics of all the samples shows two different components, a nanosecond one and a microsecond one, corresponding to the F- and S-bands. F-band, decaying in tens of nanoseconds, is clearly present in all the samples [Fig. 2(c) and Figs. 3(a1)–3(d1) 3(a2)–3(d2)]. Interestingly, if F-bands of the "standard" and the "blue" one are compared [Fig. 2(c)], one can see that the F-band has slightly blueshifted. It is important to note that we have observed this band under both continuous and pulsed excitation, contrary to findings of Kanemitsu in Ref. 6.

The S-band appears on the microsecond timescale in all the samples except for the "blue" one, where it is practically absent [Figs. 3(d1)–3(d4)]. S-band spectral position blueshifts with H_2O_2 treatment and visibly redshifts with increasing time delay, as can be seen from Figs. 3(a4)–3(d4) and 4(c). This observation leads to the conclusion that an ensemble of SiNCs is probed during the measurement, the nanocrystals with longer lifetime having a redshifted PL spectrum.[31] This can be most easily explained by the presence of differently sized nanocrystals with correspondingly different PL spectra and lifetimes in the ensemble.[33] Another possible explanation could be offered by exciton hopping effect, which in fact would be supported by the low value of β coefficient and its weak spectral dependence [Fig. 4(a)]. Furthermore, we found that β in our samples is slightly larger in "standard" SiNCs, compared to other samples, however, its value in all samples lies between 0.35 and 0.65 [Fig. 4(a)]. The decay time of the S-band shortens for shorter emission wavelengths from $13-25$ μs to less than 5 μs, with no apparent sample (size) dependence [Fig. 4(b)].

The above reported experimental observations evidence a certain linkage between the F- and S-bands: enhanced electrochemical etching entails in parallel (i) blueshift and decrease in intensity of the S-band and (ii) growth of a relative contribution of the F-band to the overall light emission. This obviously confirms different origin of the bands under discussion (which is also fully supported by their sharply different dynamics) but, on the other hand, it brings information on energy/electron transfer between relevant luminescence centers. While there is a consensus as to the origin of the S-band (quantized states in relatively large SiNCs in cooperation with surface passivation species), the provenance of the F-band is still under debate. Let us attempt to specify how the present experimental results may contribute to this polemic.

(1) Prevailing view of the F-band is that of a luminescent defect state in the surface suboxide SiO_x/SiO_2 coverage of nanocrystals.[7] Indeed, there are numerous blue-emitting defects in various types of glass, the luminescence of which may be boosted owing to progressive oxidation of SiNCs in the course of H_2O_2-enhanced etching. Simultaneously the nanocrystalline core and surface are being reduced and therefore the red S-band fades away, consistently with our observations. However, it is difficult to reconcile this view with the central issue of this article, namely, the discontinuity in the spectral blueshift. *A priori*, there is no obvious reason why the blueshift of the S-band should stop at the "magic" $\lambda \sim 590$ nm boundary rather than continue up to blue. Actually, the only plausible reason for the blueshift to stop would be that the SiNC reached its smallest possible size, which obviously does not happen when PL peaks at ~ 590 nm since SiNC with UV PL can also be prepared.[11,12]

(2) Another interpretation of the F-band is in terms of the transitions between quantum confined core states in small Si nanoparticles as proposed recently both theoretically[23] and experimentally.[25] This idea appears to be more in line with the discontinuous blue spectral shift, if we admit that the gradual oxidation of an ensemble of SiNCs increases concentration of "sufficiently small" nanocrystallites or nanoclusters where dramatic relaxation of the wavevector conservation is achieved. In such nanocrystallites an abrupt switching from the prevailing slow phonon-assisted radiative recombination (the S-band) to the fast directlike core-related one occurs, thereby inevitably inducing discontinuities in the spectral shift as well as in the luminescence dynamics.

(3) Yet another possibility is that the F- and S-bands occur simultaneously in a given (relatively large) nanocrystal but the F-band, unlike the slow S-one, originates through the direct Γ-Γ transitions. This idea, being proposed some time ago,[34] seems to be reevoked recently on a more solid experimental and theoretical basis.[35] This interpretation does not contradict the observed discontinuity in the blueshift either: Large SiNCs contribute only marginally to the F-emission but ultimately virtually all of them terminate, on oxidation, by an abrupt switching to the Γ-Γ radiation mode. It is worth noting that the blue direct Γ-Γ radiative channel is expected to open instantaneously, which agrees with spectral-temporal maps displayed in Fig. 3; during very short time the remaining stored excitation energy moves to lower-lying states of the conduction band (minimum near the X point) producing the S-red emission, which gradually fades away on a microsecond time scale (Fig. 3).

Experimental results of this work therefore support interpretations of the F-band in terms of quasidirect transition in silicon nanocrystals/nanostructures rather than in terms of exclusively silicon oxide related defect states. However, a simultaneous occurrence of some of the radiative channels discussed above (1)–(3) still cannot be excluded at the present state of knowledge.

VI. CONCLUSION

We studied PL emission by time-resolved spectroscopy in oxidized SiNCs of various sizes. Core diameter decreases with the enhancement of the H_2O_2 treatment. The spectral shift in the steady state and time-resolved S-band PL is not continuous and is replaced by abrupt switching from one emission mechanism (S-band) to another (F-band). Although the reasons for this discontinuity are not yet fully understood, a mechanism based on spatial restructuralization is proposed. Moreover, our results support the view of the F-band being, at least partially, due to quasidirect radiative recombination inside a nanoparticle core.

The unattainability of intense stable room temperature blue-green and green steady-state PL emission from oxidized SiNCs limits their application outlooks and also represents a challenge for the basic physics and chemistry of SiNCs, requiring further investigations.

ACKNOWLEDGMENTS

[1] L. T. Canham, Appl. Phys. Lett. **57**, 1046 (1990).

[2] A. Uhlir, Jr., Bell Syst. Tech. J. **35**, 333 (1956).

[3] Y. Kanemitsu, H. Uto, Y. Masumoto, T. Matsumoto, T. Futagi, and H. Mimura, Phys. Rev. B **48**, 2827 (1993).

[4] Y. Kanemitsu, T. Ogawa, K. Shiraishi, and K. Takeda, Phys. Rev. B **48**, 4883 (1993).

[5] Y. Kanemitsu, Phys. Rev. B **48**, 12357 (1993).

[6] Y. Kanemitsu, Phys. Rev. B **49**, 16845 (1994).

[7] L. Tsybeskov, J. V. Vandyshev, and P. M. Fauchet, Phys. Rev. B **49**, 7821 (1994).

[8] M. Cazzanelli, D. Kovalev, L. Dal Negro, Z. Gaburro, and L. Pavesi, Phys. Rev. Lett. **93**, 207402 (2004).

[9] G. Belomoin, J. Therrien, and M. Nayfeh, Appl. Phys. Lett. **77**, 779 (2000).

[10] A. S. Heintz, M. J. Fink, and B. S. Mitchell, Adv. Mater. **19**, 3984 (2007).

[11] R. D. Tilley, J. H. Warner, K. Yamamoto, I. Matsui, and H. Fujimori, Chem. Commun. (Cambridge) **2005**, 1833.

[12] J. H. Warner, H. Rubinsztein-Dunlop, and R. D. Tilley, J. Phys. Chem. B **109**, 19064 (2005).

[13] M. V. Wolkin, J. Jorne, P. M. Fauchet, G. Allan, and C. Delerue, Phys. Rev. Lett. **82**, 197 (1999).

[14] M. L. Brongersma, A. Polman, K. S. Min, E. Boer, T. Tambo, and H. A. Atwater, Appl. Phys. Lett. **72**, 2577 (1998).

[15] L. Pavesi, L. Dal Negro, L. Mazzoleni, G. Franzo, and F. Priolo, Nature (London) **408**, 440 (2000).

[16] M. Fujii, A. Mimura, S. Hayashi, and K. Yamamoto, Appl. Phys. Lett. **75**, 184 (1999).

[17] L. Dal Negro, M. Cazzanelli, N. Daldosso, Z. Gaburro, L. Pavesi, F. Priolo, D. Pacifci, G. Franzo, and F. Iacona, Physica E (Amsterdam) **16**, 297 (2003).

[18] L. Khriachtchev, M. Räsänen, S. Novikov, and J. Lahtinen, J. Appl. Phys. **95**, 7592 (2004).

[19] F. Hua, F. Erogbogbo, M. T. Swihart, and E. Ruckenstein, Langmuir **22**, 4363 (2006).

[20] K. Dohnalová, K. Žídek, L. Ondič, K. Kůsová, O. Cibulka, and I. Pelant, J. Phys. D **42**, 135102 (2009).

[21] K. Dohnalová, K. Kůsová, and I. Pelant, Appl. Phys. Lett. **94**, 211903 (2009).

[22] D. K. Yu, R. Q. Zhang, and S. T. Lee, Phys. Rev. B **65**, 245417 (2002).

[23] X. Wang, R. Q. Zhang, S. T. Lee, T. A. Niehaus, and Th. Frauenheim, Appl. Phys. Lett. **90**, 123116 (2007).

[24] K. Dohnalová, I. Pelant, K. Kůsová, P. Gilliot, M. Galart, O. Crégut, J.-L. Rehspringer, B. Hőnerlage, T. Ostatnický, and S. Bakardjieva, New J. Phys. **10**, 063014 (2008).

[25] J. Valenta, A. Fučíková, I. Pelant, K. Kůsová, K. Dohnalová, A. Aleknavičius, O. Cibulka, A. Fojtík, and G. Kada, New J. Phys. **10**, 073022 (2008).

[26] G. Socrates, *Infrared and Raman Characteristic Group Frequencies: Tables and Charts*, 3rd ed. (Wiley, New York, 2001), pp. 241–246.

[27] T. Kudo and S. Nagase, J. Phys. Chem. **88**, 2833 (1984).

[28] F. Trojánek, K. Neudert, P. Malý, K. Dohnalová, and I. Pelant, J. Appl. Phys. **99**, 116108 (2006).

[29] O. Edholm and C. Blomberg, Chem. Phys. **252**, 221 (2000).

[30] S. Sato and M. T. Swihart, Chem. Mater. **18**, 4083 (2006).

[31] R. Lockwood and A. Meldrum, Phys. Status Solidi A **206**, 965 (2009).

[32] G. Allan and C. Delerue, Phys. Rev. B **75**, 195311 (2007).

[33] J. Valenta, A. Fučíková, F. Vácha, F. Adamec, J. Humpolíčková, M. Hof, I. Pelant, K. Kůsová, K. Dohnalová, and J. Linnros, Adv. Funct. Mater. **18**, 2666 (2008).

[34] D. Babic and R. Tsu, Superlattices Microstruct. **22**, 581 (1997).

[35] A. A. Prokofiev, A. S. Moskalenko, I. N. Yassievich, W. de Boer, D. Timmerman, H. Zhang, W. J. Buma, and T. Gregorkiewicz, e-print arXiv:0901.4268[cond-mat.mtrl-sci].

3.5 Enclosure

Luminescence of free-standing versus matrix-embedded oxide-passivated silicon nanocrystals: The role of matrix-induced strain

K. Kůsová, **L. Ondič**, E. Klimešová, K. Herynková, I. Pelant , S. Daniš, J. Valenta, M. Gallart, M. Ziegler, B. Hönerlage and P. Gilliot

Luminescence of free-standing versus matrix-embedded oxide-passivated silicon nanocrystals: The role of matrix-induced strain

Kateřina Kůsová,[1,a)] Lukáš Ondič,[1,2,3] Eva Klimešová,[1] Kateřina Herynková,[1] Ivan Pelant,[1] Stanislav Daniš,[3] Jan Valenta,[3] Mathieu Gallart,[2] Marc Ziegler,[2] Bernd Hönerlage,[2] and Pierre Gilliot[2]

[1]*Institute of Physics, Academy of Sciences of the Czech Republic, v.v.i., Cukrovarnická 10, 162 53, Prague 6, Czech Republic*
[2]*IPCMS-DON Unité Mixte, UMR 7504, CNRS-ULP, 23 rue du Loess, BP 43, 67034 Strasbourg Cedex 2, France*
[3]*Faculty of Mathematics and Physics, Charles University, Ke Karlovu 3, 121 16 Prague 2, Czech Republic*

(Received 8 June 2012; accepted 14 September 2012; published online 1 October 2012)

We collect a large number of experimental data from various sources to demonstrate that free-standing (FS) oxide-passivated silicon nanocrystals (SiNCs) exhibit considerably blueshifted emission, by 200 meV on average, compared to those prepared as matrix-embedded (ME) ones of the same size. This is suggested to arise from compressive strain, exerted on the nanocrystals by their matrix, which plays an important role in the light-emission process; this strain has been neglected up to now as opposed to the impact of quantum confinement or surface passivation. Our conclusion is also supported by the comparison of low-temperature behavior of photoluminescence of matrix-embedded and free-standing silicon nanocrystals. © *2012 American Institute of Physics.* [http://dx.doi.org/10.1063/1.4756696]

Silicon nanocrystals (SiNCs) are a material of intense scientific interest due to their prospective applications as nanoscale light emitters both in optoelectronics[1] and as fluorescent markers[2] in bio-imaging, and, moreover, for enhancing the efficiency of photovoltaic solar cells.[3] SiNCs emit light quite efficiently in contrast to their bulk counterpart. The origin of this light emission is still not fully understood in detail. It is generally believed that their slow red/orange emission (the so-called S band) results from indirect $\Delta_1 - \Gamma_{25'}$ transition,[4,5] being influenced by a complex interplay of quantum confinement[6] and surface terminating species.[7] The effect of quantum confinement is most easily demonstrable in SiNCs with "intrinsic" hydrogen surface termination as their photoluminescence (PL) is easily tunable between green and deep red emission (550–800 nm) by changing the size of the crystalline core.[8]

Since hydrogen surface termination is highly unstable in air and such nanocrystals are strongly prone to oxidation,[9,10] such nanocrystals have to be surface-treated. The surface capping layer of stable SiNC can be either made up by silicon oxide or by a specially prepared layer of organic molecules if oxidation is intentionally avoided.[9] The detailed chemical composition of the surface terminating layer significantly influences the spectral PL position of the sample; therefore, here, we focus on oxide-capped SiNCs to minimize the effect of surface chemistry on the proposed reasoning.

In oxide-passivated SiNCs, the oxide-related surface states profoundly influence PL[7,10] because of the formation of discrete states inside the bandgap. For example, the emission of green-emitting (2.35 eV) hydrogen-terminated SiNCs shifts to the red spectral region (1.85 eV) upon oxidation.[10] PL of oxide-capped SiNCs is also size-tunable to some extent: e.g., spectral shifts from 1.32 to 2.4 eV were observed upon the decrease in size from 7.8 to 2 nm by Ledoux

et al.,[11] or spectral shifts from 1.2 to 1.36 eV upon size decrease from 9 to 4.7 nm were observed by Takeoka et al.[12] However, the wavelength tunability is somewhat limited when compared to hydrogen termination[13] and, even if only oxide-capped SiNCs are considered, their PL is influenced by defects and/or the core/shell interface.[14,15]

In general, SiNCs can be prepared via a wide range of techniques. For the purposes of this article, it is useful to divide SiNC samples into those prepared as free-standing (FS) or matrix-embedded (ME). A wide variety of colloidal FS SiNCs can be prepared by chemical synthesis,[9] but these nanocrystals are quite exclusively very small (<1.8 nm) with organic surface capping, and therefore their PL emission does not include the S band, being situated in the UV/blue spectral region. Focusing on FS oxide-passivated SiNCs, they can be prepared by various kinds of wet etching (either electrochemical HF-based etching[7,16] or simple chemical HF/HNO$_3$ etching[17] of variously prepared Si powders constituted by particles with sizes <30 nm, further reducing the core sizes by chemical etching) or synthesis in plasma from silane.[11,18] The etching or synthesis is then followed by slow oxidation in ambient conditions; the FS powder can also be deposited on a substrate or form a suspension/colloidal dispersion in liquid. ME oxide-capped SiNCs, on the other hand, can be prepared by the deposition of SiO$_x$/SiO$_2$ superlattices[3,19,20] or Si-rich SiO$_2$,[12,14,21,22] by the implantation of Si ions into SiO$_2$ matrix,[23] or by chemical synthesis in a polymer-based matrix.[24] After the deposition or implantation step, the samples are typically annealed (>1000 °C), which results in the formation of SiNC, either as small inclusions inside an SiO$_2$-based matrix or as densely packed thin films overgrown with SiO$_2$.

All the references mentioned in the previous paragraph report reliable data on the room-temperature PL spectra of oxide-passivated SiNCs along with the corresponding particle sizes. All these data, measured on more than 100 samples

---

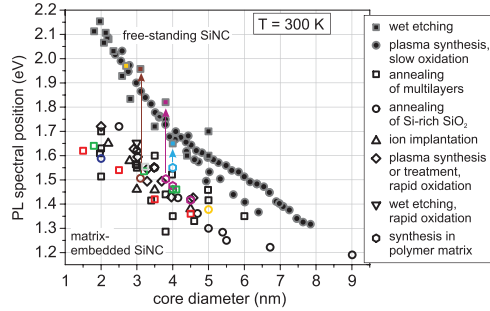a)Electronic mail: kusova@fzu.cz.

FIG. 1. Summary of experiments reporting photoluminescence spectral maximum as a function of size of oxidized SiNCs ($T = 300$ K). Gray-outlined solid symbols correspond to samples prepared as FS (wet etching taken from Refs. 7, 16, and 17; plasma synthesis and slow oxidation taken from Refs. 11 and 18), open symbols denote samples prepared as ME (SiO_x/SiO_2 superlattices taken from Refs. 3, 19, and 20, Si-rich SiO_2 taken from Refs. 12, 14, 21, and 22; Si ion implantation taken from Ref. 23; plasma synthesis taken from Ref. 25; electrochemical etching followed by thermal oxidation taken from Ref. 26; and chemical synthesis in polymer-based matrix taken from Ref. 24). Samples discussed in more detail are drawn in color, symbols connected by arrows were prepared as ME, but liberated from the matrix and their PL as FS was also measured.

by various groups worldwide, can be compiled to Fig. 1. In this plot, one can easily see the distinction between ME, denoted by open symbols, and FS samples, denoted by solid symbols: even if both the size and the type of surface passivation are the same, the PL of ME samples is considerably redshifted in comparison with the FS samples, roughly by 200 meV. This significant difference is easily visible with the naked eye, just comparing the color of PL emitted by a ME and FS sample as shown in Figs. 2(a) and 2(b).

A factor playing an important role in this spectral shift is the influence of compressive strain exerted on the ME SiNCs by their matrix. When growing inside a matrix, a ME SiNC cannot grow freely, but is constantly compressed by the matrix. On the other hand, spontaneous growth of oxide on the surface of a FS nanocrystal under ambient conditions does not exert any strain on the nanocrystalline core. However, "forced" oxidation, e.g., under high temperature, may cause the growth of a compressive outer oxide shell or even a thin-film oxide layer burying the originally FS SiNCs, causing such nanocrystals to behave as ME ones. This is the case, e.g., for samples prepared by plasma synthesis from silane by Takagi *et al.*,[25] by reactive ion etching in plasma by
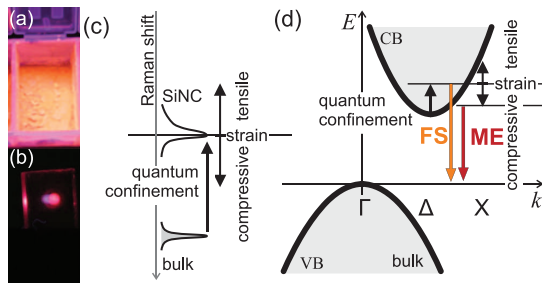

FIG. 2. Photos of PL of a (a) free-standing and (b) matrix-embedded SiNC samples. Schematics of the influence of quantum confinement and strain on (c) Raman spectra of optical phonon of Si (nano)crystal and (d) bandstructure of silicon.

Ray *et al.*,[17] and by electrochemical etching by Kanemitsu *et al.*[26] included in Fig. 1 as ME ones. On the other hand, it was shown that compressive stress could be relaxed, e.g., upon local laser annealing of ME SiNCs prepared by rapid thermal annealing of Si/SiO_2 superlattices.[27] Therefore, it is important to take into account all the steps of the preparation process to correctly determine if the "matrix-induced" compression is present in the investigated sample and if it possibly influences its PL. Inevitably, different levels of stress will be present in different samples; this is indirectly supported also by the larger variability in the PL spectral position versus core diameter dependence in the ME-prepared SiNCs when compared to the FS-prepared ones in Fig. 1.

In some cases, namely in samples prepared by annealing of Si-rich SiO_2 layers by Matsuhisa *et al.*[21] (brown symbols in Fig. 1) and by synthesis in a polymer-based matrix reported on in Ref. 24 (cyan and magenta symbols in Fig. 1, respectively), the ME SiNCs were liberated from the SiO_2 matrix by HF etching, giving rise to FS SiNC samples (the correspondingly colored solid points in Fig. 1 are connected by arrows). Evidently, this ME → FS transition is accompanied by a PL blueshift: Fig. 1 demonstrates that the PL spectral position of ME SiNCs after etching well accords with that of the FS-prepared SiNCs.[28] This blueshift, whose origin is, interestingly enough, not commented on in the original studies, confirms the connection between the PL shift and the matrix: when a nanocrystal is released from the matrix, the matrix-induced compressive strain is relaxed and is no longer present, giving rise to a FS SiNC.

The idea that compressive stress is present in ME SiNCs is not completely new, but it comes to mind much more naturally in connection with Raman measurements than with PL. The combined influence of quantum confinement and strain on the SiNC phonon Raman peak is quite complex (see Fig. 2(c)) and, therefore, extreme care has to be taken during such an analysis. Due to the possibility of systematic error, samples in which the size was determined solely by analysis of SiNC Raman spectra were not included in Fig. 1.

Some analyses of Raman measurements of ME oxide-passivated SiNCs detected the presence of compressive stress. Namely, Arguirov *et al.*[27] observed an unusual up-shift in the ME SiNC phonon Raman frequency of SiNCs prepared by annealing of Si/SiO_2 superlattices, implying that in this case, the stress is compressive regardless of the used confinement model. The corresponding deduced compressive stress amounted to ∼5 GPa. Indeed, PL spectra of samples prepared by the same group and reported on by Rölver *et al.*[29] exhibit a significantly redshifted PL maximum (please note that the same type of samples is later discussed in Fig. 5(b)). Furthermore, Hernández *et al.*[30] identified compressive stresses of 3.5 GPa in ME SiNCs prepared by annealing of substechiometric SiO_x films; the maximum of the PL spectrum of the corresponding sample[22] is drawn as open yellow circle in Fig. 1. Zatryb *et al.*[31] confirmed somewhat lower levels of compressive stress between 0.4 and 0.8 GPa in ME SiNCs prepared by annealing of Si/SiO_2 superlattices, PL of the corresponding sample[19] is denoted by open light gray square in Fig. 1. Surprisingly, lattice contraction corresponding to stress of several GPa was confirmed also by HRTEM measurements of SiNCs prepared by inert gas arc evaporation,[32] and the

presence of stress was confirmed by x-ray measurements in ME SiNC samples based on superlattices.[33]

Stress can be found also in cases slightly different from but analogical to oxide-passivated ME SiNCs. For example, SiNCs prepared by ion implantation to a sapphire matrix[34] and subsequent annealing exhibited a small lattice contraction of 0.04%–0.11%, corresponding to compressive stresses around 2 GPa. Moreover, the compressive effect of the matrix was also identified in CdS_xSe_{1-x} nanocrystals[35] via Raman measurements, and the comparison of Raman spectra of oxide-passivated ME SiNCs[36] with alkylated FS SiNCs also suggest compression by the matrix (although in this case, SiNCs with different surface passivations are studied). On the other hand, porous-silicon-based SiNC layers were found to exhibit lattice expansion[37] by HRTEM measurements.

Although the presence of stress in SiNCs samples was considered in the past, rarely has it been connected with the PL properties; such a connection was only indicated by theoretical calculations of very small clusters[38] consisting of less than 100 Si atoms. Another theoretical calculation studying stress in SiNCs, which, however, disregards the implications for PL, was carried out by Yilmaz et al.[39]

The concept that matrix-induced compressive stress can be in many cases one of important factors determining the spectral position of SiNC samples can be inferred from basic solid state physics. If we consider that the PL in oxidized SiNCs arises from indirect $\Delta_1 - \Gamma_{25'}$ transitions in the silicon bandstructure,[4,5] we can calculate the compressive strain necessary for down-shifting the Δ_1 minimum by 200 meV, the value determined from Fig. 1. Compared to bulk Si, bandgap energy in SiNCs is increased as the Δ_1 conduction-band minimum up-shifts with decreasing size of the nano-crystal due to quantum confinement.[40] Strain can then either further up-shift or down-shift this energy gap depending on its sign, see Fig. 2(d); the effect of strain on the quantum-confinement energy, though, will be negligible because strain-induced volume changes will be very small. The effect of strain on the bandstructure of solids is then usually expressed in terms of deformation potential[41] $a_n(\mathbf{k})$

$$\delta E_n(\mathbf{k}) = a_n(\mathbf{k})\,(\delta V/V), \tag{1}$$

which links the shift of the energy of a particular band extreme $\delta E_n(\mathbf{k})$ with the relative change in volume $\delta V/V$. To gain a simple estimate of the order of magnitude of this effect, we can use the deformation potential values for bulk Si, being[41] $a(\Delta) = 14$ eV for the indirect bandgap. This implies that the energy shift of 200 meV corresponds to the volume change of the primitive cell by as little as 1.4%. This value translates into a mere 0.7% change in lattice constant ($\sqrt[3]{0.986} = 0.993$). Still using the bulk Si approximation, stress δp of the order of ~ 2 GPa is needed to induce such a change in volume (bulk modulus of bulk Si $K = \delta p/(\delta V/V) \sim 100$ GPa is a good approximation of that of nanocrystals[5,42]). This is a reasonable number, because it is well below the first pressure-induced phase transition in silicon[43] from diamond to β-tin structure, which occurs at 12 GPa and which would certainly be easily detectable in HRTEM imaging. Our estimate of ~ 2 GPa also well accords with the stress values measured by various groups as mentioned above.

In order to further support the proposed idea of matrix-induced strain, we carried out three types of experiments to complement the above compilation of literature data. First, apart from SiNC samples prepared from Si/SiO_2 superlattices and substechiometric SiO_x films, compressive stress can be found also in ion-implanted samples, as supported by our x-ray diffraction[44] (XRD) measurements presented in Fig. 3. Lattice constant of Si in SiNCs was determined from the position of the 2θ angle of observed diffraction maximum corresponding to the (220) diffraction line. The maximum of the diffraction peak was measured at $2\theta = (47.556 \pm 0.002)°$, which gives the lattice parameter (5.40 ± 0.01) Å (the lattice parameter of bulk silicon $a_{Si} = 5.431$ Å would correspond to the diffraction peak observed at a diffraction angle of $2\theta = 47.3°$). Thus, the lattice parameter is contracted by $\sim 0.6\%$, which very well accords with the above estimate of lattice contraction based on deformation potential. Correspondingly, the PL spectrum of the same sample (inset in Fig. 3) peaks at 860 nm, which is a value considerably redshifted compared to FS samples.

Second, we addressed the issue if a nanocrystalline material behaves analogically to bulk when it comes to compression. Our measurements of the dependence of PL spectra of ethanoic suspensions of FS SiNCs on external hydrostatic pressure in a diamond cell[44] are presented in Fig. 4. The PL maximum indeed redshifts with compressive pressure, this shift is, however, somewhat lower when compared to our above estimate. Very similar shifts of PL maxima of alkane-capped FS SiNCs have been reported recently.[5] More effects can be responsible for this difference. First, theoretical calculations of strain fields in ME SiNCs suggest[39] that stress is inhomogeneously distributed in the volume of an oxide-capped SiNC, being more compressive near the nanocrystal's surface. In oxide-capped SiNCs, the optical excitation is trapped at the surface, therefore, it might locally "feel" higher compressive stresses than those measured by Raman, HRTEM, or XRD, being averaged over the whole core. Second, the microscopic composition of the surface terminating layer can be to a certain extent different in the ME and FS
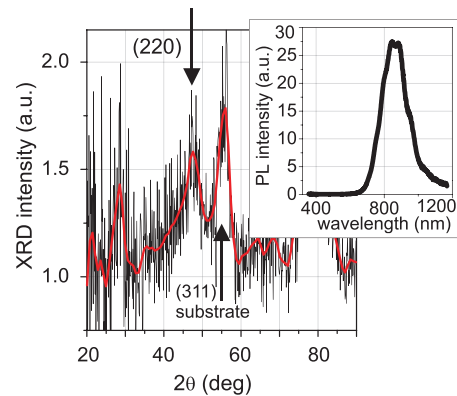

FIG. 3. XRD measurements of ion-implanted ME SiNCs. Raw data (black curve) were smoothed by cubic spline (red curve). The (220) Bragg peak originates in SiNCs, the (311) Bragg peak comes from the substrate, the remaining peaks are false peaks arising from the subtraction of background. The inset shows PL spectrum of the same sample.
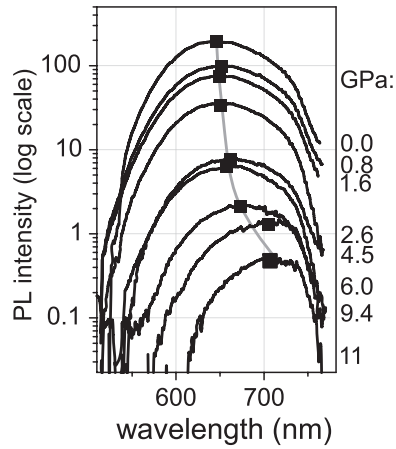
FIG. 4. Changes in PL spectra of FS SiNCs with external applied pressure, the squares correspond to the maximum of a Gaussian fit.
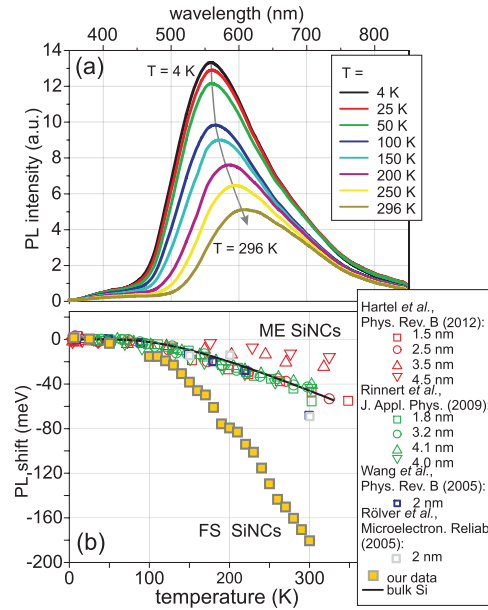

FIG. 5. (a) Measured spectra of FS SiNCs, the arrow denotes increasing temperature. (b) Temperature dependence of the PL shift with respect to the spectral position at the lowest experimental temperatures. Data of ME SiNCs (open symbols) are taken from the literature (see the legend), data of FS SiNCs (solid symbols) correspond to spectral positions from panel (a). Bulk Si temperature dependence is drawn in black line for comparison. Colors correspond to those in Fig. 1.

samples, also giving rise to a redshift; this scenario is supported by the fact that SiNC samples annealed at different ambients exhibit spectral shifts.[14]

Last, the difference between ME- and FS-prepared SiNCs can be further tested using the measurements of temperature dependence of PL. Several experiments[14,20,45,46] have already reported on the temperature dependence of PL for ME samples. All of them concluded that the PL blueshift with decreasing temperature behaves very similarly to that of bulk Si, i.e., that PL blueshifts by about 50 meV when the temperature drops from 300 to 3 K, see Fig. 5(b). (The same samples as those in Fig. 5(b) are also included in room-temperature PL in Fig. 1; colors of the symbols in the two figures are chosen to match.)

Our measurements of the temperature dependence of PL of FS SiNC samples[44] suggest that significantly larger blueshift occurs at FS-prepared SiNC. Fig. 5(a) presents selected PL spectra (smoothed, corrected for the spectral sensitivity of the setup) of FS SiNCs measured at different temperatures, while Fig. 5(b) plots the temperature dependence of energy shift of PL maximum with regards to the lowest experimentally attainable temperatures for our measurements of FS samples along with the literature data on ME samples.[14,20] Clearly, the PL blueshift is significantly larger for FS SiNCs, of about 180 meV with respect to the ME value of 50 meV.

This difference can once again be explained by the presence of strain, which emerges in the FS sample when it is cooled down. It is obvious that a FS SiNC with a silica outer shell will tend to shrink with decreasing temperature.[47] Judging simply from the thermal coefficients of expansion for bulk silicon and silica (3 vs. $0.3 \times 10^{-6}\,K^{-1}$), we can see that the silicon core will have much stronger tendency to shrink than the outer shell. Therefore, the volume change of the "hollow" SiO_2 shell can be neglected. Unlike the bulk modulus,[42] however, coefficient of thermal expansion α in a nanocrystalline material can be expected to be several times higher than that in bulk[48] (i.e., $\alpha_{SiNC} \approx 3 \times 3 \times 10^{-6}\,K^{-1} = 9 \times 10^{-6}\,K^{-1}$) due to non-negligible influence of the surface. Consequently, the volume change of a nanocrystal when the temperature changes

by 300 K can be estimated to be $(1 - 9 \times 10^{-6}\,K^{-1} \times 300\,K)^3$ = 0.992, i.e., the core has a tendency to shrink by about 0.8%, but this shrinkage is prevented by the outer shell. If we take into account the above "calibration" based on deformation potential, we can estimate that this effect should induce tensile strain acting on the core of the nanocrystal corresponding to the shift in PL energy of about 110 meV.

On the other hand, ME SiNCs are under compressive strain of the matrix. This compressive strain relaxes on cooling, however, it is never completely lifted (compare the volume change of 1.8% due to matrix compression versus the much smaller 0.8% change due to temperature-induced tensile strain in FS SiNCs). Therefore, the PL energy shift in ME SiNCs with the decrease in temperature from 300 to 5 K will be driven by the inherent properties of the silicon lattice, i.e., will be roughly the same as in bulk Si (∼50 meV), whereas in the FS SiNCs, the tensile strain adds up to this value and the overall PL energy shift will amount to ∼160 meV, which is in reasonable accordance with our experimental results (see Fig. 5).

In conclusion, we show that a clear distinction exists between oxide-passivated SiNCs prepared as free-standing and matrix embedded. Data from the literature summarizing the size dependence of PL spectral position show that the ME SiNC samples are systematically redshifted by about 200 meV when compared to FS samples of roughly the same size. We propose that non-negligible compressive stress (∼2 GPa) exerted on the SiNC by the matrix is an important factor inducing this redshift (in addition to the traditionally considered effect of surface capping layer). To support the

proposed idea, we complement literature data by three types of dedicated experiments, studying XRD of ME SiNCs, pressure-dependence of PL of FS SiNCs, and carrying out temperature-dependent PL measurements on FS SiNCs. Importantly, the role of matrix-induced strain should not be overlooked in analyses of SiNC phonon mode in Raman measurements.

[1]N. Daldosso and L. Pavesi, Laser Photon. Rev. **3**, 508 (2009).

[2]J.-H. Park, L. Gu, G. von Maltzahn, E. Ruoslahti, S. N. Bhatia, and M. J. Sailor, Nature Mater. **8**, 331 (2009).

[3]G. Conibeer, M. Green, R. Corkish, Y. Cho, E.-C. Cho, C.-W. Jiang, T. Fangsuwannarak, E. Pink, Y. Huang, T. Puzzer, T. Trupke, B. Richards, A. Shalav, and K.-L. Lin, Thin Solid Films **511–512**, 654 (2006).

[4]D. Kovalev, H. Heckler, M. Ben-Chorin, G. Polisski, M. Schwartzkopff, and F. Koch, Phys. Rev. Lett. **81**, 2803 (1998).

[5]D. C. Hannah, J. Yang, P. Podsiadlo, M. K. Chan, A. Demortiére, D. J. Gosztola, V. B. Prakapenka, G. C. Schatz, U. Kortshagen, and R. D. Schaller, Nano Lett. **12**, 4200 (2012).

[6]L. Canham, Appl. Phys. Lett. **57**, 1046 (1990).

[7]M. V. Wolkin, J. Jorne, P. M. Fauchet, G. Allan, and C. Delerue, Phys. Rev. Lett. **82**, 197 (1999).

[8]A. Gupta, M. T. Swihart, and H. Wiggers, Adv. Funct. Mater. **19**, 696 (2009).

[9]N. Shirahata, Phys. Chem. Chem. Phys. **13**, 7284 (2011).

[10]K. Dohnalová, K. Kůsová, and I. Pelant, Appl. Phys. Lett. **94**, 211903 (2009).

[11]G. Ledoux, J. Gong, F. Huisken, O. Guillois, and C. Reynaud, Appl. Phys. Lett. **80**, 4834 (2002).

[12]S. Takeoka, M. Fujii, and S. Hayashi, Phys. Rev. B **62**, 16820 (2000).

[13]K. Dohnalová, L. Ondič, K. Kůsová, I. Pelant, J. L. Rehspringer, and R.-R. Mafouana, J. Appl. Phys. **107**, 053102 (2010).

[14]X. X. Wang, J. G. Zhang, L. Ding, B. W. Cheng, W. K. Ge, J. Z. Yu, and Q. M. Wang, Phys. Rev. B **72**, 195313 (2005).

[15]J. Heitmann, F. Müller, M. Zacharias, and U. Gösele, Adv. Mater. **17**, 795 (2005).

[16]K. Dohnalová, I. Pelant, K. Kůsová, P. Gilliot, M. Gallart, O. Crégut, J.-L. Rehspringer, B. Hönerlage, T. Ostatnický, and S. Bakardjieva, New J. Phys. **10**, 063014 (2008).

[17]A. Vladimirov, S. Korovin, A. Surkov, E. Kelm, and V. Pustovoy, Laser Phys. **21**, 830 (2011); A. Gupta and H. Wiggers, Nanotechnology **22**, 055707 (2011); M. Ray, S. M. Hossain, R. F. Klie, K. Banerjee, and S. Ghosh, Nanotechnology **21**, 505602 (2010).

[18]M. Ehrecht, B. Kohn, F. Huisken, M. A. Laguna, and V. Paillard, Phys. Rev. B **56**, 6958 (1997).

[19]M. Zacharias, J. Heitmann, R. Scholz, U. Kahler, M. Schmidt, and J. Bläsing, Appl. Phys. Lett. **80**, 661 (2002); S. Kim, D. H. Shin, D. Y. Shin, C. O. Kim, J. H. Park, S. B. Yang, S.-H. Choi, S. J. Yoo, and J.-G. Kim, J. Nanomater. **2012**, 572746 (2012); L. Khriachtchev, S. Novikov, J. Lahtinen, and M. Räsänen, J. Phys.: Condens. Matter. **16**, 3219 (2004); L. X. Yi, J. Heitmann, R. Scholz, and M. Zacharias, Appl. Phys. Lett. **81**, 4248 (2002); X. Yu, R. Zhang, Z. Xu, D. Zhang, H. Zhao, Y. Zheng, and L. Chen, J. Non-Cryst. Solids **357**, 3524 (2011); M. Cazzanelli, D. Navarro-Urriós, F. Riboli, N. Daldosso, L. Pavesi, J. Heitmann, L. X. Yi, R. Scholz, M. Zacharias, and U. Gösele, J. Appl. Phys. **96**, 3164 (2004); X. J. Hao, A. P. Podhorodecki, Y. S. Shen, G. Zatryb, J. Misiewicz, and M. A. Green, Nanotechnology **20**, 485703 (2009).

[20]H. Rinnert, O. Jambois, and M. Vergnat, J. Appl. Phys. **106**, 023501 (2009); A. M. Hartel, S. Gutsch, D. Hiller, and M. Zacharias, Phys. Rev. B **85**, 165306 (2012).

[21]K. Matsuhisa, M. Fujii, K. Imakita, and S. Hayashi, J. Lumin. **132**, 1157 (2012); in this case, the size of the nanocrystal for Fig.1 is taken from [Y. Kanzawa, T. Kageyama, S. Takeoka, M. Fujii, S. Hayashi, and K. Yamamoto, Solid State Commun. **102**, 533 (1997)].

[22]W. D. A. M. de Boer, D. Timmerman, K. Dohnalova, I. N. Yassievich, H. Zhang, W. J. Buma, and T. Gregorkiewicz, Nat. Nanotechnol. **5**, 878 (2010); Y. Lebour, P. Pellegrino, S. Hernández, A. Martínez, E. Jordana, J.-M. Fedeli, and B. Garrido, Physica E **41**, 990 (2009).

[23]S. Guha, J. Appl. Phys. **84**, 5210 (1998); L. Pavesi, L. D. Negro, L. Mazzoleni, G. Franzò, and F. Priolo, Nature **408**, 440 (2000); G. A. Kachurin, S. G. Cherkova, D. V. Marin, R. A. Yankov, and M. Deutschmann, Nanotechnology **19**, 355305 (2008); O. Korotchenkov, A. Podolian, V. Kuryliuk, B. Romanyuk, V. Melnik, and I. Khatsevich, J. Appl. Phys. **111**, 063501 (2012).

[24]E. J. Henderson, J. A. Kelly, and J. G. C. Veinot, Chem. Mater. **21**, 5426 (2009); C. M. Hessel, E. J. Henderson, and J. G. C. Veinot, Chem. Mater. **18**, 6139 (2006).

[25]H. Takagi, H. Ogawa, Y. Yamazaki, A. lshizaki, and T. Nakagiri, Appl. Phys. Lett. **56**, 2379 (2000).

[26]Y. Kanemitsu, T. Futagi, T. Matsumoto, and H. Mimura, Phys. Rev. B **49**, 14732 (1994).

[27]T. Arguirov, T. Mchedlidze, M. Kittler, R. Rölver, B. Berghoff, M. Först, and B. Spangenberg, Appl. Phys. Lett. **89**, 053111 (2006).

[28]The etching procedure can be connected with some size shrinkage and a subsequent PL blueshift. However, this size shrinkage should definitely not be larger than ~0.3 nm if the nanoparticles are not intentionally left in the HF acid for too long.

[29]R. Rölver, S. Bruninghoff, M. Forst, B. Spangenberg, and H. Kurz, J. Vac. Sci. Technol. B **23**, 3214 (2005).

[30]S. Hernández, A. Martínez, P. Pellegrino, Y. Lebour, B. Garrido, E. Jordana, and J. M. Fedeli, J. Appl. Phys. **104**, 044304 (2008).

[31]G. Zatryb, A. Podhorodecki, X. J. Hao, J. Misiewicz, Y. S. Shen, and M. A. Green, Nanotechnology **22**, 335703 (2011).

[32]H. Hofmeister and P. Ködderitzsch, Nanostruct. Mater. **12**, 203 (1999).

[33]M. Zacharias, J. Blasing, P. Veit, L. Tsybeskov, K. Hirschman, and P. M. Fauchet, Appl. Phys. Lett. **74**, 2614 (1999).

[34]S. Yerci, U. Serincan, I. Dogan, S. Tokay, M. Genisel, A. Aydinli, and R. Turan, J. Appl. Phys. **100**, 074301 (2006).

[35]G. Scamarcio, M. Lugará, and D. Manno, Phys. Rev. B **45**, 13792 (1992).

[36]C. M. Hessel, J. Wei, D. Reid, H. Fujii, M. C. Downer, and B. A. Korgel, J. Phys. Chem. Lett. **3**, 1089 (2012).

[37]R. J. Martín-Palma, L. Pascual, P. Herrero, and J. M. Martínez-Duart, Appl. Phys. Lett. **81**, 25 (2002).

[38]R. Guerra, E. Degoli, and S. Ossicini, Phys. Rev. B **80**, 155332 (2009).

[39]D. E. Yilmaz, C. Bulutay, and T. Çağin, Appl. Phys. Lett. **94**, 191914 (2009);in their calculations, the authors employ the matrix embedment as insertion of a crystalline core into a void in the SiO_2 matrix with exactly the same volume as the inserted nanocrystals; therefore, the matrix-induced strain discussed here is not included in these calculations.

[40]I. Yassievich, A. Moskalenko, and A. Prokofiev, Mater. Sci. Eng., C **27**, 1386 (2007).

[41]P. Yu and M. Cardona, *Fundamentals of Semiconductors* (Springer Berlin, 1996).

[42]R. Cherian, C. Gerard, P. Mahadevan, N. T. Cuong, and R. Maezono, Phys. Rev. B **82**, 235321 (2010).

[43]J. Hu and I. Spain, Solid State Commun. **51**, 263 (1984).

[44]See supplementary material at http://dx.doi.org/10.1063/1.4756696 for experimental details of the measurements presented in this article, including the used samples.

[45]R. Rölver, O. Winkler, M. Först, B. Spangenberg, and H. Kurz, Microelectron. Reliab. **45**, 915 (2005); the authors identify a defect band in the PL of their samples, see [R. Rölver, M. Forst, O. Winkler, B. Spangenberg, and H. Kurz, J. Vac. Sci. Technol. A **24**, 141 (2006)]; therefore, the PL spectra in Ref. 45 were fitted with two Gaussians with one fixed at the PL position of the defect and only the SiNC-related peak was plotted in Fig. 5(b).

[46]M. Ray, N. R. Bandyopadhyay, U. Ghanta, R. F. Klie, A. K. Pramanick, S. Das, S. K. Ray, and S. M. Hossain, J. Appl. Phys. **110**, 094309 (2011).

[47]The shrinking will apply only for temperatures above the temperature interval of anomalous thermal expansion, which is between 18–120 K for pure silicon. However, in nanocrystals, this region can be expected to shift to much narrower temperature interval, see Ref. 48, and therefore anomalous thermal expansion can be neglected in the simple-case reasoning.

[48]E. S. Freitas Neto, N. O. Dantas, S. W. da Silva, P. C. Morais, M. A. P. da Silva, A. J. D. Moreno, V. López-Richard, G. E. Marques, and C. Trallero-Giner, Nanotechnology **23**, 125701 (2012).

3.6   Enclosure

Complex study of the fast blue luminescence of oxidized silicon nanocrystals: The role of the core

L. Ondič, K. Kůsová, M. Ziegler, L. Fekete, V. Gärtnerová, V. Cháb, V. Holý, O. Cibulka, K. Herynková, M. Gallart, P. Gilliot, B. Hönerlage and I. Pelant

manuscript submitted to Nanoscale, 2013

Complex study of the fast blue luminescence of oxidized silicon nanocrystals: The role of the core[†]

Lukáš Ondič,[*a,b] **Kateřina Kůsová**[a]**, Marc Ziegler**[b]**, Ladislav Fekete**[c]**, Viera Gärtnerová**[c]**, Vladimír Cháb**[c]**, Václav Holý**[d]**, Ondřej Cibulka**[a]**, Kateřina Herynková** [a]**, Mathieu Gallart**[b]**, Pierre Gilliot**[b]**, Bernd Hönerlage**[b] **and Ivan Pelant**[a]

Silicon nanocrystals (SiNCs) smaller than 5 nm are a material with strong visible photoluminescence (PL). However, the physical origin of the PL, which, in the case of oxide-passivated SiNCs, is typically composed of a slow-decaying red-orange band (S-band) and of a fast-decaying blue-green band (F-band), is still not fully understood. Here we present a physical interpretation of the F-band origin based on the results of an experimental study, in which we combine temperature (4-296K), temporally (picosecond resolution) and spectrally resolved luminescence spectroscopy of free-standing oxide-passivated SiNCs. Our complex study shows that the F-band red-shifts only by 35 meV with increasing temperature, which is almost 6 times less than the red-shift of the S-band in a similar temperature range. In addition, the F-band characteristic decay time obtained from a stretched-exponential fit decreases only slightly with increasing temperature. These data strongly suggest that the F-band arises from the core-related quasi-direct radiative recombination governed by slowly thermalizing photoholes.

1 Introduction

Since the discovery of efficient room-temperature photoluminescence (PL) of porous silicon by Canham[1], silicon nanostructures became an interesting topic within the scientific community due to their possible applications in photonics, photovoltaics and biology[2,3].

Many methods for the preparation of few-nm-sized luminescent silicon quantum dots or nanocrystals (NCs) were developed[4,5]. Besides the size of NCs, also the type of surface passivation has striking influence on their optical properties due to a large surface area of a NC with respect to its volume. Important for practical application is the stability of SiNCs passivation in air which can be either realized by silicon oxide or by various organic species covering their surface. Oxide-passivated SiNCs can be either embedded in a solid matrix[3] (typically SiO_2) or can exist as a "free-standing" ensemble of NCs[6,7] (either in the form of a powder or a colloidal dispersion). A typical PL spectrum of such SiNCs (with sizes above

$\sim$ 2 nm) contains two emission bands, one located in the red-orange spectral range with slow μs decay, termed S-band, and a second one located in the blue-green range with fast ns dynamics, termed F-band. While it has been convincingly shown via pressure-dependent experiments that the S-band is linked with the indirect $\Delta - \Gamma$ radiative recombination[8] (although the corresponding wavefunction might be real-space extended to embrace in part also subsurface/surface atoms and thus sensitive to the surface[9,10]), the physical origin of the F-band is still unclear and under debate. There exist at least two possible explanations that were proposed some time ago. One group of authors[11–13] claim that oxide-defects present in the SiO_x capping layer are responsible for the blue PL. A second group of authors[14–17] identify the F-band with the core PL from very small nanocrystals. We should also mention that it has been recently shown experimentally that it is possible to obtain direct $\Gamma - \Gamma$ recombination at the Γ-point of the Brillouin zone in SiNCs under specific excitation conditions[18] and that for certain sizes of SiNCs, a spectral overlap of the $\Gamma - \Gamma$ radiative recombination and the oxide-related PL is expected.

In this letter we present temporally and temperature-resolved PL measurements of free-standing oxide-passivated SiNCs. Our results point mainly at the interpretation of the F-band emission as originating from the core of SiNCs. Fast sub-nanosecond dynamics, a relatively small spectral shift with the variation of temperature (4-296 K) and a stretched-exponential decay character of the F-band led us to the conclusion that it can be attributed to the quasi-direct (phononless) recombi-

nation between energetic levels which arise from bulk states positioned in the vicinity of the Γ-point of the Si band structure. We also link the slower ns component of the F-band with the slow cooling of photoholes. The possibility of slow thermalization is advantageous for the realization of a "hot carrier solar cell", in which the energy otherwise lost due to thermalization losses is efficiently harvested. This concept has been demonstrated in PbSe nanocrystals[19].

2 Experimental

The preparation technique of SiNCs is based on electrochemical etching of a monocrystalline Si wafer with orientation $\langle 100 \rangle$ in a solution comprising hydrofluoric acid, ethanol and H_2O_2 (1:2.85:0.15) at the current density of 2.5 mA/cm^2 for two hours. This procedure leads to the formation of a porous layer on the wafer surface. The size of the pores is further decreased by a post-etching treatment during which the wafer with the porous layer is placed into H_2O_2 bath and etched again for several minutes. Details of this method can be found in Ref.[6], in which the SiNCs under study here are designated 'white' SiNCs. After exposing the sample to the ambient atmosphere, oxide SiO_x/SiO_2 covers the surface, forming an oxide shell around the nanocrystals within the pores. Finally, the porous layer is pulverized yielding the powder of SiNCs. The powder comprises big clusters (up to hundreds of microns) of interconnected SiNCs, which are ultrasonically treated in an ethanol bath in order to separate them into single NCs. Then, the sample is left to sediment and only a supernatant is used for characterization measurements. For photoluminescence measurements presented in this study, the colloidal dispersion of SiNCs in ethanol was drop-casted onto a cleaned Si wafer, forming a thin layer of SiNCs.

Structural characterization of the fabricated SiNCs was performed first of all by employing X-ray diffraction (XRD) method. For this measurement we used a standard high-resolution diffractometer with a Cu K$_\alpha$ line-focus tube operated at 40 kV and 35 mA. The primary X-ray beam was collimated by a parabolic multilayer mirror and monochromatized by a Baertels (4x220 Ge) monochromator. XRD was applied to the native porous Si layer attached to the wafer (before pulverizing), in the directions both parallel (x) and perpendicular (z) to the surface. Samples used for all remaining characterization techniques described below were prepared from a highly diluted colloidal dispersion of SiNCs, which was drop-casted on various types of substrates.

High-resolution transmission electron microscopy (HRTEM) was carried out with FEI Tecnai G2 F20 X-TWIN system and the sample used for this characterization was represented by SiNCs dispersed over a carbon film on 300 mesh copper grid.

The mean size of SiNCs was evaluated from Atomic force microscopy (AFM) measurements with NTEGRA Prima NT MDT system (under ambient conditions) using SiNCs drop-casted on a polished Si wafer. The sample was scanned using an HA-NC Etalon tip with tip curvature radius around 10 nm, employing the semi contact mode. The microscope was calibrated before the measurements with a calibration grid of SiC with a 1.5 nm step. The height of the particles was determined as a difference between the local maximum and local minimum in a circle slightly wider than each particle. The total number of found particles higher than 1 nm reached almost 5000, measured from four images with areas of 3x3 μm^2 in high resolution (1024x1024 points^2). The small size of SiNCs was confirmed also by the analysis of the lateral sizes of particles using autocorrelation function[20] from areas excluding the sparse larger particles. This analysis implies that AFM pictures contain images of particles enlarged in the lateral size due to the convolution with the AFM tip.

To obtain information on the chemical composition of SiNCs, X-ray photoelectron spectroscopy (XPS) was applied. The experiments were performed at the Materials Science Beamline at the Elettra synchrotron light source in Trieste. The beamline is equipped with a plane grating monochromator providing synchrotron light in the energy range 40-800 eV, a Specs Phoibos 150 hemispherical electron energy analyzer, Low Energy Electron Diffraction (LEED) optics and a dual-anode X-ray source. The base pressure in the main chamber was lower than 10^{-10} Torr. The investigated SiNCs were deposited by drop-casting on a Pt foil. The sample was examined using XPS with the overall energy resolution of 0.3 eV.

A steady-state PL characterization at room-temperature was performed under continuous-wave (cw) excitation of three different wavelengths: 325, 442, and 473 nm. The PL signal was detected by a Peltier-cooled charge-coupled device (CCD) attached to a spectrograph.

Time-resolved and temperature dependent experiments were performed with the sample placed in a He-flow cryostat (Oxford Instruments) enabling us to cover the temperature range from 4K to room temperature. Due to time consuming measurements, emission spectra were recorded in relatively large steps (about 50 K) starting at 4K. The sample was excited with 100 fs long pulses generated from the frequency-doubled output of an amplified Ti:Saphire laser at 400 nm, with 200 kHz repetition rate. The excitation power was set to be very low (400 nW) in order to avoid local heating of the sample.

Time-resolved spectra were recorded using a streak camera (Hamamatsu, 30 ps resolution, in a photon counting mode), coupled with a spectrograph. The output of measurements were 2D maps of intensity (in number of photons) as a function of a given time window (0–2 μs, 0–10 ns, 0–2 ns) and wavelength (423 to 661 nm). In order to visualize the acquired information, the signal was integrated over defined temporal
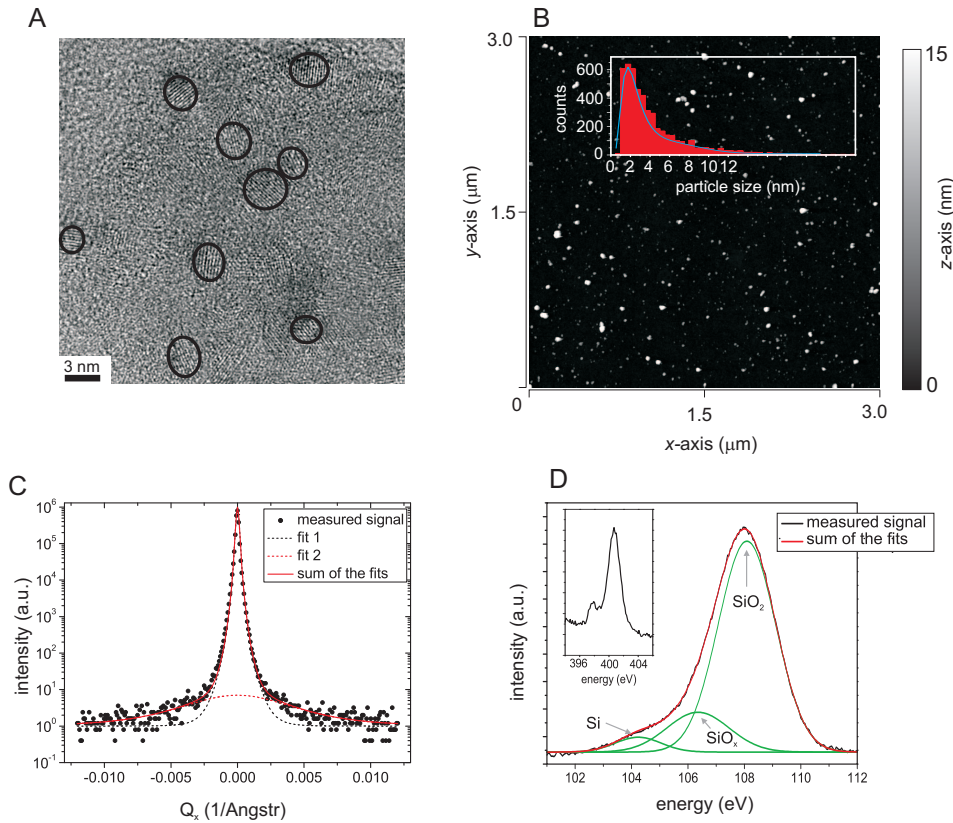
Fig. 1 Structural characterization of the SiNCs under study. (A) HRTEM image. Visibility of SiNCs is enhanced by ringing. (B) AFM image with the *z*-axis normalized to 15 nm. Inset shows a histogram of sizes of SiNCs taken from AFM measurements conducted at four different places of the sample. (C) XRD omega scan – distribution of diffracted intensity in reciprocal space along the horizontal Q_x axis – the narrower component is the substrate peak (broadened by the resolution function), the broader component stems from SiNCs. (D) Si 2p XPS spectrum containing Si, SiO_x and SiO_2 ingredients. Inset shows the N 1s spectrum.

or spectral intervals, as presented further.

The spectra were corrected for the spectral response of the detection system.

3 Results

3.1 Characterization of the silicon nanocrystals

First of all, we present the results evidencing crystallinity and small size of our SiNCs. It should be noted that more results on characterization can be found in Refs [21,22].

It is reasonable to expect that a product of our fabrication method (SiNCs), which starts from a mono-crystalline Si wafer, will be also of crystalline nature. This has been

confirmed in two independent ways. First, the results of the application of XRD measurements on as-prepared porous silicon layer (attached to the Si substrate) along the horizontal Q_x axis are displayed in Fig. 1C, which shows the distribution of diffracted intensity in reciprocal space. The experimental curve can be fitted with a superposition of two well-known Pearson VII profile functions [23]. The narrower peak corresponds to the diffracted signal from the Si substrate while the low-intensity wide one is characteristic of the SiNCs (porous) layer. The finite width of the latter proves that (i) the Si nanoparticles in the layer are of crystalline nature and (ii) all of these nanoparticles are oriented equally, i.e. crystallographically correlated to the bulk substrate (otherwise the Q_x scan would be extremely large, corresponding to a Debye circle of

a nanocrystal). Scan in the Q_z direction is included in Supplementary information.

Second, the application of HRTEM on the powder of SiNCs fabricated by pulverizing the porous layer and dispersed in methanol showed a considerable number of small Si nanoparticles with clearly visible lattice plane fringes (Fig. 1A). It is obvious that SiNCs are in this case oriented randomly, as expected upon the nanoparticles being detached from the substrate.

Figure 1B shows a representative AFM image of the SiNCs drop-casted on a Si-wafer. The vertical z-axis is scaled to the maximum of 15 nm in order to enhance the visibility of small NCs. A relatively large number of particles (almost 5000 SiNCs) on an image with high resolution allowed to statistically evaluate the mean size of SiNCs. The size distribution shown in the inset of Fig. 1B was derived as a sum from 4 different places on the sample. It peaks at around 2 nm with most particles in the interval of (1.5-3 nm). This result is in good agreement with the HRTEM measurements. Also bigger particles are present, which are either crystallites with a large core or clusters of interconnected small SiNCs that were not broken apart during the ultrasonic treatment. The measured distribution of sizes can be satisfactorily described with a wide lognormal distribution (median 2.5 nm, mean 2.9 nm, standard deviation 1.7 nm) with a Gaussian tail (mean 7.2 nm, standard deviation 3.7 nm). More AFM images can be found in Supplementary information.

XPS measurements were performed in the energy window corresponding to the Si 2p peak (Fig. 1D) and N 1s peak (inset). Given the fact that our SiNCs underwent an intense post-etch oxidation in H_2O_2, they are covered with a relatively thick silicon dioxide SiO_2/silicon suboxide SiO_x ($x < 1$) shell. In the detection window around the Si 2p peak, it is thus expected to find predominantly a SiO_2/SiO_x band, located on the high-energy wing of the pure Si 2p position. This can be clearly seen in Fig. 1D, indeed, where we fitted the acquired spectrum (upon subtracting background) with three peaks characteristic of the Si binding energy in bulk Si, silicon suboxide SiO_x and silicon dioxide SiO_2[24], the latter peak in Fig. 1D having the highest intensity. At the same time, however, the whole motif is considerably shifted to the higher binding energy, by about 5 eV with respect to the usual position of these peaks in SiNCs[24,25]. This can be explained in a natural way to be due to charging of SiNCs during the measurements, as a consequence of their thick insulating SiO_2 shell.

Recently, Dasog et al.[25] have put forward a hypothesis that the fast blue emission in SiNCs can be facilitated owing to trace nitrogen contamination. In our XPS sample, we detected even two N 1s peaks (inset in Fig. 1D): a stronger one at ~ 401 eV and a small wing at ~ 398 eV. The peak at ~ 401 eV can be tentatively classified as belonging to unintentional ni-

trogen substrate contamination of the sample during its preparation and manipulation. The second wing agrees in its spectral position with manifestation of nitrogen impurities located on the inside or subsurface of SiNCs[26] and it is thus tempting to ascribe it to nitrogen traces in the vicinity of SiNCs. However, in view of the above mentioned charging effects, such interpretation cannot be considered to be definite. Furthermore, the existence of a possible second XPS peak corresponding to a Si-N bond in the Si 2p spectrum cannot be easily determined from the main spectrum in Fig. 1D due to the fact that the Si-N peak should be spectrally coincident with the SiO_2/SiO_x band[25], i.e. the presence of nitrogen in close vicinity to SiNCs cannot be confirmed. Thus, although we cannot completely rule out some influence of nitrogen on the F-band luminescence in our SiNCs, we would like to point out that in Ref.[25] the situation was different: the exposition of red luminescent SiNCs to nitrogen changed the whole emission spectrum to the blue, while in our case the both bands, red (S) and blue (F), are all the time present in the cw excited PL spectrum (Fig. 2).
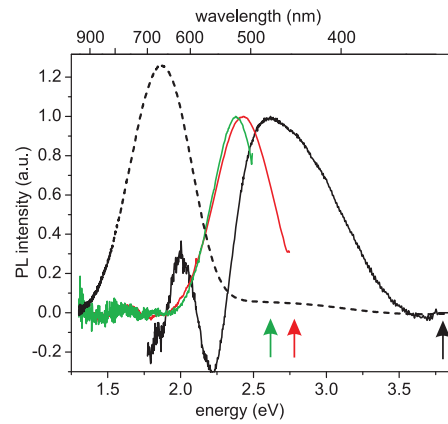

Fig. 2 PL spectra of SiNCs under 325 nm cw excitation (black dashed curve). F-band of SiNCs excited with different excitation photon energies depicted by vertical arrows: 325 nm (black curve), 442 nm (red curve), 473 nm (green curve).

3.2 Steady-state photoluminescence

The room-temperature PL characterization of the sample under UV (325 nm) cw excitation is shown in Fig. 2 (the dashed curve). The spectrum has two main components: an intense band peaking at about 1.9 eV with μs dynamics (S-band) and another emission band peaking at about 2.7 eV (F-band), much less intense than the S-band, possessing nanosecond dynamics.

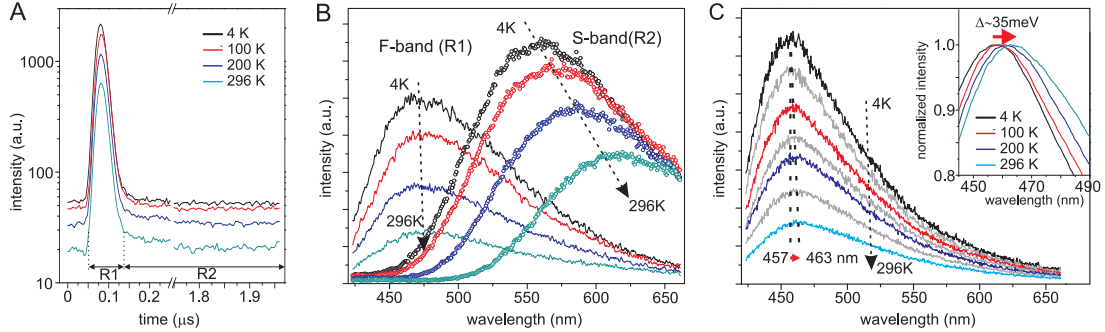The F-band's spectral position depends strongly on the ex-

Fig. 3 (A) PL decay curves integrated over the whole spectral detection window (420 - 661 nm) at different sample temperatures (4K, 100K, 200K and 296K). (B) The F-band and S-band PL spectra integrated over the time intervals R1 and R2 (see panel A), respectively, at different sample temperatures. (C) The F-band spectra integrated over the short temporal window of 2 ns, at different sample temperatures. The inset shows a zoom-in on the maxima of normalized F-band spectra.

citation photon energy as already reported by our group [17]. Here, we plot the F-band (extracted from the cw measurement by fitting first the S-band with a Gaussian function and subtracting the fit from the overall spectrum) for three different cw excitations of 325, 442, and 473 nm. We can clearly see the red-shift of the F-band maximum with increasing excitation wavelength, which strongly suggests that the light emitting species are SiNCs with a large size distribution rather than defects, whose emission energy is typically excitation-energy independent. The relatively large width of the size distribution was also supported by HRTEM and AFM measurements (Fig. 1).

3.3 Time-resolved photoluminescence in 2 μs window

First, the possible contributions of the S- and F-bands to the overall detected temporally-resolved PL signal need to be assessed. Therefore, we integrate the PL signal over the whole spectral detection window and plot the spectrally-integrated PL decay curves in a relatively long time interval of about 2 μs as a function of temperature, as shown in Fig. 3A.

The fast PL component (F-band) reveals itself as a faster decay present only in several tens of nanosecond after the excitation. Therefore, we can define an interval R1 spanning approximately the width of 70 ns after the excitation event (see Fig. 3A) as the interval with the dominating contribution of the F-band. Indeed, the temporal integration of the detected signal solely over the R1 interval yields a spectrally resolved peak at around 473 nm, as plotted in Fig. 3B (the solid lines). This peak exhibits only a very small spectral shift with temperature, as will be discussed in detail further.

Second, we will address the influence of the S-band on our analysis of the F-band's behavior. Going back to Fig. 3A, at longer delays, solely a slow component (S-band) with μs

decay constant is observed[*]. Thus, we can define an S-band-related temporal window R2 (between 0.13 and 2 μs). Spectra integrated in the temporal window R2 are plotted in Fig. 3B (the open circles). The S-band's maximum shifts considerably with increasing temperature to longer wavelengths (from 558 to 615 nm, i.e. by $\approx$ 206 meV) and the intensity of the S-band gradually decreases when heating the sample from 4K to room temperature. These results prove the assignment to the S-band[5,27].

In order to correctly investigate properties of the F-band, its time-resolved optical characterization was conducted in short temporal windows of 10 and 2 ns. In these detection windows the intensity of the S-band is much lower than that of the F-band and thus its influence on the F-band is only marginal. We have verified that within the first 10 ns, the S-band does not affect the spectral shift of the F-band (the S-band may cause only slight broadening of the F-band spectra on its long-wavelength part, see Fig. S5 in Supplementary information).

3.4 Time-resolved photoluminescence in 10 and 2 ns windows

Now we finally proceed to the analysis of the temporally and temperature-resolved F-band's behavior. Figures 4A and B show normalized PL spectra at different time delays after excitation at 4 K and room temperature, respectively. It is clear that the F-band maximum spectrally red-shifts with time delay

---

[*] Due to the long decay of the S-band and the relatively high repetition rate of the excitation laser (200 kHz), the S-band signal does not completely fade away between two successive 5μs-separated excitation events, which is apparent at the very beginning of the time window where the signal is not zero. More specifically, there is almost no change in the intensity of the S-band within the 2 μs interval (see also Fig. S4 in Supplementary information), which means that the S-band does not fully relax.
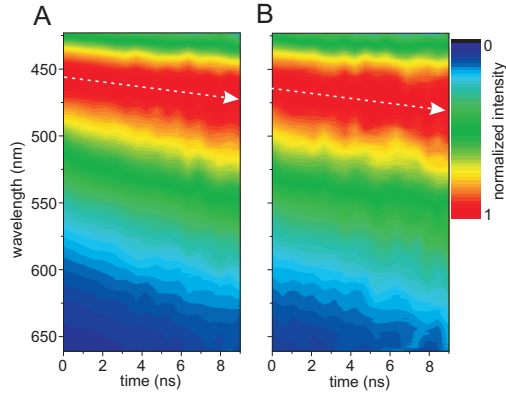
Fig. 4 F-band's temporal and spectral evolution in a 10 ns detection window at (A) 4 K and (B) room temperature. Intensity is normalized to the signal maximum at each time delay. One spectral profile in the map is integrated over the detection interval of 0.5 ns in order to decrease the noise. The white arrow is the guide for the eye and depicts the spectral shift of the signal maximum with time ($\sim$ 70 meV).

(see the white arrows in Fig. 4) and the shift of about 70 meV is similar for all studied sample temperatures[†] (see also Fig. S5 in Supplementary information). This spectral shift with time delay serves as another argument for assigning the origin of the F-band to the nanocrystals, as this behavior is once again atypical of defects[28].

In order to avoid the influence of the above-discussed red-shift on the spectra analysis, the F-band was further studied in even shorter temporal window of 2 ns. Figure 3C shows PL spectra of SiNCs as a function of temperature (4 K to 296 K, with the step of $\sim$ 50 K), which were obtained by integrating the measured signal over the whole 2 ns detection time window (in order to increase the signal-to-noise ratio). The PL maximum shifts with increasing temperature from about 457 to 463 nm ($\delta \sim$ 35 meV, see the inset in Fig 3C). An energetically equal red-shift was also measured in the temporal window of 10 ns (see Fig. S6 in Supplementary information).

The decay curves of the F-band emission were extracted around their relevant spectral maxima by integrating the signal over the spectral interval of (PL maximum±5 nm). Figures 5A and B show normalized decay of the F-band PL signal at 4 K and at room temperature in the 2 ns and 10 ns detection windows, respectively. The response of the detector to the excitation laser pulse is also plotted in Fig. 5A by the gray shaded area. PL signals in the 2 ns window (Fig. 5A) can be

fitted by a double exponential function ($I \sim A \exp\left[-(t/\tau_1)\right] + B \exp\left[-(t/\tau_2)\right]$), of which, however, the longer component τ_2 has a large error due to the fact that the signal lasts beyond the duration of the detection window. However, the first ultra-fast component can be fitted reliably. Its decay time $\tau_1 \sim$ 80 ps is, within the fitting error, similar for all studied temperatures.

The longer, nanosecond decay component of the F-band can be fitted with sufficient accuracy in the 10 ns detection window (Fig. 5B) by using a stretched exponential function $I \sim \exp\left[-(t/\tau)^{\beta}\right]$ (in the 2 ns window approximated by the exponential function with τ_2)[‡]. Fitting parameters as a function of sample temperature are plotted in Fig. 5C. The decay time τ drops only slightly from about 2 ns to 1.2 ns when heating the sample from 4K to room temperature. Parameter β drops from about 0.8 to 0.6 with increasing temperature. Parameter β is less than unity, which corresponds to a broad distribution of lifetimes of the relaxation processes present mainly due to the large size distribution. The stretched-exponential decay of the F-band is linked with its time-delay-related red-shift shown in Fig. 4.

To summarize, the temporal evolution of the F-band signal is characterized by an ultra-fast, ps or shorter, exponential decay at the beginning, followed by nanosecond stretched-exponential decay. Both these decays are only very weakly temperature dependent.

4 Discussion

First, we should briefly comment here on the widespread interpretation of the F-band origin in terms of a defect-state luminescence from the silicon oxide interface/shell. Even if rather convincing experiments in favor of this idea have been put forward recently[13,29], the idea is not in line with the results obtained in our sample. In particular, a blue defect-related emission band in amorphous SiO_2 at 2.7 eV, ascribed to an Si atom with only two neighboring oxygens[30,31], was reported to increase in intensity when heating from 100K to 300K, which is in contradiction with our observation (Figs. 3B, C). Besides the silicon oxide defects, nitrogen has been indicated as the origin of the blue emission in alkyl-passivated SiNCs quite recently[25]. In our samples, the presence of trace nitrogen was confirmed by XPS measurements. However, the observed optical characteristics of the F-band emission, namely, the shift of emission maximum with changing excitation wavelength (Fig. 2) as well as the spectral shift with increasing time delay (Fig. 4) are quite atypical of defects, suggesting a different origin. Nevertheless, defects of any kind can influence into some extent the spatial distribution of the carriers' wavefunction and

[†] The S-band exhibited qualitatively a very similar behavior at room temperature, however, on the μs time scale, as studied elsewhere[6]. Corresponding shift under 355 nm nanosecond pumping was about 180 meV in the 50 μs long time interval.

[‡] Let us note here that also a double-exponential fit can be used to fit the signal decay, however, with much larger fitting error than the stretched-exponential fit.
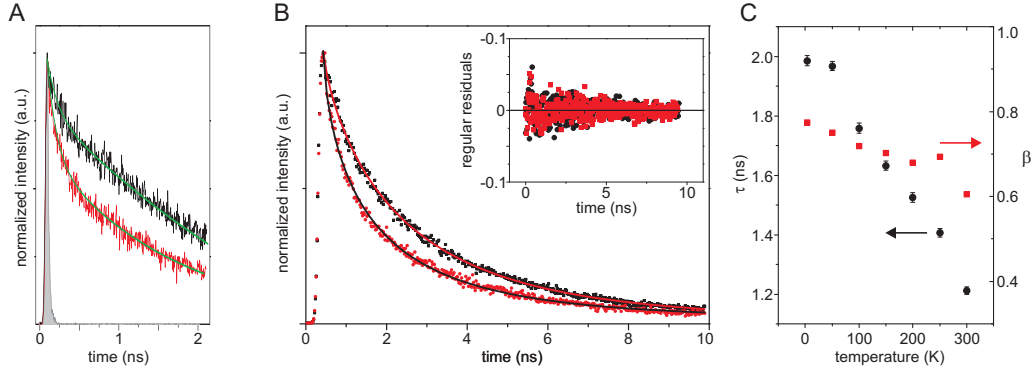
Fig. 5 Normalized decay curves of the PL signal taken at the F-band spectral maximum at 4K (black curve) and room temperature (red curve). (A) Decay in 2 ns time window fitted with a double-exponential function. The gray shaded area shows the response of the detector to the excitation laser pulse. (B) Decay in the 10 ns temporal window fitted with a stretched exponential function. The inset depicts the residuals of the fits. (C) Parameters τ (circles) and β (squares) of the stretched exponential fits of the F-band decay at various sample temperatures.

the position of the corresponding energy level.

Another reason which favors the role of the core in the F-band luminescence with respect to the defects is the top-down technique (etching) we use for the preparation of our nanocrystals, starting from perfectly crystalline material with low content of impurities. Unlike various synthesis-based techniques, our top-down approach yields pure crystalline, not amorphous, nanoparticles, as confirmed by both HRTEM and XRD analyses. Owing to that, the origin of the luminescence in SiNCs under study here can be discussed in the framework of the Si electronic energy band structure E(**k**), sketched for the $\Gamma-X$ direction in Fig. 6. Theoretical calculations showed that the concept of E(**k**) is still applicable for SiNCs larger than ~ 1.5 nm[9]. Interestingly, the electronic band diagram of such NCs, even though strongly affected by quantum confinement effect, still qualitatively copies that of bulk Si[9]. However, as a result of the quantum confinement, the indirect $\Gamma-\Delta$ band gap of SiNCs is blue-shifted compared to the bulk and discrete (in energy) electronic levels are formed. The discrete character of levels is mostly apparent at the band edges, where the density of states is rather low. Furthermore, in line with real-space confinement of the carriers in a small volume of NC, the electronic states are delocalized in the **k**-space (see Figs. 10,11 in Ref.[9]).

Before discussing in detail the origin of the F-band we will briefly comment on the relatively large (206 meV) red-shift of the S-band spectral maximum upon heating the sample. As it was already stated, the S-band originates from the indirect recombination[8] between the conduction band valley Δ_1 near the X point and the maximum of the valence band Γ'_{25} (red arrow in Fig. 6). Temperature dependent change of the indirect band gap of bulk Si[32] is well-known to be about 47 meV (from

4K to 296K), however, this is more than 4 times less than in the case of our free-standing oxide-passivated SiNCs. This difference can be explained by considering the effect of tensile strain on the bulk Si band diagram as was recently exploited by Kůsová et al[5]. Briefly, when the sample is cooled down to 4K, tensile strain acting on the NC core builds up as a result of the difference between the thermal expansion coefficients of the Si core and the SiO_2 shell. The much lower thermal expansion coefficient of SiO_2 compared to Si causes that the expected cooling-induced contraction of the Si lattice is substantially reduced. It can be imagined such as if the Si atoms in the SiNCs are held back by the SiO_2 shell and thus almost do not move, which leads to the tensile strain acting on the core[5]. The positive sign of the deformation potential pertinent to the silicon indirect band gap[33] causes that the tensile strain results in the increase of the indirect band gap at low temperatures (green arrow in Fig. 6) and thus adds up to the effect of the variation of the indirect bulk Si band gap upon cooling (black arrow in Fig. 6).

Therefore, during the process of increasing the temperature of the sample from 4 K to 296 K, the tensile strain acting on the core gradually diminishes and the Si atoms relax. Together with the effect of natural variation of the indirect Si band gap, it leads to the observed shrinkage of the band gap and thus to the considerable redshift of the S-band PL spectra upon heating the sample. However, to obtain full quantitative support for this idea, reliable data on thermal expansion coefficients of $2-3$ nm SiNCs and/or theoretical computations would be needed. It is important to note that a direct measurement of the presence of the tensile strain at low temperatures is not easily feasible. However, the argument of tensile strain was already used to explain behavior of PL in Si nanopillars[34] and
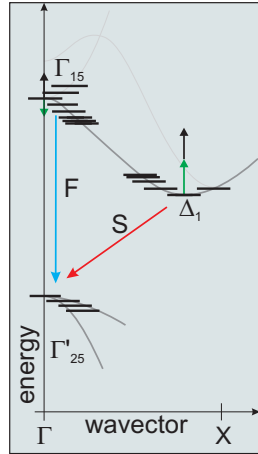
Fig. 6 A schematic illustration of the silicon band diagram E(**k**) in the $\Gamma - X$ direction showing the discretization of energy levels around the local extremes of conduction and valence bands, which results from quantum confinement of carriers in Si NCs. Temperature (upon cooling) and strain-induced shift of the Δ_1-valley and Γ_{15}-point are depicted by black and green arrows, respectively. Radiative paths of the F- and S-band are also shown.

also studied by means of computer simulation recently in Si nanowires[35].

Next, we can finally comment on the explanation of the origin of the F-band in our samples. When compared to the S-band, the F-band's (i) energetically higher position and (ii) much faster (nanosecond) dynamics imply that a phonon-less radiative recombination between the valence and conduction band states positioned in the vicinity of the Γ-point is a good candidate (see the blue arrow in Fig. 6). Namely, it comprises a strictly direct $\Gamma - \Gamma$-recombination and a quasi-direct recombination allowed due to the **k**-space overlap of the electron and hole wavefunctions of levels near the Γ-point, which increases the probability of radiative transitions between these states. The arguments speaking for this interpretation can be summarized as follows:

(a) The first characteristic of the F-band which can be understood within the interpretation of the F-band as a quasi-direct recombination between the levels near the Γ-point is the fact that the F-band is spectrally always very close to the excitation energy (Fig. 2). If the excitation energy is high enough to excite directly the electron close to the Γ-point, this electron either contributes to the F-band emission or relaxes to the Δ_1-valley. Nanocrystals with energy of their direct band gap close to the excitation energy will be those contributing the most to the F-band emission. In other words, the excitation energy basically defines which

SiNCs from an ensemble will contribute to the F-band emission.

(b) During the thermalization process of the excited electron towards the Δ_1-valley, electron can still recombine with a hole (the blue arrow in Fig. 6) if the **k**-space radiative transition probability is high enough. This leads to a spectral red-shift in the PL with time delay as observed in Fig. 4. (Besides, similarly to the S-band, the time-delay-related red-shift can be attributed also to the size dependence of radiative rates when probing a broad-sized ensemble of NCs[36], resulting in both these bands having a stretched-exponential decay as discussed further in item (d)[§])

(c) The above-discussion may explain also a relatively low dependence of the F-band maximum on the temperature variation. Namely, as discussed in item (a), it is the value of excitation energy which determines the F-band emission spectrum. It means that at different temperatures, differently sized SiNCs may contribute to the F-band luminescence keeping the spectral maximum almost unaffected. In addition to this effect, when changing temperature of an ensemble of SiNCs, the above discussed tensile strain counteracts the bulk-Si-like temperature-caused direct band gap variation (Fig. 6) due to the negative sign of the $a(\Gamma_{15}) - a(\Gamma'_{25})$ deformation potential[33], making the energy of the Γ_{15} state much less temperature sensitive than that of the Δ_1 valley. See also Supplementary information for detailed discussion on the stress-induced effects.

(d) The measured dynamics of the F-band, characterized by the sum of the exponential function (with picosecond decay) and the stretched-exponential function ($\tau \sim 1 - 2$ ns), can be addressed by a comparison with results of a computer simulation. Moskalenko et al.[37] studied theoretically the dynamics of multiphonon relaxation of moderately excited carriers confined in Si/SiO_2 NCs as a function of the NC size and temperature. The results of their simulation show that relaxation rates between the highest hole levels near the valence band edge (Γ'_{25} state) are in the picosecond to nanosecond range, depending on the size of the nanocrystal. This implies, as shown by the authors of Ref.[37], that the population decay of a particular hole level within an ensemble of SiNCs with different sizes has two components – an ultrafast one in the picosecond range and a slower one in the nanosecond range (Fig. 5 in Ref.[37]). The authors also computed that the

§ It has been shown experimentally that decay of single SiNC (even though only in the case of the S-band) can be described by a single exponential function. However, when the ensemble of SiNCs with a size distribution is considered, the decay character changes into stretched exponential due to summation of many single exponentials with different decay parameters[36].

slow component possesses a stretched exponential decay as a consequence of the size distribution. Moreover, they showed that the decay times decrease only moderately when the system temperature increases. These computational results are in complete agreement with our observations and therefore, we believe that the dynamics of the F-band is governed by the relaxation of holes between the levels located in the vicinity of the valence band Γ'_{25} state; these (slightly hot) holes radiatively recombine with hot electrons located close to the Γ_{15} conduction band extremum (the blue arrow in Fig. 6). Although such a type of radiative recombination might seem counterintuitive at first sight, in real experiment a large number of nanocrystals is excited (10^{10} or more). This means that even if the probability of radiative recombination like this is (much) lower than the probability of intraband relaxation (say for example thousand times), some of the electron–hole pairs (one in a thousand) are statistically bound to recombine radiatively. Given the temporal window we choose to measure in (e.g. 0–2 ns after excitation), these electron–hole pairs will be the ones we can detect, whereas the rest will simply relax to lower states. Naturally, the probability of the radiative recombination event must be large enough to allow for the emitted light to be observable. This is true, however, since the $\mathbf{k}$-space overlap of hot close-to-Γ-point electron and hole wavefunctions is larger than that in the indirect Γ-Δ radiative transition, the probability of radiative transitions increases drastically when we move from indirect to quasi-direct transitions, i.e. towards higher photon energies. Such behavior was also suggested by computer simulations (see Fig. 3 in Ref.[38]).

Now, let us shortly compare and contrast our interpretation of the F-band with other observations of blue PL in silicon. An interpretation of fast luminescence in SiNCs in terms of $\Gamma - \Gamma$ transition has been proposed recently also by de Boer et al.[18] on the basis of time-resolved PL spectroscopy in size-selected SiO_2-matrix-embedded SiNCs. A quasi-direct recombination was observed in organically-capped small SiNCs[39]. However, it was attributed to the recombination of already thermalized electrons (in the Δ_1-valley) and holes. Kiba et al.[40] have recently reported on four PL emission bands in Si nanodiscs with SiC barriers. They observed non-monotous temperature dependence of PL intensity, achieving maximum values at ~ 250 K. Their interpretation in terms of thermal electron excitation and escape (hopping among neighboring nanodiscs) thus can be hardly applied to our observation. Finally, it should be also noted that in bulk Si, the so called 'hot luminescence' is a source of light emission of energies higher than that of the indirect band gap[41]. The difference between the quasi-direct recombination in our SiNCs and hot luminescence in bulk Si is that the recombination of hot electrons with

relaxed holes must be, in the case of bulk Si, phonon-assisted.

In the end, we would like to state explicitly that we do not want to contradict the statement that in some types of SiNCs the blue emission can be connected with or strongly influenced by defects, as show the recent studies e.g. by Dasog et al.[25] or Romero et al[42]. However, in our type of sample, containing oxidized Si nanocrystals etched from high-purity crystalline silicon, the defect explanation is not in accordance with the observed phenomena (and neither is e.g. in Refs.[17] or[39]). Therefore, we believe that the origin of the blue PL in SiNCs can vary depending on the particularities of the studied sample: preparation method, surface passivation, size, etc.

5 Conclusions

In conclusion, the results of ultrafast PL spectroscopy performed in a wide temperature range show that the F-band origin in oxidized SiNCs prepared by etching of Si wafer lies predominantly in the core-related quasi-direct (phononless) radiative recombination between the states in the vicinity of the Γ-point. The observed phenomena include: (i) temperature-independent spectral shift at longer time delays, attributed to the size-dependence of radiative rates, (ii) a very small spectral shift (~ 35 meV) with temperature change ($4 - 296$ K) and (iii) the presence of two temporal components, namely a single-exponentially decaying, ultrafast $\sim$ps one and a much slower, stretched-exponentially decaying nanosecond one. Both of these temporal components exhibit only a weak temperature dependence. We have linked the nanosecond component of the F-band to slowly cooling photoholes. Knowledge of the origin of the fast-decaying PL band in SiNCs is important also from the point of view of silicon photonics, as it possess positive values of optical gain coefficient[43,44].

References

1 L. T. Canham, *Appl. Phys. Lett.*, 1990, **57**, 1046.
2 *Silicon Nanophotonics: Basic Principles, Current Status and Perspectives*, ed. L. Khriachtchev, Pan Stanford Publishing, 2009.
3 *Silicon Nanocrystals*, ed. L. Pavesi and R. Turan, Wiley-VCH, 2010.
4 J. Veinot, *Chem. Commun.*, 2006, **40**, 4160–4168.

5 K. Kůsová, L. Ondič, E. Klimešová, K. Herynková, I. Pelant, S. Daniš, J. Valenta, M. Gallart, M. Ziegler, B. Hönerlage and P. Gilliot, *Appl. Phys. Lett.*, 2012, **101**, 143101.

6 K. Dohnalová, L. Ondič, K. Kůsová, I. Pelant, J. L. Rehspringer and R.-R. Mafouana, *J. Appl. Phys.*, 2010, **107**, 053102.

7 F. Huisken, G. Ledoux, O. Guillois and C. Reynaud, *Adv. Mater.*, 2002, **14**, 1861–1865.

8 D. C. Hannah, J. Yang, P. Podsiadlo, M. K. Chan, A. Demortiere, D. J. Gosztola, V. B. Prakapenka, G. C. Schatz, U. Kortshagen and R. D. Schaller, *Nano Lett.*, 2012, **12**, 4200–4205.

9 P. Hapala, K. Kůsová, I. Pelant and P. Jelínek, *Phys. Rev. B*, 2013, **87**, 195420.

10 M. V. Wolkin, J. Jorne, P. M. Fauchet, G. Allan and C. Delerue, *Phys. Rev. Lett*, 1999, **82**, 197.

11 L. Tsybeskov, J. V. Vandyshev and P. M. Fauchet, *Phys. Rev. B*, 1994, **49**, 7821.

12 A. Brewer and K. Von Haeften, *Appl. Phys. Lett.*, 2009, **94**, 261102.

13 M. Kořínek, M. Kozák, F. Trojánek, D. Hiller, A. Hartel, S. Gutsch, M. Zacharias and P. Malý, *Physica E*, 2014, **56**, 177 – 182.

14 Y. Kanemitsu, T. Futagi, T. Matsumoto and H. Mimura, *Phys. Rev. B*, 1994, **49**, 14732–14735.

15 J. P. Wilcoxon, G. A. Samara and P. N. Provencio, *Phys. Rev. B*, 1999, **60**, 2704–2714.

16 M. Ray, T. Basu, A. Jana, N. Bandyopadhyay, S. Hossain, A. Pramanick and R. Klie, *J. Appl. Phys.*, 2010, **107**, 064311.

17 J. Valenta, A. Fucikova, I. Pelant, K. Kůsová, K. Dohnalová, A. Aleknavičius, O. Cibulka, A. Fojtík and G. Kada, *New J. Phys.*, 2008, **10**, 073022.

18 W. D. A. M. de Boer, D. Timmerman, K. Dohnalová, I. N. Yassievich, H. Zhang, W. J. Buma and T. Gregorkiewicz, *Nat. Nanotechnol.*, 2010, **5**, 878–884.

19 W. A. Tisdale, K. J. Williams, B. A. Timp, D. J. Norris, E. S. Aydil and X.-Y. Zhu, *Science*, 2010, **328**, 1543–1547.

20 L. Fekete, K. Kůsová, V. Petrák and I. Kratochvílová, *J. Nanopart. Res.*, 2012, **14**, 1062.

21 K. Dohnalová, I.Pelant, K. Kůsová, P. Gilliot, M. Gallart, O. Crégut, J.-L. Rehspringer, B. Honerlage, T. Ostatnický and S. Bakardjeva, *New J. Phys.*, 2008, **10**, 063014.

22 E. Klimešová, K. Kůsová, J. Vacík, V. Holý and I. Pelant, *J. Appl. Phys.*, 2012, **112**, 064322.

23 P. W. Elderton and N. L. Johnson, *Systems of Frequency Curves*, Cambridge University Press, London, 1969.

24 L. Khriachtchev, T. Nikitin, C. J. Oton, R. Velagapudi, J. Sainio, J. Lahtinen and S. Novikov, *J. Appl. Phys.*, 2008, **104**, –.

25 M. Dasog, Z. Yang, S. Regli, T. M. Atkins, A. Faramus, M. P. Singh, E. Muthuswamy, S. M. Kauzlarich, R. D. Tilley and J. G. C. Veinot, *ACS Nano*, 2013, **7**, 2676–2685.

26 H.-L. Zhu, F.-D. Han, J.-Q. Bi, Y.-J. Bai, Y.-X. Qi, L.-L. Pang, C.-G. Wang, S.-J. Li and C.-W. Lu, *J. Amer. Ceram. Soc.*, 2009, **92**, 535–538.

27 A. M. Hartel, S. Gutsch, D. Hiller and M. Zacharias, *Phys. Rev. B*, 2012, **85**, 165306.

28 L. Skuja, *J. Non-Cryst. Solids*, 1992, **149**, 77–95.

29 A. Gupta and H. Wiggers, *Nanotechnology*, 2011, **22**, 055707.

30 L. N. Skuja, A. N. Streletsky and A. B. Pakovich, *Solid State Commun.*, 1984, **50**, 1069–1072.

31 A. Anedda, G. Bongiovanni, M. Cannas, F. Congiu, A. Mura and M. Martini, *J. Appl. Phys.*, 1993, **74**, 6993–6995.

32 A. Dargys and J. Kundrotas, *Handbook on physical properties of Ge, Si, GaAs and InP*, Science and Encyclopedia Publishers, Vilnius, 1994.

33 P. Yu and M. Cardona, *Fundamentals of Semiconductors*, Springer, Berlin, 1996.

34 S. S. Walavalkar, C. E. Hofmann, A. P. Homyk, M. D. Henry, H. A. At-

water and A. Scherer, *Nano Lett.*, 2010, **10**, 4423–4428.

35 D. Shiri, A. Verma, C. R. Selvakumar and M. P. Anantram, *Sci. Rep.*, 2012, **2**, 461.

36 F. Sangghaleh, B. Bruhn, T. Schmidt and J. Linnros, *Nanotechnology*, 2013, **24**, 225204.

37 A. S. Moskalenko, J. Berakdar, A. N. Poddubny, A. A. Prokofiev, I. N. Yassievich and S. V. Goupalov, *Phys. Rev. B*, 2012, **85**, 085432.

38 A. N. Poddubny, A. A. Prokofiev and I. N. Yassievich, *Appl. Phys. Lett.*, 2010, **97**, 231116.

39 K. Dohnalová, A. N. Poddubny, A. A. Prokofiev, W. D. A. M. de Boer, C. P. Umesh, J. M. J. Paulusse, H. Zuilhof and T. Gregorkiewicz, *Light: Science & Applications*, 2013, **2**, e47.

40 T. Kiba, Y. Mizushima, M. Igarashi, C.-H. Huang, S. Samukawa and A. Murayama, *Nanoscale Res. Lett.*, 2013, **8**, 223.

41 C.-H. Cho, C. O. Aspetti, J. Park and R. Agarwal, *Nat. Photon.*, 2013, **7**, 285–289.

42 J. J. Romero, M. J. Llansola-Portolés, M. L. Dell' Arciprete, H. B. Rodríguez, A. L. Moore and M. C. Gonzalez, *Chem. Mat.*, 2013, **25**, 3488–3498.

43 K. Dohnalová, K. Kůsová, O. Cibulka, L. Ondič and I. Pelant, *Phys. Scr.*, 2010, **T141**, 014011.

44 K. Žídek, I. Pelant, F. Trojánek, P. Malý, P. Gilliot, B. Hönerlage, J. Oberlé, L. Šiller, R. Little and B. R. Horrocks, *Phys. Rev. B*, 2011, **84**, 085321.

Electronic Supplementary Information

Complex study of the fast blue luminescence of oxidized silicon nanocrystals:
The role of the core

Lukáš Ondič,[1, 2, a)] Kateřina Kůsová,[1] Marc Ziegler,[2] Ladislav Fekete,[3] Viera Gärtnerová,[3] Vladimír Cháb,[3] Václav Holý,[4] Ondřej Cibulka,[1] Kateřina Herynková,[1] Mathieu Gallart,[2] Pierre Gilliot,[2] Bernd Hönerlage,[2] and Ivan Pelant[1]

[1)] *Institute of Physics, Academy of Sciences of the Czech Republic, v.v.i.,*
Cukrovarnická 10, 162 53, Prague 6, Czech Republic

[2)] *IPCMS, CNRS and Université de Strasbourg, 23, rue du Loess,*
F-67034 Strasbourg, France

[3)] *Institute of Physics, Academy of Sciences of the Czech Republic, v.v.i.,*
Na Slovance 1999/2, 182 21, Prague 8, Czech Republic

[4)] *Faculty of Mathematics and Physics, Charles University, Ke Karlovu 3,*
121 16 Prague 2, Czech Republic

[a)]Electronic mail: ondic@fzu.cz

1

I. STRUCTURAL AND MICROSCOPY CHARACTERIZATION

In this section, results of the structural characterization of silicon nanocrystals (SiNCs) investigated in this study are presented.
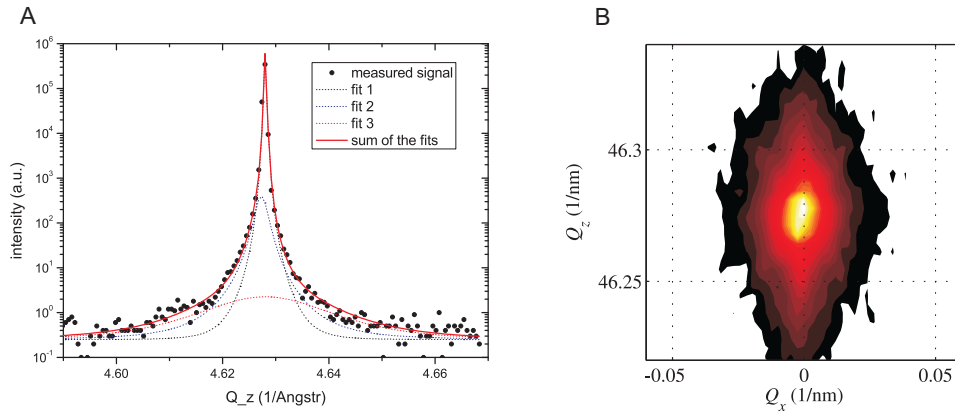
A. X-ray diffraction (XRD) spectra

Figure S 1: XRD spectra of the porous layer comprising interconnected SiNCs on the Si wafer. For details see the text.

XRD spectra were measured on as-prepared porous layer of SiNCs attached to the Si wafer. Figure S1A plots the omega/2 theta scan fitted with three functions. The narrower component is the substrate peak and the broadest component originates from the SiNCs. Figure S1B shows a reciprocal-space map. The vertical narrow streaks stems from the substrate, wheras the broader elliptical cloud is due to the nanocrystals. The fact that this cloud is vertically elongated implies that the shape of SiNCs is slightly anisotropic. However, the influence of inhomogeneous elastic deformation in the nanocrystals is neglected, which broadens the nanocrystals maximum too.

B.   Atomic force microscopy (AFM) measurements

Highly dilluted colloidal suspension of SiNCs in ethanol was drop-casted on a Si wafer and investigate by the AFM method. Figure 2 shows the representative image of a line profile taken from the measured AFM image. Figure 3 shows the AFM images taken at four different places on the sample.
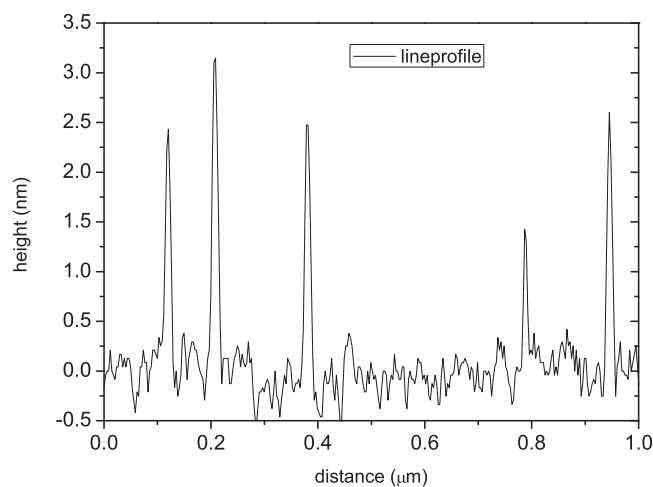

Figure S 2: A line profile taken from an AFM image measured on SiNCs drop-casted on a Si wafer. It manifests that the lateral dimensions of the nanoparticles are broadened due to the convolution with the AFM tip. On the other hand, the measured heights represents correct values.
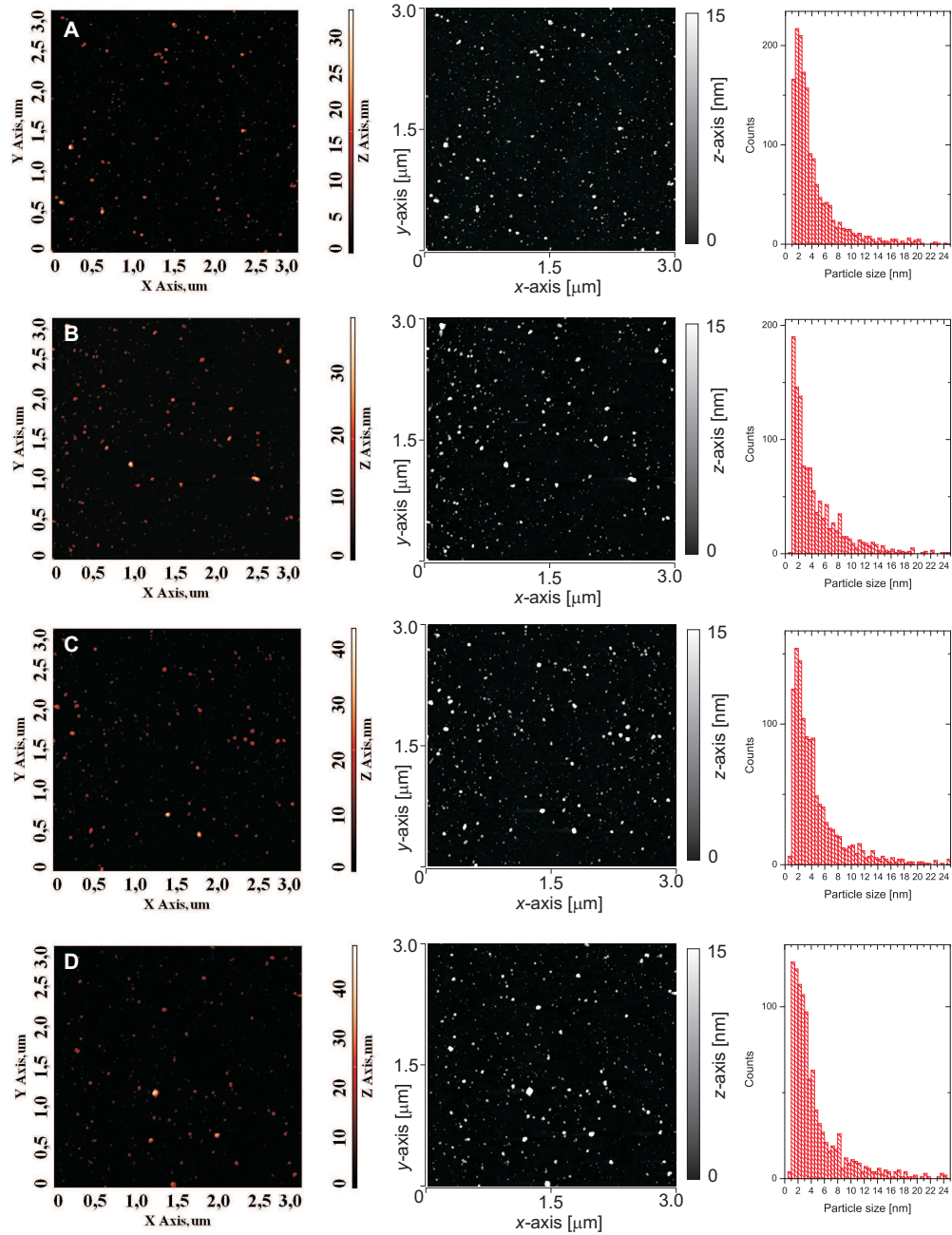
Figure S 3: AFM images from four different places on the sample. Each row comprises: (i) the AFM image with the z-axis normalized to the size of the tallest object, (ii) the AFM image (in blackwhite color scale) with the z-axis normalized to 15 nm in order to enhance the visibility of smaller SiNCs, and (iii) a histogram of the sizes of the objects derived from the images on the left.

4

II. OPTICAL CHARACTERIZATION

A. Measurements in the 2 μs temporal window.

The S-band photoluminescence (PL) spectra of silicon nanocrystals (SiNCs) at 4 K and at room temperature are shown in Figs. S4A and B, respectively. In order to compare the S-band intensity at the beginning and at the end of the 2 μs detection time window, signal was integrated over a 100 ns long time interval at the time delay of 100 ns (black curve) and 1.7 μs (red curve). Even though the signal is noisy, it is evident that the S-band PL intensity drops only negligibly for both temperatures (slightly more for the room temperature). This shows that the S-band does not fully relax between two consecutive excitation events, separated in time by a 5 μs interval.
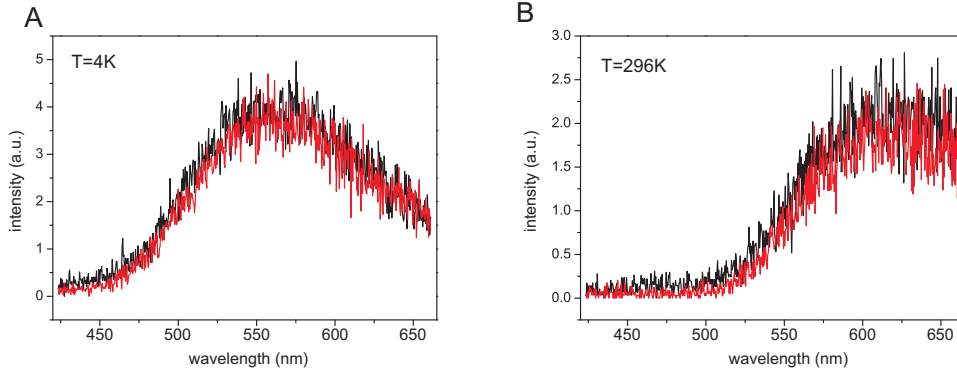

Figure S 4: The S-band emission spectra of SiNCs integrated over a 100 ns time interval, taken at different time delays: 100 ns (black curve) and 1.7 μs (red curve) after the excitation event at 4K (A) and room temperature (B).

B. Measurements in the 10 ns temporal window.

Normalized PL spectra taken at the beginning (integrated from 0 to 0.5 ns) and at the end (integrated from 8.5 to 9 ns) of the 10 ns time window are shown in Figs.S5 (A1) and (B1) for 4K and room temperature, respectively. Very similar F-band redshift with time was measured for both temperatures. In order to demonstrate that the red-shift of the F-band with time (at least in the first 10 ns after excitation) is not caused by the decrease
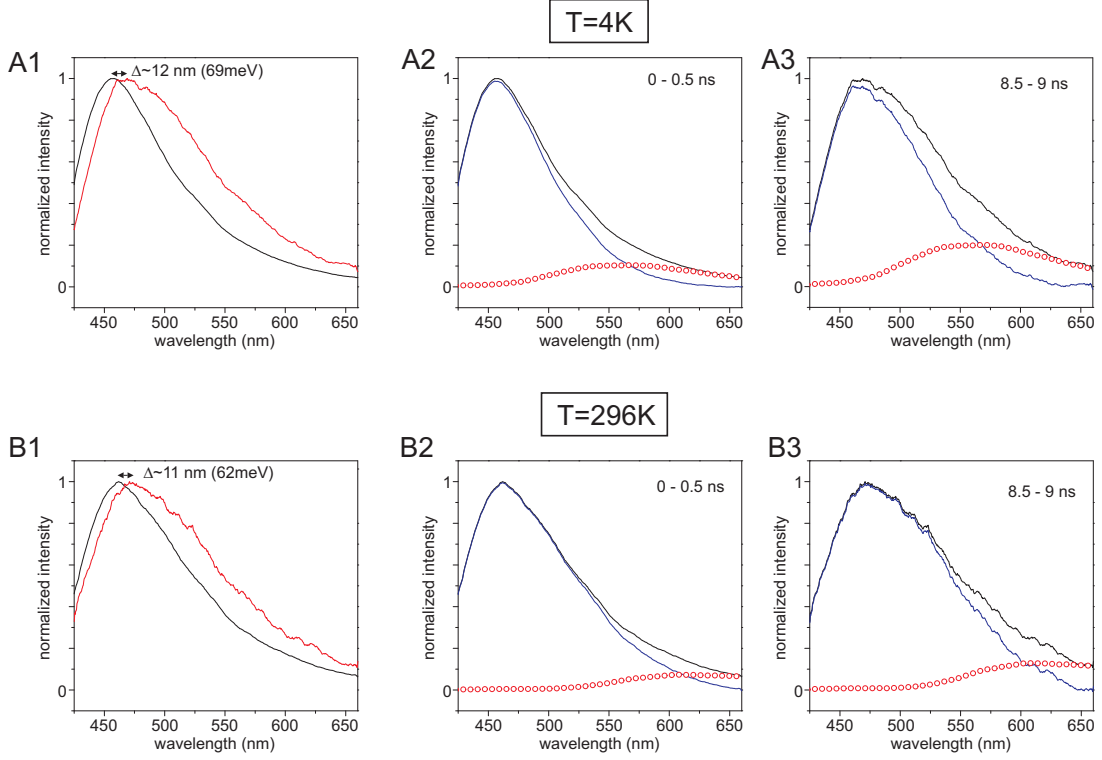
5

Figure S 5: The F-band's red-shift with time delay at 4 K (A1) and at 296 K (B1) is demonstrated by plotting the PL spectra integrated over the time window of 0-0.5 ns (black curve) and 8.5-9 ns (red curve). The A-row (B-row) comprises of spectra taken at 4 K (296K). (A2-3) and (B2-3) depict the difference spectra (blue curve) obtained as a difference between the measured F-band spectra (black curve) and the normalized S-band spectra (red opened circles) integrated over the time window $t = 0 - 0.5$ ns (A2, B2) and $t = 8.5 - 9$ ns (A3, B3).

of its intensity compared to the S-band intensity, we plot the difference (blue curve) of the F-band (black curve) and the S-band (red open circles) spectra (Figs.S5 (A2-3), (B2-3)). We assumed that the orange-red part (tail) of the F-band is caused by the S-band admixing and therefore, the S-band spectra were normalized so that their long-wavelength wing matches the F-band's orange tail. This gives us the upper estimate of the possible S-band's influence. PL peak positions of the difference spectrum and the measured F-band spectrum agree in the case of spectra taken at $t = 8.5 - 9$ ns at room temperature and at $t = 0 - 0.5$ ns at both K and room temperature, see Figs.S5(A2), (B2) and (B3). There is only a negligible

difference in the case of the spectra at $t = 8.5 - 9$ ns at 4 K, see Fig.S5(A3). Based on this observation, we can claim that the measured F-band's red-shift with time (at least in the first 10 ns after excitation) is its intrinsic property.

The F-band spectra integrated over the whole detection time window of 10 ns are shown in Fig.S6. The spectra are plotted in a temperature range going from 4 K to 296 K, with the step of 50 K. PL maximum shifts with increasing temperature from about 460 to 466 nm, which is approximately 35 meV. An energetically equal red-shift was also measured in the time window of 2 ns (see the main text).
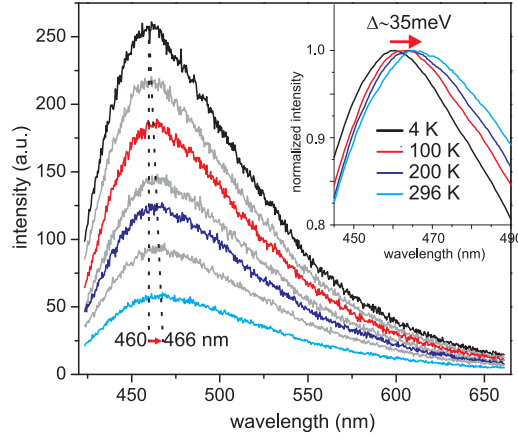

Figure S 6: Temperature dependent PL spectra integrated over a 10 ns detection window. Spectra start at 4K (black curve) and finish at 296K (light blue curve) with the step of about 50 K. The inset depicts normalized PL spectra zoomed-in around the signal maximum for selected sample temperatures.

III.   COMMENT ON THE TEMPERATURE-INDUCED SHIFT OF THE F-BAND SPECTRAL MAXIMUM

The interpretation of the F-band as a quasi-direct recombination between the levels near the Γ-point is also supported by the observed relatively low dependence of the F-band's spectral location on sample temperature. It can be partly explained by considering the effect of tensile strain on the Si direct band gap. It is well-known that the direct band gap of bulk Si becomes wider by about 30 meV upon 296K $\rightarrow$ 4 K cooling[1]. However, the situation is

not so straightforward in free-standing SiNCs with oxide-capping. In bulk Si, cooling of the material decreases the amplitude of Si-atom vibrations around their equilibrium positions, which results in a reduced overlap of electron clouds and thereby it induces shrinking of the conduction and valence band widths, increasing the bandgap value. This is, however, to a certain extent compensated by the increased overlap of the electronic wavefunctions caused by the fact that Si atoms are getting closer to each other upon cooling. In free-standing SiNCs covered with a SiO_2 shell, as used in the present study, on the one hand the cooling-induced contraction of the silicon lattice is substantially reduced because of the much larger thermal expansion coefficient of silicon compared to SiO_2, i.e. Si atoms in SiNCs are held back by the SiO_2 shell ($\rightarrow$tensile strain) and thus almost do not move compared to those in bulk when cooling down. This should lead to a larger temperature variation of the band gap in our SiNCs than in bulk Si.

On the other hand, because of the negative sign of the $a\left(\Gamma_{15}\right) - a\left(\Gamma'_{25}\right)$ deformation potential[2], the introduced tensile strain will act against the direct (F-band) band gap opening (Fig. 6 in the main text) and the balance between these two phenomena might explain the observed small value of ~ 35 meV for the temperature-induced shift. Moreover, the positive sign of the deformation potential pertinent to the silicon indirect band gap ($\Delta_{conduction} - \Gamma_{valence}$) makes the tensile strain cooperate with the cooling-induced widening of the indirect band gap (47 meV in bulk Si[2]) and, therefore, enables us to explain in a natural way the observed very large indirect (S-band) gap opening of 200 meV (Fig. 6 in the main text). In order to support this idea quantitatively, however, reliable data on thermal expansion coefficients of 3 nm SiNCs and/or theoretical computations would be needed.

REFERENCES

[1]A. Dargys and J. Kundrotas, *Handbook on physical properties of Ge, Si, GaAs and InP*, Science and Encyclopedia Publishers, Vilnius, 1994.

[2]P. Yu and M. Cardona, *Fundamentals of Semiconductors*, Springer, Berlin, 1996.

Chapter 4

Optical gain
of silicon nanocrystals

In this chapter, the measurements and simulations of optical gain in SiNCs are presented. First, the experimental method used to evaluate optical gain is described. Then the results of measurements carried out on various types of the SiNCs samples at room temperature are discussed. Finally, the possibility of enhancing optical gain by the photonic crystal approach is simulated.

4.1   Experimentals

Variable stripe length (VSL) technique [103] in combination with the Shifting excitation spot (SES) method [104] were applied to evaluate the presence of optical gain in different types of samples containing SiNCs.
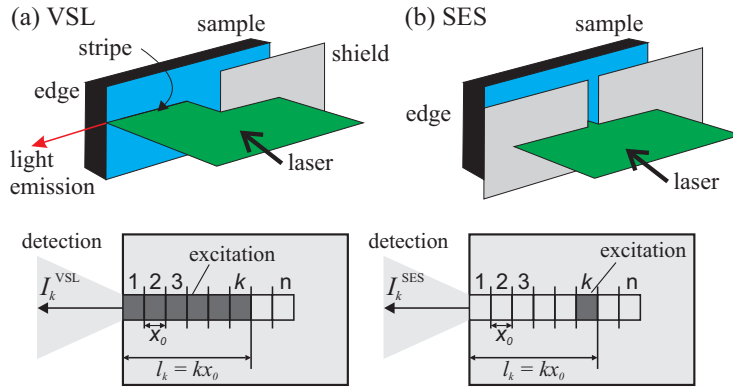

Figure 4.1: A simplified illustration of the VSL (a) and SES (b) experimental setup. The VSL stripe length is varied by placing a shield with sharp edge into the path of a laser beam focused by a cylindrical lens into the line-like shape. Two shields with sharp edges are employed in order to select only a small excitation spot (length x_0 and width ~ 30 μm) used with the SES technique. The length of the stripe l_k (or the position of the k-th spot) is adjusted by shifting the shield(s) along the stripe. In order to achieve a precise shifting step, the shields are attached to a motorized base controlled by a computer. Light emission is detected from the edge of a sample. Picture was adapted from Ref. [105].

In the VSL method, a sample is excited by an intense laser beam focused by a cylindrical lens into a narrow line, i.e. into an excitation stripe which is usually about 30 μm wide. The length $l_k = kx_0$ ($k = 0, 1, 2, ...$) of the excitation stripe is during the experiment increased by small steps $x_0 \sim 50$ μm starting from the sample edge (Fig. 4.1(a)). When nanocrystals are in an excited state,[1] the number of photons emitted via spontaneous emission, which propagate along the direction of the stripe, can be enhanced by stimulated emission characterized by the optical gain coefficient[2] g. The enhanced signal is then sometimes referred to as an Amplified spontaneous emission. This effect is, however, limited or can be even outweighed by losses due to free carrier absorption (FCA, characterized by a coefficient α_{FCA}), band-to-band reabsorption (coefficient α), and light scattering (coefficient K) on the sample imperfections. In the VSL stripe, the effect of band-to-band reabsorption decreases with increasing the number of excited NCs (i.e. with increasing pump power) and completely vanishes when all the NCs are excited (the saturation regime). However, if more than two electron-hole pairs were excited per NC, then the probability of Auger recombination would increase dramatically. Therefore,

---

[1]The special case is when all nanocrystals are in an excited state, i.e. in a saturation regime, in which no band-to-band reabsorption occurs.

[2]In the saturation regime, optical gain is equal to the band-to-band absorption coefficient α, i.e. $g = |\alpha|$

most probably the saturation regime with one electron-hole pair per excited nanocrystal is the ideal case for the light amplification.

The VSL signal I_k^{VSL} in a 1D model (stripe width $<<$ stripe length) collected from the sample edge in parallel with the stripe axis as a function of the excitation stripe length l_k is given as [105]

$$I_k^{\text{VSL}}(l_k, \lambda) = I_{SpE}(\lambda) \frac{1 - e^{-\alpha_{ind}(\lambda)l_k}}{\alpha_{ind}(\lambda)}, \tag{4.1}$$

where I_{SpE} stands for the spontaneous emission intensity per unit length and α_{ind} is the laser-induced absorption coefficient defined as

$$\alpha_{ind} = \alpha_{FCA} + (1 - \xi)\alpha + K - g. \tag{4.2}$$

Parameter $\xi \in \langle 0, 1 \rangle$ is a filling factor of NCs by the electron-hole pairs, i.e. in the "ideal" saturation regime[3] $\xi = 1$. In the case of $\alpha_{ind} < 0$, light (originating from the spontaneous emission) propagating in the direction of the VSL stripe will be amplified and the VSL signal will exponentially increase with increasing l_k. In the case of $\alpha_{ind} > 0$, the FCA and scattering dominate over stimulated emission and the propagating light will be attenuated. The parameter α_{ind} can be obtained by fitting the measured VSL signal with Eq. (4.1). In the saturation regime, g can be extracted from Eq. (4.2), provided losses α_{FCA} and K are known.

However, in the mode of evaluating the optical gain by using solely the VSL method, various gain-like artifacts can occur originating mostly from the discrepancy between the 1D VSL model and a real experimental setup [104]. Or, for example, sometimes very promising exponential-like increase at the VSL signal beginning may be caused by diffraction effects on the edge of the movable shield, which defines the stripe length. Consequently, VSL results are recommended to be compared with results of the SES method. In the SES experiment, only a small part of the stripe of length x_0 is used for excitation and PL emerging from this tiny excitation spot (approximately 50x30 μm^2) propagates to the sample edge through the non-excited area (see Fig. 4.1(b)). It is important to ensure that the size x_0 of the SES excitation spot is sufficiently small in order to prevent stimulated emission onset in it. Next, the experimental setup must be carefully adjusted such that the SES spot size x_0 is equal to its differential shifting step (so that two subsequent excitation spots k and $k+1$ neither do overlap nor are spatially separated from each other), and, moreover, that x_0 is equal to the step of increase of the VSL excitation stripe length, i.e. the value of x_0 is the same for the VSL and SES setups as depicted in Fig. 4.1. Furthermore, it is required to have constant pumping intensity along the whole VSL stripe. This is typically achieved by putting a beam expander (telescope) into a laser beam of the Gaussian cross-section, which expands the diameter of the beam profile and afterwards, the slit is employed to extract a flat intensity profile along the stripe axes.[4]

Typically, the detected SES signal follows the Beer-Lambert law given by the following equation:[5]

$$I_k^{\text{SES}} = x_0 I_{SpE} e^{-\alpha_0 l_k}, \tag{4.3}$$

$$\alpha_0 = \alpha + K, \tag{4.4}$$

where α_0 characterizes losses in the non-excited material due to band-to-band absorption α and scattering K, and l_k represents a distance of the excited segment from the sample edge

---

[3]Multi-exciton generation is not taken into account in this discussion.

[4]This operation is not required if the excitation laser beam itself has a flat profile (e.g. excimer lasers).

[5]As a consequence of the fact that instead of point-like excitation, the small rectangular area is excited, the typical Beer-Lambert law must by multiplied by the length of the excited segment x_0.

(see Fig. 4.1(b)). In order to compare the results of the VSL (I_k^{VSL}) and SES, the SES signal must be integrated over all excitation segments up to the stripe length l_k

$$I_k^{\text{intSES}} = \sum_{j=1}^{k} I_j^{\text{SES}}. \tag{4.5}$$

An explicit expression for I_k^{intSES} can be evaluated which will show a benefit mediated by comparing the VSL curve (Eq. (4.1)) with the integrated SES curve (Eq. (4.5)). Inserting Eq. (4.3) into (4.5) yields[6]

$$I_k^{\text{intSES}} = x_0 I_{SpE} \sum_{j=1}^{k} e^{-\alpha_0 j x_0} = x_0 I_{SpE} e^{-\alpha_0 x_0} \left(\frac{1 - e^{-\alpha_0 x_0 k}}{1 - e^{-\alpha_0 x_0}} \right) \approx I_{SpE} \left(\frac{1 - e^{-\alpha_0 l_k}}{\alpha_0} \right), \tag{4.6}$$

where we did a reasonable approximation $\alpha_0 x_0 \ll 1$ (usually $\alpha_0 \leq 50$ cm^{-1} in samples of good optical quality, and $x_0 = 50$ μm).[7]

Now, the experimental VSL curves and integrated SES (intSES) curves (evaluated from a large number of single SES measurements) can be compared in order to draw a quick conclusion about the presence or absence of optical gain in the sample under study. Based on the graphical comparison of the two curves, one of the following situations can occur:

1. **The curves overlap with each other**, i.e. $I_k^{\text{VSL}} = I_k^{\text{intSES}}$.

   Then from comparison of Eq. (4.1) and Eq. (4.6) immediately follows that

   $$\alpha_{ind} = \alpha_0 > 0,$$

   which means (using Eq. (4.2)) that

   $$\alpha_{FCA} + (1 - \xi)\alpha + K > g.$$

   Therefore, in this case, the sample does not exhibit positive net optical gain defined as $G \equiv g - \alpha_{FCA} - (1 - \xi)\alpha - K$, even though the gain g itself can be positive, and spontaneous emission is attenuated instead of to be amplified when propagating inside the excited stripe. Furthermore, in case of saturation (all SiNCs are excited, i.e. $\xi = 1$) the α magnitude determines the maximal optical gain coefficient $g = |\alpha|$ and it directly follows from relation $\alpha_{ind} = \alpha_0$ that

   $$\alpha_{FCA} + K - g = \alpha + K$$
   $$\alpha_{FCA} - g = g$$
   $$\alpha_{FCA} = 2g. \tag{4.7}$$

2. **VSL curve above intSES**, i.e.

   $$\frac{1 - e^{-\alpha_{ind} l}}{\alpha_{ind}} > \frac{1 - e^{-\alpha_0 l}}{\alpha_0},$$

   where for brevity $l_k = l$. Two cases may happen:

---

[6] $\sum_{n=0}^{N} a^{bn} = \frac{1 - a^{b(N+1)}}{1 - a^b}$

[7] $e^{-\alpha_0 x_0} \to 1$ for $\alpha_0 x_0 \to 0$ and $1 - e^{-\alpha_0 x_0} \sim 1 - (1 - \alpha_0 x_0) = \alpha_0 x_0$ for $\alpha_0 x_0 \to 0$

(a) $\alpha_{ind} < 0$, i.e. $\alpha_{FCA} + (1 - \xi)\alpha + K < g$ (gain exceeds losses).

By denoting $-\alpha_{ind} \equiv G = g - \alpha_{FCA} - (1 - \xi)\alpha - K > 0$, the above equation reads

$$\frac{e^{Gl} - 1}{G} > \frac{1 - e^{-\alpha_0 l}}{\alpha_0}.$$

Next, by denoting $-\alpha_0 \equiv G' < 0$ it follows that

$$\frac{e^{Gl} - 1}{G} > \frac{e^{G'l} - 1}{G'},$$

which is valid for any $G > 0 > G'$ since the function $(e^{xl} - 1)/x$ is monotonously increasing convex function for $-\infty < x < \infty$ and $l > 0$. Therefore, net optical gain $G > 0$ (and thus signal amplification) is present in the sample if $\alpha_{ind} < 0$.

If G is large enough (i.e. $g \gg \alpha_{FCA} + (1 - \xi)\alpha + K$, $G \approx g$) so that $\exp(Gl) \gg 1$, from Eq. (4.1) then follows that

$$I_k^{\text{VSL}} = I_{SpE} \frac{e^{Gl} - 1}{G} \simeq e^{Gl}.$$

Therefore, the VSL signal increases exponentially with stripe length l and G can be easily extracted as a fitting parameter of the above equation.

(b) $\alpha_{ind} > 0 \wedge \alpha_{ind} < \alpha_0$

It immediately follows that both curves, VSL and intSES ones, are of concave shape. Furthermore, it holds (from Eq. 4.2) that $\alpha_{FCA} + (1 - \xi)\alpha + K > g$, thus no net optical gain is present and no conclusion can be made concerning the occurrence or absence of material gain g unless accurate data on α_{FCA} and K are known.

3. **VSL below intSES**, i.e.
$$\frac{1 - e^{-\alpha_{ind} l}}{\alpha_{ind}} < \frac{1 - e^{-\alpha_0 l}}{\alpha_0}.$$

The above noted monotonous increase of the function $(e^{xl} - 1)/x$ implies that

$$\alpha_{ind} > \alpha_0 > 0.$$

It directly follows that $\alpha_{FCA} + (1 - \xi)\alpha + K > g$ but also that $\alpha_{FCA} > 2g$ (in the saturation regime, $\xi = 1$). Therefore, much like in the cases (1) and (2b), no amplification of PL occurs. Nevertheless, in principle it is still possible to draw some quantitative information on material gain g, provided one manages to work in the saturation regime ($\xi = 1$). In this case $g = \alpha_{FCA} + K - \alpha_{ind}$, as it follows from Eq. (4.2). The coefficient α_{ind} is relatively easy to obtain as a fitting parameter in Eq. (4.1) or via the construction of the so-called differential VSL described in Ref. [105]. However, data on α_{FCA} and K have to be acquired from complimentary experiments, which is not an easy task, though. Upper bound for g can be also set as $g < \alpha_{FCA}/2$.

To summarize, the condition for the presence of net optical gain (i.e. situation when optical gain outweigh the losses) is that the experimental VSL curve is positioned above the intSES curve together with the convex shape of the VSL signal. The signal increase can be fitted with Eq. (4.1) to determine the value of net optical gain as demonstrated for laser dye in Paragraph 4.2.1. The exponential-like growth, however, is sometimes hard to notice in the

measured signal in the case of materials with low optical gain and/or large losses. As a consequence, a simple fit of the VSL data with Eq. (4.1) does not yield a reliable answer and additional methods must be used to determine the value of net optical gain. Net optical gain should be also confirmed via observation of narrowing of the VSL spectra for longer stripes, by observing super-linear increase of the detected VSL signal vs pump intensity and possibly also by shortening of the emission decay time.

As pointed out above, the material optical gain g can be present in the sample even if the VSL curve is equal or below the intSES curve. But in this case, losses of the system prevent the enhancement of the signal via stimulated emission. The value of optical gain coefficient can be determined in case the losses are precisely evaluated as shown by Ha et al. in Ref. [105] and discussed in this chapter in Section 4.2.2 for the samples containing the SiNCs/SiO$_2$ multilayers (which were, however, only marginally studied in this thesis).

Finally, it should be stressed that even if the VSL curve is positioned above the intSES curve, it does not automatically imply the presence of net optical (see the case 2(b) above).

4.2 Results and Discussion

In this section, optical gain of different samples is studied under different excitation conditions employing the VSL and SES methods. First, the correctness of the methods is demonstrated on laser dye Coumarin 480 (C480). Then, the methods are applied to samples containing SiNCs, namely SiNCs/SiO$_2$ multilayers, colloidal oxide- and organically-passivated SiNCs, and finally to the SiNCs embedded in a sol-gel SiO$_2$-matrix. All experiments presented in this section were performed at room temperature.

4.2.1 Laser dye

Laser dye Coumarin[8] 480 was chosen to test the VSL and SES methods due to its ability to exhibit stimulated emission under excitation in the UV spectral region. The sample was prepared by mixing the C480 powder with ethanol (2 mg/ml) yielding a yellow clear (no-scattering) solution. The typical PL spectrum of this sample under 355 nm nanosecond excitation peaks at about 475 nm (black curve in Fig. 4.2(b)). The detection was performed in a relatively short 100 ns detection window due to fast dynamics of the PL signal (see Chapter 3, Section 3.1 for details on the experimental setup).

The results of the VSL and SES measurements are summarized in Fig. 4.2 for two excitation energy densities E_{exc}: 0.04 mJ/cm^2 (first row) and 0.4 mJ/cm^2 (second row). Under low pumping energy density the VSL curve lies above the intSES one and both curves are of concave shape (Fig. 4.2(a)), therefore the above discussed case (2b) occurs and no net optical gain is present. Spectra shown in Fig. 4.2(b) indicate, however, that the material is close to the amplification ("lasing") threshold because the VSL spectrum at the stripe length of 3 mm gets slightly narrower compared to the SES spectrum. Nevertheless, this could be caused also by reabsorption of the blue part of the PL spectrum in the excitation stripe. Under high excitation energy density of 0.4 mJ/cm^2 the VSL curve lies also above the intSES curve but, in addition, in this case it grows exponentially with increasing stripe length (Fig. 4.2(c)). Thus the case (2a) applies—net optical gain is present beyond any doubt, as confirmed also by substantial line narrowing in Fig. 4.2(d). The value of net optical gain for this specific excitation energy is $G \sim 18$ cm^{-1} as determined by fitting the VSL curve with Eq. (4.1). (Here instead of FCA, triplet-triplet absorption and light scattering are factors acting against

---
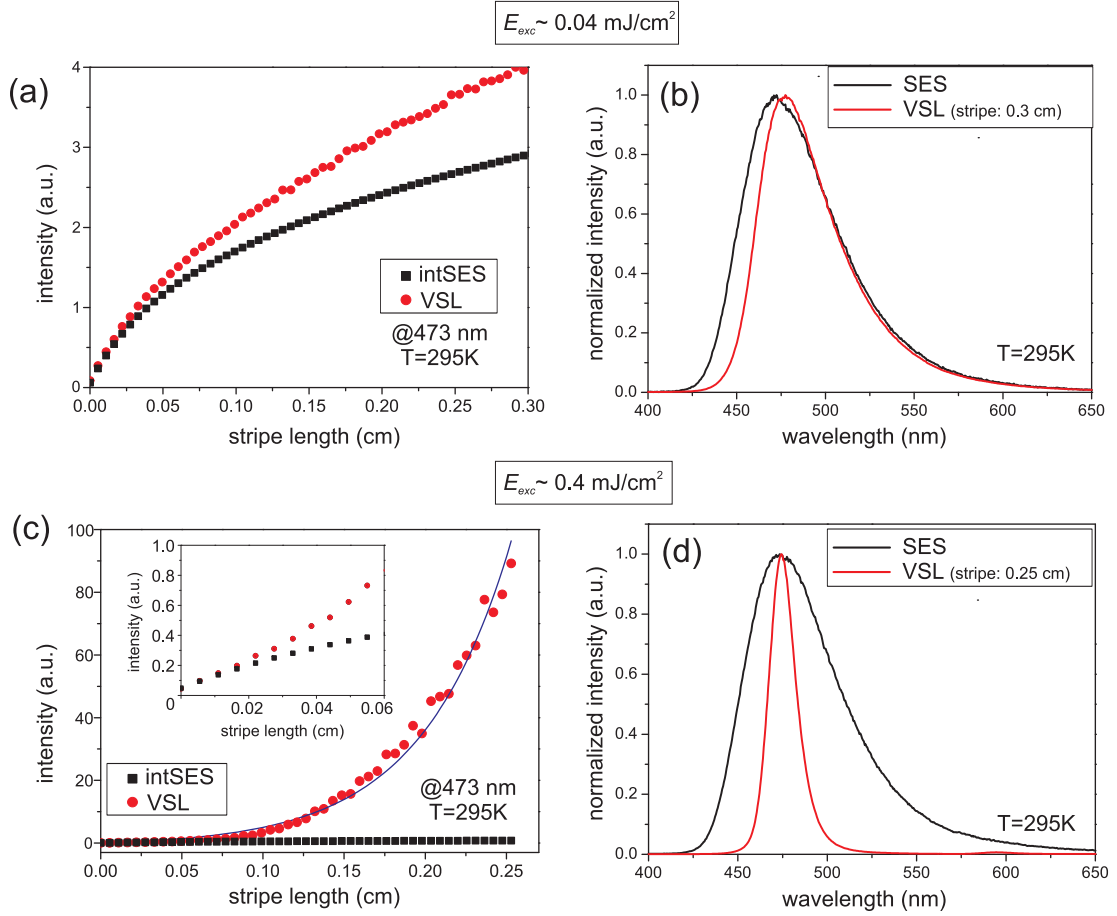
[8]Manufactured by Exciton company.

Figure 4.2: The room-temperature results of the VSL and SES methods applied on organic laser dye C480 pumped with nanosecond laser pulses with two excitation energy densities E_{exc}: 0.04 mJ/cm^2 (first row) and 0.4 mJ/cm^2 (second row). (a, c) VSL (red) and intSES (black) signal as a function of the excitation stripe length taken at the PL maximum at 473 nm. Inset in (c) shows a zoom-in on the beginning of the signal. The presence of stimulated emission is evidenced by the convex shape (exponential-like growth) of the VSL signal in (c), which is fitted using Eq. (4.1) (blue curve). (b, d) PL spectra measured with the SES spot near the edge of the sample and with the VSL stripe of the length of 3 and 2.5 mm, respectively.

light amplification.) The overlap of the VSL and intSES curves for the short lengths of the stripe, which is clearly visible in the inset of Fig. 4.2(c), evidences that the size of the SES spot is equal to the VSL differential shift step x_0. This must be fulfilled in order to obtain correct results, as already stressed in Section 4.1. Videos showing measurements with the SES and VSL methods on the C480 solution are attached to this thesis. One of them also demonstrates the stimulated emission onset in the C480 sample obtained with the VSL method. See Appendix for more information.

In order to obtain information on the time evolution of the stimulated emission signal, the femtosecond excitation with an appropriate fast detector (laser Tangerine and a streak camera Hamamatsu, see Chapter 3, Section 3.1 for details) were used with the VSL/SES experimental setup and applied again to the organic dye C480. The experiments were conducted for one excitation energy density and for several stripe lengths. Figure 4.3(a) shows the VSL spectra obtained by integrating the detected time-resolved signal over the entire 1 ns long detection
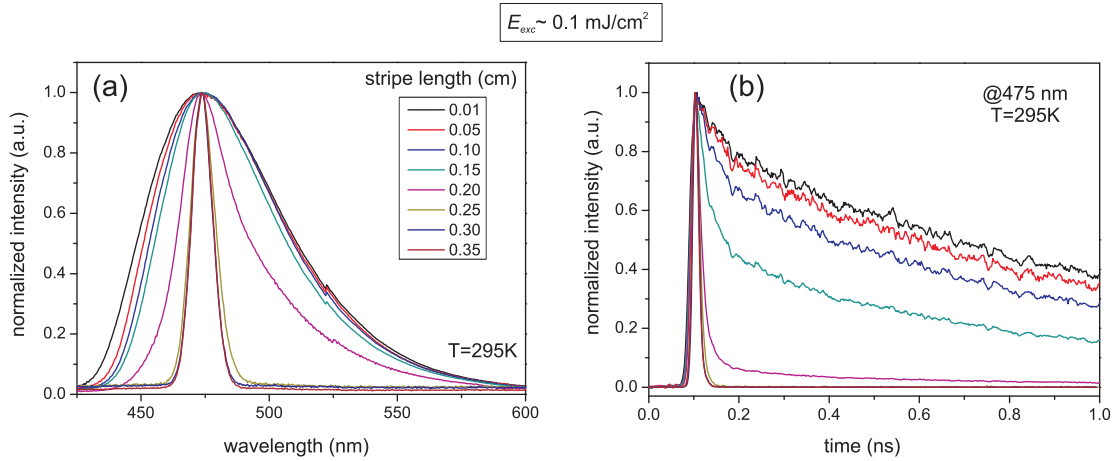
$E_{exc} \sim 0.1$ mJ/cm^2

Figure 4.3: The room-temperature results of the VSL and SES methods applied on organic laser dye C480 pumped with femtosecond laser pulses of energy density $E_{exc} \sim 0.1$ mJ/cm^2. (a) VSL spectra as a function of the excitation stripe length (signal integrated over the 1 ns detection window). (b) Time decay of the PL signal at ~475 nm measured in 1 ns detection window. The presence of stimulated emission in the stripe is evidenced by obvious narrowing of the spectra and shortening of the decay time with increasing the excitation stripe length.

window. The onset of the stimulated emission is evidenced by narrowing of the VSL spectra with increase of the stripe length. This is accompanied also by shortening of the PL decay time down to the limit of the detection system as shown in Fig. 4.3(b).

4.2.2 SiNCs/SiO$_2$ multilayers

Samples consisting of SiNCs/SiO$_2$ multilayers (100 of NC-rich layers) were prepared by chemical vapor deposition and subsequent thermal annealing by the group of Prof. M. Zacharias in Freiburg (Germany) [96]. Two types of the samples differing in the thickness of the SiNCs-rich layer, which basically defines the size of NCs, were investigated by the VSL and SES methods. Namely, these were the samples with 2 and 3 nm sized SiNCs as evidenced by the HRTEM method (not shown). However, due to the qualitatively similar results for both samples, only a series of measurements carried out on the sample with the thickness of the layers of 2 nm are presented. Luminescence of the sample is spectrally located at the red end of the visible region (black curve in Fig. 4.4). Photoluminescence quantum yield is very high (up to 90%). Moreover, it is transparent to eye, which implies that the scattering losses are minimal, i.e. $K \sim 0$ (also verified by transmission measurements—not shown). As discussed below, FCA is probably the main loss mechanism depleting population inversion of the excited carriers and so preventing optical amplification.

Samples were pumped with the 355 nm nanosecond pulses employing three different excitation energy densities E_{exc}: 7, 50 and 500 mJ/cm^2. The lowest one was chosen so as to assure still detectable SES signal with a reasonable signal-to-noise ratio.

Comparison of the PL emission spectra measured with the SES (single excited segment x_0 and VSL (stripe length of 0.25 cm) methods at the highest excitation energy density is shown in Fig. 4.4.
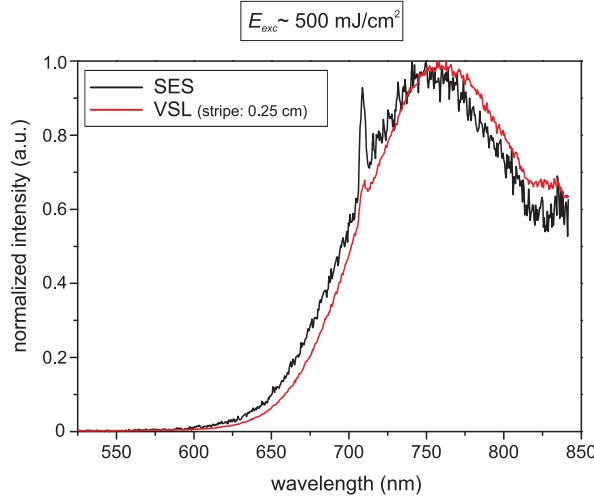

Figure 4.4: Normalized room-temperature emission spectra of the SiNCs/SiO$_2$ multilayers (one layer ~ 2 nm thick) on a silica substrate measured with the VSL and SES methods (excitation energy density $E_{exc} \sim 500$ mJ/cm^2). The peak at 710 nm is the second order of the pump laser line.

Summary of the VSL and SES results of the SiNCs/SiO$_2$ sample is shown in Fig. 4.5 (each column represents one excitation energy density). The first row (a-c) presents experimentally obtained VSL data (red circles) and SES curves (green triangles) taken at the signal spectral maximum at around 757 nm. The integrated SES curves computed from the measured ones using Eq. (4.5) are also plotted in Figs 4.5(a-c) as black squares. It is evident that the experimental results for the case of $\lambda \sim 757$ nm belong either to the above discussed (Section 4.1) case (1) (i.e. VSL=intSES, Fig. 4.5(a)) or to the case (3) (i.e. VSL<intSES, Figs. 4.5(b,c)). The very same holds true also for the whole emission spectrum as evidenced by the intensity maps of difference between VSL and intSES curves as a function of the wavelength and the
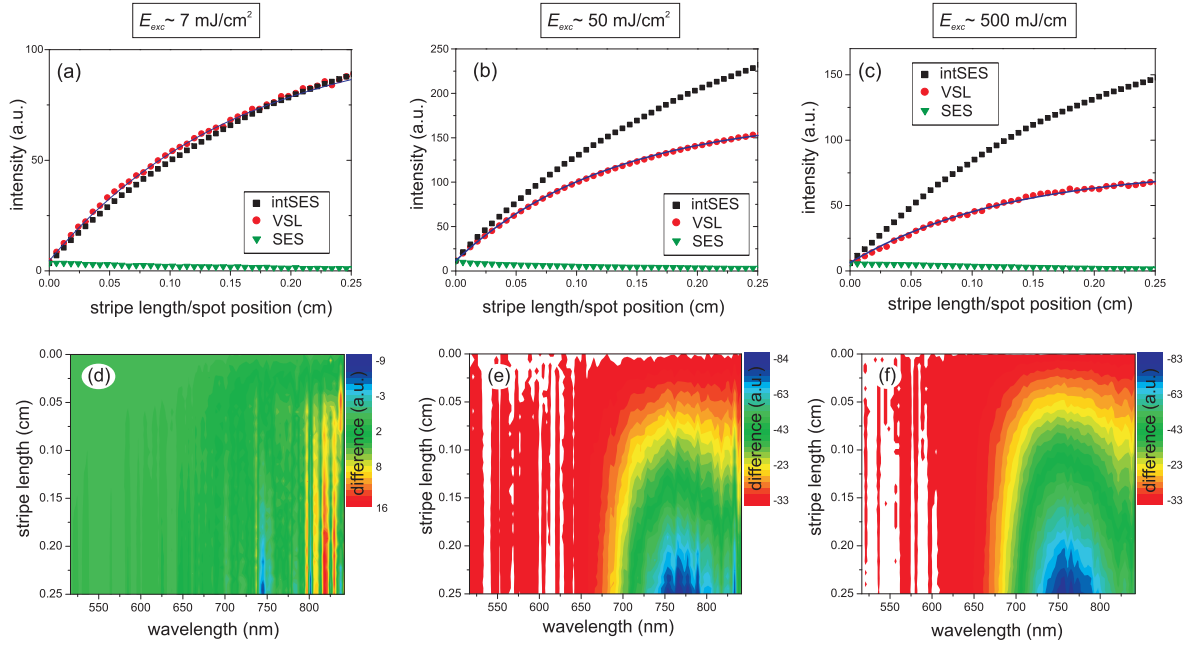
Figure 4.5: The results of the room-temperature VSL and SES measurements performed on SiNCs/SiO$_2$ multilayers (one layer $\sim$ 2 nm thick) deposited on a silica substrate. Excitation energy densities used in the experiments were 7 mJ/cm^2 (first column), 50 mJ/cm^2 (second column), 500 mJ/cm^2 (third column). (a-c) VSL (red), SES (green) and integrated SES (black) signal as a function of the stripe length/spot position. Blue curves depict the results of fitting the VSL curves with the Eq. (4.1). (d-f) Difference between the VSL and integrated SES curves as a function of the stripe length and wavelength.

excitation stripe length shown in Figs. 4.5(d–f).

These results points towards the fact that the sample of SiNCs/SiO$_2$ (100 NC-rich layers, 2 nm layer thickness) exhibits no net optical gain under a nanosecond UV (355 nm) pumping. This conclusion is also supported by the spectra displayed in Fig. 4.4, in which no line narrowing in the VSL with respect to the SES spectra occurs.

An attempt was made to get some insight into whether or not a material gain g, expressed from Eq. (4.2) as $g = \alpha_{FCA} + (1 - \xi)\alpha - \alpha_{ind}$, is present in the studied sample (supposing scattering losses $K = 0$). By fitting the relevant VSL curves by Eq. (4.1), values of α_{ind} can be determined and the results of the fits (blue curves in Figs. 4.5(a–c)) are summarized below

$$\alpha_{ind}(E_{exc} = 7 \text{ mJ/cm}^2) = 6.4 \text{ cm}^{-1}$$

$$\alpha_{ind}(E_{exc} = 50 \text{ mJ/cm}^2) = 7.7 \text{ cm}^{-1}$$

$$\alpha_{ind}(E_{exc} = 500 \text{ mJ/cm}^2) = 7.7 \text{ cm}^{-1}.$$

Free carrier absorption coefficient α_{FCA} can be estimated from data on FCA cross-section in SiNCs (σ_{FCA}) published by Kekatpure and Brongersma [54]. It can be supposed that $\alpha_{FCA} = \sigma_{FCA} n_{NC} \xi$, where n_{NC} is volume density of NCs. Based on the experimental absorption data obtained for the sample under study, the value of n_{NC} was estimated to be $\sim 10^{19}$ cm^{-3}. As a consequence of high pumping intensity, the filling factor is close to unity, i.e. $\xi = 1$. Now, considering $\sigma_{FCA}(\lambda = 750 \text{ nm}) \approx 2\text{x}10^{-17}$ cm^2 [54], it follows that $\alpha_{FCA} \approx 200$ cm^{-1}. And because $\alpha_{ind} \approx 10$ cm^{-1}, from $g = \alpha_{FCA} - \alpha_{ind}$ we get relatively high optical gain $g \approx 190$ cm^{-1}. This number is, however, weighted by a large error coming from

an experimental inaccuracy in determining the coefficient σ_{FCA}. Nevertheless, optical gain g must scale with FCA absorption coefficient, as will be shown by the following reflection. In the SES experiment, light propagating towards the edge of the sample is not influenced by FCA losses because it passes through the non-excited volume. This is completely inverse in the case of the VSL experiment. Light propagating along the excitation stripe will be absorbed by free-carriers, however this is to a some extent compensated (VSL=intSES) or outweighed (amplification) by the positive optical gain. If there were no gain present, the VSL signal would be then much lower than the intSES signal. Therefore, even if the estimated value of g may appear very high, it does not have to be unrealistic.

It should be also noted that from the relation $\alpha_{FCA} = 2g$ (Eq. (4.7)), which holds for the saturation regime ($\xi = 1$), it directly follows $g \approx 100$ cm^{-1}. This value differs (but in fact not too much) from the above estimate of $g \approx 190$ cm^{-1}. The difference can be due to the fact that not all SiNCs in the sample fulfill exactly the condition $\xi = 1$.

Conclusions

The VSL/SES experiments show unambiguously that the SiNCs/SiO$_2$ multilayers (100 of NC-rich layers, one layer thickness of 2 and 3 nm) do not exhibit net optical gain under nanosecond optical excitation at room temperature. Possible material gain, if any, is overwhelmed by FCA. This absorption is generally believed to hinder optical amplification in bulk silicon, and it turns out that its adverse effect persists even in these investigated SiNCs. This demonstrates that high PL quantum yield alone (present in the samples under discussion) does not guarantee the occurrence of optical amplification. Since the coefficient of FCA scales quadratically with PL wavelength [54], SiNCs emitting at significantly shorter wavelengths than ~ 750 nm may be expected to be better candidates.

4.2.3 Colloidal SiNCs

Silicon nanocrystals fabricated by electrochemical etching of a Si-wafer (see Chapter 3 for details on the fabrication method) can be prepared to emit light with wavelengths down to $\sim$ 600 nm. Therefore, optical gain in these samples was evaluated. The experimental setup was based on the Tangerine femtosecond laser, the VSL and SES setup, and the streak camera detector. Samples in the form of a colloidal dispersion of SiNCs were investigated. The repetition rate of the laser was set to be 1 kHz in order to let the sample cool down between two consecutive excitation events and so to prevent burning and degradation of SiNCs. In addition, the dispersion was mixed using a magnetic stirrer in order to minimize photodegradation. The first type of sample comprised the so-called "white" SiNCs powder having the PL emission maximum at around 600 nm (under UV pumping), diluted in UV ethanol (2 mg of the powder per 200 μl of ethanol).[9] Even after the process of ultrasonication, the colloidal sample contained not only well-separated single SiNCs but still comprised some amount of SiNCs aggregates. Therefore it was not optically clear, which caused scattering losses to the propagating light. The second type of sample was prepared from the powder of SiNCs which underwent a sophisticated post-etch treatment: periodically repeated UV (325 nm) irradiation under intense mixing of the colloid followed by careful filtration (for details see Ref. [55]). The product of this process is an optically clear colloidal dispersion with intense yellow luminescence peaked at $\sim$ 570 nm. The UV irradiation triggers photochemical changes on the sample surface, specifically, the oxide-passivation is substituted with organic species. Besides the blueshift of the PL band (600 $\rightarrow$ 570 nm), the decay dynamics changes dramatically. The dynamics switches from the microsecond to nanosecond time scale when the surface passivation is changed from oxide to organic methyl ($-CH_3$) capping [55].

Oxide-passivated SiNCs in ethanol

The idea behind the investigation presented below was to extend the optical gain measurements carried out recently by Žídek et al [53]. The authors of Ref. [53] derived from the time-integrated measurements that ultrafast ($<$ 1 ps) net optical gain with values up to 200 cm^{-1} occurred in the colloidal SiNCs sample which is studied in this paragraph (designated as a sample "OXW" in Ref. [53]). The amplified signal, however, accounted for less than 1% of the overall time-integrated signal (due to the long microsecond decay of the spontaneous emission signal). Therefore, by adding a temporal resolution into detection, more precise information on the ultrafast gain may be obtained. We employed a streak camera for the signal detection, which allowed us to add a high temporal resolution into the VSL/SES gain measurements. One of the most important conditions to observe the ultrafast signal amplification is excitation with short and powerful pulses in order to create, in a short time, the instant population inversion between the energy levels from which the transient stimulated emission occurs before the upper level depopulates.

The results of the VSL and SES experiment conducted on the SiNCs/ethanol colloidal sample at room-temperature are shown in Fig. 4.6. As the aim of this study was to look at the ultrafast gain present shortly after the excitation, the shortest available time window of 1 ns was set for detection with the streak camera. To evaluate the results, the measured signal was always integrated over the entire detection window in order to increase signal-to-noise ratio. To further decrease the noise, the SES spot size along with the VSL differential step x_0 were increased to 200 μm.

---

[9]UV ethanol accounts for only a marginal PL signal in the overall detected PL because its PL intensity is much lower compared to that of SiNCs.
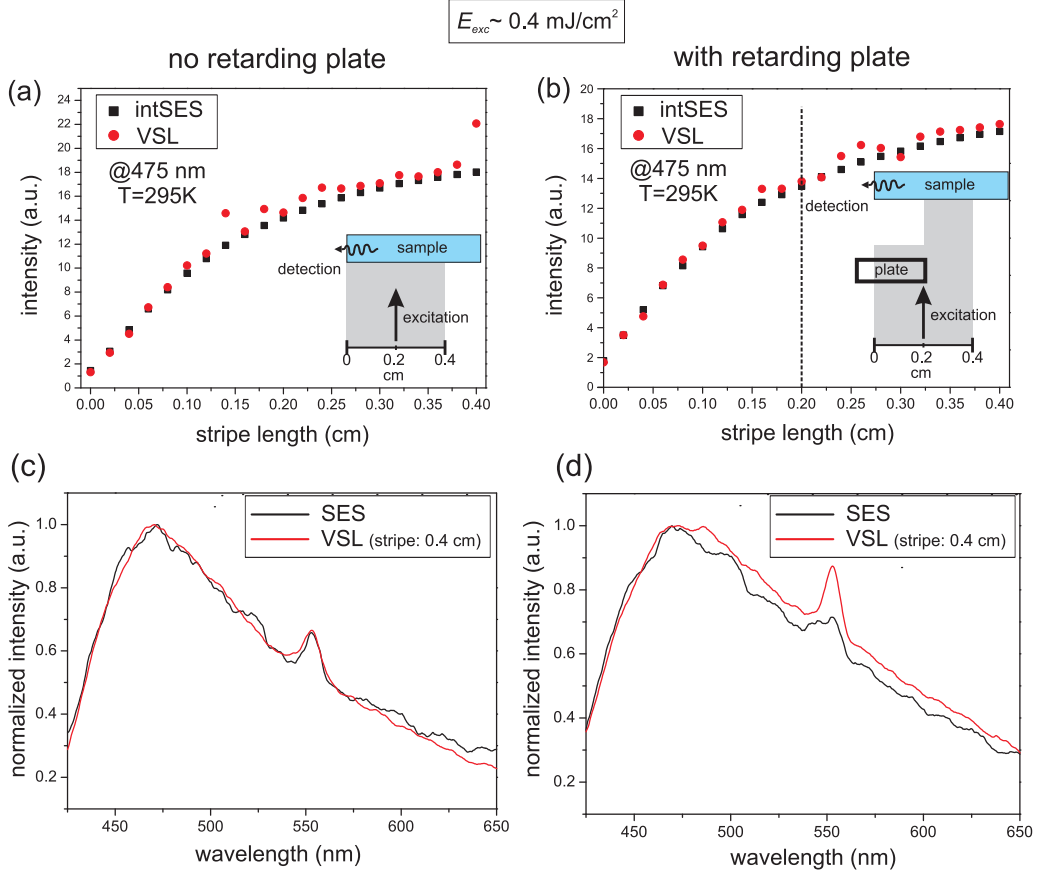
Figure 4.6: The room-temperature results of the VSL and SES measurements performed on the oxide-passivated SiNCs dispersed in ethanol excited with femtosecond pulses ($E_{exc} \sim 0.4$ mJ/cm^2). The first column contains data obtained with the conventional experimental setup (inset of (a)) and the second column shows results with a retarding (delay) plate inserted in the path of the excitation beam (inset of (b)). The time-resolved signal was detected in a 1 ns temporal window by employing a streak camera detector. The plotted VSL (red) and intSES (black) signal (a, b) was extracted from the emission spectra integrated over the entire detection time window. The dashed vertical line in (b) depicts the position of the edge of the retarding plate. (c, d) SES spectrum (black) detected with the SES spot positioned close to the sample edge compared to the VSL (red) signal measured for the stripe length of 4 mm. Spectra are integrated over the entire detection time window, smoothed and normalized to the signal maximum.

Even for the highest available excitation energy density of 0.4 mJ/cm^2, the VSL and integrated SES curves as a function of the excitation stripe length were found to be almost identical (Fig. 4.6(a)). Taken together with the fact that the shape of the VSL (stripe length of 4 mm) and SES spectra is also similar (Fig. 4.6c), it follows that no net ultrafast optical gain is present in the sample under investigation.

Additional measurements with a retarding glass (quartz) plate placed into the path of the excitation laser beam (see the inset of Fig. 4.6(b)) did not reveal any sign of transient stimulated emission in the VSL signal either—see Figs. 4.6(b,d). The quartz plate was inserted into the beam in order to introduce a time delay of about 7 ps to delivering excitation energy to the first half of the stripe $(0 - 0.2$ cm$)$ with respect to the rest of the stripe $(0.2 - 0.4$ cm$)$. The idea behind such a setup, which was introduced in Ref. [53], is very simple and is based on the following concept. In our sample, light needs approximately 5 ps to pass over 1 mm of

the stripe length (refractive index of the sample $\sim$ 1.4). It therefore follows that in the case of the transient ultrafast stimulated emission, the signal cannot be amplified any more after passing very short distance of less than 1 mm due to the already depleted upper (excited) level. By delaying properly the delivery of excitation closer to the sample edge, the number of photons propagating within the stripe towards the sample edge can be further enhanced via stimulated emission in the later-excited stripe region. Even if some increase in the VSL signal compared to the intSES signal starting from 0.2 cm can be recognized in Fig. 4.6(b), it can be hardly interpreted as the result of stimulated emission because a very similar structure can be found in the VSL curve measured without the delay plate (Fig. 4.6(a)) at the same stripe length. It must be therefore rather connected with the experimental setup itself.

The only plausible explanation of not seeing any signal amplification in the studied sample is the insufficient peak power of the excitation pulses. The excitation energy density used in the above presented experiment is comparable to that employed in the measurements discussed in Ref. [53]. However, the length of the pulse is about 3.5 times larger in the present study, which is probably crucial. It follows that the peak power is lower and less electrons are excited in the given time instant. Due to the ultrashort lifetime of the excited electronic level, population inversion is not achieved and therefore stimulated emission cannot occur under the experimentally available excitation conditions.

Methyl-passivated SiNCs in xylene

The fabricated organically-passivated SiNCs compared to the oxide-passivated ones have many physical properties which should favor the occurrence of stimulated emission: (i) the PL emission band peaking at about $\sim$ 570 nm $\rightarrow$ lower FCA losses, (ii) fast nanosecond radiative lifetime [55] much like as in laser dyes, (iii) the transparent colloidal form $\rightarrow$ negligible scattering losses. However, the main drawback seems to be the low concentration of these samples, which is day by day only very slowly increased due to the time-consuming fabrication process.

The VSL and SES spectra were measured for three different excitation energy densities ($0.1E_{exc}$(max), $0.5E_{exc}$(max) and E_{exc}(max), where E_{exc}(max) = 52 μJ/cm^2 per pulse) in two detection time windows: 10 ns and 1 ns. Because the decay constant of the PL signal is $\sim$ 2 ns (as derived from a single exponential fit—see Fig. 4.7(d)), the 10 ns long detection window covered the whole PL signal of the sample. To compare the outputs of the VSL and SES method, the PL signal was typically integrated over the whole detection window in order to minimize noise. This integrated signal, stored for each length of the excitation stripe into a two dimensional array, can be plotted as a 2D map of the signal intensity as shown for the highest excitation energy density in Fig. 4.7(a). The horizontal cut then yields the VSL spectrum at a particular stripe length, while the vertical cut is the VSL signal at a particular wavelength. A comparison of the normalized VSL signals (detected with different excitation energy densities) and the integrated SES signal taken at the spectral maximum of the PL spectrum ($\sim$ 575 nm) is plotted in Fig. 4.7(c). Clearly, no net optical gain is present in the sample as the intSES curve lies above the VSL curves for the excitation energy densities of $0.1E_{exc}$(max) and $0.5E_{exc}$(max) or is identical to the VSL curve in the case of the highest excitation energy density E_{exc}(max). This statement is also confirmed by the fact that the normalized VSL (the stripe length of 3 mm, the excitation energy density E_{exc}(max)) and SES spectrum are almost identical without any sign of spectral narrowing (Fig. 4.7(b)). Furthermore, this negative conclusion is also supported by the character of the PL temporal evolution, which is similar for both, the VSL (stripe length of 3 mm, excitation energy E_{exc}(max)) and SES signals as plotted in Fig. 4.7(d). The possibility of the presence of net optical gain at different wavelengths was also verified (not shown), however, with a
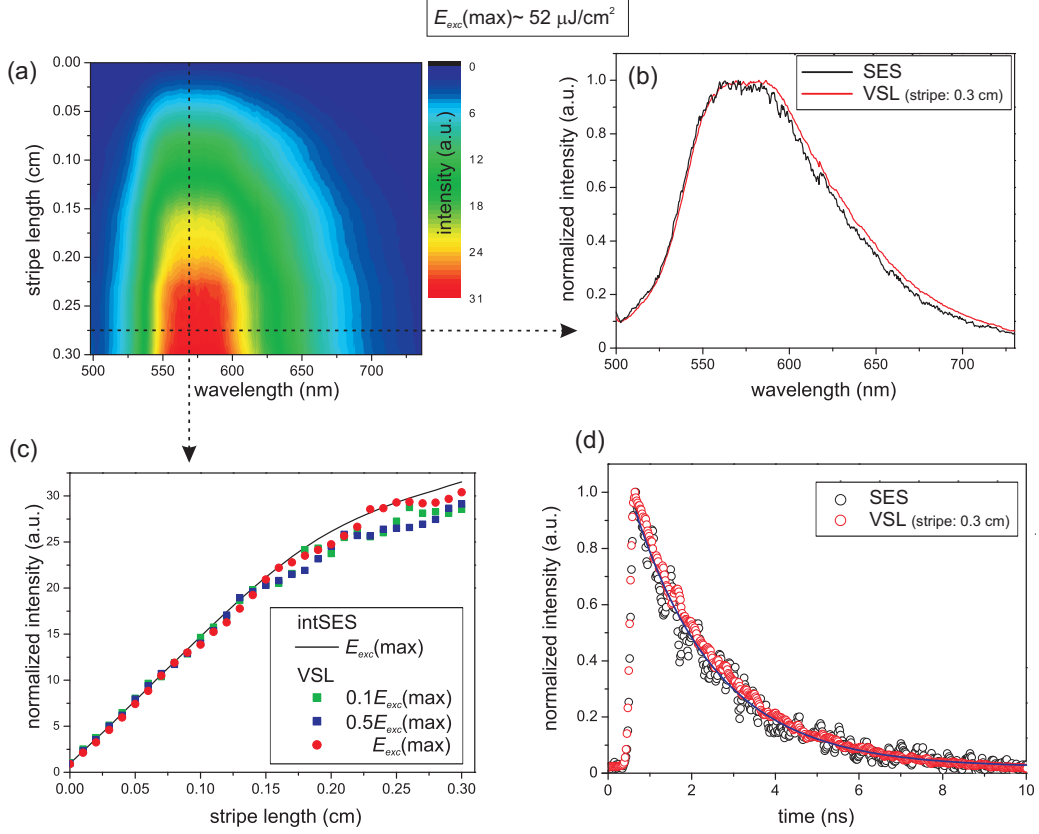
Figure 4.7: The room-temperature results of the VSL and SES measurements performed on the methyl-capped SiNCs dispersed in xylene with femtosecond excitation. Signal ploted in (a, b, c) was integrated over whole detection time window of 10 ns. (a) Intensity map of the VSL spectra as a function of the stripe length for $E_{exc}(\text{max}) = 52$ μJ/cm^2 per pulse. Each row of the matrix comprises one VSL spectrum at a particular stripe length. (b) SES (black) spectrum detected with the SES spot positioned close to the sample edge compared to the VSL (red) signal measured for the stripe length of 3 mm (excitation energy density $E_{exc}(\text{max})$). Spectra are normalized to the signal maximum. (c) Normalized VSL and intSES curves at the signal spectral maximum for three different excitation energy densities: $0.1E_{exc}(\text{max})$, $0.5E_{exc}(\text{max})$ and $1E_{exc}(\text{max})$. (d) The transient VSL signal (stripe length of 3 mm) fitted with a single exponential function (blue curve) and the transient SES signal, both taken at the PL spectral maximum.

negative outcome. The optical gain measurements conducted in the 1 ns window are, with respect to the presence or absence of net optical gain, qualitatively similar to those discussed above and therefore are not shown here.

The main reason of no sign of stimulated emission in the studied sample even under very high excitation energy lies most probably in very low concentration of SiNCs in the solution. This concentration is estimated to be $\sim 10^{16} - 10^{17}$ cm^{-3} [106] while the simple 4-level model of optical amplification in SiNCs requires minimum SiNCs concentration of 10^{18} cm^{-3} [28, 107].

4.2.4 SiNCs/SiO$_2$ solgel samples

None of the experiments discussed previously in this chapter resulted in the observation of positive net optical gain in SiNCs. The reader might thus come to believe that optical gain in SiNCs does not occur at all. However, this is not the case. Samples discussed in this paragraph do exhibit optical gain, as documented in Refs. [52, 108]. The negative observations have been included into the thesis mainly to demonstrate that the experimental findings of light amplification in SiNCs is neither easy nor automatic. Suitable samples and a proper combination of experimental parameters are indispensable prerequisites.

Sol-gel derived samples containing the oxide-passivated SiNCs in a transparent SiO$_2$-matrix were fabricated from the SiNCs powder prepared by electrochemical etching. The powder (~ 2 mg) was mixed with a Phosphorus doped SiO$_2$-based sol-gel (Spin-On-Difusant P509 made by Filmtronics Inc. corporation). This liquid mixture was poured to a glass (quartz) cuvette and ultrasonicated for about 30 minutes. Afterwards an approximately 50 μm thick layer of densely packed SiNCs was formed at the bottom of the cuvette by using the centrifuge treatment for several minutes. Finally, the sample was left to solidify in air for several days under ambient conditions. Details of the preparation method can be found in Ref. [49].

As already discussed in Chapter 3, this sample (containing oxide-passivated SiNCs) exhibits the efficient PL under the UV excitation, which comprises the slowly decaying S-band peaked at about 600 mn and the rapidly decaying F-band peaked at about 430 nm. Optical gain originating in the S-band of this kind of samples was previously observed by Luterová et al [47] and further discussed by Dohnalová et al [49]. On the other hand, the time-resolved optical gain at the F-band has not been investigated in this type of samples so far, even though several publications discussing the F-band optical gain in different types of samples do exist [109, 110]. Therefore, this issue has been exploited mainly during the master thesis of the author and partly also within this doctoral thesis.

Dohnalová et al. [52] present strong experimental evidence for the onset of stimulated emission at the F-band of SiNCs/SiO$_2$ sol-gel sample. The presence of the positive net optical gain coefficient is supported by the observed positive difference between the VSL and integrated SES curves, by the observed narrowing of the VSL spectra for longer stripes in the case of high power excitation and finally by the occurrence of the lasing threshold in the dependence of the emission intensity versus pump power.

Reference [108], attached as Enclosure 4.4, represents the summary of the time-resolved VSL/SES experiments conducted on the SiNCs/SiO$_2$ sol-gel sample, which demonstrates the presence of optical gain of the order of tens of cm^{-1} in both PL emission bands.

4.3 Optical gain enhancement in 2D photonic crystals (computational approach)

As immediately follows from the results presented throughout this chapter, the net optical gain G of SiNCs is either rather low[10] (of the order of tens of cm^{-1} for the best samples) or even negative, i.e. stimulated emission characterized by the optical gain coefficient g is, if any, overcome by losses.

Periodic patterning of the surface of a sample containing the gain medium (SiNCs) in one or two dimensions may help to obtain a stimulated emission and lasing from a material with low optical gain and to win against the losses. Two-dimensional photonic crystals provide optical feedback to the electromagnetic radiation propagating in all azimuthal (planar) directions, therefore they may outperform the classical 1D DFB lasers. As a result of multiple reflections within the material, the patterned gain medium enhances the intensity of propagating light much more effectively than the non-patterned one, therefore it behaves as it had much larger optical gain even though the internal intrinsic gain does not change. The physics of this so-called optical gain enhancement effect is in detail explained in Chapter 2, Section 2.5.

The possibility of enhancing optical gain of a light-emitting source by embedding it into a 2D photonic crystal and into a photonic crystal slab is presented in Ref. [63], attached as Enclosure 4.5. As demonstrated in the enclosure by means of a FDTD computer simulation, the increase of the intensity of light propagating through a 2D photonic crystal (infinitely high) with optical gain is almost 10 times higher than that of light propagating through a homogeneous active material with the same optical gain. However, the more interesting output of this simulation is that even in the real case of a photonic crystal slab (finite height) with optical gain, up to 3.5-fold enhancement in the intensity of light propagating through it can be achieved in comparison with the intensity of light penetrating through a homogeneous medium.

---

[10]Apart from the ultrafast gain [53].

4.4 Enclosure

Time-resolved measurements of optical gain and photoluminescence in silicon nanocrystals

K. Dohnalová, K. Kůsová, O. Cibulka, **L. Ondič** and I. Pelant

Time-resolved measurements of optical gain and photoluminescence in silicon nanocrystals

K Dohnalová[1,2]**, K Kůsová**[1]**, O Cibulka**[1]**, L Ondič**[1] **and I Pelant**[1]

[1] Institute of Physics, Academy of Sciences of the Czech Republic, v.v.i., Cukrovarnická 10, CZ-162 53, Prague 6, Czech Republic

E-mail: dohnalova@fzu.cz

Abstract
In this paper, we present time-resolved optical gain spectroscopy using a combination of the variable stripe length and the shifting excitation spot techniques under pulsed nanosecond excitation at 355 nm. Optical gain measurements in the temporal detection window of 10 ns width, coincident with the excitation pulse, revealed induced absorption losses, whereas measurements with a different detection gate width and delay in two main photoluminescence components (a fast band at ∼430 nm decaying in nanoseconds and a slow band at ∼620 nm decaying in microseconds) show a positive optical gain of the order of tens of cm^{-1}.

PACS numbers: 78.45.+h, 78.67.−n, 81.07.−b

(Some figures in this article are in colour only in the electronic version.)

Optical gain in nanocomposite materials containing silicon nanocrystals (Si-ncs) embedded using various techniques into a SiO_2 matrix has been intensively studied in the past 10 years. These materials show many attractive properties such as high photoluminescence (PL) efficiency at room temperature [1] and a positive single-passage optical gain [2–5]. However, despite the positive optical gain observation and intensive effort devoted to this topic, no laser device based on this material has been built yet and even the conditions for reaching positive optical gain itself remain unclear. This may be due to severe requirements imposed on the structure and preparation of samples (small Si-ncs core size, high density of Si-ncs in the matrix, blue-shifted luminescence, optimal surface passivation and high optical quality) and also lack of theoretical models dealing with relevant predictions for optical gain occurrence in 2–5 nm diameter oxidized Si-ncs (that are mostly studied). Another difficulty may arise from unsuitable experimental conditions, when artifacts may appear and act gain-like, hindering the real stimulated emission (StE) effects. Therefore, we use a combination of the variable stripe length (VSL) [6] and the shifting excitation

spot (SES) techniques [7, 8]. Special care must be taken to avoid waveguiding properties, which are not included in the standard one-dimensional (1D) VSL model [6], because waveguiding properties can influence not only the spontaneous emission spectral shape but also the observation of gain [7, 9, 10].

In this paper, we present the detailed temporally and spectrally resolved study of optical gain in Si-ncs embedded at high densities into a SiO_2 matrix.

1. Experimental

1.1. Samples

Samples were prepared using modified electrochemical etching (for details, see e.g. [11]). Samples contain ∼2 mg of 'yellow' oxidized Si-ncs powder (figure 1(a)) confined within a ∼50 μm thick layer of SiO_2-based matrix [11, 12]. The resulting samples (figure 1(b)) consist of a planar active Si-ncs-rich layer (10^{19} ncs cm^{-3}, i.e. ∼10–20 vol.%) of 1×1 cm area with no waveguiding properties (the layer randomly varies in width on the micrometer scale). The average diameter of the SiNCs core is 2–3 nm [11].

[2] Van der Waals–Zeeman Institute, University of Amsterdam, Valckenierstraat 65, 1018XE Amsterdam, The Netherlands
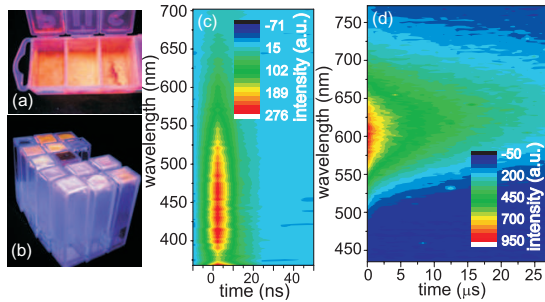
106

Phys. Scr. **T141** (2010) 014011   K Dohnalová *et al*

Figure 1. (a, b) Photographs of a UV lamp excited PL emission of Si-ncs powder (a) and Si-ncs/SiO$_2$ samples (b). (c, d) PL spectra kinetic series of the Si-ncs powder measured with (c) the detection gate width of 5 ns shifted by a step of 5 ns and (d) the detection gate width of 1 μs shifted by a step of 1 μs; signal is in both the cases pre-triggered.

1.2. Time-resolved PL spectra and optical gain measurements

Time-resolved PL spectra and optical gain measurements were done using a Q-switched Nd:YAG pulsed laser at 355 nm (10 Hz, 7 ns). Signal was detected using a UV-grade optical fibre coupled to an Andor Shamrock SR163i imaging spectrograph and an intensified Andor iStar iCCD camera (cooled to $-25\,^{\circ}$C, time resolution of $\sim$5 ns). The optical gain coefficient G and amplified spontaneous emission (ASE) spectra were measured using the standard VSL method combined with the SES method proposed in [7, 10] (the reason for combining the VSL and SES methods is to distinguish undoubtedly a small optical gain from experimental gain-like artifacts, caused by the discrepancy between the 1D VSL model and a real experimental setup). We measured 2D spectral maps of the difference between the VSL signal and the SES signal integrated over the stripe length (VSL/intSES difference) as explained e.g. in [11]. In case the difference is of a negative value, the dominant effect is induced absorption, while a positive difference indicates positive optical gain. If the difference is zero, only standard losses take place.

2. Experimental results

Photographs of the PL emitted by Si-ncs powder and Si-ncs/SiO$_2$ samples placed in quartz cuvettes under a UV lamp are shown in figures 1(a) and (b). Time-resolved PL spectra of the Si-ncs powder alone (to eliminate any contribution of the SiO$_2$ matrix) in the F-band and the S-band are separately plotted in figures 1(c) and (d). In agreement with our previous studies [11, 13, 14], we found out that PL emission spectra mainly consist of two components—a fast F-band component at $\sim$430 nm, decaying on a nanosecond scale with a double-exponential decay law ($\tau_1 = 2.7$ ns, $\tau_2 = 27$ ns [13]) and a slow S-band component at $\sim$580–650 nm, decaying on the microsecond scale by a stretched-exponential law ($\tau \approx 10\,\mu$s, $\beta = 0.8$–1.0 [14]). These two components can be clearly distinguished and separated by careful detection-gate positioning.

The optical gain was investigated separately in the two emission components by varying the detection gate widths and delays, with respect to the excitation pulse onset ($t = 0$ ns)

(figure 2). The optical gain from the emission temporally coincident with the excitation pulse was measured with the gate position of 0–10 ns (sketch in figure 2, first row). To measure the optical gain separately from the F-band and S-band, we set the detection gate positions to 0–50 ns (F-band only; sketch in figure 2, second row) and 200 ns–100 μs (S-band only; sketch in figure 2, third row). The last measurement was done with the detection gate 0–100 μs, covering the total light emission from our sample (F-band and S-band together). The 2D spectral maps of the VSL/intSES difference [11] in each temporal window (rows) are plotted in three columns (a), (b) and (c) in figure 2 for three excitation densities indicated in the figures. The VSL and integrated SES curves for a single emission wavelength are shown in the insets. Column (d) displays PL spectra taken at the depicted temporal windows (red lines) and the spectral profile of the VSL/intSES difference (grey area) at the maximal excitation density and the longest stripe length, i.e. taken from the 2D spectral maps in column (c) as a horizontal profile at the uppermost part of the maps. The optical gain coefficient value G is calculated approximately from the VSL/intSES differences and plotted in column (d) (black points, right y-axis).

3. Discussion

Measurements in the 0–10 ns gate (first row in figure 2) revealed a negative difference of the VSL/intSES signal, caused by induced absorption. This is in good agreement with the measurements on Si-ncs of similar size and surface passivation in SiO$_2$ matrix done by Vijaylakshmi *et al* by Z-scan [15], showing a high increase of the nonlinear absorption under the same excitation conditions. The spectral profile of the induced absorption as measured by VSL/SES is plotted in figure 2(d). Here, one has to consider that the VSL/SES measurement represents a degenerate pump and probe method, where the probe beam is realized by spontaneous emission of the sample itself. Therefore, the observed effect is much lower than in [15] and spectrally dependent due to the PL emission spectral shape of the sample. However, as the induced absorption is dominant in this temporal regime, no optical gain has been observed.

The F-band optical gain was investigated separately using a detection gate of 0–50 ns (figure 2, second row), over which the F-band component dominates. The results show a positive VSL/intSES difference, increasing with increasing excitation intensity. A more detailed study of this phenomenon was published elsewhere [16]. Since the spectral profile of the VSL/intSES difference (and therefore also optical gain spectrum) is not spectrally flat, the emission spectra get narrower with increasing excitation density and stripe length, as was expected for StE onset (see [16]). The origin of this emission band still remains unclear (Si-ncs oxide-shell luminescence [17] versus small Si-ncs core luminescence [13]).

The optical gain from the S-band was separately investigated using a gate delay 200 ns–100 μs (figure 2, third row). The observation reveals in several samples and certain places a positive VSL/intSES difference, which is a good indicator of StE onset. This might appear surprising, since
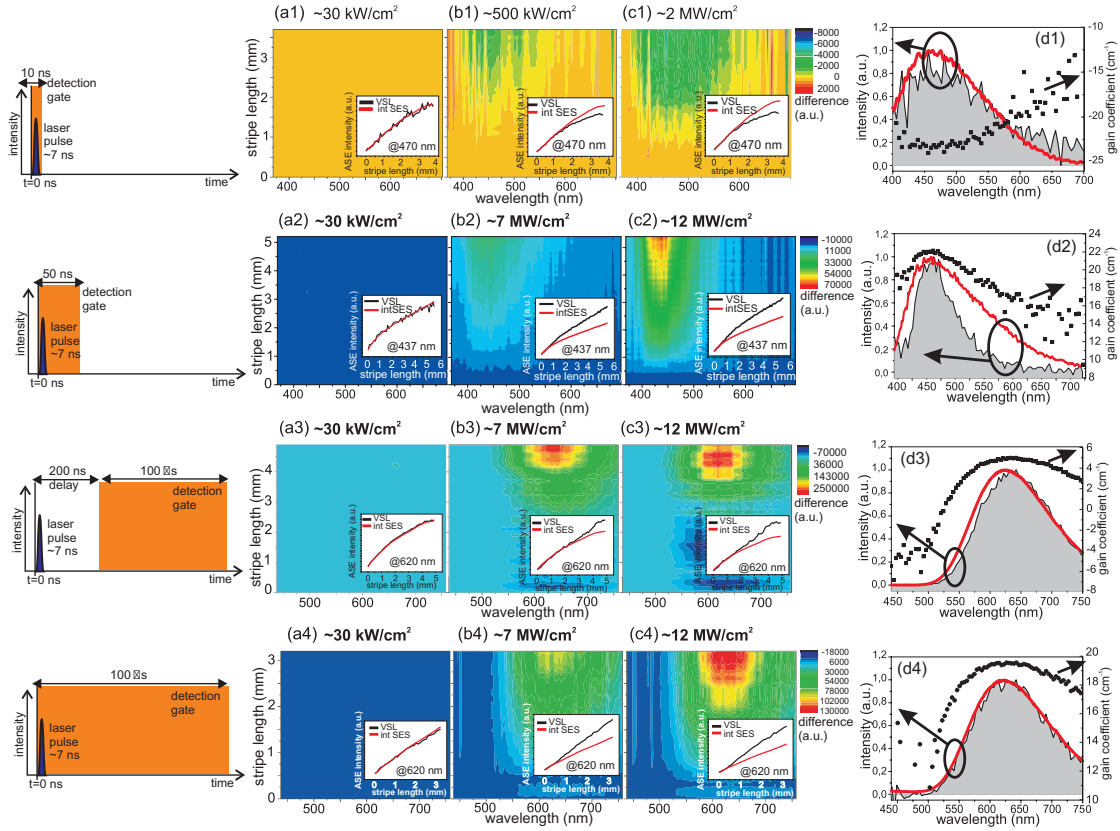
Figure 2. The detection gate window position with respect to laser pulse is depicted in the first column. Columns (a–c) show 2D maps of the VSL/intSES difference measured in the SiNCs/SiO$_2$ sample with a detection gate width of 0–10 ns (1st row), 0–50 (2nd row), 200 ns–100 μs (3rd row) and 0–100 μs (4th row). Excitation densities are noted in the figure. Comparisons of the VSL and integrated SES curves at a single emission wavelength are plotted in the insets. Column (d) represents PL spectra (red line), spectral dependence of the VSL/intSES difference at the highest excitation intensity and the longest stripe length (grey area) and optical gain spectrum extracted approximately from the VSL/intSES difference (points).

many people argue that optical gain can appear only in the fast temporal regime, because the inverted population is depopulated very rapidly by a nonradiative Auger mechanism. The answer to this may lie in ultrafast photocarrier trapping into luminescent surface states related to the oxide shell (from which the S-band component originates), as observed in our samples [14]. Trapped carriers are spatially separated, which leads to a reduced electron–hole wavefunctions overlap and therefore to slow decay on the microsecond scale and to a suppressed Auger mechanism [18]. This effect may be dependent on the type of surface passivation, since single- and double-bonded oxygens at the Si-ncs surface lead to different energy states within the confined optical band gap [19].

The optical gain measurement in 0–100 μs (figure 2, fourth row), i.e. F-band and S-band together, revealed a dominant role of the S-band in the integrated optical gain measurement as observed earlier [2–5, 11]. The gain coefficient G is evidently lower in the 200 ns–100 μs window, compared to 0–100 μs measurement, and the spectral profile of the VSL/intSES difference is slightly different. In the 200 ns–100 μs detection window, the VSL/intSES difference (grey area) shows a missing high-energy wing of the spectrum —compared to the PL spectra (red line) and VSL/intSES difference in 0–100 μs. This might be due to the fact that the emission at the high-energy wing of the spectrum has a shorter decay (see e.g. [14]), which contributes more in shorter times <200 ns.

4. Conclusions

In this paper, we discuss time-resolved optical gain spectroscopy in samples of non-waveguiding planar Si-ncs-rich layers in SiO$_2$-based matrix. The time-resolved study of optical gain revealed an induced absorption in the temporal window coincident with the nanosecond excitation laser pulse, but the positive optical gain from both the F-band and the S-band separately. In the integrated optical gain measurements, the S-band optical gain contribution dominates over the fast F-band. This might be due to massive ultrafast trapping of excited carriers into the surface states related to the Si-ncs oxide shell (S-band), leading to a spatial separation of carriers, i.e. to a slow decay of the S-band and suppressed Auger recombination. The approximate evaluation of the optical gain coefficient revealed a gain coefficient of tens of centimetres.

3

K Dohnalová *et al*

Acknowledgments

References

[1] Jurbergs D, Rogojina E, Mangolini L and Kortshagen U 2006 *Appl. Phys. Lett.* **88** 233116
[2] Pavesi L, Dal Negro L, Mazzoleni L, Franzó G and Priolo F 2000 *Nature* **408** 440
[3] Khriachtchev L, Räsänen M, Novikov S and Sinkkonen J 2001 *Appl. Phys. Lett.* **79** 1249
[4] Ruan J, Fauchet P M, Dal Negro L, Cazzanelli M and Pavesi L 2003 *Appl. Phys. Lett.* **83** 5479
[5] Luterová K, Dohnalová K, Švrček V, Pelant I, Likforman J-P, Crégut O, Gilliot P and Hönerlage B 2004 *Appl. Phys. Lett.* **84** 3280–2
[6] Shaklee K L and Leheny R F 1971 *Appl. Phys. Lett.* **18** 475
[7] Valenta J, Pelant I and Linnros J 2002 *Appl. Phys. Lett.* **81** 1396
[8] Dal Negro L, Bettotti P, Cazzanelli M, Pacifici D and Pavesi L 2004 *Opt. Commun.* **229** 337
[9] Ostatnický T, Rejman M, Valenta J, Herynková K and Pelant I 2008 Guiding and amplification of light due to silicon nanocrystals embeded in waveguides *Silicon Nanophotonics: Basic Principles, Present Status and Perspectives* ed L Khriachtchev (Singapore: World Scientific) chapter 10 pp 267–95
[10] Valenta J, Luterová K, Tomasiunas R, Dohnalová K, Hönerlage B and Pelant I 2003 Optical gain measurements with variable stripe length technique *NATO Science Series II, Towards the First Silicon Laser* vol 93, ed L Pavesi, S Gaponenko and L Dal Negro (Dordrecht: Kluwer) pp 223–42
[11] Dohnalová K, Pelant I, Kůsová K, Gilliot P, Galart M, Crégut O, Rehspringer J-L, Hönerlage B, Ostatnický T and Bakardjieva S 2008 *New J. Phys.* **10** 063014
[12] Švrček V, Pelant I, Rehspringer J-L, Gilliot P, Ohlmann D, Crégut O, Hönerlage B, Chvojka T, Valenta J and Dian J 2002 *Mater. Sci. Eng.* C **19** 233
[13] Valenta J, Fučíková A, Pelant I, Kůsová K, Dohnalová K, Aleknavičius A, Cibulka O, Fojtík A and Kada G 2008 *New J. Phys.* **10** 073022
[14] Trojánek F, Neudert K, Malý P, Dohnalová K and Pelant I 2006 *J. Appl. Phys.* **99** 116108
[15] Vijayalakshmi S, Grebel H, Yaglioglu G, Pino R, Dorsinville R and White C W 2000 *J. Appl. Phys.* **88** 6418
[16] Dohnalová K, Žídek K, Ondič L, Kůsová K, Cibulka O and Pelant I 2009 *J. Phys. D: Appl. Phys.* **42** 135102
[17] Tsybeskov L, Vandyshev J V and Fauchet P M 1994 *Phys. Rev.* B **49** 7821–4
[18] Kamenev B V and Nassiopoulou A G 2001 *J. Appl. Phys.* **90** 5735–40
[19] Puzder A, Williamson A J, Grossman J C and Galli G 2002 *Phys. Rev. Lett.* **88** 097401

4.5 Enclosure

Efficient light amplification in low gain materials due to a photonic band edge effect

L. Ondič and I. Pelant

Efficient light amplification in low gain materials due to a photonic band edge effect

L. Ondič[1,2,3,*] **and I. Pelant**[1]

[1] *Institute of Physics, Academy of Sciences of the Czech Republic, v.v.i., Cukrovarnická 10, 162 53, Prague 6, Czech Republic*

[2] *Faculty of Mathematics and Physics, Charles University, Ke Karlovu 3, 121 16 Prague 2, Czech Republic*

[3] *IPCMS−DON Unité Mixte, UMR 7504, CNRS−ULP, 23 rue du Loess, BP 43, 67034 Strasbourg Cedex 2, France*

* ondic@fzu.cz

Abstract: One of the possibilities of increasing optical gain of a light emitting source is by embedding it into a photonic crystal (PhC). If the properties of the PhC are tuned so that the emission wavelength of the light source with gain falls close to the photonic band edge of the PhC, then due to low group velocity of the light modes near the band edge caused by many multiple reflections of light on the photonic structure, the stimulated emission can be significantly enhanced. Here, we perform simulation of the photonic band edge effect on the light intensity of spectrally broad source interacting with a diamond PhC with low optical gain. We show that even for the case of low gain, up to 10-fold increase of light intensity output can be obtained for the two-dimensional PhC consisting of only 19 periodic layers of infinitely high diamond rods ordered into a square lattice. Moreover, considering the experimentally feasible structure composed of diamond rods of finite height - PhC slab - we show that the gain enhancement, even if reduced compared to the ideal case of infinite rods, still remains relatively high. For this particular structure, we show that up to 3.5-fold enhancement of light intensity can be achieved.

© 2012 Optical Society of America

OCIS codes: (050.5298) Photonic crystals; (310.6628) Subwavelength structures, nanostructures; (310.6805) Theory and design.

References and links

1. E. Yablonovitch, "Inhibited spontaneous emission in solid-state physics and electronics," Phys. Rev. Lett. **58**, 2059–2062 (1987).
2. J. D. Joannopoulous, S. G. Johnson, J. N. Winn, and R. D. Meade, *Photonic Crystals: Molding the Flow of Light* (Princeton University Press, 2008).
3. J. C. Knight, J. Broeng, T. A. Birks, and P. St. J. Russell, "Photonic band gap guidance in optical fibers," Science **282**, 1476–1478 (1998).
4. H.-G. Park, C. J. Barrelet, Y. Wu, B. Tian, F. Qian, and C. M. Lieber, "A wavelength-selective photonic-crystal waveguide coupled to a nanowire light source," Nat. Photon. **2**, 622–626 (2008).
5. S. Noda, M. Fujita, and T. Asano, "Spontaneous-emission control by photonic crystals and nanocavities," Nat. Photon. **1**, 449–458 (2007).
6. D. Taillaert, P. Bienstman, and R. Baets, "Compact efficient broadband grating coupler for silicon-on-insulator waveguides," Opt. Lett. **29**, 2749–2751 (2004).

7. S. Fan, P. R. Villeneuve, J. D. Joannopoulos, and E. F. Schubert, "High extraction efficiency of spontaneous emission from slabs of photonic crystals," Phys. Rev. Lett. **78**, 3294–3297 (1997).

8. M. Fujita, S. Takahashi, Y. Tanaka, T. Asano, and S. Noda, "Simultaneous inhibition and redistribution of spontaneous light emission in photonic crystals," Science **308**, 1296–1298 (2005).

9. J. J. Wierer, A. David, and M. M. Megens, "III-nitride photonic-crystal light-emitting diodes with high extraction efficiency," Nat. Photon. **3**, 163–169 (2009).

10. T. F. Krauss, "Slow light in photonic crystal waveguides," J. Phys. D: Appl. Phys. **40**, 2666–2670 (2007).

11. J. Grgic, J. Pedersen, S. Xiao, and N. Mortensen, "Group index limitations in slow-light photonic crystals," Photon. Nano. **8**, 56–61 (2010).

12. J. P. Dowling, M. Scalora, M. J. Bloemer, and C. M. Bowden, "The photonic band-edge laser: A new approach to gain enhancement," J. Appl. Phys. **75**, 1896 (1994).

13. Y. A. Vlasov, K. Luterova, I. Pelant, B. Honerlage, and V. N. Astratov, "Enhancement of optical gain of semiconductors embedded in three-dimensional photonic crystals," Appl. Phys. Lett. **71**, 1616 (1997).

14. M. Nomura, S. Iwamoto, A. Tandaechanurat, Y. Ota, N. Kumagai, and Y. Arakawa, "Photonic band-edge micro lasers with quantum dot gain," Opt. Express **17**, 640–648 (2009).

15. K. Sakoda, "Enhanced light amplification due to group-velocity anomaly peculiar to two- and three-dimensional photonic crystals," Opt. Express **4**, 167–176 (1999).

16. D. Wiersma, "The smallest random laser," Nature **406**, 132–135 (2000).

17. J. Andreasen, A. A. Asatryan, L. C. Botten, M. A. Byrne, H. Cao, L. Ge, L. Labonté, P. Sebbah, A. D. Stone, H. E. Türeci, and C. Vanneste, "Modes of random lasers," Adv. Opt. Photon. **3**, 88–127 (2011).

18. S. Ossicini, L. Pavesi, and F. Priolo, *Light Emitting Silicon for Microphotonics* (Springer, 2003).

19. H. Chen, J. H. Shin, and P. M. Fauchet, "Optical gain in silicon nanocrystal waveguides," in *Silicon Nanophotonics: Basic Principles, Present Status and Perspectives,* L. Khriachtchev, ed. (World Scientific Publishing, 2009), pp. 89–117.

20. K. Dohnalová, K. Žídek, L. Ondič, K. Kůsová, O. Cibulka, and I. Pelant, "Optical gain at the F-band of oxidized silicon nanocrystals," J. Phys. D: Appl. Phys. **42**, 135102 (2009).

21. A. M. Zaitsev, *Optical Properties of Diamond: A Data Handbook* (Springer, 2001).

22. I. Aharonovich, A. D. Greentree, and S. Prawer, "Diamond photonics," Nature Photon. **5**, 397–405 (2011).

23. A. Kromka, B. Rezek, Z. Remes, M. Michalka, M. Ledinsky, J. Zemek, J. Potmesil, and M. Vanecek, "Formation of continuous nanocrystalline diamond layers on glass and silicon at low temperatures," Chem. Vap. Deposition **14**, 181–186 (2008).

24. S. Tomljenovic-Hanic, M. J. Steel, C. M. de Sterke, and J. Salzman, "Diamond based photonic crystal microcavities," Opt. Express **14**, 3556–3562 (2006).

25. J. W. Baldwin, M. Zalalutdinov, T. Feygelson, J. E. Butler, and B. H. Houston, "Fabrication of short-wavelength photonic crystals in wide-band-gap nanocrystalline diamond films," J. Vac. Sci. Technol. B **24**, 50 (2006).

26. C. F. Wang, R. Hanson, D. D. Awschalom, E. L. Hu, T. Feygelson, J. Yang, and J. E. Butler, "Fabrication and characterization of two-dimensional photonic crystal microcavities in nanocrystalline diamond," Appl. Phys. Lett. **91**, 201112 (2007).

27. L. Ondič, K. Dohnalová, M. Ledinský, A. Kromka, O. Babchenko, and B. Rezek, "Effective extraction of photoluminescence from a diamond layer with a photonic crystal," ACS Nano **5**, 346–350 (2011).

28. S. G. Johnson and J. D. Joannopoulos, "Block-iterative frequency-domain methods for Maxwell's equations in a planewave basis," Opt. Express **8**, 173–190 (2001).

29. A. F. Oskooi, D. Roundy, M. Ibanescu, P. Bermel, J. D. Joannopoulos, and S. G. Johnson, "Meep: A flexible free-software package for electromagnetic simulations by the FDTD method," Comput. Phys. Commun. **181**, 687–702 (2010).

30. S. G. Johnson, S. Fan, P. R. Villeneuve, J. D. Joannopoulos, and L. A. Kolodziejski, "Guided modes in photonic crystal slabs," Phys. Rev. B **60**, 5751–5758 (1999).

31. W. M. Robertson, G. Arjavalingam, R. D. Meade, K. D. Brommer, A. M. Rappe, and J. D. Joannopoulos, "Measurement of photonic band structure in a two-dimensional periodic dielectric array," Phys. Rev. Lett. **68**, 2023–2026 (1992).

32. K. Sakoda, "Symmetry, degeneracy, and uncoupled modes in two-dimensional photonic lattices," Phys. Rev. B **52**, 7982–7986 (1995).

33. N. Ganesh, W. Zhang, P. C. Mathias, E. Chow, J. A. N. T. Soares, V. Malyarchuk, A. D. Smith, and B. T. Cunningham, "Enhanced fluorescence emission from quantum dots on a photonic crystal surface," Nature Nanotech. **2**, 515–520 (2007).

34. E. Chow, S. Y. Lin, S. G. Johnson, P. R. Villeneuve, J. D. Joannopoulos, J. R. Wendt, G. A. Vawter, W. Zubrzycki, H. Hou, and A. Alleman, "Three-dimensional control of light in a two-dimensional photonic crystal slab," Nature **407**, 983–986 (2000).

35. R. Sprik, B. A. van Tiggelen, and A. Lagendijk, "Optical emission in periodic dielectrics," Europhys. Lett. **35**, 265 (1996).

36. A. Asatryan, S. Fabre, K. Busch, R. McPhedran, L. Botten, M. de Sterke, and N. A. Nicorovici, "Two-dimensional local density of states in two-dimensional photonic crystals," Opt. Express **8**, 191–196 (2001).

37. A. F. Koenderink, M. Kafesaki, C. M. Soukoulis, and V. Sandoghdar, "Spontaneous emission rates of dipoles in photonic crystal membranes," JOSA B **23**, 1196–1206 (2006).
38. Q. Wang, S. Stobbe, and P. Lodahl, "Mapping the local density of optical states of a photonic crystal with single quantum dots," Phys. Rev. Lett. **107**, 167404 (2011).

1. Introduction

Photonic crystals (PhCs) are materials possessing a periodicity in refractive index which offer control of the way light propagates in the medium [1, 2]. They are extensively studied because of their interesting optical properties which can be used to prepare photonic waveguides [3, 4], cavities [5], couplers [6] or outcouplers [7–9] of light and other optical devices with dimensions comparable or smaller than the wavelengths of light that they are designed for. Further devices may also take advantage of slow-light modes [10, 11], namely the ability to enhance stimulated emission due to the effects occurring near the photonic band edge. Near the band edge, the group velocity of the photon propagating through the structure is strongly reduced due to a large number of multiple reflections within the PhC. In case when a material in the state of population inversion is present this effect may lead to enhancement of effective optical gain [12]. This idea was already experimentally realized for semiconductor quantum dots (QDs) exhibiting relatively high values of optical gain [13, 14]. It was also shown that in two-dimensional (2D) PhCs with only several periodic layers the so-called group velocity anomaly may affect the stimulated emission more strongly than the photonic band edge effect itself [15]. Let us note here that even in disordered gain materials the principle of multiple light scattering may also lead to the light amplification and lasing - the so-called random lasing (for a review, see [16, 17]). Nevertheless, in this article, we will focus only on periodic structures.

The principal feasibility of enhancing optical gain via PhCs appears, naturally, even more attractive when considering active materials with low optical gain coefficient, i.e. materials with the optical gain coefficient lower than is the typical gain coefficient for direct band gap semiconductors (where it amounts to several hundreds up to thousands of cm^{-1}). The driving force behind the present study stems from the state-of-the-art of silicon photonics, where the crucial issue of a suitable light source - a silicon-based laser - has not been satisfactorily solved up to now. Luminescent silicon nanocrystals (SiNCs) seem to be one of the possible solutions [18], however, their optical gain is rather low [19, 20]. Therefore, SiNCs (the active laser medium) incorporated into the PhC serving as the optical resonator may be a solution.

In order to obtain effective gain enhancement, a material possessing both high refractive index and low optical losses should be used. Moreover, it should possess high thermal conductivity in order to withstand high power pumping, and also good optical quality is required - diamond therefore seems to be one of good candidates [21, 22]. Compared to other materials (Si, InP, etc.) generally used for a PhC preparation, it has a wide electronic band gap thus possessing very low losses in the visible spectral region. This is important property as the SiNCs shine at around 600-800 nm. Growth of nanocrystalline diamond (NCD) layers [23] represent viable approach as compared with expensive bulk diamond. Simulations studying the possibility of realizing cavity in NCD have already been performed [24] and nano-patterning of NCD layers has already been well developed [25–27].

In this article, we aim to demonstrate the photonic band edge effect by means of computer simulation of the transmission and gain-influenced transmission spectra (gain spectra) in two types of PhC with 2D planar periodicity in dielectric constant. One of them has an infinite height, the so-called 2D PhC and the other one features a finite height, the so-called PhC slab. Compared to other authors [12, 15], we consider the optical gain to be very low and, moreover, we take into account the finite height of real-life PhC which also reduces the enhancement in comparison to the infinitely high 2D PhC. The results are applicable to any material with low

optical gain, distributed uniformly in a suitable PhC.

2. Results and discussion

2.1. Simulation in general

Photonic band diagrams were computed using the Plane-wave-expansion technique [28].

Transmission and gain spectra were simulated using Finite-Difference Time-Domain (FDTD) method [29] considering a spectrally broad pulse as a light source.

In simulation, the system is described by a complex dielectric constant $\varepsilon = \varepsilon_1 + i\varepsilon_2$, which varies periodically with the position vector $\mathbf{r}$. However, in spectroscopy in the visible region a complex refractive index $N = n + i\kappa$ is more commonly used, where the real part n indicates phase velocity of light in the medium and its value is ~ 2.4 for diamond. The imaginary part κ describes, depending on its sign, the effect of absorption loss or gain when the electromagnetic wave propagates through the material.

When κ is negative, the intensity of light propagating within material will exponentially increase. Therefore, optical gain can be in first approximation implemented by considering the imaginary part of the dielectric constant to be negative. A gain saturation will be neglected in the model describing the case when the intensity of propagating light is relatively low. One can imagine the simulation to be equivalent to a situation when gain active semiconductor QDs (e.g., SiNCs) are uniformly distributed inside a dielectric medium (PhC).

As we wish to apply this approach to low gain material we will consider relatively low optical gain coefficient value $\alpha \sim -126$ cm^{-1} at a (vacuum) wavelength of 500 nm. This is equivalent to $\kappa \sim -0.0005$ based on the relation $\alpha = 2\kappa\frac{\omega}{c}$. Finally, we get $\varepsilon_2 = 2n\kappa \sim -0.0024$.

As we are interested in describing the physical effect of the gain enhancement, the simulation will be performed at the spectrally broad region keeping in mind that in reality the gain material emission is spectrally narrow. And due to the spectrally narrow gain, we can neglect the spectral dependence of refractive index and gain in the simulation.

2.2. 2D PhC

We start with investigation of the 2D PhC consisting of infinitely long dielectric rods with refractive index $n = 2.4$ ordered into a lattice with the square symmetry surrounded by air. Radius of rods is $r = 0.3a$, where a is a lattice constant. All the units used within this article are expressed in units of the lattice constant a. This PhC has a complete band gap for TM modes (modes odd with respect to the mirror plane $z = 0$ perpendicular to the rods) [30]. Experimentally, this structure can be realized in the case that the incident light beam does not "see" edges of the sample and its wavefront is not affected by the finite height of the sample [31].

Photonic band diagrams for the two experimentally accessible crystal directions of this structure, the Γ-X and Γ-M, are shown in Fig. 1(a) and 1(b), respectively. The insets show an electric field patterns of the modes as computed for each band at $k_x = 0.3$, $k_y = 0$ in (a) and $k_x = 0.3$, $k_y = 0.3$ in (b) where k_x, k_y are the in-plane components of the wavevector given by relation $\mathbf{k}_{||} = \frac{2\pi}{a}(k_x, k_y)$. Border of each rod is depicted with an open circle. One can clearly recognize the wave fronts of propagating light waves with direction of propagation marked by black arrows. The first, second and fourth (not shown) field patterns are symmetric with respect to the mirror plane depicted by solid black line and therefore these modes can be excited by the incoming plane wave coming from outside in the indicated direction because it possesses the similar mirror symmetry [31,32]. On the other hand, modes of the third photonic band (dashed line) are asymmetric with respect to the mirror plane and therefore cannot be excited by the incident plane wave. This effect is reproduced in the transmission spectra obtained for 19 periods of rods having refractive index N purely real (no losses/gain), as plotted on the right-hand side of the band diagrams in Fig. 1, and it can be clearly recognized that for example in the case
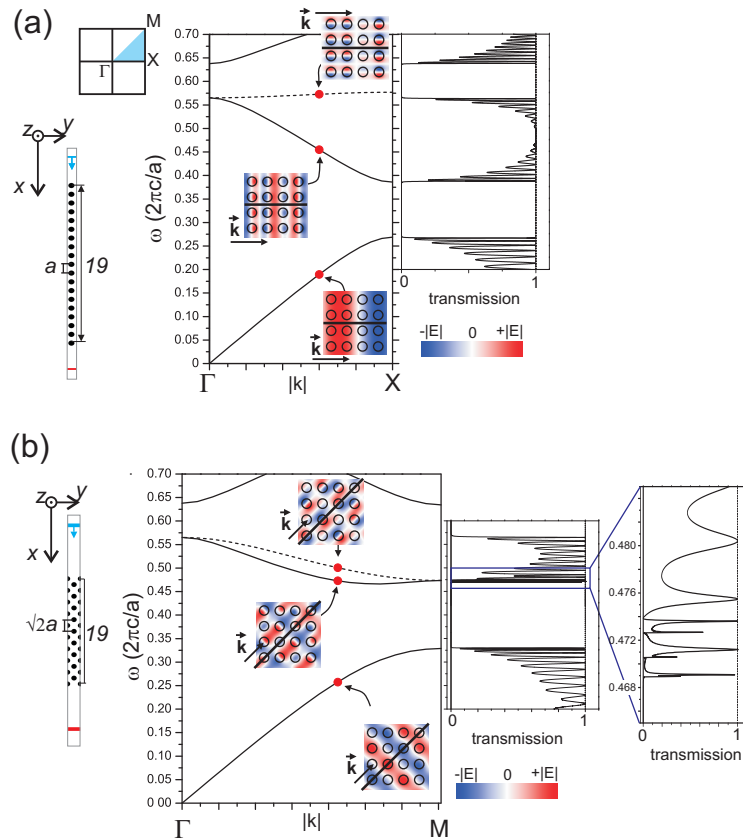
Fig. 1. Photonic diagrams for TM modes in the Γ-X (a) and Γ-M (b) directions of the square array of infinitely high diamond rods (2D PhC) with radius $r = 0.3a$, where a is the lattice constant. The insets show the electric field (parallel to the rods, z-direction) patterns of the modes for each band at the wavevector marked by the red spot. Bands whose mode patterns are symmetric and asymmetric with respect to the mirror plane (a black line in each field pattern) are plotted with solid and dashed line, respectively. The left-hand side of the photonic band diagram in each panel shows the computational domain used for computation of the transmission spectra shown on the right-hand side of the band diagram. The blue and red rectangles represent a light source and a detector, respectively.

of transmission spectrum computed for the Γ-X direction, the bottom edge of the second band gap is defined by the top of the second band at Γ point and not by the top of the third band at X point (Fig. 1(a)).

The 2D computational domains used for the simulation of transmission spectra are shown in the left part of Fig. 1(a) and 1(b) for the Γ-X and Γ-M directions, respectively. The domain includes the material under study (19 rods layers). On the top and bottom surfaces of the computational domain, we impose the Perfectly Matched Layer absorbing boundary conditions. For the remaining two surfaces, we impose a Bloch periodic boundary condition on the electric fields [29]. We generate an incident plane wave from the line source (blue rectangle) with a wavefront parallel to the rods and detect the transmitted flux (red rectangle).

On the basis of the shape of the photonic bands we see that the states with low group velocity ($v_g \sim \frac{\partial \omega}{\partial k}$) are mostly formed near the points of high symmetry and for them the high enhance-
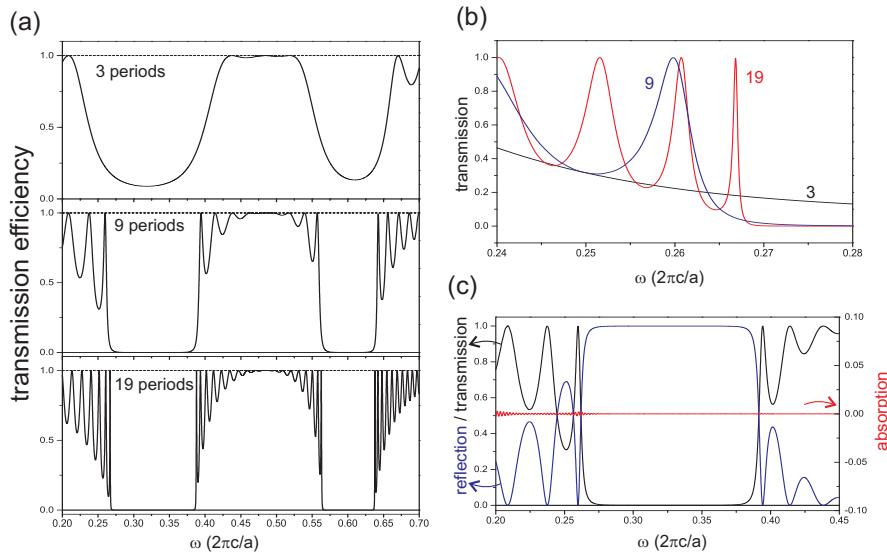
Fig. 2. (a) Transmission spectra of the 2D PhC in the Γ-X direction simulated considering 3, 9 and 19 lattice periods of infinite diamond columns with the lattice constant *a*. (b) Detail of the transmission spectra - formation of photonic states near the band edge with increasing number of lattice periods. (c) Transmission (T) and reflection (R) spectra of the PhC with 9 lattice periods demonstrating the correctness of the FDTD simulation. The red curve shows the absorption (A) calculated by the formula A=1−T−R.

ment of light intensity is expected in the case the optical gain is present. Moreover it is worth noticing that around the frequency of 0.46 in Γ-M direction (Fig. 1(b)) we obtained relatively wide frequency range with a small group velocity (photonic band with very low slope) - the so-called group velocity anomaly region [15] which, as we will see, gives raise to high gain enhancement. The singular shape of the transmission curve in this frequency region (right-hand side of Fig. 1(b)) is due to the convex shape of the band. The photonic band gap is well reproduced in the transmission spectra computed for the structure composed of 19 layers of diamond rods and therefore this structure will be also considered in gain simulations.

The formation of band gap and band edge states with increasing number of layers is plotted in Fig. 2(a) and in detail in Fig. 2(b). The correctness of FDTD simulation is demonstrated in Fig. 2(c) where the transmission and reflection curves are depicted together with the appropriate absorption given by the relation (unity − transmission − reflection). In a non-absorbing medium, this relation should be equal to zero which is in our case fulfilled.

As the next step we introduce the optical gain into the rods ($N = 2.4 − i0.0005$). In this case the incident pulse triggers the stimulated emission in the PhC and the amplified transmitted flux (gain spectrum) is detected. Let us note here that also the intensity of modes reflected on the PhC is increased, however for the sake of clarity we do not plot them.

Gain-influenced transmission spectra for the Γ-X and Γ-M directions are shown in Fig. 3(a) and (b), respectively. The red horizontal curve depicts increased intensity after a single light pass along the given direction, simulated with the refractive index $N = 1 − i0.0005$ in the position of rods and $N = 1$ elsewhere. Its value is ~ 1.017 (1.013) for the Γ-X (Γ-M) crystal direction which means that light intensity was increased only by $\sim 1.7\%$ (1.3%) compared to the reference signal intensity. The values are nearly equal to unity mainly due to low optical gain of our material. On the other hand, the transmitted light intensity is considerably enhanced
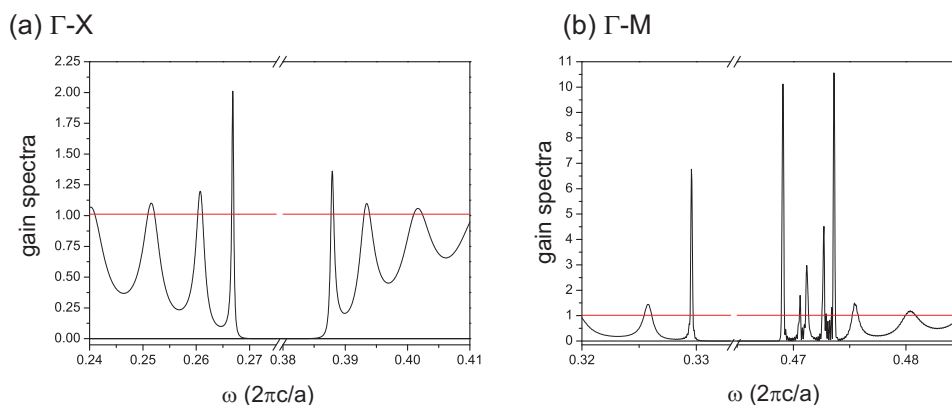
Fig. 3. Gain-influenced transmission spectra (black curve) computed for the TM polarized plane wave incident in the Γ-X (a) and Γ-M (b) crystal directions of the square array of 19 layers of infinitely high diamond rods possessing optical gain. The red horizontal line depicts the single pass light amplification when the periodicity is not present.

Table 1. Fraction of electric field energy confined in the rods computed for the mode at the band edge.

	X-point		M-point	
	2D PhC	PhC slab	2D PhC	PhC slab
band 1	0.88	0.67	0.95	0.75
band 2	0.56	0.56	0.75	0.75

when it propagates through the PhC with the same value of optical gain. For the Γ-X crystal direction, the enhancement is up to 2-fold compared to the reference signal at frequencies of light coupled to the states near the photonic band edge. Even higher increase of transmitted intensity is observed for the Γ-M crystal direction compared to the Γ-X, where three main peaks with the enhancement efficiency from ~ 6 to ~ 10 arise due to photonic band edge effect and due to the group velocity anomaly. The reason for the large intensity enhancement can be readily understood from the intensity amplitude amplification factor derived by Sakoda in [15] which depends on the following four factors. It is inversely proportional to the group velocity of the mode, and thus intensity of light propagating in modes with low group velocity is expected to be greatly increased. Next it holds that the more the mode energy is confined in the active material (rods in our case) the higher the enhancement can be expected. The fraction of the electric field energy confined in rods computed for the modes at the X and M points of the Brillouin zone, given as a ratio of mode energy concentrated in rods and total mode energy, is summarized in Table 1. Lastly, the higher the frequency of the mode the higher the amplification factor. All the above mentioned factors together contribute to the final computed gain spectrum. Nevertheless, it would be unrealistic to expect extremely large output intensity enhancement because the amplification factor scales linearly with the gain coefficient, and thus the anticipated low value of gain keeps the enhancement within moderate limits.

2.3. PhC slab

As a photonic crystal slab we consider a structure consisting of dielectric rods with finite height ($h = 2a$), surrounded by air, and having the same square symmetry and planar dimensions as the 2D PhC discussed in previous section. This structure can be realized experimentally, e.g.
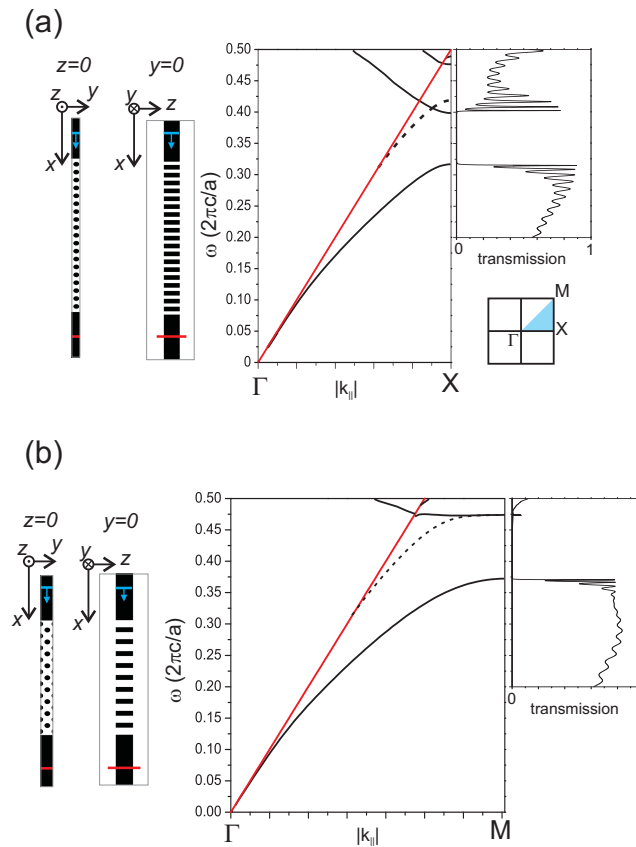
(a)

(b)

Fig. 4. Projected photonic band diagrams for TM modes in the Γ-X (a) and Γ-M (b) crystal directions of the PhC slab consisting of a square array of diamond rods with radius $r = 0.3a$ and height $h = 2a$, where a is a lattice constant. Modes that are symmetric (asymmetric) with respect to the mirror plane parallel to the direction of mode propagation are plotted with black solid (dashed) lines. The air lightline is depicted with the red line. On the left side of each panel, a computational domain is depicted (a top-view and a side-view) used for simulation of transmission spectra plotted on the right side of each panel. Blue rectangles represent a source of TM polarized light incident in the relevant direction for 19 layers of rods. Red rectangles represent detector plane. Origin of the coordinate system is in the middle of the computational domain.

by using a substrate with very low refractive index ([33] - nanoglass with refractive index of 1.17) or even by patterning the low index substrate in the same manner as the PhC (extending the rods into the substrate) [34]. Then photonic properties of such a structure will only slightly differ from the one we are investigating here.

Projected photonic band diagrams in the Γ-X and Γ-M symmetry directions of our PhC slab for TM-like modes are shown in Fig. 4(a) and 4(b), respectively. Modes that are positioned below the lightline (red line) are confined within the PhC. Strictly speaking, there is no longer any photonic band gap in TM-like modes, however, modes of the second band (marked by dashed line) are asymmetric (not shown) with respect to the mirror plane parallel to the direction of light propagation. Similarly to the previous case of the 2D PhC, the asymmetric modes will not be excited by the incident TM polarized wave and thus photonic band gap actually opens
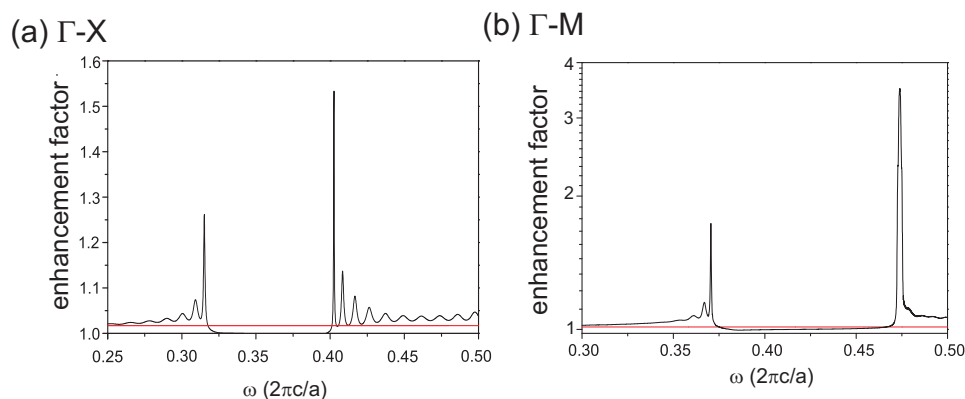
(a) Γ-X

(b) Γ-M

Fig. 5. Photon flux enhancement spectra (black curve) in the Γ-X (a) and Γ-M (b) crystal directions of the PhC slab depicted in Fig. 4, computed as a ratio of the gain-influenced and ordinary transmission spectra. The red horizontal line depicts the single pass enhancement.

for light incident along the Γ-X or Γ-M directions.

Transmission spectra were computed using 3D computational domain. A top and side view of the domain with the PhC slab consisting of 19 layers of rods are shown in the left part of Fig. 4(a) and 4(b) for the Γ-X and Γ-M directions, respectively. On the two surfaces of the computational domain parallel to the *xz*-plane, we impose a Bloch periodic boundary condition on the electric fields. For the remaining four surfaces of the computational domain, we impose the Perfectly Matched Layer absorbing boundary conditions [29]. Light emitted from the source positioned in the uncorrugated part of the diamond layer (blue rectangle) is at first coupled to the guided modes of the layer, then it couples to the PhC and afterwards couples back again to the uncorrugated layer where the flux guided (transmitted) through the PhC is computed (red rectangle). In order to stay consistent with the previous section, we use the term transmitted signal (transmission spectra) in the sense of the flux guided within the PhC and/or the uncorrugated layer. Transmission spectra of the PhC were normalized by the transmission spectra computed for only the uncorrugated layer without PhC and thus contains also information about the efficiency of guided modes coupling between the layer and the PhC.

Photonic states formed near the band edge can be clearly recognized in transmission spectra shown in Fig. 4 at the right-hand side of each photonic band diagram. Sharp peaks occur near the top of the first band and bottom of the third band in both investigated crystal directions. In the case of the Γ-M direction, only two peaks with very low transmission (~ 0.07) occur around the edge of the third band which happens due to the shape of this band below the lightline where the region of nearly zero group velocity is formed. Even for guided modes, the transmission is lower than unity, which happens due to the losses/reflections introduced during the light coupling to (from) the PhC. On the other hand, modes positioned above the lightline are not purely guided modes and can radiate to air as they propagate within the PhC [7], which explains why the transmission efficiency of modes above the lightline decreases.

A relevant parameter describing enhancement of the transmitted signal through the PhC slab with gain compared to the one without, given by the ratio of gain-influenced (not shown) to ordinary transmission spectra, is plotted in Fig. 5(a) and 5(b) for the Γ-X and Γ-M directions, respectively. The red curve depicts the single pass intensity amplification simulated in such a way that the gain regions are introduced into the uncorrugated layer on the same positions as the rods are distributed over the PhC; due to the low optical gain its value is nearly equal to unity. Thus we can directly read that we obtained up to ~ 1.5-fold enhancement of light intensity in

the Γ-X crystal direction due to the band edge effect compared to the single pass enhancement despite the finite height of the PhC. In the case of the Γ-M direction, the intensity amplification amounts up to 1.7-fold near the band edge of the first band at point M, and even up to 3.5-fold near the band edge of the third band, again due to the group velocity anomaly.

Results of our simulation show that the enhancement of optical gain occurs always near the band edge and is even higher when a region of group velocity anomaly is present there. As it was shown, the existence of the complete optical band gap is not a necessary condition for obtaining the enhancement. On the other hand, it is very important to adjust dimensions of the PhC based on the refractive index of the material so that the emission spectrum of the gain material overlaps with modes possessing very low group velocity.

Comparison of the results of the two different PhC structures show that the incident light amplification is in the case of the PhC slab lower than in the case of the 2D PhC, which obviously arises from the different nature of these structures, as reflected in the shape of photonic bands (thus the group velocity). Next, due to the finite height of the PhC slab, the mode is extended into air in the vertical z-direction and less mode energy is concentrated in the rods than in the case of the 2D PhC (for comparison see Table. 1). Nevertheless, the enhancement factor in the PhC slab is still much higher than the value of the single pass enhancement suggesting that this approach may be applicable when constructing optical resonators for materials with low optical gain coefficient.

Let us note here that the complementary description of light amplification enhancement due to the photonic band edge effect is possible via the physical quantity called local density of optical states (LDOS) [35]. The LDOS determines the dynamics of radiation sources embedded at a particular position in a PhC. Computation results for the 2D PhC composed of infinitely high rods [36] or the PhC membranes [37] are consistent with results of our simulation. Namely, the LDOS is strongly enhanced for the band edge modes compared to other modes of different frequencies. Moreover, spatial variation of the LDOS is consistent with the electric energy spatial distribution of these modes shown in Table 1. The same effect of enhanced LDOS at the band edges was recently determined experimentally from the decay times of luminescence of QDs embedded in the PhC membranes [38].

3. Conclusions

We demonstrated, by means of a computer simulation, the enhancement of light amplification in a material with low optical gain with the aid of 2D photonic structures. We showed that by introducing the periodicity into the refractive index of the active material, the intensity of light propagating through the structure composed of only 19 periodic layers can be increased by factor varying from 1.5 up to 10. The enhancement arises from the photonic band edge effect and the highest values were obtained when this effect is combined with the group velocity anomaly regime. Comparison of the 2D PhC (infinite height) and PhC slab revealed that both these structure can take the advantage from the photonic band edge effect. For the diamond PhC slab, which is experimentally feasible structure, we obtained up to 3.5-fold enhancement of the optical gain (for the case of 19 periodic layers), which we believe may be useful when constructing optical resonators for the low gain materials operating in the visible region.

Acknowledgments

Enhancement of light extraction from a diamond layer with a photonic crystal

Within this thesis, one of the main goals was to understand light behavior in photonic crystals, specifically photonic crystal slabs, and to learn how to simulate and measure optical properties of these structures. One of the applications we were keeping in mind when designing a 2D photonic crystal slab prepared on a nanocrystalline diamond (NCD) thin layer was to increase the light extraction efficiency from this layer. This may be advantageous in diamond photonics [111, 112]—applicable for example in diamond-based LEDs—or within diamond-based quantum photonics [113]. Light in our samples originated from various diamond defects [114, 115] (color centers) introduced during the growth of the layers. The light emission of these defects spectrally covered the whole visible range. Diamond material was chosen due to two main reasons. First, diamond has great physical and chemical properties [115, 116, 117]. Thanks to its high thermal conductivity, it withstands high optical power pumping which is desirable for obtaining stimulated emission. As will be presented in the next chapter, we tried to use these layers as a matrix for our light emitting SiNCs. Second, the preparation and patterning process of the NCD layers is well developed at the Institute of Physics, ASCR in Prague.

In this section, the results of computation and experiments obtained on a NCD photonic crystal slab are presented. First, the preparation method of the sample is described. Second, the detection techniques and computational methods are presented. Finally, a brief description of the main experimental findings presented in Refs. [118, 78], attached as Enclosures 5.4 and 5.5, is given.

5.1 Fabrication and design

NCD layers were grown on an optically transparent glass (quartz) substrate, starting from the powder of diamond nanocrystals and employing Plasma-enhanced chemical-vapor deposition (PECVD) method. This technique was developed some time ago at the IoP, ASCR and allows to prepare diamond layers with thickness varying from about 50 to 600 nm. Details of this method can be found in Ref. [119].

It should be, however, stressed here that optical properties of these layers are much worse than those of their bulk counterparts. This is given first of all by their nanocrystalline nature—the NCD layer is in fact composed of diamond grains—which introduces optical losses caused by light scattering (for details see Ref. [120]). The thicker the layer, the bigger the diamond grains and thus the higher probability of the visible light scattering. However, what is probably even more significant loss mechanism is the optical absorption in the sp^2 carbon-like phase present in the NCD layers next to the sp^3 diamond-like phase. Nevertheless, despite the above discussed optical losses, the high extraction efficiency of light can be obtained by creating a photonic crystal on the top of the NCD layer.

A technique allowing to prepare periodic structures was developed at the IoP, ASCR basically on our demand and it is still under development. The process comprises in principle 6 main steps which are schematically shown in Fig. 5.1: 1. Growth of the layer. 2. Coating with electron sensitive polymer. 3. Electron beam patterning. 4. Metal (Au or Ni) masking layer evaporation. 5. Lift-off processing. 6. Diamond plasma etching and Au/Ni wet etching. Details of this method can be found in Ref. [118]. The fabrication of samples was completely in hands of our colleagues, for which we would like to express our deep gratitude.

On the other hand, the theoretical design of the photonic crystal samples, their thorough experimental investigation and the proof of concept were in hands of the author and were realized for the most part in the Department of Thin Films and Nanostructures of the IoP in Prague.
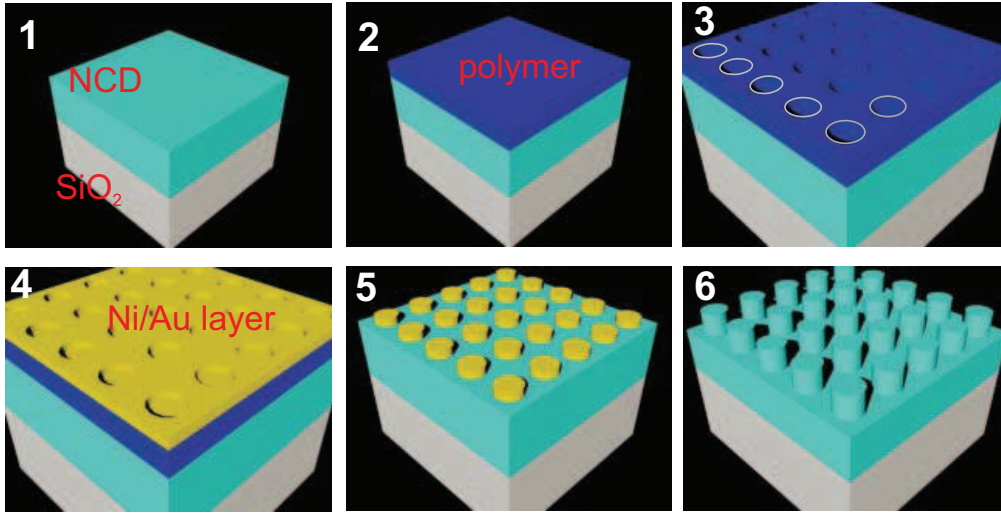
Figure 5.1: Schematic illustrations of the main steps of the preparation proccess of a NCD photonic crystal slab. See the main text for details.

The dimensions of the photonic structure that would operate as an efficient visible photoluminescence outcoupler were searched typically by computing a photonic band diagram. However, we were restricted by the preparation technique that enabled to obtain only photonic crystals consisting of columns arranged into a square lattice[1] (as the one sketched in Fig. 5.1). Therefore the type of the structure was basically given and the parameters that needed to be tuned were only the lattice constant, the radius and height of the columns and the layer overall thickness. We started from a good guess taking into account results and suggestions from literature [71, 121] and then fine-tuned the results in order to have a spectral overlap of the photonic crystal leaky modes with the PL emission spectrum of the NCD layer. As the emission spectrum covers the whole visible range, the aim was to obtain the overlap with the leaky modes possessing visible frequencies, i.e. we wanted to have all the photonic crystal modes with visible frequencies positioned above the air lightline (see the band diagram plotted in Fig. 4 in Enclosure 5.4).

In order to compute the photonic band diagrams and electromagnetic modes of periodic dielectric structures, three different computational methods depending on the desired output were employed.

MIT photonic-bands (**MPB**) free-package [64] is based on a conjugate gradient plane-wave method and allows to compute photonic band diagrams in a relatively short time period. First, the geometry of a photonic crystal is defined in a primitive computational cell which comprises one period of the structure. Depending on the structure under study, this cell can be 1, 2 or 3D. Then, the computational problem is solved by imposing the Bloch periodic boundary condition of the electro-magnetic fields on all boundaries (surfaces) of the computational cell in order to periodically repeat the pattern and to reconstruct the photonic crystal. It therefore naturally follows that, for example in the case of a 3D cell used for computing the band structures of photonic crystal slabs, the results of the simulation describe the properties of a system which has infinite length and width. Nevertheless, such results can be applied also to real structures with finite dimensions provided their width and length are much larger than their height. The crucial idea is, however, that the Bloch periodicity is applied also in

---

[1]At the moment, structures based on a hexagonal symmetry are being prepared.

the vertical direction, which in the case of the simulation of photonic crystal slabs results in the fact that not all modes that occur above the air lightline represent a physical solution. In order to find the dispersion of leaky modes, also the electromagnetic fields of the computed states need to be analyzed as very often the photonic band is just the artifact of simulation coming from the periodic conditions.

MIT electromagnetic equation propagation (**MEEP**) free-package [77] is based on a Finite-difference time-domain (FDTD) method. It can be applied to compute band diagrams, allows to compute quite reliably the photonic bands of leaky modes, and can be used to simulate electromagnetic field propagation in periodic media.

DiffractMOD is a commercial software package based on a Rigorous coupled-wave analysis technique (RCWA) and developed by the RSoft Design group. It allows to compute transmission and reflection spectra of periodic dielectric media. The band diagram of leaky modes can be derived from these spectra. Access to this software was provided by prof. J. Čtyroký from the Institute of Photonics and Electronics, ASCR, for which we would like to express our deep gratitude.

5.2   Experimentals

A photonic band diagram is a tool to describe light propagation in photonic crystal slabs. More specifically, as we are dealing with the light extraction phenomenon, leaky modes are of our interest. Leaky modes are positioned in the region above the air lightline of a photonic band diagram as explained in Chapter 2 and therefore they are accessible from outside by different experimental techniques. The physical mechanism used to probe leaky modes is as follows. When externally incident light interacts with a photonic crystal slab, only the zeroth-order forward- and backward-diffracted waves can propagate. However, the periodicity also allows light coupling into localized leaky modes supported by the photonic structure in case that the incident light fulfills the Bragg-diffraction condition. Once excited, leaky modes propagate in the slab and are again diffracted in both the forward (transmitted) and backward (specular) directions. The backward re-radiated waves are in phase and constructively interfere with the zeroth backward-diffracted order, whereas the forward re-radiated waves are out of phase with the zeroth forward-diffracted order by π, causing destructive interference and consequently zero transmission. Thus, the external excitation of leaky modes is associated with a 0% transmission efficiency for a resonant wavelength, assuming a defect-free, lossless system [122, 123].

Therefore, an experimental setup allowing to measure transmission and/or reflection as a function of the incident angle is a tool to investigate the photonic band diagram of leaky modes. Within this thesis, we built up a new system for measuring the band diagrams of leaky modes based on three main parts: a stable white light source (tungsten or halogen lamp), a sample holder and an optical fiber for the signal collection. Light from the white lamp was coupled to an optical fiber. In front of the optical fiber output, a pinhole was placed to obtain a point source and a convex lens with the pinhole in its focus formed a white beam with negligible divergence. A polarizer was put into the path of the beam to obtain either S- or P-polarized light. The sample holder (rotational stage) allowed to tilt the sample with respect to the vertical z-axis and thus to change the angle of incidence θ in the interval of (-30°, 30°), $\theta = 0°$ being the angle of normal incidence (Fig. 5.2(a)). Because the rotational stage was motorized, high angular resolution in the angle θ was obtained. The holder also allowed to rotate the sample around the z-axis and therefore enabled to probe leaky modes along the both high-symmetry directions of a square lattice: $\Gamma-X$ and $\Gamma-M$. Another optical
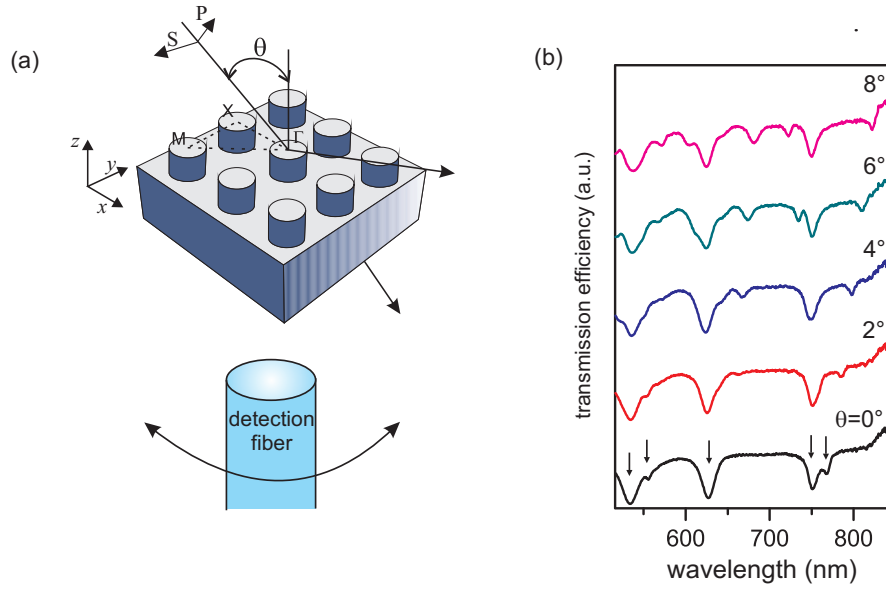
Figure 5.2: (a) A schematic illustration of an experimental setup used for angle-resolved transmission measurements. (b) The S-polarized transmission spectra of a NCD photonic crystal slab as a function of the angle θ, detected along the $\Gamma-X$ crystal direction.

fiber, used for the detection of transmitted/reflected radiation, was coupled to the input of a spectrograph equipped with an iCCD detector. In the transmission setup, the detection optical fiber was positioned below the sample in a direction parallel to the incident light and only the sample was rotated by the angle θ. The measurement was computer-controlled and the output was a set of transmission curves with respect to the angle θ.

In the real system as the one investigated in this chapter, leaky modes are characterized by relatively deep minima in transmission curves. Figure 5.2(b) shows the $\Gamma-X$ transmission spectra (for several angles θ) of the NCD photonic crystal slab which was discussed in the previous section. In the case of the curve of normal transmission ($\theta = 0°$), 5 minima marked by the black arrows can be identified within the plotted spectral range which means that 5 leaky modes occur at different light wavelengths. When changing θ, the minima shift spectrally following the photonic band diagram of the structure. Therefore, the band diagram in $\lambda - \theta$ representation can be constructed by ordering these transmission curves next to each other in a matrix[2] and then plotting the 2D map of transmission efficiency as a function of θ and air wavelength λ (see, e.g. Fig. 6(b) in Enclosure[3] 5.5).

The effect of the fabricated NCD photonic crystal slab on the PL extraction efficiency of diamond color centers was investigated by employing several experimental setups. The qualitative pictures of light extraction enhancement were obtained using a fluorescence microscope (for details see Ref. [118]). Spectrally-resolved PL in a relatively large detection cone was measured from above the sample with a micro-PL setup. The micro-PL setup comprises excitation with a 325 nm cw laser focused on the sample by an optical objective. The same objective is then used for the collection of emitted light. The numerical aperture of the objective defines the collection angle. Spectrally and angle-resolved PL spectra were obtained by fixing the sample at $\theta = 0°$ in a similar sample holder as used for the transmission measurements

---

[2]Columns being different angles θ, rows being different wavelengths.

[3]In this publication, a symbol α is used for the angle of extraction instead of a symbol θ employed in this chapter.

(Fig. 5.2(a)). The sample was excited by a cw 325 nm laser at a fixed (non-resonant) angle of incidence and the emitted radiation was detected by tilting the detection fiber with respect to the z-axis. By changing the distance between the fiber and the sample, the angle-resolution was tuned.

5.3   Results and Discussion

In this section, the main results obtained in the NCD photonic crystal slabs are summarized. Figures and detailed information can be found in Refs. [118, 78], attached as Enclosures 5.4 and 5.5.

A 2D photonic crystal, characteristic dimensions of which were choosen based on the results of our simulations, was etched into a thin NCD layer ($\sim$ 420 nm) deposited on a glass substrate. It was composed of 135 nm high columns with the diameter of $\sim$ 220 nm ordered in a square lattice with the lattice constant $a = 350$ nm. The SEM and AFM images of the sample are shown in Fig. 1 in Enclosure 5.4. The main result of this article is the experimental verification of the light extraction phenomenon via the leaky modes of the photonic structure. The micro-PL measurements showed that at the red part of the PL spectrum, the extraction enhancement of the factor of 6 (detection cone semi-angle of 30°) can be achieved for the photonic crystal compared to the smooth planar NCD layer and also compared to the randomly-patterned NCD layer (see Fig. 3 in Enclosure 5.4). This value is comparable to enhancement factors published by other authors (compare with Table 2.1 in Chapter 2, Section 2.4). The design of the periodic structure might be tuned to obtain even higher enhancement factors. It should be noted that photonic structures with different dimensions were also fabricated and characterized but the one presented here possessed the best performance.

The results of Enclosure 5.5 extends the previous findings by presenting the photonic band diagram and the angle-resolved PL of the NCD photonic crystal slab. The complementarity of the photonic crystal transmission and PL spectra evidences that the light extraction enhancement comes from the Bragg-diffraction of leaky modes on the photonic crystal periodicity. As it is expected, the highest enhancement occurs for the modes at the Γ-point, i.e. for the modes out-coupled in the direction $\theta = 0°$ (see Fig. 4(b) in Enclosure 5.5), due to the degeneracy of the modes at $|\mathbf{k}_{||}| = 0$. It should be also noted that leaky modes with small $|\mathbf{k}_{||}| \sim \theta$ are more efficiently extracted than others due to their higher spatial overlap with the periodicity at the surface. As a consequence, radiation from the layer is most intense at around the normal direction, which implies that photonic-crystal LEDs can be applied as directional sources.

To summarize, our results may find an application in the field of optics and optoelectronics when tuning and increasing the emission properties of diamond LEDs or they can be applied in the construction of light couplers to NCD waveguides.

5.4 Enclosure

Effective Extraction of Photoluminescence from a Diamond Layer with a Photonic Crystal

L. Ondič, K. Dohnalová, M. Ledinský, A. Kromka, O. Babchenko and B. Rezek

ARTICLE

Effective Extraction of Photoluminescence from a Diamond Layer with a Photonic Crystal

Lukáš Ondič,[†,‡,‖,]* Kateřina Dohnalová,[†,§] Martin Ledinský,[†] Alexander Kromka,[†] Oleg Babchenko,[†] and Bohuslav Rezek[†]

[†]Institute of Physics, Academy of Sciences of the Czech Republic, v.v.i., Cukrovarnická 10, 162 53, Prague 6, Czech Republic, [‡]Faculty of Mathematics and Physics, Charles University, Ke Karlovu 3, 121 16 Prague 2, Czech Republic, and [‖]IPCMS—DON Unité Mixte, UMR 7504, CNRS—ULP, 23 rue du Loess, BP 43, 67034 Strasbourg Cedex 2, France, and [§]Van der Waals-Zeeman Institute, University of Amsterdam, Valckenierstraat 65, NL-1018 XE Amsterdam, The Netherlands

ABSTRACT Diamond-based materials possess many unique properties, one of them being a broad-band visible photoluminescence due to a variety of color centers. However, a high material refractive index makes the extraction of photoluminescence (PL) from a diamond layer inefficient. In this paper, we show that by periodical nanopatterning of the film's surface into a form of two-dimensional photonic crystal, the extraction of PL can be strongly enhanced within the whole visible spectrum compared to the extraction of PL in a pristine or randomly nanopatterned film. On the basis of theoretical calculations, enhancement is shown to be due to the photonic crystal effect, including efficient coupling of an excitation laser into the diamond.

KEYWORDS: photonic crystals · spontaneous emission · light extraction · diffraction · nanocrystalline diamond films

Diamond-based materials exhibit an unique combination of physical properties, such as extreme hardness, high acoustic velocity, high breakdown field, high thermal conductivity, and many others.[1] Hence diamond as a matrix can support high optical power and high electrical current. Its potential use covers many different fields from electronic devices operating at high frequency, high speed, high power, or extreme conditions through various opto-mechanic, acousto-optics devices, quantum information processing to its use in bio applications due to biocompatibility, and chemical inertness. Diamond has a wide bandgap of 5.5 eV, corresponding to a far UV excitonic luminescence at 225 nm, stable even at high temperatures.[2] By introducing defects and impurities, efficient subgap luminescence can be achieved.[3] Single nitrogen-vacancy (N-V) centers, for example, show a photostable photoluminescence (PL) at room temperature[4] with controllable blinking effects,[5] which makes them especially promising for quantum information processing[6] and single photon generation.[7] The efficient collection of this emission, however,

is strongly limited by the large solid angle of the total internal reflection because of the high refractive index of diamond. Therefore, light generated in the thin film is mostly coupled to the guided modes of the structure. In general, light extraction efficiency from such a structure can be increased by introducing scattering centers, or even two-dimensional (2D) photonic crystals (PhC) inside the planar layer. If the PhC penetrates through the whole layer and the part of the emission spectrum lies within the photonic band gap, then the emission into the guided modes is decreased and therefore extracted out of plane. This is called the band gap approach.[8−10] The second approach is based on the idea that a relatively thin PhC structure placed at the top of the active layer and having a lattice constant comparable to the material emission wavelengths can act as a Bragg diffraction grating.[11,12] Simultaneously, the filling factor f (ratio between the material/air surface area) should lie within the interval of $f \approx 0.3-0.6$,[12] and the height of the PhC should be comparable to the remaining layer thickness[13] to obtain the maximal possible extraction efficiency. However, neither of these methods have been so far utilized in order to increase the extraction of the intrinsic light emission from diamond.

In our contribution we apply the latter idea and compare the effect of two different nanopatternings of thin nanocrystalline-diamond (NCD) layers on the extraction efficiency of the PL in the vertical direction (with respect to the thin film plane). The first structure is a NCD layer with shallow 2D-PhC and the second one, used as a reference sample, consists of randomly
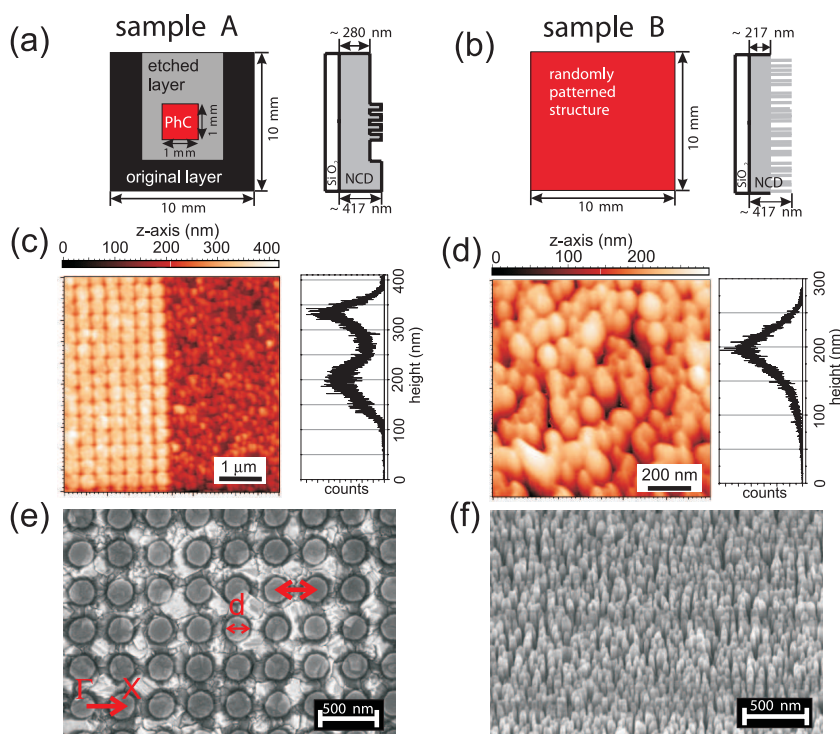
Figure 1. Characteristics of prepared samples. Left column refers to a periodically patterned sample A and right column to a randomly patterned sample B. (a,b) Schematic top-view and cross-section (not in scale) of the sample macroscopic structure. (c,d) AFM scan and height of pillars estimated from the measurement; (e,f) SEM picture.

distributed nanopillars with narrow spacing. We employ two different experimental methods, the first providing us with qualitative and the second providing us with spectrally resolved information about the vertical PL. Both methods reveal strong enhancement of PL extraction from PhC compared to reference samples.

RESULTS AND DISCUSSION

Samples were prepared by nanopatterning of the NCD layers grown on quartz substrate (surface area of 10×10 mm^2). These layers exhibit relatively strong subgap PL in the visible region[14] that could be even increased by employing an additional nitrogen doping. The thickness of the NCD films, estimated from the position of the Fabry−Pérot peaks in transmission measurements (not shown here), was ∼417 nm. First, the shallow 2D-PhC with the surface area of 1×1 mm^2 placed in middle of sample A (Figure 1a) was prepared by electron beam litography. The PhC consists of diamond nanopillars ordered into the square lattice with the following parameters: lattice constant $\Lambda \approx 350$ nm chosen in order to satisfy the Bragg diffraction condition[15] for the whole diamond emission spectrum (400−800 nm); the diameter of nanopillar $d \approx 220$ nm (which leads to $f \approx 0.31$) and the height of 135 ± 15 nm as obtained from the SEM (Figure 1e) and AFM measurements (Figure 1c), respectively. Hence, below the

PhC remained the ∼280 nm thick nonstructured NCD layer (Figure 1a, cross-section).

As a reference sample, besides the original NCD layer, we used sample B with randomly distributed diamond nanopillars prepared on the entire surface of the layer (Figure 1b). The randomly oriented nanopillars were 30 ± 10 nm in diameter (Figure 1f) and up to 200 nm in height (Figure 1d).

The qualitative comparison of the vertical PL from diverse structures placed side-by-side was investigated using a fluorescence microscope. Bright field images of sample B being placed next to the edge of a nonpatterned layer and sample A with part of the PhC structure area (small rhombuses in the middle are the litography markers) are shown in Figure 2 panels a and c, respectively. First, we compare the PL in the red spectral region (575−625 nm) from both structures under green excitation (530−550 nm). It is obvious that in the case of sample B and the nonpatterned layer, nearly no PL emission is outcoupled into the vertical direction; most of the PL is guided within the layer and can be observed at the sample edges (in the middle of the Figure 2b). The small fraction of the generated light is diffracted on the surface defects or scratches on the surface, evidenced by red spots. On the other hand, compared to the nonpatterned and randomly nanopatterned layers, the PL emission into the vertical direction
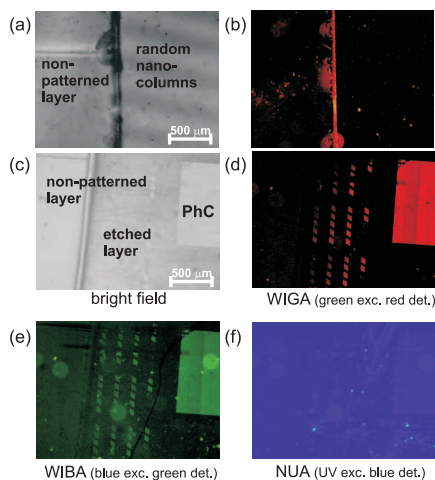
ARTICLE

Figure 2. Image from fluorescence microscope. (a) Bright field and (b) WIGA (green excitation and red detection) image of nonpatterned NCD layer compared to randomly nanopatterned layer of sample B. (c) Bright field, (d) WIGA (green excitation and red detection), (e) WIBA (blue excitation and green detection) and (f) NUA (UV excitation and blue detection) image of the PhC structure compared to the surrounding nonpatterned original NCD layer in sample A. Light out-coupling from the PhC is clearly enhanced in the case of the red and green detection.
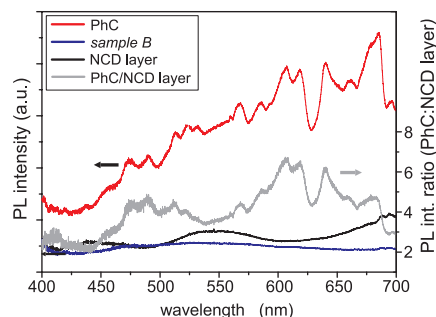

Figure 3. PL emission spectra measured by a micro-Raman Renishaw spectrometer setup (excited by HeCd at 325 nm c.w., 0.3 mW, detected by CCD). The three different types of layers were examined—nonpatterned reference region (black curve), randomly positioned nanopillars (sample B; blue curve), and PhC structure in sample A (red curve). Ratio of the PL intensity of the PhC and original unetched NCD layer is depicted by the gray line showing 6-fold enhancement of light extraction near 600 nm.

is greatly enhanced under the same experimental conditions from the PhC structure (Figure 2d). The similar effect of enhanced extraction efficiency on the PhC is obtained with a blue excitation (460−495 nm) and detection in a green spectral region (510−550 nm) (Figure 2e), whereas it does not occur for an UV excitation (360−370 nm) and detection in a blue spectral region (420−460 nm) (Figure 2f), which is probably due to the low intensity of diamond intrinsic PL in the blue spectral region.

Spectrally resolved PL spectra of the PhC structure in sample A, randomly patterned sample B and nonpatterned layer obtained by micro-PL measurements (subgap excitation and detection from the top) are compared in Figure 3. The original nonpatterned PL spectra of the NCD layer are spectrally broad between 400 nm and more than 700 nm with the oscillations due to Fabry−Pérot resonances between the quartz substrate and the diamond−air interface. Sample B PL spectrum agrees with a broad PL of NCD layer and does not show any enhancement. Here, the emitted light with wavelengths much higher than diameters of randomly positioned pillars "feels" only a negligible material perturbation and behaves as it was passing through a quasi-homogeneous layer, and therefore no diffraction and only some scattering can occur. On the other hand, the PL intensity of the PhC in sample B shows strong enhancement in the vertical direction, when compared to the other layers. The ratio of the PL intensity of the PhC in sample A and original unetched NCD layer (Figure 3, gray line) reveals ∼6-fold enhancement of PL in-

tensity near 600 nm. We would obtain a very similar ratio of the PL intensity if we consider sample B instead of the original layer.

Observed enhancement might originate from several effects: (i) the increased number of emitting centers by introducing more surface defects during the sample etching; (ii) influence of adsorbed water;[14] (iii) increased scattering/diffraction of the excitation laser on the nanopatterned surface;[16] (iv) enhanced Fabry−Pérot resonances;[11,17] (v) photonic crystal effect.[11,12] Since effects (i) and (ii) should be of a comparable magnitude in both structures, or even stronger in sample B because of higher surface area, we can conclude that they are not the dominant ones. The scattering/diffraction effect (iii) of the excitation laser will be stronger in the case of the PhC, which in this case works as a 2D diffraction grating with sizes comparable to the excitation wavelength that directly couple light from the pump laser into the layer. This may lead to enhanced pumping efficiency due to the multiple passage of the excitation within the NCD layer, thus increasing the number of emitting centers which finally contribute to the increase of the overall PL intensity. Fabry−Pérot contribution to the outcoupled PL emission (iv) of the PhC originates from the simple fact that the thickness of the PhC and the underlying NCD layer is comparable, but on the other hand their refractive index is different (effective refractive index of the PhC is ∼1.6 if we consider the refractive index of diamond to be ∼2.4 for the whole visible spectrum). Therefore, in the first approximation, the structure behaves as a bilayer in which the Fabry−Pérot resonances are enhanced compared to the original layer or randomly patterned layer. The PhC effect (v) (present only in the PhC) can be understood from the photonic band structure calculation. The projected band structure of the PhC (Figure 4), including the diamond material underneath, was calculated using a conjugate gradient plane-
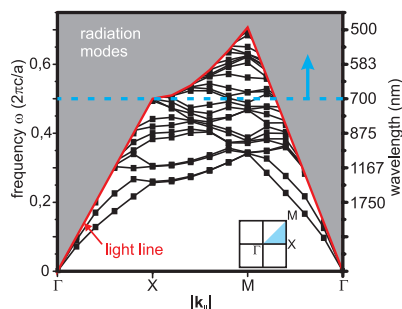
Figure 4. Projected band structure. Computed band structure[18] **for the PhC (sample A). Modes lying inside an air light cone (shaded area) are effectively extracted from the layer due to the Bragg diffraction. PL emission spectrum of diamond is above the blue dashed line allowing most of the light to be outcoupled from the layer.**

wave expansion method.[18] Modes lying below the air light line (defined as $\omega = c|\mathbf{k}_0|$, where $\mathbf{k}_0$ is the in-plane wave vector in air) are guided modes, localized to the plane of the slab. On the other hand, modes lying in the light cone (shaded area in Figure 4 above the air light line) with the in-plane wave vector of the emitted light propagating inside the layer $|\mathbf{k}| < |\mathbf{k}_0|$ can be diffracted on the PhC and become "leaky" modes that propagate easily to the free space. A phase matching condition $\mathbf{k}_0 = \mathbf{k} \pm \mathbf{G}$ ($\mathbf{G}$ is a reciprocal lattice vector of the PhC) needed in order to obtain Bragg diffraction is fulfilled for these modes due to the continuum of available radiation modes above the light line,[8,9] and therefore they can be efficiently extracted from the layer.

Under our conditions, we continuously excite a number of defect centers, which radiatively emit different colored light that is coupled to the modes of the NCD layer. These modes would be usually guided in a nonpatterned layer; however, due to the presence of the PhC, most of them appear above the light line in the photonic band structure of our sample (Figure 4) and thus can effectively radiate into the free space. On the

basis of the parameters of the micro-PL detection, the apex angle of the detection cone was ~60 degrees which covered a large portion of the diffracted light that was propagating to all symmetry directions of the PhC. In terms of the photonic band structure diagram it means our detection covered most of the "leaky" modes lying simultaneously above the air light line and above the blue dashed line, which represents the marginal detected wavelength. The PhC effect and the Fabry−Pérot resonances together explain the fine structure of the PL emission in Figure 3.

CONCLUSION

We have prepared two types of nanopatterned NCD layer: (i) sample A consisting of a nonpatterned NCD layer reference area and a 2D-PhC layer with the square lattice symmetry and (ii) sample B with randomly positioned nanopillars. The PhC structure in sample A showed approximately 6-fold enhancement of the vertical PL intensity near 600 nm when compared to the nonpatterned areas and sample B. By comparison with the random nanopatterning, influence of the scattering centers, the possibly increased number of the surface defects and other surface related effects can be ruled out. Most of the enhancement of light extraction can be thus attributed to the Bragg diffraction of the formerly guided modes on PhC superimposed on the Fabry−Pérot background. In addition, efficient input coupling of the pump laser on the PhC contributes to the enhancement. Further investigations, such as angular far-field PL measurements, are needed to resolve these contributions in more detail. Nevertheless, the observed effect is promising for taking advantage of the diamond PL in optical, opto-electronic, and biological applications. For instance, it could be used to increase external quantum efficiency of the diamond LEDs or improve light coupling into diamond waveguiding structures.

METHODS

Sample Preparation. The NCD films were grown by microwave plasma-assisted chemical vapor deposition (CVD) using an ellipsoidal cavity resonator (Aixtron P6, GmbH). Before the CVD growth, high quality quartz substrates (UQG, Ultrasil, $10 \times 10 \times 1$ mm³) were cleaned in isopropyl alcohol and dried by a nitrogen gun. Then, they were seeded in a liquid suspension of ultradispersed detonation diamond powder with an average size of $ca.$ 5−10 nm in diameter (NanoAmando, New Metals and Chemicals Corp. Ltd., Kyobashi) using an ultrasonic treatment procedure for 40 min (for details, see ref 19). The NCD films were grown in hydrogen (99%) and a methane (1%) based gas mixture. The CVD process parameters were as follows: microwave power 1.4 kW, 1% methane in hydrogen, total gas pressure 30 mbar, and the substrate temperature 560 °C. There was no applied additional nitrogen dopping.

2D-PhC in sample A was fabricated as follows: the NCD films were coated with electron sensitive polymer (PMMA, 120 nm in thickness). The PMMA polymer was nanopatterned by electron beam lithography (EBL) using "e-LiNE system" (Raith GmbH)

forming the base matrix with regularly repeated openings (250 ± 5 nm in diameter) ordered into a square lattice with a lattice constant of $\Lambda \approx 350$ nm. Then, a nickel layer of 25 nm thickness was evaporated and processed by lift-off strategy to form a masking matrix. Plasma etching by using capacitively coupled RF-plasma in a CF_4/O_2 gas mixture (Phantom LT RIE System, Trion Technology) (for parameters of etching process see ref 20) led to formation of geometrically ordered nanopillars (PhC structure) with the surface area of 1×1 mm² placed in the middle of the sample A and surrounded by the nonpatterned etched and the original unetched NCD planar area.

Randomly distributed nanopillars in sample B were fabricated as follows: the nanocrystalline diamond films were coated with a 3 nm thin nickel layer using an evaporation process. Then, the samples were treated for 5 min in hydrogen plasma (total gas pressure 30 mbar, microwave power 1300 W, substrate temperature about 600 °C) to form nanosized Ni particles. The diameter of formed nickel nanoparticles ranged from 15 to 25 nm, and these were quasi-homogeneously distributed over the

whole NCD surface. NCD samples covered with Ni nanoparticles, which were used as the masking material, were structured by plasma etching. Details of the fabrication process can be found in ref 20.

Finally, the remaining nickel mask on both types of samples was removed by wet etching in nitro-hydrochloric acid for 5 min.

Characterization. Atomic force microscopy (AFM) images were taken in tapping mode using silicon tip Multi75Al. Scanning electron microscopy (SEM) pictures were obtained with eLINE system Raith GmbH microscope using an accelerating voltage of 10 kV and working distance of 8 mm.

Optical Measurements. All the spectra presented in this study are corrected for the spectral response of the experimental setup. Direct qualitative comparison of the photoluminescence from different samples was obtained with a fluorescence microscope system Olympus IX71 with an objective UPlanFL N 4× (numerical aperture of 0.13). Spectrally resolved vertical PL was measured at room-temperature using the micro-PL spectroscopy system Renishaw (InVia REFLEX) in backscattering geometry. A continuous-wave HeCd laser with an excitation wavelength of 325 nm and power of ~0.3 mW was focused on the sample using a microscope objective lens Leica NPlan 40× (numerical aperture = 0.5, excitation spot diameter, ~3 μm) in the normal direction. The PL emission was collected by the same objective as used for focusing the excitation beam coupled to a charge coupled device (CCD)

REFERENCES AND NOTES

1. Nebel, C. E. From Gemstone to Semiconductor, *Nat. Mater.* **2003**, *2*, 431–432.
2. Takeuchi, D.; Makino, T.; Kato, H.; Ogura, M.; Tokuda, N.; Oyama, K.; Matsumoto, T.; Hirabayashi, I.; Okushi, H.; Yamasaki, S. Electron Emission from a Diamond (111) p-i-n(+) Junction Diode with Negative Electron Affinity during Room Temperature Operation. *Appl. Phys. Express* **2010**, *3*, 041301.
3. Zaitsev, A. M., *Optical Properties of Diamond: A Data Handbook*; Springer: Berlin, 2001.
4. Gruber, A.; Drabenstedt, A.; Tietz, C.; Fleury, L.; Wrachtrup, J.; von Borczyskowski, C. Scanning Confocal Optical Microscopy and Magnetic Resonance on Single Defect Centers. *Science* **1997**, *276*, 2012–2014.
5. Bradac, C.; Gaebel, T.; Naidoo, N.; Sellars, M. J.; Twamley, J.; Brown, L. J.; Barnard, A. S.; Plakhotnik, T.; Zvyagin, A. V.; Rabeau, J. R. Observation and Control of Blinking Nitrogen-Vacancy Centres in Discrete Nanodiamonds. *Nat. Nanotechnol.* **2010**, *5*, 345–349.
6. Prawer, S.; Greentree, A. D. Applied Physics—Diamond for Quantum Computing. *Science* **2008**, *320*, 1601–1602.
7. Babinec, T. M.; Hausmann, B. J. M.; Khan, M.; Zhang, Y.; Maze, J. R.; Hemmer, P. R.; Lončar, M. A Diamond Nanowire Single-Photon Source. *Nat. Nanotechnol.* **2010**, *5*, 195–199.
8. Fan, S.; Villeneuve, P. R.; Joannopoulos, J. D.; Schubert, E. F. High Extraction Efficiency of Spontaneous Emission from Slabs of Photonic Crystals. *Phys. Rev. Lett.* **1997**, *78*, 3294–3297.
9. Fujita, M.; Takahashi, S.; Tanaka, Y.; Asano, T.; Noda, S. Simultaneous Inhibition and Redistribution of Spontaneous Light Emission in Photonic Crystals. *Science* **2005**, *308*, 1296–1298.
10. Ryu, H. Y.; Lee, Y. H.; Sellin, R. L.; Bimberg, D. Over 30-fold Enhancement of Light Extraction from Free-Standing Photonic Crystal Slabs with InGaAs Quantum Dots at Low Temperature. *Appl. Phys. Lett.* **2001**, *79*, 3573–3575.
11. Wierer, J. J.; David, A.; Megens, M. M., III. Nitride Photonic-Crystal Light-Emitting Diodes with High Extraction Efficiency. *Nat. Photonics* **2009**, *3*, 163–169.
12. Wiesmann, Ch.; Bergenek, K.; Schwarz, U. T. Photonic Crystal LEDs—Designing Light Extraction. *Laser Photonics Rev.* **2009**, *3*, 262–286.
13. David, A.; Benisty, H.; Weisbuch, C. Optimization of Light-Diffracting Photonic-Crystals for High Extraction Efficiency LEDs. *J. Disp. Technol.* **2007**, *3*, 133–148.
14. Dzurnak, B.; Trojanek, F.; Preclikova, J.; Kromka, A.; Rezek, B.; Maly, P. Subgap Photoluminescence Spectroscopy of Nanocrystalline Diamond Films. *Diamond Relat. Mater.* **2009**, *18*, 776–778.
15. Carrol, J.; Whiteaway, J.; Plumb, D. *Distributed Feedback Semiconductor Lasers*; IEE Circuits, Devices and Systems Series; Industrial Electronic Engineers: London, 1998; Vol. 10.
16. Erchak, A. A.; Ripin, D. J.; Fan, S.; Rakich, P.; Joannopoulos, J. D.; Ippen, E. P.; Petrich, G. S.; Kolodziejski, L. A. Enhanced Coupling to Vertical Radiation Using a Two-Dimensional Photonic Crystal in a Semiconductor Light-Emitting Diode. *Appl. Phys. Lett.* **2001**, *78*, 563–565.
17. Bergenek, K.; Wiesmann, Ch.; Wirth, R.; O'Faolain, L.; Lindner, N.; Streubel, K.; Krauss, T. F. Enhanced Light Extraction Efficiency from AlGaInP Thin-Film Light-emitting Diodes with Photonic Crystals. *Appl. Phys. Lett.* **2008**, *93*, 041105.
18. Johnson, S. G.; Joannopoulos, J. D. Block-Iterative Frequency-Domain Methods for Maxwell's Equations in a Planewave Basis. *Opt. Express* **2001**, *8*, 173–190.
19. Kromka, A.; Rezek, B.; Remes, Z.; Michalka, M.; Ledinsky, M.; Zemek, J.; Potmesil, J.; Vanecek, M. Formation of Continuous Nanocrystalline Diamond Layers on Glass and Silicon at Low Temperatures. *Chem. Vap. Deposition* **2008**, *14*, 181–186.
20. Babchenko, O.; Kromka, A.; Hruska, K.; Kalbacova, M.; Broz, A.; Vanecek, M. Fabrication of Nanostructured Diamond Films for SAOS-2 Cell Cultivation. *Phys. Status Solidi A* **2009**, *206*, 2033–2037.

5.5 Enclosure

Enhanced photoluminescence extraction efficiency from a diamond photonic crystal via leaky modes

L. Ondič, K. Kusová, O. Cibulka, I. Pelant, K. Dohnalová, B. Rezek, A. Kromka, O. Babchenko and N. Ganesh

New Journal of Physics

The open–access journal for physics

Enhanced photoluminescence extraction efficiency from a diamond photonic crystal via leaky modes

L Ondič[1,2,3,6], **K Kůsová**[1], **O Cibulka**[1], **I Pelant**[1], **K Dohnalová**[1,4], **B Rezek**[1], **O Babchenko**[1], **A Kromka**[1] **and N Ganesh**[5,7]

[1] Institute of Physics, Academy of Sciences of the Czech Republic, v.v.i., Cukrovarnická 10, CZ-162 53, Prague 6, Czech Republic
[2] Faculty of Mathematics and Physics, Charles University, Ke Karlovu 3, 121 16 Prague 2, Czech Republic
[3] IPCMS–DON Unité Mixte, UMR 7504, CNRS–ULP, 23 rue du Loess, BP 43, 67034 Strasbourg Cedex 2, France
[4] Van der Waals–Zeeman Institute, University of Amsterdam, Valckenierstraat 65, NL-1018 XE Amsterdam, The Netherlands
[5] Nano Sensors Group, University of Illinois at Urbana-Champaign, Champaign, IL, USA
E-mail: ondic@fzu.cz

Abstract. Two-dimensional photonic crystal can be exploited as the top part of a light source in order to increase its extraction efficiency. Here, we report on the room-temperature intrinsic photoluminescence (PL) behavior of a nanocrystalline diamond (NCD) layer with diamond columns prepared on the top and periodically ordered into the lattice with square symmetry. Angle-resolved far-field measurements in the Γ–X crystal direction of broadband visible PL revealed up to six-fold enhancement of extraction efficiency as compared to a smooth NCD layer. A photonic band diagram above the lightcone derived from these measurements is in agreement with the diagram obtained from transmission measurements and simulation, suggesting that the enhancement is primarily due to light's coupling to leaky modes.

[6] Author to whom any correspondence should be addressed.
[7] Current address: Intel Corporation, 2501 NW 229th Street, Hillsboro, OR, USA.

Contents

1. Introduction

Diamond is a material that possesses very good physical and chemical properties (such as extreme hardness, high thermal conductivity, high electric breakdown field, negative electron affinity and chemical inertness [1–3]). Owing to its wide energy bandgap (5.47 eV), diamond is promising for optoelectronic applications, raising the possibility of, for example, the preparation of ultraviolet (UV) light-emitting diodes (LEDs) [4, 5]. Moreover, under green external illumination, diamond exhibits relatively strong photoluminescence (PL) in the red region of the visible spectrum due to nitrogen-vacancy (N-V) defect centers with short excited-state lifetimes of the order of ns [6]. Apart from the N-V centers, which are studied the most, many other defects (color centers) [1] can be excited by UV irradiation and made to emit light in the red, green or blue spectral region. Therefore, diamond, if pumped electrically, could also be used as a 'white' LED. The main obstacle seems to be a high refractive index of diamond in the visible spectrum, strongly limiting the light extraction efficiency due to a high total internal reflection. Several methods of increasing an LED's light extraction efficiency are available: for example, flip-chip LEDs [7], thin-film rough-surface LEDs [8] or photonic crystal (PhC) LEDs (see the review on PhC LEDs in [9, 10]). The last group can be divided into the following two categories.

1. *Strongly coupled PhC*. The PhC structure penetrates the entire device and its photonic bandgap is tuned so that it spectrally overlaps with the emission spectrum of the light source, which leads to an enhancement of extraction efficiency of LEDs; this type of PhC was theoretically studied by, e.g., Fan *et al* [11] and experimentally by Fujita *et al* [12].

2. *Weakly coupled PhC*. A two-dimensional (2D) PhC etched only at the top of the waveguiding layer is used as a diffraction grating that allows outcoupling of the guided modes from the layer [13, 14]. Moreover, the angular pattern of the emission can be controlled by tuning the characteristics of the PhC.

We will now focus our attention on the latter, the weakly coupled PhC. Usually, an electrically pumped quantum well with a relatively narrow emission spectrum is used as a light source inside the photonic structure and the dimensions/properties of the PhC are chosen to fit the

3

IOP Institute of Physics **Φ** DEUTSCHE PHYSIKALISCHE GESELLSCHAFT

emitted spectrum in order to increase the extraction efficiency of such a spectrally narrow source [13–15]. In the present case of a spectrally wide emission spectrum of diamond nanocrystals, we aimed to calculate the properties of the PhC in order to efficiently extract a wide range of wavelengths from the structure, in contrast to the usual narrow spectral line extraction. In addition, the spectrally broad PL emission of nanocrystalline diamond (NCD) can be used to study the effect of the PhC over a broad spectral region.

One of the experimental methods used for the characterization of the PhC effect on the luminescence of an integrated light source is an angularly and spectrally resolved far-field radiation measurement [10, 16]. It reveals how the extraction efficiency of luminescence from a sample with the PhC differs from that without it. Moreover, the photonic band diagram (dispersion relations) within the lightcone of free photons[8], which corresponds to modes that are extended to the air surrounding the waveguide, can be extracted from the far-field radiation pattern.

Another commonly used experimental technique that can reveal the PhC band diagram inside the lightcone is the measurement of the transmitivity or reflectivity of the sample. In this case, the incident plane wave of a given frequency, polarization and incidence angle is coupled to the structure only if both the energy and in-plane wavevector match the PhC dispersions. Transmission or reflection spectra obtained from the PhC show resonant features superimposed on the Fabry–Pérot (F–P) background [17–19].

In this paper, we apply both the above-described experimental methods to a 2D PhC with a square lattice symmetry prepared at the top of an NCD layer, in order to study the PhC effect on the intrinsic PL characteristics of diamond. Combination of these methods allows the identification of modes lying in the air lightcone whose character is in agreement with a simple model of band folding of uncorrugated waveguide dispersions. These results considerably extend our previous work on the enhancement of light extraction from an NCD layer with PhC [20], and they allow us to show directly that the increase in extraction efficiency from an NCD layer is mainly due to light's coupling to leaky modes.

2. Experimental

2.1. Preparation of the sample

2.1.1. Nanocrystalline diamond (NCD) layer. An NCD layer was grown on a quartz substrate by plasma-enhanced chemical vapor deposition (PECVD). Here we will give only a brief description of this process; the details can be found in [21]. First, a cleaned quartz substrate with surface area of $10 \times 10\,mm^2$ was ultrasonically treated in a suspension of ultradispersed diamond powder for $\sim$40 min. Then, the NCD layer was grown by PECVD (microwave power 1.4 kW, 1% methane in hydrogen, total gas pressure 30 mbar and substrate temperature 560 °C). No additional nitrogen doping was applied during this process. The final thickness of the NCD film was estimated to be $\sim$417 nm by optical transmission measurements. A typical PL spectrum of these layers covers the whole visible region [22].

2.1.2. Photonic crystal (PhC) grating. PhC structure, prepared at the top of the NCD layer, consists of periodically ordered diamond nanopillars with a square lattice symmetry.

---

[8] An air lightcone is defined as a region of light frequencies $\omega > c|\mathbf{k}_\parallel|$, where $\mathbf{k}_\parallel$ is an in-plane wavevector.
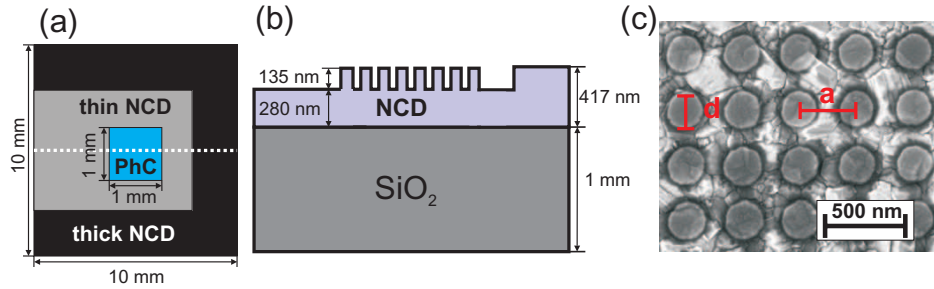
Figure 1. (a) Overall dimensional sketch of the sample, with a square PhC structure located in the middle (top view). (b) Cross-section of the sample along the white dotted line depicted in (a). (c) Top view SEM image of a part of the PhC pillar structure.

Characteristic dimensions were chosen in order to achieve effective extraction of optical guided modes within the whole NCD emission spectrum, based on suggestions given in [9, 23]. The PhC preparation process involved the following steps. The NCD films were coated with an electron-sensitive polymer, which was nanopatterned by electron beam lithography (EBL) using the e-LiNE system (Raith GmbH). The base matrix consisted of regularly repeated holes with a diameter of 250 nm ordered into a square lattice with a lattice constant of $a \sim 350$ nm. Then, a masking matrix was formed by evaporating a nickel layer on the polymer followed by the lift-off strategy. The plasma etching that followed led to the formation of geometrically ordered nanopillars having a height of 135 ± 15 nm (measured by AFM, not shown here) and a diameter of $d \sim 220$ nm (figure 1(c)—as measured by SEM). The PhC structure with a surface area of 1×1 mm^2 was placed in the middle of the NCD layer (figure 1(a)) and surrounded by the non-patterned NCD planar layer. Below the PhC, a 280 nm-thick non-structured NCD layer remained (figure 1(b)). Finally, the residual nickel mask was removed by performing wet etching in nitro-hydrochloric acid for 5 min.

2.2. Angle-resolved photoluminescence (PL) measurements

PL measurements were carried out under continuous wave excitation of 50 W cm^{-2} at 325 nm (along the normal to the sample) provided by a HeCd laser (Kimmon) with a plasma filter. An excitation laser beam with a diameter of $\sim 500\,\mu$m was focused on the PhC structure placed in the middle of the sample (figure 2(a)). The emitted light propagating in the Γ–X crystal direction and diffracted by the PhC was detected by an optical fiber bundle (3.2 mm in diameter, NA $= 0.22$) placed into a rotational holder at 23 mm distance from the sample. By mounting a circular slit (1 mm in diameter) at the input of the fiber, we obtained an angular resolution of $\sim 4°$. In order to achieve angle-resolved far-field radiation measurements with no overlap between two adjacent angular windows, the optical fiber was rotated around the sample by varying the angle α in steps of 5°. The output of the optical fiber was coupled to a spectrometer equipped with a CCD camera (Andor).

2.3. Transmission and reflection measurements

As a light source, a broadband halogen lamp was used while the detection was performed using an optical fiber mounted with a beam coupler (5 mm in diameter) at the input, and
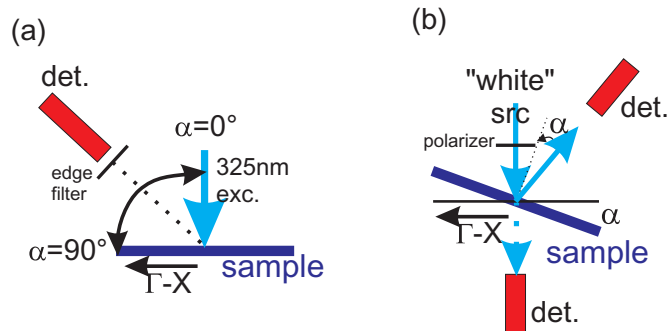
(a)

(b)

Figure 2. Sketch of the experimental setup of (a) angle-resolved PL and (b) transmission/reflection measurements.

connected to a spectrometer with an intensified CCD camera (Andor) at the output. Randomly polarized light from the source was focused on the sample through a polarizer, enabling us to carry out measurements with TE (electric field perpendicular to the plane of incidence) and TM (magnetic field perpendicular to the plane of incidence) polarized incident light. A light beam with negligible divergence (angular spread lower than $1°$) and diameter around 1 mm was obtained using a pinhole and a series of lenses. The sample was rotated by the angle α around the axis parallel to the Γ–X crystal direction, allowing us to measure transmission/reflection spectra as a function of the incidence angle with a step of $2°$ (figure 2(b)). As a result, the component of the incident wavevector parallel to the sample plane always lay in the Γ–X direction.

In all measurements, we carefully checked the position of the fiber so that it was always facing towards the center of the excitation spot. All the presented spectra were measured at room temperature and corrected for the spectral response of the detection system.

3. Types of waveguide modes and the principle of light extraction

In this section, we describe how the waveguide modes of the smooth planar layer are affected by the introduction of a shallow PhC at the top of the layer. We apply effective index theory to describe our system and substitute the PhC part of the layer with a homogeneous medium having effective refractive index $n_{eff} = 1.6$ as computed by considering the dimensions of the PhC. Thus, the PhC acts as a superstrate layer above the NCD core layer ($n_{NCD} \sim 2.41$), which is positioned at the quartz substrate ($n_s \sim 1.46$). A sketch of such a waveguiding structure is shown in figure 3(a).

Radiation of the light source can couple only to those states of field that are allowed by boundary conditions. These states, the so-called modes of the waveguide, are characterized by the in-plane wavevector $\mathbf{k}_{\parallel} = |\mathbf{k}| \sin \theta$, θ being an angle of mode propagation within the core, and the mode frequency ω, which are related through the dispersion relation (photonic band diagram) $\omega(\mathbf{k}_{\parallel})$ of the waveguide. Figure 3(b) shows a photonic band diagram of the structure depicted in figure 3(a). Based on the field profile of the mode within the waveguide, modes can be divided into guided modes, substrate, superstrate and radiation modes.

The field profile of radiation modes is extended to air and the substrate/superstrate. In the band diagram, radiation modes form a continuum of states above the air lightline $\omega = c|\mathbf{k}_{\parallel}|$ (red
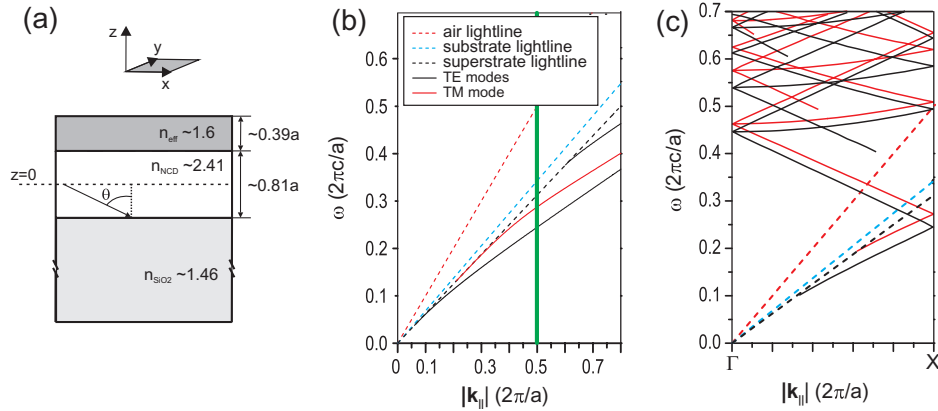
6

Figure 3. (a) Cross-section of our waveguide structure in the case where the effective index medium is considered instead of the PhC. Heights of the layers are expressed with respect to the lattice constant $a = 350$ nm. (b) Photonic band diagram of the fundamental TE and TM modes, and the higher-order TE mode for a plane waveguide shown in (a). The straight vertical green line denotes the edge of the irreducible BZ in the Γ–X crystal direction of the square lattice. (c) Photonic band diagram of the PhC with a square lattice with lattice constant a in the *weak PhC* regime. Red, blue and black dashed lines represent the air, substrate and superstrate lightlines, respectively.

dashed line in figure 3), and only these modes can be detected by the far-field measurements of PL from a smooth planar layer.

Substrate modes can radiate to the substrate but due to the total reflection at the diamond–superstrate interface, they do not propagate into air. These modes lie between the air and substrate lightline $\omega = c|\mathbf{k}_\parallel|/n_s$ (blue dashed line in figure 3). Superstrate modes are in the photonic band diagram located between the substrate and superstrate lightline $\omega = c|\mathbf{k}_\parallel|/n_{\mathrm{eff}}$ (black dashed line in figure 3).

Finally, the modes whose field profile is localized within the core and evanescent in air and the substrate/superstrate, are called the guided modes. They are characterized by an in-plane wavevector $\mathbf{k}_{\parallel\mathbf{m}}$, where m is a mode number that identifies the energy profile within the core. In the band diagram, these modes form discrete bands under the superstrate lightline.

Introducing either weakly or strongly coupled PhC into the planar layer brings the periodicity in the refractive index, which allows one to express guided modes in the form of Bloch modes, and the fundamental guided modes $\mathbf{k}_{\parallel\mathbf{m}}$ are now coupled to other harmonics $\mathbf{k}_{\parallel\mathbf{m}} + p\mathbf{G}$ by the reciprocal vector $|\mathbf{G}| = 2\pi/a$ [13], where p is an integer identifying the harmonic. Those harmonics which satisfy a diffraction condition $|\mathbf{k}_{\parallel\mathbf{m}} + p\mathbf{G}| < 2\pi/\lambda$ are diffracted by the PhC into the surrounding air during their propagation in the core. These are the so-called leaky modes[9], or guided resonances [18], which couple with the radiation modes inside the air lightcone.

[9] The term 'leaky modes' in the case of the planar uncorrugated waveguide can correspond to extended modes at the boundary of the lightcone that are traveling parallel to the boundary.

As for a PhC, the photonic band diagram is expressed along the high-symmetry directions of the irreducible Brillouin zone (BZ) of the crystal lattice and can be computed by several computational methods from the characteristics of the structure. However, the qualitative picture of the band diagram of a shallow PhC at the top of the waveguiding layer can be derived from dispersion relations of the planar uncorrugated waveguide by folding the bands at the edges of the irreducible BZ [9]—the edge of the BZ in the Γ–X direction of the square lattice is in figure 3(b) denoted by the green vertical line.

The folded photonic band diagram in the Γ–X crystal direction of a square lattice of the planar waveguide (figure 3(c)) was computed by the finite-difference time-domain method [24]. A light source positioned in the plane $z = 0$ and having either an electric or a magnetic field parallel to the layer was used in order to excite TE (black curves) or TM modes (red curves). TM modes have the same shape of dispersion curve as TE modes but slightly shifted towards higher frequencies. One can clearly see folding of the first-order TE and TM modes at the edge of the BZ, which leads to the fact that discrete bands—leaky modes—appear above the air lightline. Other bands arising from folding of higher-order TE and TM modes start at higher frequencies. As they occur above the air lightline, they can be accessible by the far-field PL measurements. A qualitatively very similar band diagram can be computed for the Γ–M crystal direction, leading to a similar physical phenomenon (coupling to leaky modes) as in the Γ–X direction. Photonic properties in this direction are not studied here; however, it should be noted that the extraction efficiency in this direction would be dependent on the leaky-mode band structure and consequent spectral overlap with the emission of the diamond, along with the modal coupling efficiencies.

The diffraction efficiency of the PhC depends strongly on the spatial overlap of the guided mode with the PhC [9]. Therefore, guided modes that penetrate into the PhC are well extracted, whereas modes that are strongly confined in the core are diffracted only poorly. Also the lattice spatial symmetry affects the extraction properties of the PhC. It was shown that the lattice with square symmetry allows high extraction efficiency in a larger wavelength and angular bandwidth compared to the triangular lattice, which mostly extracts in the direction normal to the sample plane [15]. In addition to guided modes, the substrate modes can also interact with the PhC and thus be diffracted. However, most of these modes have low field overlap with the PhC and are usually lost in the substrate.

4. Experimental results and discussion

4.1. Enhancement of PL extraction

Angular far-field PL radiation patterns for both the planar 417 nm-thick NCD layer and the PhC in the Γ–X direction are shown in figures 4(a) and (b), respectively (note the identical intensity scale). The PL spectra of the planar NCD layer (figure 4(a)) exhibit a relatively flat profile of emission intensities across the whole visible region with two broad PL maxima for each detection angle α due to the F–P resonances of radiation modes between the diamond–silica and the diamond–air interface (figures 4(c) and (d)—red line). The reason for the very poor light extraction is that most of the light emitted from the diamond defects in the uncorrugated NCD layer is coupled either to guided or substrate modes and only ∼4% of the overall light power reaches air.
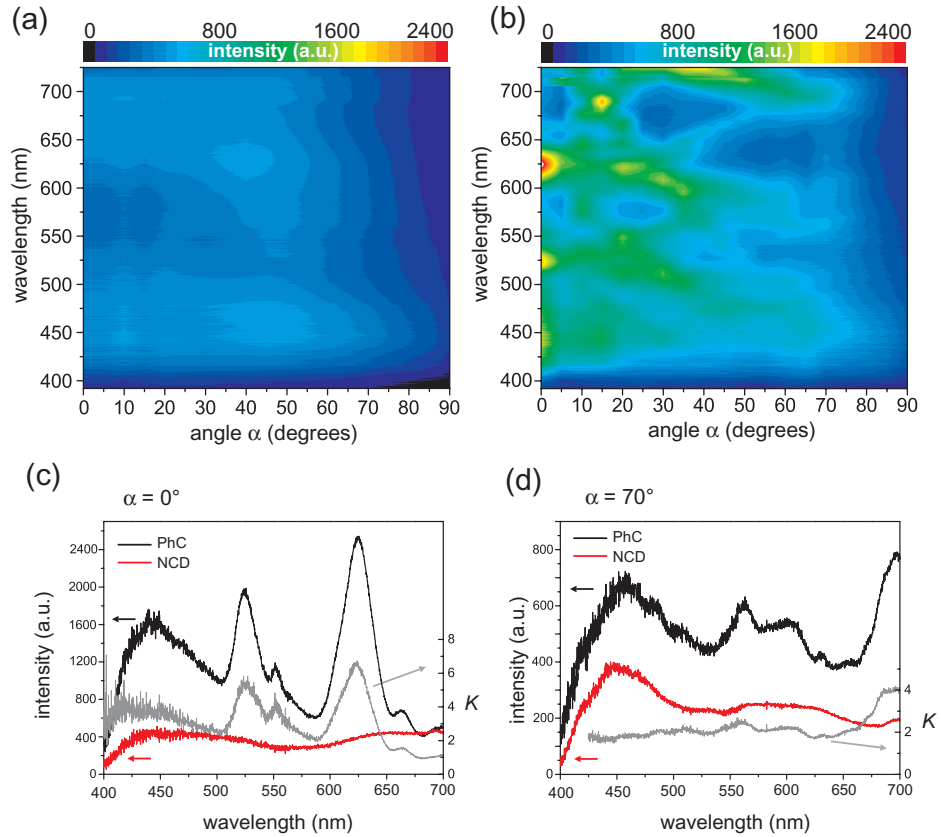
Figure 4. Angular far-field patterns of PL emitted in the Γ–X direction from (a) the planar 417 nm-thick NCD layer itself and (b) the NCD layer with PhC structure. Profile graphs of PL taken from (a) and (b) for the detection angle $\alpha = 0°$ (c) and $\alpha = 70°$ (d), and the relevant ratio K of the PL intensities of the PhC structure and the uncorrugated NCD layer.

On the other hand, PL spectra of the NCD layer with the PhC strongly dependent on wavelength and detection angle, exhibit a distinct structure composed of several peaks for each detection angle superimposed on a broad F–P background (figures 4(c) and (d)—black line). We can assume that the intensity I_{PhC} detected from the PhC is related to the PL intensity from the uncorrugated NCD layer I_{NCD} via the relation

$$I_{PhC}(\lambda, \alpha) = K(\lambda, \alpha) I_{NCD}(\lambda, \alpha), \tag{1}$$

where $K(\lambda, \alpha)$ is a factor depending on the parameters of the PhC and consisting of several contributions, which will be discussed further. It also defines the enhancement of PL extraction efficiency from the PhC compared to the uncorrugated layer. Maximal, up to six-fold, enhancement was detected for the direction normal to the sample ($\alpha = 0°$, figure 4(c)), which occurs due to the degeneracy of leaky modes at the Γ-point. Even though most of the extracted light power is focused into the directions close to the sample normal, more than two-fold enhancement over the whole spectral region is still present for larger detection angles as depicted

for $\alpha = 70°$ in figure 4(d). The PL enhancement K clearly arises from the presence of the PhC and may comprise several effects that will be discussed later.

The origin of the PL from the NCD layer is presumably due to dislocations and other defects that are introduced within grains [25] (either in their volume or at their surface) of which the layer is composed. Therefore, simple variations in geometry themselves may play a role in the enhancement of extraction efficiency. First, an active surface area $S_0 = 1\,\text{mm}^2$ of the NCD planar layer is increased by its nanopatterning to the value $S = S_0 + \Delta S$, where $\Delta S \sim 0.79\,\text{mm}^2$, which leads to an increased amount of light-emitting centers positioned at the surface of the pillars emitting directly to the surrounding air. We shall, in crude approximation, assume that the changes in surface area and number of surface centers are related to each other linearly. Next, we will consider only the following three main processes to occur. Part of the light emitted from the surface defects goes directly to the detector and another part gets diffracted on surrounding pillars either into air or into the underlying NCD layer. We shall assume all three processes have comparable weight due to their randomness. Therefore, only two thirds of the emitted light will contribute to the enhancement due to increased active surface. The remaining one third will penetrate into the layer.

Secondly, when forming nanopillars on the layer, part of the material was taken away, decreasing the active volume of the PhC structure with the underlying layer from a value V_0 of the uncorrugated layer to a smaller value V. Considering our dimensions of the PhC structure (figure 1(b)), we obtain a ratio $\Delta V / V_0 \sim -0.23$, where $\Delta V = V - V_0$.

Thirdly, the coupling of the excitation laser light into the layer may be enhanced by the presence of the PhC [26]. The incident 325 nm light becomes diffracted on the periodically ordered nanopillars and thus excites a larger amount of the volume of the material than is the actual volume of the PhC structure. Its contribution can be expressed with the factor $C_{\text{exc}} \sim 1.3$, whose value was estimated from a ray optics model of diffraction on the grating. Taken together, we can express the parameter K as

$$K(\lambda, \alpha) = A_{\text{PhC}}(\lambda, \alpha) C_{\text{exc}} [1 + \Delta V / V_0]^{\frac{2}{3}} [1 + \Delta S / S_0] \sim 1.2\, A_{\text{PhC}}, \tag{2}$$

where A_{PhC} is a parameter that characterizes the contribution of the PhC effect to the overall enhancement. This relation assumes that the probability of emission from the defect positioned at the surface of the layer and from the defect located inside is similar. This is reasonable because the origin of these defects is believed to be identical, both being introduced during the preparation process [25]. If we consider the experimental value $K \in (2\text{–}6)$, we get $A_{\text{PhC}} \in (1.7\text{–}5)$, which produces a rather high enhancement of extraction efficiency due to the influence of PhC on the guided modes as described in section 3. The remaining effects cause merely an increased background in PhC PL spectra.

4.2. Photonic band diagram analysis

Leaky modes manifest themselves as relatively narrow minima in the transmission spectra superimposed on slowly varying F–P resonances [19]. The depth of these minima reflects the efficiency of the light coupling into the structure, and at the same time it indicates how effectively the light generated inside the structure will interact with the PhC and be outcoupled from the structure. On the other hand, in reflection spectra, Fano-like shaped maxima occur at the same spectral positions. This effect is demonstrated for our PhC sample in figures 5(a) and (b) for TE and TM polarized light incident at the angle $\alpha = 20°$, respectively. From a comparison
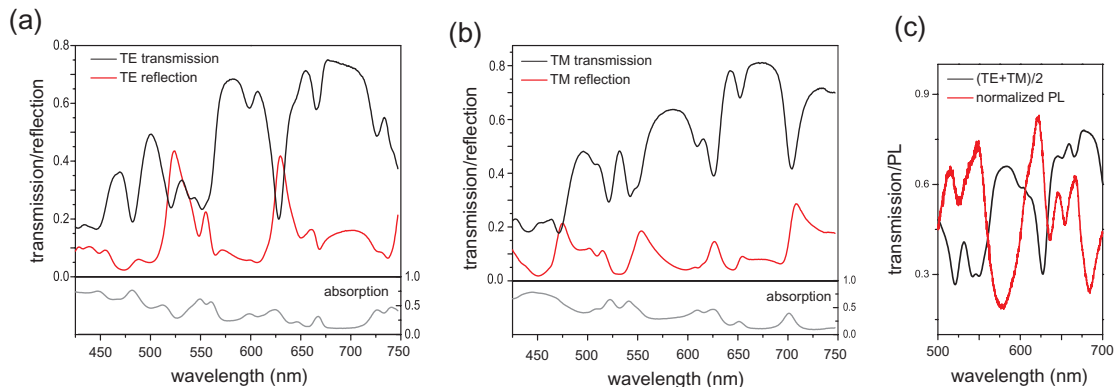
Figure 5. Transmission, reflection and absorption $(1 - \text{transmission} - \text{reflection})$ spectra from the PhC obtained with (a) TE and (b) TM polarized light incident at $\alpha = 20°$ along the Γ–X symmetry direction. (c) Comparison of normalized PL spectra and averaged TE and TM transmission spectra for $\alpha = 20°$ within the narrow spectral region.

of these two figures, we see that each light polarization excites different modes based on their symmetry. The gray curve depicts absorption given by the relation $(1 - \text{transmission} - \text{reflection})$ and it slowly rises towards the lower wavelengths, suggesting that the NCD layer is more absorbing in the blue spectral region. Furthermore, peaks in absorption being at the spectrally same position as leaky modes suggests that some part of the incident coupled light remains in the structure without being outcoupled forward or backward.

Direct comparison of the normalized PL emission spectra with the averaged TE and TM transmission curves [(TE + TM)/2] of the PhC for $\alpha = 20°$ (figure 5(c)) shows that the PL maxima occur at nearly the same spectral position as transmission minima and so at the same position as leaky modes. It indicates that the light outcoupling from the PhC occurs via the same radiative channel, leaky modes, as the coupling into the structure.

A PhC band diagram (figure 6(a)), in the angle–wavelength representation, within the investigated spectral region in the Γ–X symmetry direction was derived from the PL spectra shown in figure 4(b) by normalizing to the maximum at each angle and by correcting for the source spectrum profile obtained from the uncorrugated layer. Moreover, it is overlaid with the computed photonic band diagram derived from TE dispersion relations shown in figure 3(c) by converting its axes into the angle–wavelength representation and having the bands that occur in the measured band diagram as the most intense ones, highlighted by black lines. Despite the simple approximation of the effective refractive index used in the calculation in order to describe the real structure, the shape of the measured bands is very well reproduced in the simulation. The slight difference in the spectral position of computed and measured bands was compensated by shifting the simulated bands to match the spectral position of measured ones. TM modes are not shown in order to keep the diagram lucid; however, they would appear shifted towards lower wavelengths with the same dispersion behavior as TE bands.

The photonic band diagram derived from PL measurements is in good agreement with a photonic band diagram (figure 6(b)) derived from unpolarized transmission spectra measured for angles 0°–26° by normalizing on the absorption profile of the NCD.
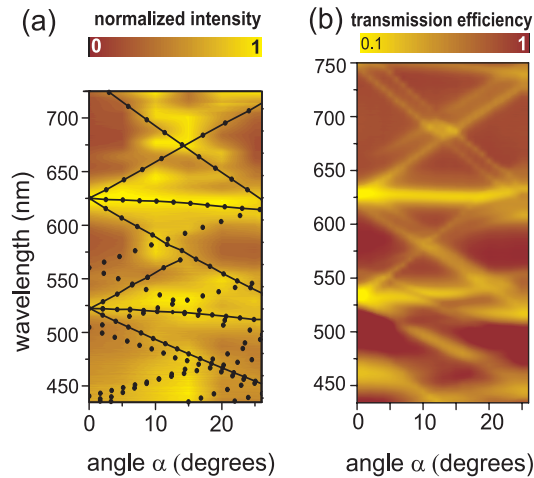
Figure 6. Photonic band diagram of the PhC in the α–λ representation: (a) derived from the PL measurements shown in figure 4(b) and overlaid with the calculated TE band diagram shown in figure 3(c); and (b) derived from transmission spectra of the PhC.

Relatively narrow photonic bands of leaky modes starting at ∼625 nm and ∼530 nm can be identified in both the diagrams. For the wavelengths below 500 nm, PL peaks or similarly transmission minima lose their fine structure and become broader but still, even for them, PL extraction remains enhanced compared with PL of the smooth layer. This suggests that the broad band starting at ∼460 nm arises from overlapping of many leaky modes located close together in the band diagram, which is also supported by the results of photonic band diagram simulation in which densely positioned modes are present in the blue spectral region.

In the spectral region of 630–750 nm, bands closely spaced and parallel to each other can be seen, which arises due to TE–TM splitting. Moreover, it is worth noting that diffraction efficiency is very high in areas where the crossing between two bands occurs (compare figures 4(b) and 6(b)).

We can thus summarize that the agreement between theory and experiment signifies that we still operate in *the weak PhC* regime even though the PhC structure is relatively deeply etched into the NCD layer and that the extraction of the light emitted inside the NCD layer is enhanced mainly due to the light being coupled to leaky modes.

5. Conclusions

In conclusion, we demonstrated up to six-fold enhancement of extraction of intrinsic PL from an NCD layer by nanopatterning its top part into a PhC. We tuned the design of the PhC so that the enhancement was high within a broad spectral region. We showed that the physics underlying this effect consists in the fact that the PhC structure, on the one hand, serves as a coupler of the excitation laser radiation into the structure allowing efficient excitation of diamond defects and, more importantly, acts as a Bragg diffraction grating, which diffracts light emitted from the diamond defects into air. The complementarity between the angular far-field

PL and transmission measurements of the PhC was demonstrated, and the photonic diagram extracted from both of these measurements is in qualitative agreement with the simulated one. The results of this study might be useful for applications in the field of optics and optoelectronics while tuning and increasing the emission properties of diamond LEDs or can be applied in the construction of light couplers to NCD waveguides.

Acknowledgments

References

[1] Zaitsev A M 2001 *Optical Properties of Diamond: A Data Handbook* (Berlin: Springer)
[2] Pan L S (ed) 1995 *Diamond: Electronic Properties and Applications* (New York: Kluwer Academic)
[3] Field J E (ed) 1992 *Properties of Natural and Synthetic Diamond* (New York: Academic)
[4] Koizumi S, Watanabe K, Hasegawa M and Kanda H 2001 Ultraviolet emission from a diamond pn junction *Science* **292** 1899
[5] Takeuchi D, Makino T, Kato H, Ogura M, Tokuda N, Oyama K, Matsumoto T, Hirabayashi I, Okushi H and Yamasaki S 2010 Electron emission from a diamond (111) p–i–n(+) junction diode with negative electron affinity during room temperature operation *Appl. Phys. Express* **3** 041301
[6] Gruber A, Dräbenstedt A, Tietz C, Fleury L, Wrachtrup J and von Borczyskowski C 1997 Scanning confocal optical microscopy and magnetic resonance on single defect centers *Science* **276** 2012–4
[7] Wierer J J *et al* 2001 High-power AlGaInN flip-chip light-emitting diodes *Appl. Phys. Lett.* **78** 3379
[8] Fujii T, Gao Y, Sharma R, Hu E L, DenBaars S P and Nakamura S 2004 Increase in the extraction efficiency of GaN-based light-emitting diodes via surface roughening *Appl. Phys. Lett.* **84** 855–7
[9] Wiesmann Ch, Bergenek K and Schwarz U T 2009 Photonic crystal LEDs—designing light extraction *Laser Photonics Rev.* **3** 262–86
[10] Matioli E and Weisbuch C 2010 Impact of photonic crystals on LED light extraction efficiency: approaches and limits to vertical structure designs *J. Phys. D: Appl. Phys.* **43** 354005
[11] Fan S, Villeneuve P R, Joannopoulos J D and Schubert E F 1997 High extraction efficiency of spontaneous emission from slabs of photonic crystals *Phys. Rev. Lett.* **78** 3294–7
[12] Fujita M, Takahashi S, Tanaka Y, Asano T and Noda S 2005 Simultaneous inhibition and redistribution of spontaneous light emission in photonic crystals *Science* **308** 1296–8
[13] Wierer J J, David A and Megens M M 2009 III-nitride photonic-crystal light-emitting diodes with high extraction efficiency *Nat. Photonics* **3** 163–9
[14] Bergenek K, Wiesmann Ch, Wirth R, O'Faolain L, Linder N, Streubel K and Krauss T F 2008 Enhanced light extraction efficiency from AlGaInP thin-film light-emitting diodes with photonic crystals *Appl. Phys. Lett.* **93** 041105
[15] Ganesh N, Block I D, Mathias P C, Zhang W, Chow E, Malyarchuk V and Cunningham B T 2008 Leaky-mode assisted fluorescence extraction: application to fluorescence enhancement biosensors *Opt. Express* **16** 21626
[16] Boroditsky M, Vrijen R, Krauss T F, Coccioli R, Bhat R and Yablonovitch E 1999 Spontaneous emission extraction and Purcell enhancement from thin-film 2-D photonic crystals *J. Lightwave Technol.* **17** 2096–112

13

IOP Institute of Physics **Φ** DEUTSCHE PHYSIKALISCHE GESELLSCHAFT

[17] Astratov V N, Whittaker D M, Culshaw I S, Stevenson R M, Skolnick M S, Krauss T F and De La Rue R M 1999 Photonic band-structure effects in the reflectivity of periodically patterned waveguides *Phys. Rev.* B **60** 16255–8

[18] Fan S and Joannopoulos J D 2002 Analysis of guided resonances in photonic crystal slabs *Phys. Rev.* B **65** 235112

[19] Ganesh N, Zhang W, Mathias P C, Chow E, Soares J A N T, Malyarchuk V, Smith A D and Cunningham B T 2007 Enhanced fluorescence emission from quantum dots on a photonic crystal surface *Nat. Nanotechnol.* **2** 515–620

[20] Ondič L, Dohnalová K, Ledinský M, Kromka A, Babchenko O and Rezek B 2011 Effective extraction of photoluminescence from a diamond layer with a photonic crystal *ACS Nano* **5** 346–50

[21] Kromka A, Rezek B, Remes Z, Michalka M, Ledinsky M, Zemek J, Potmesil J and Vanecek M 2008 Formation of continuous nanocrystalline diamond layers on glass and silicon at low temperatures *Chem. Vapor Depos.* **14** 181–6

[22] Dzurnak B, Trojanek F, Preclikova J, Kromka A, Rezek B and Maly P 2009 Subgap photoluminescence spectroscopy of nanocrystalline diamond films *Diam. Relat. Mater.* **18** 776–8

[23] David A, Benisty H and Weisbuch C 2007 Optimization of light-diffracting photonic-crystals for high extraction efficiency LEDs *J. Disp. Technol.* **3** 133–48

[24] Oskooi A F, Roundy D, Ibanescu M, Bermel P, Joannopoulos J D and Johnson S G 2010 MEEP: a flexible free-software package for electromagnetic simulations by the FDTD method *Comput. Phys. Commun.* **181** 687–702

[25] Philip J, Hessa P, Butler J E, Chattopadhyay S, Chen K H and Chen L C 2003 Elastic, mechanical and thermal properties of nanocrystalline diamond films *J. Appl. Phys.* **93** 2164

[26] Erchak A A, Ripin D J, Fan S, Rakich P, Joannopoulos J D, Ippen E P, Petrich G S and Kolodziejski L A 2001 Enhanced coupling to vertical radiation using a two-dimensional photonic crystal in a semiconductor light-emitting diode *Appl. Phys. Lett.* **78** 563

Chapter 6

Photoluminescence of silicon nanocrystals combined with a photonic crystal

In this chapter, results regarding the main goal of this thesis that may be expressed as "Towards an enhancement of light emission and optical gain of silicon nanocrystals" are presented. For that to be addressed, we investigated the optical properties of SiNCs combined with photonic crystal slabs using two types of matrices. First, a NCD layer was used as a matrix for SiNCs that were prepared in the form of powder by electrochemical etching (see Ref. [124], attached as Enclosure 6.3). Second, SiNCs embedded in a SiO_2 matrix were studied in Ref. [125], attached as Enclosure 6.4.

6.1 Photoluminescence of silicon nanocrystals on a diamond photonic crystal slab

Experimentals

Despite many attempts, we were not able to embed the electrochemically prepared SiNCs directly into the bulk of the NCD matrix. This would be favorable, as NCD is an efficient heat conductor and thus high excitation optical power might be employed to pump SiNCs. The main obstacle was the growth temperature of our NCD layers. Even though it is relatively low ($\sim 300°C$) compared to other approaches, it is still high for the SiNCs in the sense that they simply stop to exhibit luminescence when heated to such a temperature.[1] Therefore, a different approach was applied.
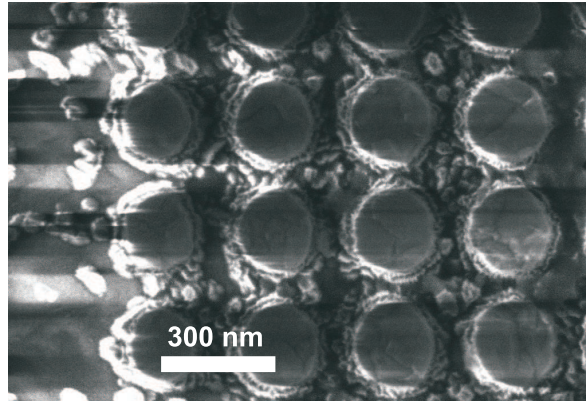
The powder of SiNCs was drop-casted directly on the surface of a NCD photonic crystal slab. In order to obtain the modification of the PL spectrum of the deposited SiNCs, it is desirable to have the spectral overlap of the SiNCs emission with the leaky modes of the photonic crystal slab. Let us recall that the NCD photonic crystal slab discussed in Chapter 5 was designed such that its leaky modes spanned over the whole visible range, therefore these leaky modes certainly overlap also the broad emission of our SiNCs, which (under 325 nm excitation) peaks at around 600 nm. Thanks to that the very same photonic crystal sample as studied in Chapter 5 could be used in experiments with SiNCs. Just to remind the reader, the photonic crystal comprised columns with the diameter $d \sim 220$ nm and the height of 135 ± 15 nm. The columns were etched on the top of the ~ 420 nm thick NCD layer and possessed the square symmetry with the lattice constant $a \sim 350$ nm. The deposited SiNCs partially filled the air voids between the diamond columns as shown in the SEM image in Fig. 6.1.

Results and Discussion

In Ref. [124], attached as Enclosure 6.3, the analysis of the NCD photonic crystal slab, already presented in Chapter 5, is extended by showing the polarization resolved photonic band diagrams measured along the $\Gamma-X$ and $\Gamma-M$ directions of the sample. The measured band diagrams show an excellent agreement with the theoretical ones computed by the RCWA technique (see Fig. 2 in Enclosure 6.3). Furthermore, an explanation of the symmetry-defined coupling of an externally incident light into the leaky modes of the photonic crystal slab is given in Enclosure 6.3 by investigating the electromagnetic mode profiles. The experimental setup and the simulation method are discussed in Chapter 5, Section 5.1.

---

[1]The sample was prepared such that a thin (~ 50 nm) diamond layer was grown first. Then, the powder of SiNCs was drop-casted on its surface. Finally the layer of SiNCs was overgrown by diamond in the furnace. After this step, however, the SiNCs did not exhibit any light emission under external pumping.

300 nm

By comparing the photonic band diagram (Fig. 2 in Enclosure 6.3) with the emission spectrum of our SiNCs (Fig. 6.2 in this Chapter—grey line), it is clear that the leaky modes at around 625 nm at the Γ-point will be involved in the light-matter interaction between the light emitted by SiNCs and the photonic crystal slab. The main result of this study, shown in Fig. 6.2, proves that this is indeed the case. This figure plots the emission spectrum of SiNCs drop-casted on the photonic crystal slab surface as detected in the direction normal to the sample plane, either from above (black curve) or from below (red curve) the sample. Compared to the PL spectrum of SiNCs deposited on a reference planar layer (grey curve), we can see that the maximum of the PL signal detected from above the sample red-shifts due to the fact that the light emitted by SiNCs is coupled into the leaky modes of the photonic structure and then re-radiated back towards the detection. Two other small local maxima (black arrows in Fig. 6.2) arise due to the same reason. On the other hand, in the PL spectrum detected from below the sample (through the substrate), minima arise at the positions of the leaky modes. Indeed, light re-radiated above must be missing in the spectrum of light propagating through the substrate.

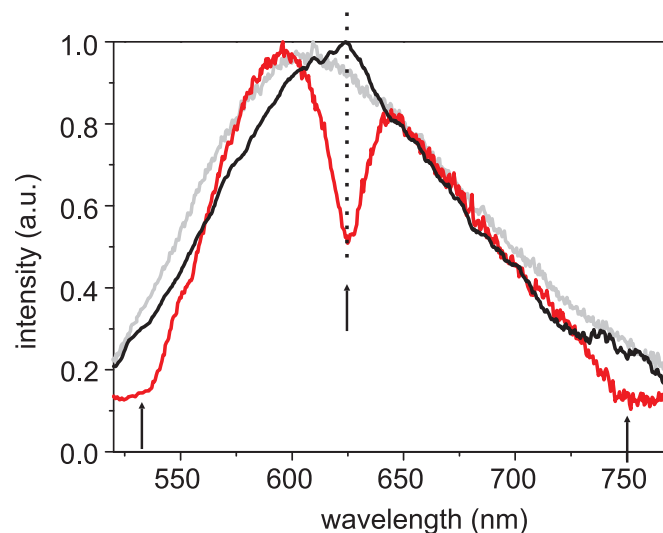Figure 6.2: The emission spectrum of SiNCs drop-casted on a thick glass (quartz) layer (grey curve) compared to the emission of SiNCs drop-casted on a NCD photonic crystal slab. In the latter case, PL was detected either from above (black curve) or from below (red curve) the sample. The vertical arrows point at the Γ-point leaky modes of the photonic crystal slab. Adapted from Ref. [124]

Unfortunately, we were not able to characterize this effect quantitatively due to the inability to experimentally ensure the same distribution density of SiNCs on the photonic crystal and on the reference planar layer. Nevertheless, if a homogeneous distribution and similar densities were achieved, the PL intensity of SiNCs on the photonic crystal would be enhanced as a consequence of the fact that the part of light directed towards the substrate is redirected upwards through the interaction with the photonic crystal. Such a PL enhancement scheme may be applied for example in biosensing in case that very low concentration of quantum dots as probes must be used. However, in order to make this effect attractive enough, the optical quality of NCD layers needs to be improved. Finally, it should be noted that we were not able to conduct any excitation power dependent measurements of the PL from SiNCs because the deposited SiNCs were burning upon high power excitation.

6.2 Enhanced light extraction from a silica photonic crystal with embedded silicon nanocrystals

Experimentals

A sample investigated in this study was prepared by employing two main steps. First, SiNCs forming a thin ($\sim$800 nm) waveguiding layer were created by Si$^+$ implantation into a polished silica, followed by a high-temperature annealing (for details see Ref. [126]). The embedded layer of SiNCs was positioned close beneath the silica polished surface. Samples were fabricated by Dr. S. Cheylan at the Australian National University in Canberra, for which we would like to express our thanks. Second, the same technological approach as was used to prepare the NCD photonic crystal slab (described in Chapter 5) was adapted to create a periodical pattern on the top of the implanted silica plate. Details and parameters of the method can be found in Ref. [125], attached as Enclosure 6.4.

The dimensions of a 2D photonic crystal were computed using the RCWA simulation method, again, with the goal to achieve a spectral overlap of leaky modes with the PL spectrum of the embedded SiNCs in order to obtain extraction enhancement of their light emission. Compared to diamond (refractive index $\sim$ 2.4), the SiNCs-rich layer have much lower refractive index (peaking at about 1.6 in the visible range) and its spatial profile varies across the waveguiding layer. Moreover, the PL spectrum of the embedded SiNCs peaks at around 775 nm, thus it is red-shifted compared to the electrochemically prepared SiNCs, discussed in the previous section. All this was successfully addressed when modeling the parameters of the photonic structure.

Beside the extraction enhancement mechanism, we also wanted to test the possible increase of the optical gain of SiNCs and the possible onset of stimulated emission taking advantage of the existence of the low group velocity modes in photonic crystal slabs. Because these modes occur mostly at the band edges, the overlap of the SiNCs emission spectrum with the photonic crystal modes at the Γ-point was needed. This was achieved for a sample composed of a square lattice of columns with the following parameters: the lattice constant $a \sim 500$ nm, the columns diameter $d \sim 265$ nm and the columns height $h \sim 300$ nm. For these parameters it is expected (based on our simulation) that the enhanced emission should out-couple in the direction normal to the sample plane as it is in the case of vertically-emitting DFB lasers. It should be finally noted, that within the existing resolution of electron beam lithography employed for the fabrication of our photonic crystals, we were not able to prepare samples that would allow enhancement of the properly guided modes (not the leaky modes), as it is in the case of first-order DFB lasers, where stimulated emission out-couples from the laser

edge. For that to be achieved, much lower lattice constants or a material with much higher refractive index would be needed.

Results and Discussion

In Ref. [125], attached as Enclosure 6.4, it is experimentally evidenced by mesuring the angle-resolved transmission and PL spectra that the Γ-point leaky modes of the silica photonic crystal slab prepared with the aforementioned dimensions overlap the emission spectrum of the embedded SiNCs. Owing to that, light emitted from SiNCs can be extracted to air via these leaky modes. At particular wavelengths, it was achieved up to 8-fold extraction enhancement of the vertically-out-coupled PL (Fig. 4(a) in Enclosure 6.4) and up to 4-fold enhancement for the emission angles up to $\sim 30°$ for both high-symmetry crystal directions (Fig. 3 in Enclosure 6.4) compared to the planar SiNCs-rich silica layer. Such a high enhancement arises also from the spatial overlap of the leaky modes with the SiNCs-rich layer which allows efficient feeding of the modes. This is somehow natural as the SiNCs-rich layer forms the optical waveguide.

However, even though the Γ-point band edge modes overlapped with the emission spectrum of SiNCs, we did not detect any onset of stimulated emission with the increasing excitation optical power. This most probably arises from the fact that the optical gain of these SiNCs is too low and is not, even with the help of the photonic crystal, able to outweigh FCA losses.

6.3 Enclosure

Diamond photonic crystal slab: Leaky modes and modified photoluminescence emission of surface-deposited quantum dots

L. Ondič, O. Babchenko, M. Varga, A. Kromka, J. Čtyroký and I. Pelant

SCIENTIFIC REPORTS

Diamond photonic crystal slab: Leaky modes and modified photoluminescence emission of surface-deposited quantum dots

Lukáš Ondič[1,2,3], Oleg Babchenko[1], Marián Varga[1], Alexander Kromka[1], Jiří Čtyroký[4] & Ivan Pelant[1]

[1]Institute of Physics, Academy of Sciences of the Czech Republic, v.v.i., Cukrovarnická 10, 162 53, Prague 6, Czech Republic, [2]Faculty of Mathematics and Physics, Charles University, Ke Karlovu 3, 121 16 Prague 2, Czech Republic, [3]IPCMS–DON Unité Mixte, UMR 7504, CNRS–ULP, 23 rue du Loess, BP 43, 67034 Strasbourg Cedex 2, France, [4]Institute of Photonics and Electronics, Academy of Sciences of the Czech Republic, v.v.i., Chaberská 57, 182 51 Prague 8, Czech Republic.

Detailed analysis of a band diagram of a photonic crystal (PhC) slab prepared on a nano-diamond layer is presented. Even though the PhC is structurally imperfect, the existence of leaky modes, determined both theoretically and experimentally in the broad spectral region, implies that an efficient light interaction with a material periodicity occurs in the sample. It is shown that the luminescence emission spectrum of a light source placed directly on the PhC surface can be modified by employing the optical modes of the studied structure. We stress also the impact of intrinsic optical losses of the nano-diamond on this modification.

P hotonic crystal (PhC) slabs are structures of finite height which are periodically patterned in the dielectric constant in two dimensions[1,2]. Light can be guided in these structures, however, compared to uncorrugated (smooth) slabs, guided modes can also occur due to the band folding at the Brillouin zone (BZ) edges above the air light line and thus can radiate out from the structure[3,4]. These radiative modes are then called guided resonances[5] or leaky modes. The physical mechanism of the light extraction can be easily understood by considering the Bragg diffraction of the guided modes on the periodic structure. Inversely, light of a suitable wavelength and an incident angle can be coupled into the structure. This effect can be utilized to experimentally determine the leaky mode band diagram of the structure from transmission and/or reflection measurements[6–8]. When the external spectrally broad light is incident on the periodic structure, it is diffracted into forward and backward direction, and waves with the particular wavelengths propagating under suitable angles of incidence can couple to leaky modes of the PhC (defined by the parameters of the structure), and can be guided in the layer. When propagating in the plane of the PhC, they are again diffracted into forward (in the direction of the incident beam) and backward direction and radiate out from the structure—thus the name leaky modes. The zeroth order transmitted wave is exactly out of the phase (π-shifted) with respect to the modes outcoupled in the forward direction leading into the destructive interference and thus into the deep minima in the transmission efficiency[9]. Symetrically, maxima will occur at the spectral position of leaky modes in the reflection spectra. Due to the Fano-like shape of these resonances, minima in transmission can be slightly spectrally shifted with respect to the maxima in reflection[10].

Here we present a detailed study of the leaky modes of a nanocrystalline diamond (NCD) PhC slab by investigating polarization resolved photonic band diagrams determined from experiment and simulation. We use an illustrative description of the symmetry based coupling to leaky modes by correlating their energy profiles with the band diagram. Next, the PhC effect on the photoluminescence (PL) of quantum dots (QDs) placed on the surface of the PhC slab is studied, indicating the ability to modify the shape of the PL spectrum and shift the PL emission maximum to a different energy driven by the dimensions of the PhC, and at the same time to filter part of light emitted from the QDs. In order to obtain this effect, the PL emission spectrum of the QDs must spectrally overlap with the leaky modes of the PhC. These effects can be utilized, e.g. to manipulate the photonic properties or to enhance the sensitivity of diamond-based sensors.
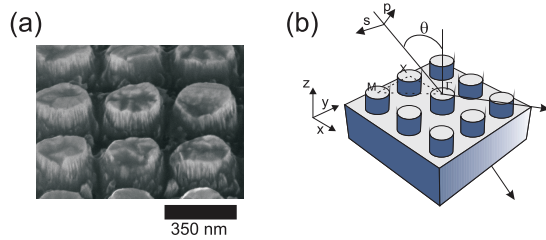
Figure 1 | SEM image and the transmission measurement setup. (a) 45° angle-view SEM image of the PhC sample. (b) Transmission measurement setup. Either S- or P-polarized collimated light is incident at the angle θ along the Γ−X or Γ−M crystal directions, respectively. Only the NCD layer with patterned surface without a substrate is shown.

Results

The measurements were realized on a NCD layer with periodically textured surface in two dimensions (Fig. 1(a)). NCD columns with the diameter $d \sim 280$ nm and the height of 135 ± 15 nm were ordered into the square lattice with the lattice constant $a \sim 350$ nm (as obtained from the SEM measurements). The total height of the layer with the columns was 420 ± 15 nm. The layer was seated on the transparent quartz substrate allowing to perform transmission measurements with negligible losses in the substrate. Details of the preparation process and positive results on enhanced extraction efficiency of the intrinsic diamond PL from the PhC were published elsewhere[11,12]. Sample dimensions, namely column diameter, stated here differ slightly from those published in[11,12] due to more precise and accurate SEM measurement performed with a conductive polymer.

The measurements were performed with the S- (electric field perpendicular to the plane of incidence) and P- (electric field in the the plane of incidence) polarized light incident along the Γ−X and Γ−M

crystal directions using the setup sketched in Fig. 1(b). Each polarization couple to different leaky modes based on their mutual symmetry. As it follows from the discussion above, relatively deep minima occur in transmission spectra at the position of leaky modes. The measured transmission curves were converted into 2D maps forming photonic band diagrams of leaky modes in angle-wavelength representation (Fig. 2(a) and (c) for the S- and P-polarized incident light, respectively). In parallel with these experiments, photonic band diagrams of leaky modes were also numerically calculated using the Rigorous Coupled Wave Analysis technique. The PhC dimensions were slightly adjusted within their detection error in order to obtain the best spectral coincidence of the simulated and measured leaky resonances at the normal incidence and at another arbitrary incident angle. As it is apparent from the comparison of the simulated (Fig. 2(b) and (d)) and measured (Fig. 2(a) and (c)) band diagrams, excellent qualitative and even quantitative agreement in a broad spectral range was obtained between the experiment and theory using the following geometrical dimensions $a = 350$ nm, $d = 280$ nm, total height 425 nm, column height 150 nm. Nevertheless, small differences occur due to the following. First, the refractive index dispersion and optical losses in the diamond were not included in the simulation and only a real constant value of refractive index $n = 2.41$ was used. Second, simulation does not take into account the structural imperfection of the columns of the real structure. And third, the computed photonic band diagrams show also spectrally very narrow features which are unresolved in the measured spectra due to the limited spectral resolution of the detection system.

The computed photonic band diagram plotted in Fig. 3(a) includes all the leaky modes of the structure and is zoomed around the first TE (transverse electric) and TM (transverse magnetic) resonance at the Γ point. Here the TE mode is the mode of which the component of the electric field parallel with the sample plane and perpendicular to the mode propagation direction carries most of its energy. In case of the mode propagating in the x-direction, it is E_y component. On the
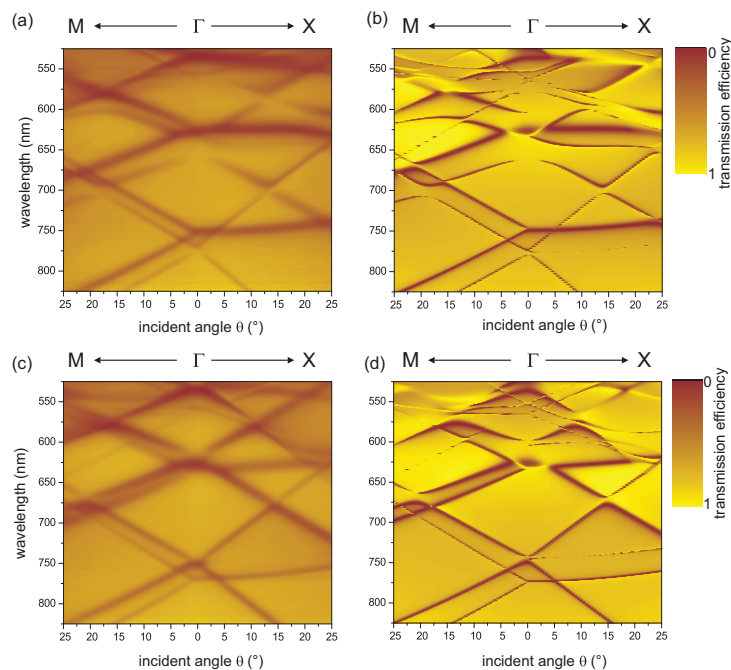

Figure 2 | Photonic band diagrams of the PhC leaky modes. Photonic band diagrams of the leaky modes derived from the transmission spectra— measured (left column) and computed (right column)—in the Γ−M and Γ−X directions with the (a,b) S- and (c,d) P-polarized incident light.
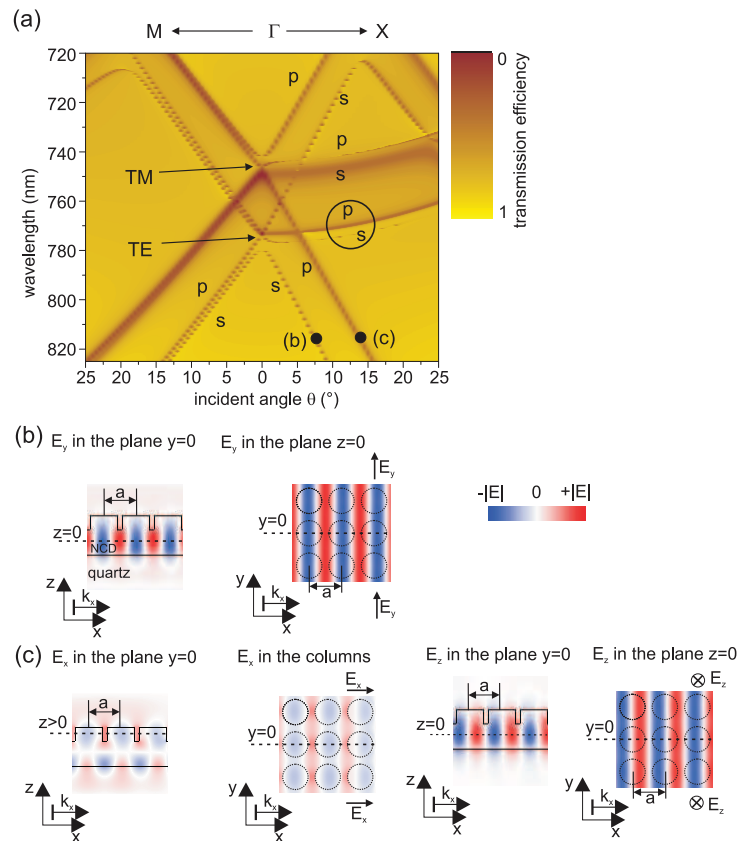
Figure 3 | Zoomed-in computed photonic band diagram and the electric field profiles of the modes. (a) Zoom into the normalized sum of the S- and P-polarized calculated photonic band diagrams. Demonstration of polarization dependent band splitting. (b) Distribution of the E_y electric field component of the lowest TE leaky mode having the similar symmetry as the S-polarized incident light. Coordinate system is shown in Fig. 1(b). (c) Distribution of the E_x and E_z electric field components of the lowest TM leaky mode having the similar symmetry as the P-polarized incident light.

other hand, energy of the TM mode propagating in the x-direction is stored comparably in both, E_x component—parallel to the mode propagation direction—and E_z component—perpendicular to the sample plane. Leaky bands, marked either by letter S or P based on light polarization that excited them, are visible in the zoomed band diagram. The general shape of the band diagram is similar to that obtained simply by folding the guided modes bands of the uncorrugated waveguide into the irreducible BZ considering the square lattice symmetry[12]. However, we can distinguish some differences—fourfold degeneracy splitting at the Γ point[5]; splitting of bands which are doubly degenerate in case of the band-folded diagram (in our case, e.g., two parallel nearly horizontal TE bands in the Γ–X direction marked by the black circle created due to splitting of doubly degenerate band based on the polarization). The similar effect of bands degeneracy lifting was computed using perturbative approach for the PhC slab with thin 2D grating[13] and measured in reflection spectra of 2D PhC slab[7].

The reason for the different S- and P-polarized coupling can be understood by investigating the electric field profile of the modes with respect to the field profile of the source. Here it is demonstrated on the two energetically lowest leaky bands in the Γ–X direction, marked by black points in Fig. 3(a), the left one excited by the S- and the right one excited by the P-polarized light.

The only non-zero component of the electric field of S-polarized light is vector E_y pointing into y-direction (Fig. 1(b)) and thus the

incident light can couple only to the E_y component of the leaky mode. Moreover, this source is odd with respect to the mirror plane $y = 0$ meaning that it can excite only mode having the same odd symmetry in E_y, i.e., mode that under mirror reflection through the plane $y = 0$ becomes its own opposite. This behaviour is demonstrated in Fig. 3(b) where the computed electric field distribution is plotted for the TE leaky mode with air wavelength of 815 nm. The field pattern is displayed for the TE mode relevant electric field component E_y in two distinct planes— on the left, the plane cutting the sample vertically through the middle of the columns in the Γ–X direction (plane $y = 0$) and on the right, the plane parallel to the sample and going through the middle of uncorrugated diamond layer ($z = 0$, borders of the columns are depicted in order to give an idea of the mode wavelength with respect to the lattice constant a). The mode is propagating in the x-direction and its wavefronts can be clearly recognized in both E_y field patterns. Most important is the fact that this mode is odd with respect to the mirror plane $y = 0$ (as can be determined from Fig. 3(b)—right) and thus can be excited with the S-polarized light source.

On the other hand, the electric field of the P-polarized light have the electric field components pointing into x- and z-direction, both possessing even symmetry with respect to the mirror plane $y = 0$, i.e., invariant under mirror reflection through the plane $y = 0$. The electric field distribution of the lowest TM mode with the air wavelength of 815 nm is plotted for the E_x and E_z electric field
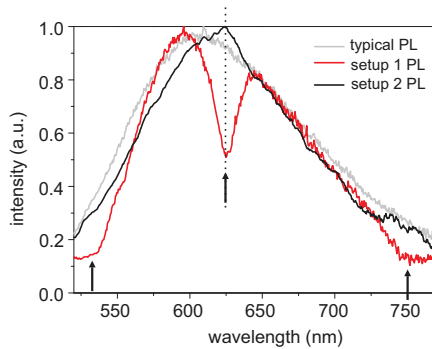
Figure 4 | Photonic crystal effect on PL of the QDs (SiNCs) on the PhC surface. PL detected from behind (setup 1) and from the front side of the sample (setup 2) compared to the typical SiNCs spectrum is plotted. All spectra are normalized to the maximum. The black arrows indicate spectral position of leaky resonances.

components in Fig. 3(c) in the same manner as in case of the TE mode. The mode possesses the similar symmetry with respect to the mirror plane $y = 0$ as the P-polarized light source and thus the external incident light with this polarization can couple into the mode.

Also the higher order modes will be either even or odd with respect to the mirror plane $y = 0$ and, as it follows from the discussion above, they will be excited either with P- or S-polarized light, respectively.

A short video of the normally incident light being coupled into the TE leaky mode of the 2D PhC slab was created in order to give a better insight into the physics involved. The video is part of Supplementary Information.

The effect of the material periodicity of the NCD PhC slab on luminescence of quantum dots on its surface was investigated using silicon nanocrystals (SiNCs). Their PL emission spectrum overlaps with spectrally broad leaky modes of the PhC. Powder of the SiNCs (preparation details in Ref. 14) consisting of small Si clusters was drop-casted on the diamond PhC forming a very thin layer (< 20 nm thick). The SiNCs were excited by an external laser source (355 nm, 8 ns pulses) from a non-resonant angle. (If the laser were coupled resonantly into the structure, the excitation field in the vicinity of the PhC would be strongly enhanced, which would cause burning of the NCs.) The detection of PL from the SiNCs was performed using two different detection setups, either through the substrate (like during the transmission measurements—setup 1) or directly from the front side of the sample (setup 2), i.e. from the side where the SiNCs were placed, in the direction normal to the PhC plane ($\theta = 0°$) with the solid detection angle of $\sim 1°$.

The signals measured in setups 1 and 2 are plotted in Fig. 4 in comparison with the typical spectrum of the SiNCs drop-casted on a thick quartz substrate (thus not modulated by the Fabry–Pérot interferences). All curves in Fig. 4 are normalized to the signal maximum in order to show the PhC impact on the shape of the PL spectra. Moreover, the non-normalized spectra cannot be displayed due to the fact that distribution of the SiNCs on the sample surface was not homogeneous.

The PL spectrum detected through the substrate (setup 1) shows strong resonant dips at the spectral positions of leaky modes (~ 750 nm, ~ 625 nm, ~ 530 nm) because part of the light emitted from the SiNCs, heading towards the substrate, is partly coupled to the leaky modes of the structure and interacts with the periodic material modulation in a very similar way as the incident light during transmission measurements does. On the other hand, PL spectrum detected directly from the top of the SiNCs on the PhC surface (setup 2) exhibit peaks at the wavelengths of the leaky modes causing the change of the spectral shape of the typical PL signal. The overall maximum of the signal is up-shifted to the ~ 625 nm and other broad peaks arise at around 750 and 530 nm. The mechanism causing the change of the PL spectrum is very similar to the effect which causes maxima in the PhC reflection spectrum at spectral position of leaky modes as explained in Introduction. However, as it is in more detail explained below, due to the existence of absorption and scattering mechanisms in nano-diamond, the resonance at 625 nm is in the setup 2 PL less pronounced than in the setup 1 PL (Fig. 4).

The influence of optical losses on the transmission and reflection spectra is demonstrated by computing the spectra for the case of normal light incidence on the PhC sample surface. The losses are simulated such that the imaginary part κ of the refractive index is set to be positive. The results of the simulation for the case of $\kappa = 0$, 0.001, 0.01 are plotted in Fig. 5. Also the absorption defined as 1–transmission–reflection efficiency is plotted. Obviously, the absorption is zero for the case of $\kappa = 0$ (Fig. 5(a)) and resonances can be recognized at the spectral position of leaky modes—Fano-like shaped maxima in the reflection and minima in the transmission spectra. In the case of $\kappa = 0.001$ (Fig. 5(b)), the presence of the absorption mechanism causes noticeable reduction of the reflected intensity at the position of the resonance, however, the transmission efficiency changes only negligibly. This is the reason why the resonances in the PL spectrum of the SiNCs on the PhC surface are less pronounced if the detection is performed from the front of the sample (i.e., reflection-like measurement) than when the detection applies from behind of the sample (i.e., transmission-like measurement). In the case of very high losses ($\kappa = 0.01$—Fig. 5(c)), the shape of reflection spectrum changes dramatically compared to the case with no or low losses and such a sample is not suitable to manipulate the PL. Losses due to light absorption in diamond defects present in our sample are comparable to the case of $\kappa = 0.001$. However, additional losses are
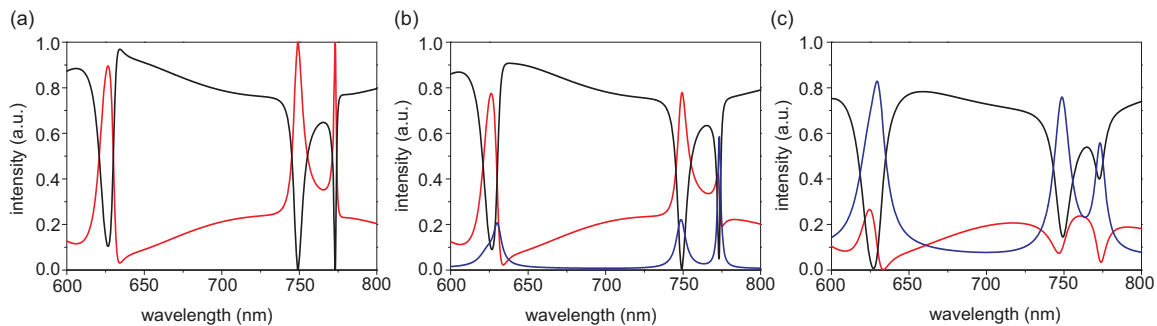

Figure 5 | Simulation of the effect of optical losses in the PhC on the transmission and reflection spectra. Transmission (black curve), reflection (red curve) and absorption (blue curve) are computed for the imaginary part of the refractive index κ equal to (a) 0 (no losses), (b) 0.001 and (c) 0.01.

present due to light scattering on imperfections of the sample surface and scattering on the NCD grains of which the layer is composed. Taking into account the latter, our experiment corresponds to the regime between the $\kappa = 0.001$ and $\kappa = 0.01$. The above discussion suggests that it is very important to design dimensions and improve the quality of the final PhC such that the losses are minimized which is the goal of our future study.

The PhC effect on the PL spectrum of the SiNCs is even more evident when the setup 1 PL spectrum is normalized by the typical shape of PL spectrum of the SiNCs as plotted in Fig. 6(a) together with the computed and measured transmission spectra for the zero angle of incidence ($\theta = 0°$). Three main effects can be recognized in this graph. First, due to losses in the real sample, the leaky resonance minima (e.g. at 750 nm) in measured transmission spectrum are shallower than in the simulated one. Second, introducing the SiNCs into voids of the sample causes the change of the PhC properties which leads to slight spectral shift of the minima in the PL signal with respect to the measured transmission minima. However, the shift is very low which suggests that the photonic properties of the PhC were only negligibly affected by the presence of the SiNCs, most probably due to very low density of nanocrystals. Third, due to the fact that not all light emitted by the SiNCs is coupled to the PhC, the dips in the red curve in Fig. 6(a) are less pronounced than those in the gray or black curve. Normalized angle-resolved PL spectra detected from behind of the sample and showing the strong interaction of light emitted from the SiNCs with the PhC, are shown in Fig. 6(b). The detection was performed through the substrate and the detection fiber was rotated along the Γ–X crystal direction with the sample being fixed. The detection was not polarization resolved. The spectra were normalized by the spectrum of the SiNCs on thick quartz substrate in order to obtain reasonable contrast between minima and maxima in the signal. Minima occur in the PL spectra due to light coupling into the leaky modes and it is evident that these minima follow very well the photonic bands of the 'pure' PhC sample (compare with Fig. 2(a) and (c)).

The absolute comparison of the signal intensity detected from the SiNCs within the PhC and from the SiNCs on the unpatterned NCD layer (which surrounded the PhC) cannot be done due to the fact that distribution of the SiNCs on the surface of the sample was not homogeneous. However, the above discussion indirectly proves that the PL of the SiNCs on the PhC surface detected from the front side of sample (setup 2) must be in principle enhanced compared to the PL of the SiNCs outside the PhC (provided the NCs are uniformly distributed over the sample) due to the fact that part of the light directed towards the substrate is redirected upwards through interaction with the PhC. Such a PL enhancement mechanism can be applied in biosensing in case a very low concentration of quantum dots as probes must be used.

Discussion

We have experimentally and theoretically characterized photonic properties of the nano-diamond PhC slab seated on the quartz substrate. Excellent agreement between the theory and experiment was obtained for the leaky modes band diagrams for different polarizations and crystal directions which proves that our structure, even though not structurally perfect, exhibits good photonic properties. However, the principal limitation is represented by optical losses owing to the fact that the layer is composed of diamond grains having surface and volume defects. We also verified the ability of the PhC sample to interact with the quantum dots drop-casted on its surface. 2D-periodic pattern allowed to manipulate light emitted from the SiNCs due to the overlap of their emission spectrum with the leaky modes of the structure. As the spectral position of the leaky modes is controlled by dimensions of the PhC, our results can be generalized to light source with an arbitrary emission wavelength. Thanks to the fact that diamond is very hard and sustainable material, sample is not damaged even after few years and maintains its photonic properties. It can also be cleaned very effectively from the species deposited on its surface. Therefore one sample can be used in combination with different light sources if their spectrum overlaps with the PhC leaky modes. Even the combination of light sources emitting different colours could be used simultaneously, if the spectral position of leaky modes was tuned carefully. To conclude, our results open the possibility to manipulate the shape of the PL spectrum of an arbitrary light source and also to shift its PL maximum to a different energy within some reasonable interval around the original maximum.
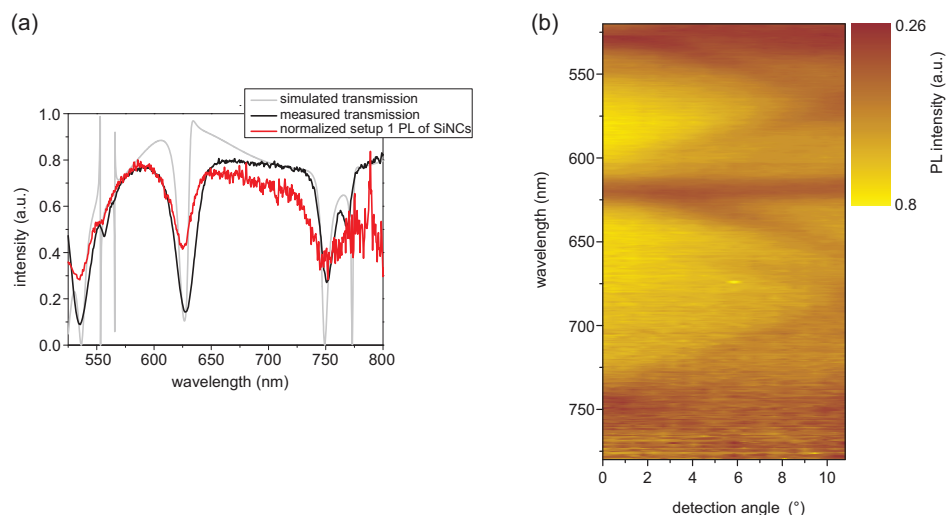
Figure 6 | Normal-incidence spectra comparison and the angle-resolved normalized setup 1 PL. (a) Comparison of the measured and computed transmission spectra measured at normal incidence to the PhC plane ($\theta = 0°$) with the PL spectrum measured in the setup 1 and normalized by the typical SiNCs spectrum. (b) Angle-resolved PL spectra of the SiNCs on the PhC surface detected along the Γ–X direction and normalized by the typical spectrum of the SiNCs.

Methods

Sample preparation. The NCD layer was grown from a diamond powder by microwave plasma-assisted chemical vapour deposition on the quartz substrate (for details see Ref. 15). 2D periodic structure was fabricated employing electron beam litography on the NCD layer coated with electron sensitive polymer. On a periodic matrix prepared in the polymer, a nickel layer was evaporated and processed by lift-off strategy to form a masking matrix. Afterwards, a plasma etching was applied leading into a periodically ordered diamond columns. In the end, the nickel layer was removed (for details see Ref. 11).

Transmission measurements. Transmission measurements were performed with the sample placed on a motorized rotational stage. The rotational stage was computer controlled and allowed to obtain transmission spectrum for the precise angle with relatively small step of $0.3°$. The collimated light beam was incident on the sample at the angle θ which was varied from $0°$ up to $25.2°$ along the Γ–X and Γ–M crystal directions (see the setup sketched in Fig. 1(b)).

Photonic band diagram and mode profiles simulations. Photonic band diagrams of leaky modes were obtained from the transmission curves at different angles. Transmission curves were computed by using the commercial software package DiffractMOD based on Rigorous Coupled Wave Analysis technique and developed by the RSoft Design Group. Also the reflection and absorption curves were obtained with this method. The electric field profiles of the leaky modes were computed using a conjugate gradient plane-wave expansion method implemented in the MIT Photonic-Bands (MPB) package[16].

1. Joannopoulous, J. D., Johnson, S. G., Winn, J. N. & Meade, R. D. *Photonic Crystals: Molding the Flow of Light* (Princeton University Press, Princeton, 2008).
2. Johnson, S. G., Fan, S., Villeneuve, P. R., Joannopoulos, J. D. & Kolodziejski, L. A. Guided modes in photonic crystal slabs. *Phys. Rev. B* **60**, 5751–5758 (1999).
3. Wierer, J. J., David, A. & Megens, M. M. III-nitride photonic-crystal light-emitting diodes with high extraction effciency. *Nature Photon.* **3**, 163–169 (2009).
4. Wiesmann, C., Bergenek, K., Linder, N. & Schwarz, U. T. Photonic crystal LEDs – designing light extraction. *Laser & Photon. Rev.* **3**, 262–286 (2009).
5. Fan, S. & Joannopoulos, J. D. Analysis of guided resonances in photonic crystal slabs. *Phys. Rev. B* **65**, 235112 (2002).
6. Astratov, V. N. *et al.* Photonic band-structure effects in the reflectivity of periodically patterned waveguides. *Phys. Rev. B* **60**, R16255–R16258 (1999).
7. Pacradouni, V. *et al.* Photonic band structure of dielectric membranes periodically textured in two dimensions. *Phys. Rev. B* **62**, 4204–4207 (2000).
8. Ganesh, N. *et al.* Enhanced fluorescence emission from quantum dots on a photonic crystal surface. *Nature Nanotech.* **2**, 515–520 (2007).
9. Rosenblatt, D., Sharon, A. & Friesem, A. A. Resonant grating waveguide structures. *IEEE J. Quantum Electron.* **33**, 2038–2059 (1997).
10. Rybin, M. V. *et al.* Bragg scattering induces Fano resonance in photonic crystals. *Phot. Nano. Fund. Appl.* **8**, 86–93 (2010).
11. Ondič, L. *et al.* Effective extraction of photoluminescence from a diamond layer with a photonic crystal. *ACS Nano* **5**, 346–350 (2011).
12. Ondič, L. *et al.* Enhanced photoluminescence extraction efficiency from a diamond photonic crystal via leaky modes. *New J. Phys.* **13**, 063005 (2011).
13. Paddon, P. & Young, J. F. Two-dimensional vector-coupled-mode theory for textured planar waveguides. *Phys. Rev. B* **61**, 2090–2101 (2000).
14. Dohnalová, K. *et al.* White-emitting oxidized silicon nanocrystals: Discontinuity in spectral development with reducing size. *J. Appl. Phys.* **107**, 053102 (2010).
15. Kromka, A. *et al.* Formation of continuous nanocrystalline diamond layers on glass and silicon at low temperatures. *Chem. Vap. Deposition* **14**, 181–186 (2008).
16. Johnson, S. G. & Joannopoulos, J. D. Block-iterative frequency-domain methods for Maxwell's equations in a planewave basis. *Opt. Express* **8**, 173–190 (2001).

Author contributions

L.O. performed the experiments. O.B., M.V. and A.K. designed and prepared the sample. L.O. and J.Č. performed simulations. L.O. and I.P. analysed the data and wrote the article. All authors discussed and reviewed the manuscript.

Additional information

Supplementary Information accompanies this paper at http://www.nature.com/scientificreports

How to cite this article: Ondič, L. *et al.* Diamond photonic crystal slab: Leaky modes and modified photoluminescence emission of surface-deposited quantum dots. *Sci. Rep.* **2**, 914; DOI:10.1038/srep00914 (2012).

6.4 Enclosure

Two-dimensional photonic crystal slab with embedded silicon nanocrystals: Efficient photoluminescence extraction

L. Ondič, M. Varga, K. Hruška, A. Kromka, K. Herynková, B. Hönerlage, and I. Pelant

Two-dimensional photonic crystal slab with embedded silicon nanocrystals: Efficient photoluminescence extraction

Lukáš Ondič,[1,2,3,a)] Marian Varga,[1] Karel Hruška,[1] Alexander Kromka,[1] Kateřina Herynková,[1] Bernd Hönerlage,[3] and Ivan Pelant[1]

[1]*Institute of Physics, Academy of Sciences of the Czech Republic, v.v.i., Cukrovarnická 10, 162 53, Prague 6, Czech Republic*
[2]*Faculty of Mathematics and Physics, Charles University, Ke Karlovu 3, 121 16, Prague 2, Czech Republic*
[3]*IPCMS–DON Unité Mixte, UMR 7504, CNRS–ULP, 23 rue du Loess, BP 43, 67034 Strasbourg Cedex 2, France*

A two-dimensional photonic crystal (PhC) slab was fabricated from a luminescent planar waveguide, formed by a (800 nm thick) layer of silicon nanocrystals (SiNCs) embedded in a polished silica plate. Dimensions of the PhC were designed so that light emitted by SiNCs under excitation with an external UV source can, during its propagation in the layer, interact with the periodicity and be Bragg-diffracted into air. This approach leads to up to 8-fold vertical extraction enhancement of SiNCs luminescence from the PhC slab compared to the bare planar layer. Results of the experiment are supported by the computer simulation. © *2013 AIP Publishing LLC*. [http://dx.doi.org/10.1063/1.4812477]

Silicon quantum dots or nanocrystals (SiNCs) sized a few nanometers in diameter are brightly fluorescent particles, which hold promise towards many potential applications: photonic light-emitting devices, biological sensors and labels, fluorescence markers, and tandem solar cells.[1–3] When employed in solid photonic light sources, SiNCs are usually embedded in a transparent solid matrix, silicon dioxide SiO_2 (silica) as a rule. Extraction of luminescence radiation, originating in SiNCs, from the device into air is then of fundamental importance, since the light output is limited by total internal reflection on the matrix-air interface. In other words, even high internal luminescence quantum yield may be annulled to a considerable extent due to total internal reflection losses. Here, two-dimensional patterning of the device active surface may help markedly. If the pattern is designed periodic in two-dimensions with a lattice constant of the order of luminescence wavelength, a two-dimensional (2D) photonic crystal (PhC) is created on the surface.[4] If dimensions of the periodicity are carefully chosen, guided light propagating in all planar directions can be Bragg-diffracted and leak into air under specific angles defined by photonic band diagram.[5,6] Guided modes are then referred to as leaky modes.[7]

Some preliminary reports on photoluminescence (PL) of SiNCs combined with PhC were already published by our group.[8,9] We have already shown that shape of the emission spectrum of SiNCs can be controlled by depositing them on the surface of a 2D-PhC made of nanocrystalline diamond.[9] However, only a modification of PL spectrum shape was achieved but no light extraction enhancement in a given direction was observed. The main reasons for that were the low quality of the photonic structure and/or insufficient overlap of spatial distribution of SiNCs with electric field of leaky modes.

In this letter, we report on experimental and theoretical investigation of silica 2D PhC slab with embedded SiNCs, prepared by advanced methods. We demonstrate that light emitted by SiNCs couples to leaky modes of the PhC and is efficiently extracted out into air in preferred directions.

The PhC sample was prepared by employing two main steps. First, SiNCs rich layer was created inside polished silica substrate using Si^+-ion implantation, forming basically a planar waveguiding layer beneath the silica surface. Second, surface of the active layer was periodically patterned by employing electron beam lithography with subsequent reactive ion etching.

Implantation of Si^+-ions (400 keV, implant fluence of 1×10^{17} cm^{-2}) into a polished 1 mm thick silica plate followed by thermal annealing at $1100\,^\circ$C and forging lead to formation of about 800 nm thick SiNCs-rich luminescent layer below the silica surface. Details of the preparation method can be found in Ref. 10. Spatial distribution of SiNCs can be approximated by an asymmetric Gaussian function with maximum located closer to the pure SiO_2 layer (see blue line in Fig. 1(a) depicting the refractive index distribution of the sample which follows the spatial distribution of SiNCs). Under external continuous wave (cw) UV laser (325 nm) excitation at room temperature, the main PL emission band is located in the red spectral region peaking at around 780 nm (Fig. 1(b), black curve). Physical origin of this emission is attributed to SiNCs with diameter of 4–5 nm (detected by Raman scattering[10]), but there exist experimental and theoretical studies indicating that also very small SiNCs may play an important role in PL mechanism.[11]

For creating a periodical pattern etched on top of the SiNCs-rich layer we adapted our method used previously for fabrication of PhC on a nanocrystalline diamond layer.[12] 2D-PhC consisting of columns arranged to a square symmetry was chosen in order to obtain a structure that can interact with guided modes propagating in all planar directions. First the implanted silica plate was cleaned by ultrasonication in acetone for 10 min and dried by a nitrogen gun. Then it was coated with a positive electron sensitive polymethyl methacrylate (PMMA) polymer resist of 120 nm in thickness. Electron
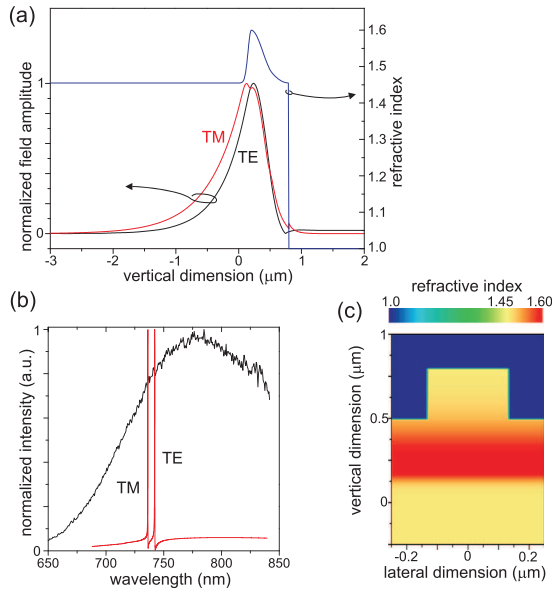
a)Electronic mail: ondic@fzu.cz

FIG. 1. (a) Blue curve depicts refractive index profile of the implanted silica plate in the vertical direction which follows the spatial distribution of SiNCs. Position "0" is at the interface of pure silica and SiNCs-rich layer. Simulated profiles of electric field amplitudes of TE_0 and TM_0 PhC leaky modes at the Γ-point, whose spectral positions are shown in (b), are plotted by black and red curves, respectively. E_y component (in the sample plane) of the TE and E_z component (normal to the sample plane) of the TM leaky mode are plotted. The intensity is normalized to unity. (b) Plot of the normalized PL emission spectrum of SiNCs embedded in SiO_2 plate compared to the simulated TE and TM leaky resonances of the PhC at the Γ-point of the photonic band diagram. (c) Vertical cut of the 3D-computation domain (zoomed in the z-direction) through the middle of the PhC column.

FIG. 2. SEM images of the final 2D-PhC structure with the 500 nm lattice constant Λ, columns diameter of 265 nm, and height of 300 nm. Directions of the high symmetries of the square lattice Brillouin zone are depicted in the left image.

beam lithography was used to create holes into the polymer with a diameter of approximately 300 nm, ordered into a square lattice with a lattice constant $\Lambda \approx 500$ nm. Then, a 70 nm thick golden layer was evaporated on the polymer filling the holes. Afterwards, lift-off of the resist was performed by ultrasonication in acetone to form a mask for the subsequent plasma etching. Capacitively coupled reactive ion etching in a pure SF_6 gas mixture was applied to form geometrically ordered columns covering the surface area of 1×1 mm^2 placed in the middle of the sample. Remaining Au mask was removed by wet etching. Columns featuring long range periodicity and having well defined diameter $d \approx 265$ nm and height $h \approx 300$ nm were obtained as shown in SEM images of the final PhC structure in Fig. 2.

Dimensions of the PhC were designed with the goal to obtain high extraction efficiency of light emitted by SiNCs and trapped in the layer and also to test a possible lasing effect that can occur due to the existence of modes with low group velocity (the so-called slow modes).[13,14] Therefore, it was desirable to obtain spectral overlap of the PhC leaky modes with the emission spectrum of SiNCs. Moreover, as the extraction is most efficient in the direction normal to the sample plane (z-direction) and also the slow modes are diffracted in this direction, we attempted to obtain overlap of the PL emission spectrum with leaky resonances located at the Γ-point of photonic band diagram.
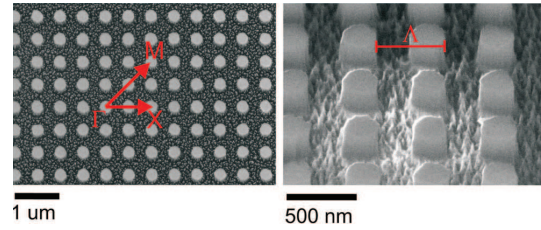
Photonic band diagram, as dispersion of photonic modes supported by the device, typically shows the modal frequency as a function of the wavevector, or in other representation, it plots modal air/vacuum wavelengths against the propagation angles in air. To simulate the problem, we used RCWA method (RSoft DiffractMOD) which allows to compute the transmission and/or reflection spectra of periodic dielectric media and locate leaky resonances which are revealed in the transmission/reflection spectra as narrow minima/maxima.[15,16] Refractive index in the SiNCs-rich layer was characterized by an asymmetric Gaussian function with maximum value equal to 1.6 (Fig. 1(a), blue curve).[10] A cut through the middle of the computation domain, zoomed in the z-direction, is shown in Fig. 1(c). Details of the simulation can be found in supplementary material.[17] By varying the lattice constant Λ, diameter d, and height of columns h we chose a suitable combination of the parameters used as input data for lithographic fabrication. The final dimensions of the prepared PhC, except the lattice constant, slightly (± 10 nm) changed during the preparation process due to the great number of steps involved; however, the overlap of the simulated TE_0 and TM_0 leaky modes (extracted in direction normal to the sample plane) with SiNCs emission spectrum was preserved as it is shown in Fig. 1(b) (dimensions obtained from the SEM images of the final PhC were used in the presented result of the simulation).

2D maps of electric field amplitude distribution of the two leaky modes are shown in supplementary material.[17] Vertical cuts taken near the maximum of the modes and showing profile of the electric field amplitudes of the E_y component of TE_0 and E_z component of the TM_0 leaky modes at the Γ-point are shown in Fig. 1(a) with respect to the refractive index profile. It is evident that modes maxima are located in the SiNCs-rich layer. We can thus expect that light emitted by SiNCs will couple to these leaky modes, thanks to both their good spectral overlap with SiNCs PL spectrum and spatial overlap with SiNCs distribution.

In order to test performance of the PhC device, we measured the PL emission intensity as a function of the detection angle with respect to sample normal. The sample was excited through the silica substrate with a 325 nm cw laser beam focused on the PhC. The PL was collected from the front side of the sample by an optical fiber (collection half-angle 1°) attached to a rotating arm, allowing to perform angle-resolved measurements. The sample was placed in a rotational holder which enabled us to investigate leaky modes along both the Γ-M and Γ-X square symmetry directions. Results of these
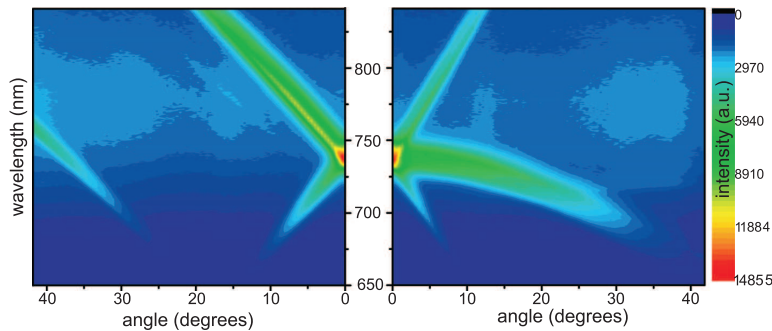
FIG. 3. PL emission spectra of SiNCs embedded in SiO$_2$ plate with 2D-PhC measured along the Γ-M (left) and Γ-X (right) crystal directions as a function of the detection angle. Angle $\theta = 0°$ is normal to the sample surface.

measurements are summarized in 2D maps of PL emission intensities (Fig. 3) where the angle $\theta = 0°$ is normal to the sample surface. Relatively narrow peaks several times more intense than the spectrally broad background are superimposed on the broad spectra, typical for the uncorrugated sample (broad band is clearly visible for the larger detection angles). These narrow peaks enhance the PL extraction efficiency in the given directions and cause that the light emission is strongly directional.

The physical mechanism underlying the PL extraction enhancement process, already briefly mentioned in the introduction, is as follows. In the case of a planar uncorrugated layer, light emitted from SiNCs and heading towards the air-sample interface is either coupled to the guided modes of the layer or it radiates out of the sample if it lies inside the air lightcone defined by the angle of total internal reflection. The latter is responsible for the broad PL emission band. However, when the PhC columns are introduced on the top, guided modes can now interact with the periodicity and in case they fulfill the Bragg diffraction condition, they are diffracted into air under the specific angles defined by the Bragg condition. Thus, they serve as efficient radiative channels for light previously "trapped" in the layer. These radiative modes are the leaky modes and in the angle-resolved PL spectra they form photonic bands as it is visible also in result of our experiment. It is also clear that the extraction of light is most efficient for small detection angles (close to the sample normal, see Fig. 3) due to degeneracy of leaky modes at the Γ-point.[18]

For the case of vertical emission, PL spectra of the PhC compared to the unpatterned layer of SiNCs in silica plate

are plotted in Fig. 4(a) (red vs black curve). As explained above, the narrow peak superimposed on the broad spectra represents emission from SiNCs extracted via leaky modes. High enhancement of extraction efficiency by a factor of 8 was achieved for the maximum located at 736 nm (Fig. 4(a), dotted blue curve). The leaky mode band can be decomposed into two Lorentzian peaks with maxima at 736 and 745 nm (Fig. 4(b)), the first one being TM and the second one TE resonance. The Q-factors, obtained from the widths of the Lorentzian fits, are 37 and 43 for the TM and TE resonance, respectively. These low Q-factors are the reason for the high extraction efficiency; light propagates for a short time only in the layer, which minimizes optical losses, and is quickly extracted out to air. The agreement between the spectral positions of the simulated leaky resonances and the measured ones (Fig. 4(b)) is very satisfying. As discussed in detail later in connection with Fig. 4(c), the slight difference in spectral positions of the TE mode obtained here can be easily explained by the uncertainty of the refractive index value used in the simulation. However, the computed resonances are much more narrower (and thus Q-factor is much larger—of the order of 1000) than the measured counterparts. This difference is caused by the presence of optical losses (absorption, scattering on the sample imperfections) in the real sample which is not included in the simulation and which would lead to broadening of the resonances. Another reason for the broadened resonances may be that the PL collection half-angle is larger compared to the simulation, approximately 1° ($\theta = 0° \pm 1°$) and thus all modes outcoupled within this angle are detected. In the simulation, only light
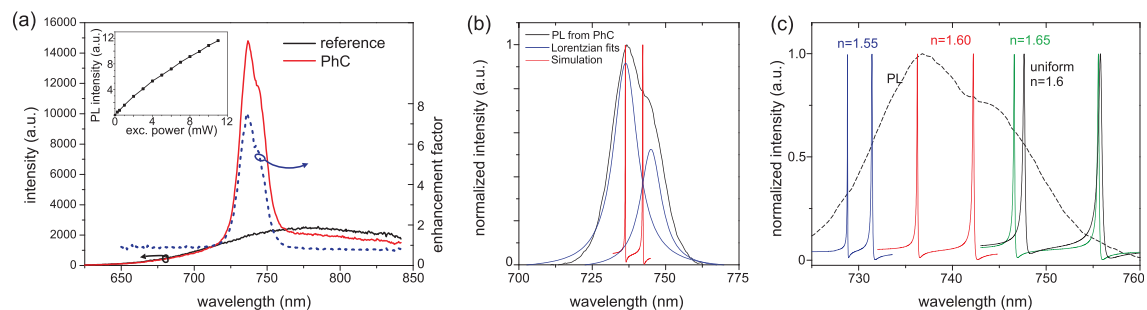
FIG. 4. (a) PL emission of SiNCs embedded in SiO$_2$ plate with and without the 2D-PhC structure together with the PL extraction enhancement curve computed as ratio of the two PL curves. Inset shows the intensity of the PhC PL maximum (maximum of the leaky resonance) as a function of the excitation power. (b) PL emission band of the PhC with subtracted broad background showing only the leaky band fitted with two Lorentzian peaks, compared with the simulated TE and TM leaky resonances of the PhC. (c) PhC leaky resonances simulated for different values of refractive index maximum of SiNCs-rich layer.

outcoupled exactly in direction normal to the sample plane ($\theta = 0°$) is considered.

In order to check possible lasing effect for the slow modes at the Γ-point, the experiment in which the excitation power was gradually increased, was carried out for the normal detection. However, the dependence of emission intensity at the leaky mode peak maximum on the excitation power (inset of Fig. 4(a)) does not show any super-linear behavior typical when the lasing threshold is achieved.

It should be finally noted that the spectral position of the leaky resonances at the Γ-point is very sensitive to the spatial profile and absolute value of the PhC refractive index as shown in Fig. 4(c). Decreasing value of the refractive index maximum (from 1.65 to 1.55) spectrally blue-shifts position of the leaky resonances and also brings TE and TM resonances closer to each other. Also, the difference between uniform and asymmetric Gaussian refractive index profiles of SiNCs-rich layer is demonstrated for the value of index equal to 1.6. Leaky modes are spectrally red-shifted when uniform index distribution in SiNCs-rich layer is supposed. This shows the importance of taking into consideration the Gaussian profile when performing the simulations.

To summarize, we demonstrated both experimentally and via modelling that the 2D-PhC structure is able to enhance extraction efficiency of PL originating in SiNCs as much as 8-times for the case of vertical emission and remains considerably high even for other emission angles. Engineering of the refractive index value and profile can lead to further increase of the enhancement factor, which may be beneficial for future photonic light sources based on silicon nanoparticles.

[1]*Silicon Nanophotonics: Basic Principles, Current Status and Perspectives*, edited by L. Khriachtchev (Pan Stanford Publishing, 2009).

[2]*Device Applications of Silicon Nanocrystals and Nanostructures*, edited by N. Koshida (Springer, 2009).

[3]*Silicon Nanocrystals*, edited by L. Pavesi and R. Turan (Wiley-VCH, 2010).

[4]J. D. Joannopoulous, S. G. Johnson, J. N. Winn, and R. D. Meade, *Photonic Crystals: Molding the Flow of Light* (Princeton University Press, Princeton, 2008).

[5]J. J. Wierer, A. David, and M. M. Megens, Nature Photon. **3**, 163 (2009).

[6]C. Wiesmann, K. Bergenek, and U. T. Schwarz, Laser Photonics Rev. **3**, 262 (2009).

[7]S. Fan and J. D. Joannopoulos, Phys. Rev. B **65**, 235112 (2002).

[8]P. Janda, J. Valenta, J.-L. Rehspringer, R. R. Mafouana, J. Linnros, and R. G. Elliman, J. Phys. D **40**, 5847–5853 (2007).

[9]L. Ondič, O. Babchenko, M. Varga, A. Kromka, J. Čtyroký, and I. Pelant, Sci. Rep. **2**, 914 (2012).

[10]T. Ostatnický, J. Valenta, I. Pelant, K. Luterová, R. Elliman, S. Cheylan, and B. Hönerlage, Opt. Mater. **27**, 781 (2005).

[11]L. Khriachtchev, S. Ossicini, F. Iacona, and F. Gourbilleau, Int. J. Photoenergy **2012**, 872576.

[12]L. Ondič, K. Dohnalová, M. Ledinský, A. Kromka, O. Babchenko, and B. Rezek, ACS Nano **5**, 346 (2011).

[13]K. Sakoda, Opt. Express **4**, 167 (1999).

[14]L. Ondič and I. Pelant, Opt. Express **20**, 7071 (2012).

[15]D. Rosenblatt, A. Sharon, and A. A. Friesem, IEEE J. Quantum Electron. **33**, 2038 (1997).

[16]N. Ganesh, W. Zhang, P. C. Mathias, E. Chow, J. A. N. T. Soares, V. Malyarchuk, A. D. Smith, and B. T. Cunningham, Nat. Nanotechnol. **2**, 515 (2007).

[17]See supplementary material at http://dx.doi.org/10.1063/1.4812477 for additional information about the computer RCWA simulation.

[18]N. Ganesh, I. D. Block, P. C. Mathias, W. Zhang, E. Chow, V. Malyarchuk, and B. T. Cunningham, Opt. Express **16**, 21626 (2008).

Supporting information to

Two-dimensional photonic crystal slab with embedded silicon nanocrystals: efficient photoluminescence extraction

Lukáš Ondič,[1,2,3,a)] Marian Varga,[1] Karel Hruška,[1] Alexander Kromka,[1] Kateřina Herynková,[1] Bernd Hönerlage,[3] and Ivan Pelant[1]

[1)]*Institute of Physics, Academy of Sciences of the Czech Republic, v.v.i., Cukrovarnická 10, 162 53, Prague 6, Czech Republic*

[2)]*Faculty of Mathematics and Physics, Charles University, Ke Karlovu 3, 121 16 Prague 2, Czech Republic*

[3)]*IPCMS−DON Unité Mixte, UMR 7504, CNRS−ULP, 23 rue du Loess, BP 43, 67034 Strasbourg Cedex 2, France*

[a)]Electronic mail: ondic@fzu.cz

Spectral position and profiles of leaky modes of our device - 2D photonic crystal (PhC) slab composed of columns ordered in square lattice - were computed using Rigorous Coupled Wave Analysis (RCWA) method implemented in a commercial software RSoft DiffractMOD. Computational 3D domain included one period of the device with periodic boundary conditions applied in x and y planar directions. Size of the domain in z-direction was chosen in order to cover spatially the whole TE and TM leaky mode profiles, sizes in x and y directions were dictated by the lattice constant. Vertical cut going through the middle of the domain is shown in Fig. S1(a) - color scale characterizes the refractive index distribution. In case of computing spectral position and profile of leaky modes at the Γ-point (i.e. modes being extracted in direction normal to the sample plane), an asymmetric gaussian profile of refractive index was considered for Si nanocrystals (NCs) rich layer (as depicted in Fig. S1(a)). In the simulation, white normally incident light with electric field amplitude normalized to the unity and pointing into y-direction (E_y) interacts with the periodicity on the surface of the layer and can couple, for certain wavelengths that meet Bragg diffraction condition, into leaky resonances of the PhC. More specifically, it couples into a TE leaky mode having relevant electric field component E_y and into a TM leaky mode having relevant electric field components E_y and E_z. TE_0 leaky mode at vacuum wavelength 742 nm and TM_0 leaky mode at vacuum wavelength 736 nm were found. Electric field of these two modes generated in response to incident monochromatic plane wave at the relevant wavelengths are shown in Figs. S1(b-d). Electric field amplitudes are normalized to the unit amplitude of the incident electric field. Maximum amplitude occurs always near the maximum of the refractive index profile, thus where the highest density of SiNCs is located. Due to the fact that TE mode profile was extracted from simulation of incident light having E_y component and that 100% of it is reflected, it has non-zero intensity in air. On the other hand, E_z component of the TM mode must be exponentially decaying in air but its E_y is carrying reflected radiation in air. This is even more clearly visible in Fig. 1(a) of the main text where the vertical profile (depicted by the dashed red lines in Figs. S1(b,c)) of the modes is shown.
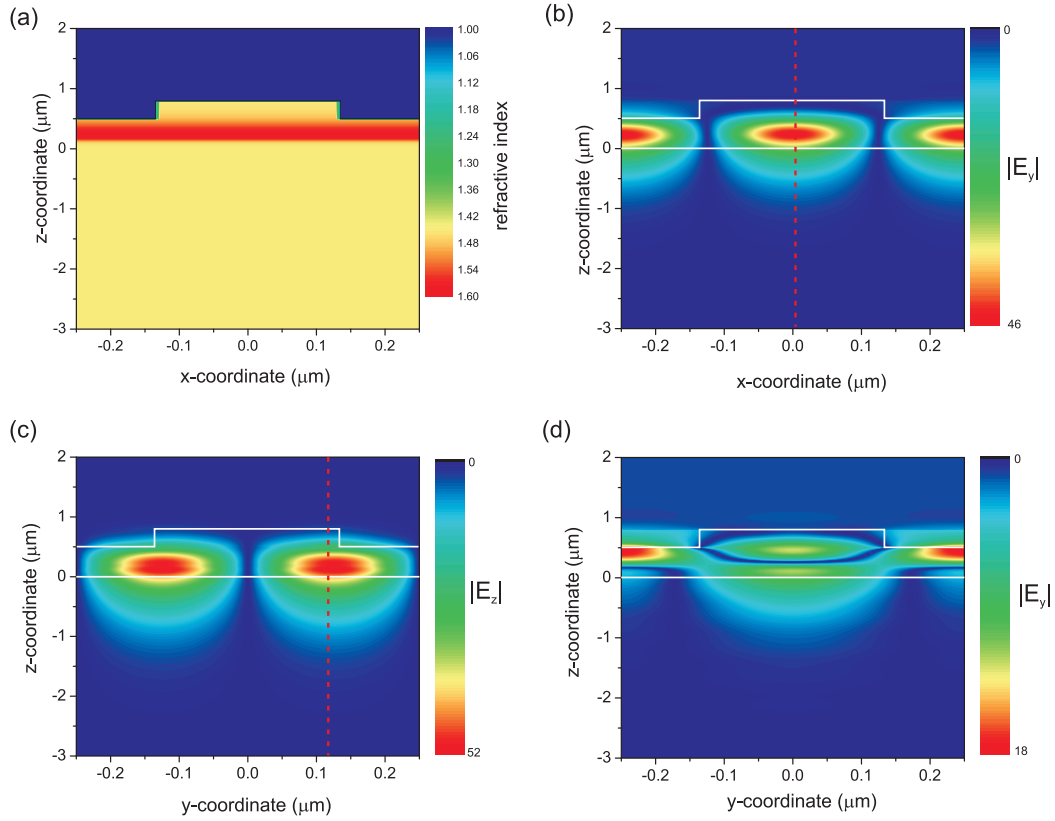
Figure S 1: (a) Cut through the plane y=0 (middle of the column) of the 3D computational domain used in the RCWA simulation of the PhC. (b) Amplitude of the E_y electric field component of the TE leaky mode at the Γ-point having vacuum wavelength of 742 nm. (c,d) Amplitudes of the E_z and E_y electric field components of the TM leaky mode at the Γ-point having vacuum wavelength of 736 nm. Both modes were excited from air by plane waves at normal incidence having E_y electric field components. Red dashed lines depict the spatial positions of the vertical cut of electric fields shown in the main text in Fig. 1(a).

Chapter 7

Conclusions

This thesis presents experimental and theoretical findings obtained in two topics: Silicon nanocrystals and photonic crystals. The results of separate investigations are merged together with a goal to improve the optical properties of SiNCs. The most important conclusions of this thesis include several points:

- The physical origin of the fast blue-green emission band in our oxide-passivated free-standing SiNCs was uncovered by means of ultrafast spectroscopy at low temperature. It was shown that the quasi-direct recombination of electron-hole pairs between the states in the close vicinity of the Si band structure Γ-point is the main radiative channel responsible for the blue band [100].

- The temperature-dependent spectral variation of the slow red-orange PL band was explained on the basis of cooperation between the temperature-induced tensile strain and Si bulk band shift [102].

- Optical gain was investigated in various types of the SiNCs samples. It was manifested, by means of time-resolved optical gain measurements, that SiNCs in a SiO_2-solgel matrix possess optical gain of the order of tens of cm^{-1} [108]. In other types of samples, namely in oxide- and methyl-passivated colloidal SiNCs and in $SiNCs/SiO_2$ multilayers, no net optical gain was observed.

- We have computed the effect of periodic patterning of an active material on the intensity of light propagating through it. Finite-difference time-domain simulations showed that the propagating light intensity may be, under specific conditions, amplified in the case of a 2D photonic crystal and a photonic crystal slab [63]. We tried to take an advantage of this phenomenon in order to increase optical gain in our samples.

- Various types of 2D periodic structures were fabricated. First, a 2D photonic crystal was etched on the surface of a NCD layer. The photonic crystal exhibited up to 6-fold extraction efficiency enhancement of light emitted by diamond defects owing to the properly-designed dimensions of the structure [118, 78]. Furthermore, the fact that the enhancement originated from the Bragg-diffraction of light on the periodicity was evidenced by a perfect agreement between the computed and measured photonic band diagrams [124].

- We have shown that the PL spectrum of SiNCs can be controlled by drop-casting them on the surface of the above-discussed 2D photonic crystal. However, SiNCs were burning under high power excitation and thus the optical gain enhancement was not achieved. Furthermore, high optical losses of the NCD layers also hindered the efficiency of this effect [124]. Therefore, we have moved to a different matrix material as discussed below.

- A 2D photonic crystal was prepared on the top of a silica layer with embedded SiNCs. The intensity of vertically-extracted light from this structure was enhanced by a factor of 7 (at the particular wavelengths) compared to a reference planar layer [125]. Even though this material exhibited low optical losses, we have not detected the onset of stimulated emission from SiNCs. We believe that this is mostly due to very high FCA losses in these SiNCs (emitting at ~ 775 nm) which originate from the fact that FCA losses increase with the square of the emission wavelength. We must, however, stress here that even though we were not able to enhance optical gain in the studied SiNCs well enough to observe the onset of stimulated emission, the obtained results will be employed in our future work.

- As a future step, we would like to apply the acquired knowledge in order to fabricate devices based on SiNCs combined with a photonic crystal that would allow to manifest the enhancement of optical gain. As follows from the results of this thesis, the combination of both, SiNCs with low FCA losses and a photonic crystal with low optical losses, is necessary. Furthermore, the properties of the photonic crystal must be computed in advance in order to ensure an overlap between the emission spectrum and leaky modes.

The contribution of the author consisted in the following. He built-up the VSL and SES setups for measuring time-resolved optical gain (Strasbourg) and an optical setup for measuring photonic band diagrams (Prague). He performed, analyzed and interpreted most of the optical measurements described in this thesis. The author carried out the low-temperature steady-state and time-resolved measurements of photoluminescence and optical gain in SiNCs. Furthermore, he also participated in the process of the preparation of oxide-passivated free-standing SiNCs. Next, the author performed all the computer simulations presented throughout this thesis that were used to design dimensions and to characterize properties of 2D photonic crystals. Last but not least, the author also carried out the thorough optical characterization of the fabricated photonic crystals.

Appendix

Videos of the SES & VSL methods

Optical gain in our samples was evaluated by the SES and VSL methods. In order to let the reader better understand principle of these methods, we have recorded videos demonstrating the SES method (video titled 'SES.avi') and the VSL method with/without achieving stimulated emission ('VSL no StE.avi'/'VSL StE.avi' applied on a solution of laser dye Coumarin 480 in a glass (quartz) cuvette.

   The experimental setup is described in Chapter 4, Section 4.1. Briefly, 355 nm nanosecond laser pulses were focused on the sample with a cylindrical lens forming a stripe-like excitation region. Videos were taken using a microscope coupled with a camera. Figure 7.1 shows an excerpt from the video 'vsl StE.avi' during the regime of stimulated emission.
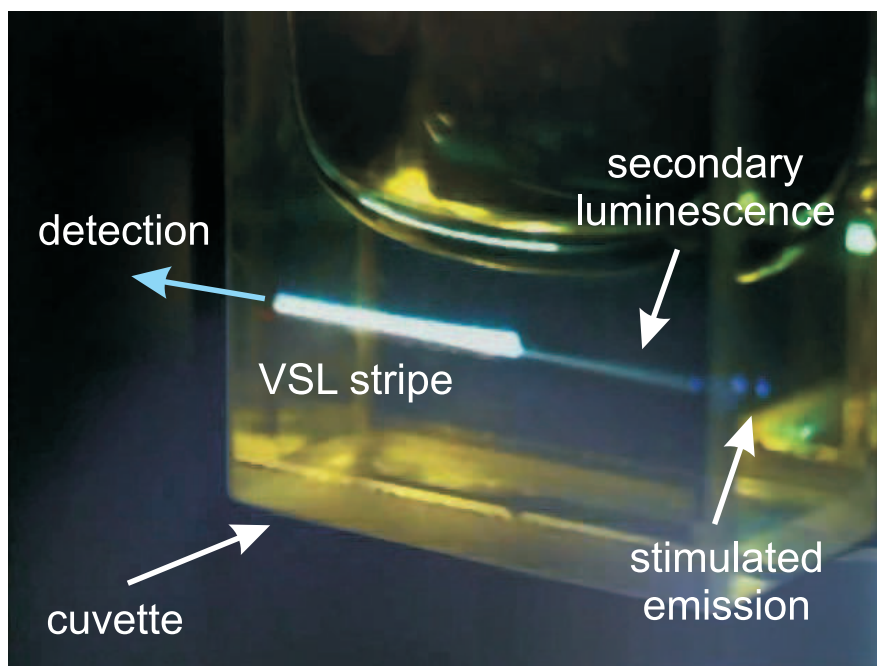

Figure 7.1: A single frame from the video 'vsl StE.avi'. A solution of laser dye Coumarin 480 in a glass (quartz) cuvette is excited with a laser beam focused into a VSL stripe and emits the blue-colored radiation. Under given experimental conditions, blue-colored stimulated emission occurs in the stripe. Photons from stimulated emission propagate along the stripe (in both directions) and excite the laser-not-excited part of the dye, which is evidenced by a secondary luminescence at the right-side with respect to the VSL stripe. The color of the secondary luminescence is slightly red-shifted from the color of stimulated emission. However this is not recognizable in the video. Stimulated emission is directional and outcouples from both edges of the cuvette—see the blue dot on the right side.

   In the videos:

1. 'SES.avi' – a single excitation spot is shifted by a given step along the excitation stripe starting from the edge of the cuvette.

2. 'VSL no StE.avi' – the excitation stripe length is gradually increased. Very low excitation energy is used for pumping.

3. 'VSL StE.avi' – the excitation stripe length is gradually increased. From a certain stripe length, high excitation energy allows for the onset of stimulated emission.

Videos of light extraction from a photonic crystal

In this section, videos demonstrating the computer simulation of light propagation in a simple planar waveguide and in a waveguide with a photonic crystal on its surface are shown. Light propagation was computed by employing a 2D-FDTD simulation [77]. The waveguiding structure with refractive index equal to 3.5 surrounded by vacuum was placed into the middle of a 2D-computational cell (see Fig. 7.2 which depicts the situation for the planar waveguide). Light was generated from a continuous line source emitting into all directions with a fixed frequency ω and with an electric field component E_z perpendicular to the waveguide. The light source was placed at the left side of the waveguide and the evolution of the electromagnetic field component E_z in time was computed at different time instants and then compiled into a single video. The frequency ω was chosen such that at least one TM guided mode was generated. Part of light, which is not totally reflected on the air-waveguide interfaces, radiates to air ($\rightarrow$ radiative modes).
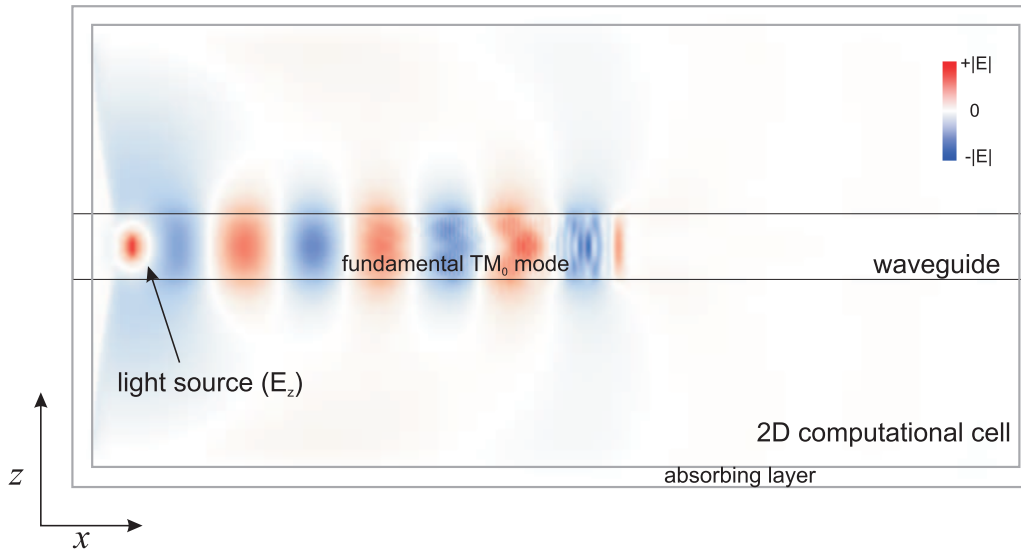

Figure 7.2: A single frame from the video 'waveguide omega1.avi' depicting a 2D FDTD computational cell used to simulate the propagation of light in a planar waveguide surrounded by vacuum. Ligth emitted from a continuous line source tuned at the frequency ω_1 couples to the fundamental TM_0 mode of the structure.

In the videos:

1. 'waveguide omega1.avi' – the propagation of light (component E_z) with the frequency ω_1 in a planar waveguide ($n = 3.5$) is shown. Clearly, only a single TM_0 mode is guided to another end of the structure.

2. 'waveguide omega2.avi' – shows the propagation of light with the frequency $\omega_2 > \omega_1$ in a similar waveguide as in the previous video. The superposition of two guided modes propagates to another end of the structure.

3. 'PhC guided mode.avi' – describes the propagation of light with the frequency ω_1 in a planar waveguide having part of its surface periodically patterned. The height of the waveguide is similar as it was in the previous two videos. First, light couples to the TM_0 mode of the planar waveguide and propagates along it. Then at the place where light couples to the photonic crystal section, some radiation losses are introduced due

to the mismatch between the $\mathbf{k}_\parallel$ vectors of the modes in the planar waveguide and in the photonic crystal-based waveguide. Nevertheless, the mismatch is relatively low and thus most of light gets through the photonic crystal and propagates to another end of the waveguide. The frequency ω_1 lays below the air lightline of the photonic crystal band diagram (Fig. 7.3(b)), i.e. an optical mode with this frequency is guided and not leaky.

4. 'PhC leaky mode.avi' – shows the propagation of light with the frequency ω_2 in the same structure as above (Fig. 7.3(a)). Light couples to the fundamental and higher-order mode (modes that possess similar ω_2 but different $\mathbf{k}_\parallel$ vectors) and propagates towards the section with a photonic crystal. Within the photonic crystal, the fundamental mode with ω_2 is on the photonic band diagram positioned above the air lightline (i.e. it is a leaky mode), whereas the higher-order mode is below it (Fig 7.3(b)). Even though the latter should be guided in the photonic crystal, it radiates to air due to the large mismatch of the $\mathbf{k}_\parallel$ wavectors in the planar waveguide and in the photonic crystal. On the other hand, the leaky mode radiates to air due to the Bragg-diffraction on the periodicity in the form of planar waves, which can be clearly seen in the right part of Fig. 7.3(a). Nevertheless, some intensity of the fundamental mode reaches the end of the waveguide because its Q-factor is still relatively high (due to a small spatial overlap of the leaky mode electric field with the photonic crystal).
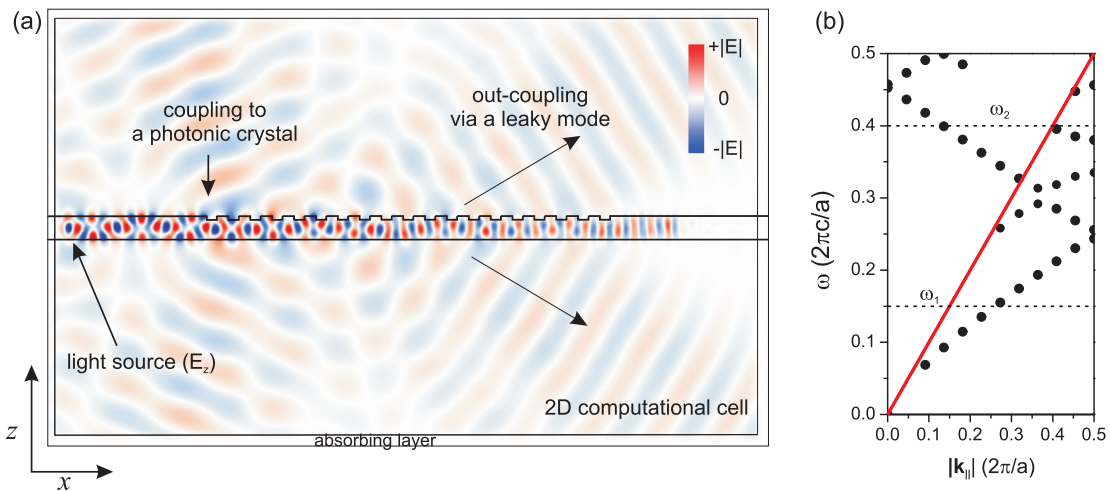
Figure 7.3: (a) A single frame from the video 'PhC leaky mode.avi' depicting a 2D computational cell with a photonic crystal on the top of a planar waveguide. The fundamental mode with ω_2 is a leaky mode and thus it is partly out-coupled to air during its propagation in the photonic crystal. The higher-order mode with ω_2 cannot couple to the photonic crystal section due to the large mismatch of its $\mathbf{k}_\parallel$ vectors in the waveguide and in the photonic crystal. (b) The TM photonic band diagram of the waveguide with the photonic crystal shown in (a). At the frequency ω_1, only one fundamental mode exists. At the frequency ω_2, two modes exist: a leaky mode originating from the folding of a fundamental mode and a guided higher-order mode.

Video of light coupling into a photonic crystal

In this section, a short video ('PhC coupling.avi') of the normally incident light being coupled into the TE leaky mode of a NCD photonic crystal slab is presented in order to give a better insight into the physics involved. The photonic crystal comprises columns ordered into a square lattice etched on the top of a thin diamond layer. It is supposed to describe the real NCD photonic crystal structure studied in Chapter 5, Section 5.3. Finite-difference time-domain simulation [77] using a 3D computational cell with one lattice period of our sample was employed. The vertical cut through the middle of the column is depicted in Fig. 7.4(a). On the four surfaces of the computational domain parallel to the xz- and yz-plane, we impose the Bloch periodic boundary condition on the electric fields. For the remaining two surfaces of the computational domain, we impose the Perfectly Matched Layer absorbing boundary conditions. We use a continuous plane wave source with the E_y electric field component positioned at the top of the computational cell. The frequency of the source matches the first TE leaky mode at the Γ-point of the photonic crystal band diagram.

In the video, we can see the effect of light coupling into the TE mode—formation of the mode in time—and the enhanced electric field inside the photonic crystal compared to the field outside. Based on the computation, zero transmission should occur for the frequency at the resonance. This effect is reproduced in the simulation, however, a negligible energy fraction passes through the photonic crystal due to the non-zero spectral width of the source frequency. A single shot from the video is shown in Fig. 7.4(b).
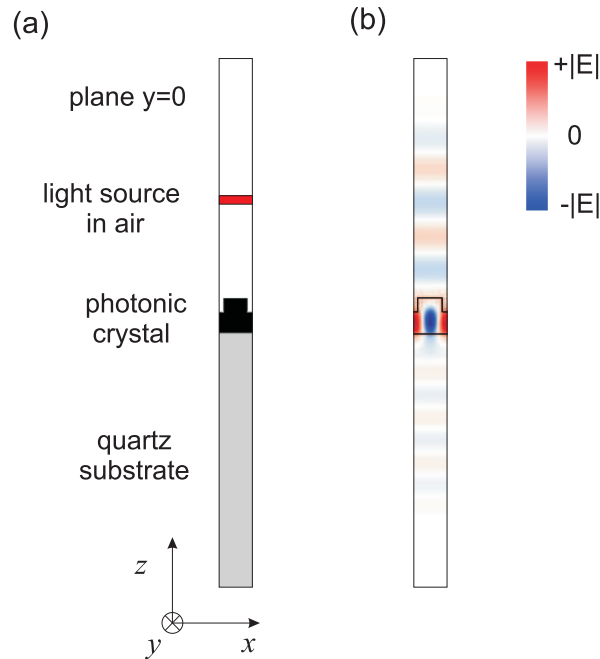

Figure 7.4: (a) A cut through the plane $y = 0$ of a 3D-FDTD computational domain. (b) A single-frame excerpt from a video simulating TE polarized light coupling into the leaky mode of a 2D photonic crystal slab.

Bibliography

[1] "http://www.techspot.com/news/49026-ibm-supercomputer-overtakes-japans-fujitsu-as-worlds-fastest.html," . (Cited on page 1.)

[2] L. Khriachtchev, ed., *Silicon Nanophotonics: Basic Principles, Current Status and Perspectives* (Pan Stanford Publishing, Singapore, 2009). (Cited on pages 1 and 34.)

[3] L. Pavesi and D. J. Lockwood, eds., *Silicon Photonics*, vol. Topics in Applied Physics 94 (Springer Berlin, 2004). (Cited on page 1.)

[4] N. Koshida, ed., *Device Applications of Silicon Nanocrystals and Nanostructures* (Springer Science+Business Media, New York, 2009). (Cited on page 1.)

[5] G. T. Reed, "Device physics: The optical age of silicon," Nature **427**, 595–596 (2004). (Cited on page 1.)

[6] G. T. Reed, G. Mashanovich, F. Y. Gardes, and D. J. Thomson, "Silicon optical modulators," Nature Photon. **4**, 518–526 (2010). (Cited on page 1.)

[7] H. Rong, A. Liu, R. Jones, O. Cohen, D. Hak, R. Nicolaescu, A. Fang, and M. Paniccia, "An all-silicon Raman laser," Nature **433**, 292–294 (2005). (Cited on page 1.)

[8] O. Boyraz and B. Jalali, "Demonstration of a silicon Raman laser," Opt. Express **12** (2004). (Cited on page 1.)

[9] G. Roelkens, L. Liu, D. Liang, R. Jones, A. Fang, B. Koch, and J. Bowers, "III–V silicon photonics for on-chip and intra-chip optical interconnects," Laser Photon. Rev. **4**, 751–779 (2010). (Cited on page 1.)

[10] "http://www.luxtera.com," . (Cited on page 1.)

[11] L. T. Canham, "Silicon quantum wire array fabrication by electrochemical and chemical dissolution of wafers," Appl. Phys. Lett. **57**, 1046 (1990). (Cited on pages 2 and 9.)

[12] I. Mihalcescu, M. Ligeon, F. Muller, R. Romestain, and J. C. Vial, "Surface passivation: a critical parameter for the visible luminescence of electrooxidised porous silicon," J. Luminescence **57**, 111–115 (1993). (Cited on page 2.)

[13] T. Suemoto, K. Tanaka, A. Nakajima, and T. Itakura, "Observation of phonon structures in porous Si luminescence," Phys. Rev. Lett., **70**, 3659 (1993). (Cited on page 2.)

[14] J. Linnros, N. Lalic, P. Knápek, K. Luterová, J. Kočka, A. Fejfar, and I. Pelant, "Instabilities in electroluminescent porous silicon diodes," Appl. Phys. Lett. **69**, 833 (1996). (Cited on page 2.)

[15] L. Pavesi and R. Turan, eds., *Silicon Nanocrystals* (Wiley-VCH, 2010). (Cited on page 2.)

[16] J. Ruan, P. M. Fauchet, L. D. Negro, M. Cazzaleni, and L. Pavesi, "Stimulated emission in nanocrystalline silicon superlattices," Appl. Phys. Lett. **83**, 5479 (2003). (Cited on pages 2 and 10.)

[17] Z. H. Lu, D. J. Lockwood, and J.-M. Baribeau, "Quantum confinement and light emission in SiO_2/Si superlattices," Nature **378**, 258 – 260 (1995). (Cited on page 2.)

[18] A. G. Nassiopoulos, S. Grigoropoulos, and D. Papadimitriou, "Electroluminescent device based on silicon nanopillars," Appl. Phys. Lett. **69**, 2267–2269 (1996). (Cited on page 2.)

[19] D. Jurbergs, E. Rogojina, L. Mangolini, and U. Kortshagen, "Silicon nanocrystals with ensemble quantum yields exceeding 60%," Appl. Phys. Lett. **88**, 233116 (2006). (Cited on page 2.)

[20] M. L. Mastronardi, F. Maier-Flaig, D. Faulkner, E. J. Henderson, C. Kübel, U. Lemmer, and G. A. Ozin, "Size-dependent absolute quantum yields for size-separated colloidally-stable silicon nanocrystals," Nano Lett. **12**, 337–342 (2012). (Cited on page 2.)

[21] L. Pavesi, "Routes toward silicon-based lasers," Mater. Today **8**, 18 – 25 (2005). (Cited on page 2.)

[22] L. Pavesi, S. Gaponenko, and L. D. Negro, eds., *Towards the first silicon laser* (NATO Science Series II, 2003). (Cited on page 2.)

[23] K. Sakoda, "Enhanced light amplification due to group-velocity anomaly peculiar to two- and three-dimensional photonic crystals," Opt. Express **4**, 167–176 (1999). (Cited on pages 2 and 29.)

[24] S. Kim, J. Lee, and H. Jeon, "Over 1 hour continuous-wave operation of photonic crystal lasers," Opt. Express **19**, 1–6 (2011). (Cited on pages 2, 30 and 31.)

[25] S. G. Cloutier, P. A. Kossyrev, and J. Xu, "Optical gain and stimulated emission in periodic nanopatterned crystalline silicon," Nature Mater. **4**, 887 – 891 (2005). (Cited on page 2.)

[26] C. Kittel, *Introduction to Solid State Physics* (John Wiley & Sons, Inc., Weinheim, 2005). (Cited on page 6.)

[27] P. Yu and M. Cardona, *Fundamentals of Semiconductors* (Springer, Berlin, 1996). (Cited on page 6.)

[28] I. Pelant and J. Valenta, *Luminescence Spectroscopy of Semiconductors* (Oxford University Press, Oxford, 2012). (Cited on pages 7, 11 and 99.)

[29] A. P. Alivisatos, "Semiconductor clusters, nanocrystals, and quantum dots," Science **271**, 933–937 (1996). (Cited on page 8.)

[30] P. Hapala, K. Kůsová, I. Pelant, and P. Jelínek, "Theoretical analysis of electronic band structure of 2- to 3-nm Si nanocrystals," Phys. Rev. B **87**, 195420 (2013). (Cited on pages 8, 9, 10 and 38.)

[31] D. C. Hannah, J. Yang, P. Podsiadlo, M. K. Chan, A. Demortiere, D. J. Gosztola, V. B. Prakapenka, G. C. Schatz, U. Kortshagen, and R. D. Schaller, "On the origin of photoluminescence in silicon nanocrystals: Pressure-dependent structural and optical studies," Nano Lett. **12**, 4200–4205 (2012). (Cited on pages 10, 34 and 38.)

[32] M. V. Wolkin, J. Jorne, P. M. Fauchet, G. Allan, and C. Delerue, "Electronic states and luminescence in porous silicon quantum dots: The role of oxygen," Phys. Rev. Lett **82**, 197 (1999). (Cited on page 10.)

[33] K. Dohnalová, A. N. Poddubny, A. A. Prokofiev, W. D. A. M. de Boer, C. P. Umesh, J. M. J. Paulusse, H. Zuilhof, and T. Gregorkiewicz, "Surface brightens up Si quantum dots: direct bandgap-like size-tunable emission," Light: Science & Applications **2**, e47 (2013). (Cited on pages 10 and 11.)

[34] L. Tsybeskov, J. V. Vandyshev, and P. M. Fauchet, "Blue emission in porous silicon: Oxygen-related photoluminescence," Phys. Rev. B **49**, 7821 (1994). (Cited on page 10.)

[35] A. Brewer and K. Von Haeften, "*In situ* passivation and blue luminescence of silicon clusters using a cluster beam/H_2O codeposition production method," Appl. Phys. Lett. **94**, 261102 (2009). (Cited on page 10.)

[36] Y. Kanemitsu, T. Futagi, T. Matsumoto, and H. Mimura, "Origin of the blue and red photoluminescence from oxidized porous silicon," Phys. Rev. B **49**, 14732–14735 (1994). (Cited on page 10.)

[37] J. P. Wilcoxon, G. A. Samara, and P. N. Provencio, "Optical and electronic properties of Si nanoclusters synthesized in inverse micelles," Phys. Rev. B **60**, 2704–2714 (1999). (Cited on page 10.)

[38] M. Ray, T. Basu, A. Jana, N. Bandyopadhyay, S. Hossain, A. Pramanick, and R. Klie, "Luminescent core-shell nanostructures of silicon and silicon oxide: Nanodots and nanorods," J. Appl. Phys. **107**, 064311 (2010). (Cited on page 10.)

[39] J. Valenta, A. Fucikova, I. Pelant, K. Kůsová, K. Dohnalová, A. Aleknavičius, O. Cibulka, A. Fojtík, and G. Kada, "On the origin of the fast photoluminescence band in small silicon nanoparticles," New J. Phys. **10**, 073022 (2008). (Cited on page 10.)

[40] W. D. A. M. de Boer, D. Timmerman, K. Dohnalová, I. N. Yassievich, H. Zhang, W. J. Buma, and T. Gregorkiewicz, "Red spectral shift and enhanced quantum efficiency in phonon-free photoluminescence from silicon nanocrystals," Nat. Nanotechnol. **5**, 878–884 (2010). (Cited on page 10.)

[41] M. C. Beard, K. P. Knutsen, P. Yu, J. M. Luther, Q. Song, W. K. Metzger, R. J. Ellingson, and A. J. Nozik, "Multiple exciton generation in colloidal silicon nanocrystals," Nano Lett. **7**, 2506–2512 (2007). (Cited on page 10.)

[42] D. Timmerman, I. Izeddin, P. Stallinga, I. N. Yassievich, and T. Gregorkiewicz, "Space-separated quantum cutting with silicon nanocrystals for photovoltaic applications," Nature Photon. **2**, 105–109 (2008). (Cited on page 10.)

[43] F. Cichos, J. Martin, and C. von Borczyskowski, "Emission intermittency in silicon nanocrystals," Phys. Rev. B **70**, 115314 (2004). (Cited on page 10.)

[44] L. Pavesi, L. D. Negro, C. Mazzoleni, G. Franzo, and F. Priolo, "Optical gain in silicon nanocrystals," Nature **408**, 440 (2000). (Cited on pages 10 and 11.)

[45] L. D. Negro, M. Cazzaleni, L. Pavesi, S. Ossicini, D. Pacifici, G. Franzo, F. Priolo, and F. Iacona, "Dynamics of stimulated emission in silicon nanocrystals," Appl. Phys. Lett. **82**, 4636 (2003). (Cited on page 10.)

[46] L. Khriachtchev, M. Rasanen, S. Novikov, and J. Sinkkonen, "Optical gain in Si/SiO$_2$ lattice: Experimental evidence with nanosecond pulses," Appl. Phys. Lett. **79**, 1249 (2001). (Cited on page 10.)

[47] K. Luterová, K. Dohnalová, V. Švrček, I. Pelant, J. P. Likforman, O. Crégut, P. Gilliot, and B. Hönerlage, "Optical gain in porous silicon grains embedded in sol-gel derived SiO$_2$ matrix under femtosecond excitation," Appl. Phys. Lett. **84**, 3280 (2004). (Cited on pages 10 and 100.)

[48] P. M. Fauchet, J. Ruan, H. Chen, L. Pavesi, L. D. Negro, M. Cazzaleni, R. G. Elliman, N. Smith, M. Samoc, and B. Luther-Davies, "Optical gain in different silicon nanocrystal systems," Opt. Mater. **27**, 745 (2005). (Cited on page 10.)

[49] K. Dohnalová, I.Pelant, K. Kůsová, P. Gilliot, M. Gallart, O. Crégut, J.-L. Rehspringer, B. Honerlage, T. Ostatnický, and S. Bakardjeva, "Closely packed luminescent silicon nanocrystals in a distributed-feedback laser cavity," New J. Phys. **10** (2008). (Cited on pages 10, 34 and 100.)

[50] B. M. Monroy, O. Crégut, M. Gallart, B. Hönerlage, and P. Gilliot, "Optical gain observation on silicon nanocrystals embedded in silicon nitride under femtosecond pumping," Appl. Phys. Lett. **98**, 261108 (2011). (Cited on page 10.)

[51] M. Cazzaleni, D. Kovalev, L. D. Negro, Z. Gaburro, and L. Pavesi, "Polarized optical gain and polarization-narrowing of heavily oxidized porous silicon," Phys. Rev. Lett. **93**, 207402 (2004). (Cited on page 10.)

[52] K. Dohnalová, K. Žídek, L. Ondič, K. Kůsová, O. Cibulka, and I. Pelant, "Optical gain at the F-band of oxidized silicon nanocrystals," J. Phys. D: Appl. Phys. **42**, 135102 (2009). (Cited on pages 10 and 100.)

[53] K. Žídek, I. Pelant, F. Trojánek, P. Malý, P. Gilliot, B. Hönerlage, J. Oberlé, L. Šiller, R. Little, and B. R. Horrocks, "Ultrafast stimulated emission due to quasidirect transitions in silicon nanocrystals," Phys. Rev. B **84**, 085321 (2011). (Cited on pages 11, 96, 97, 98 and 101.)

[54] R. D. Kekatpure and M. L. Brongersma, "Quantification of free-carrier absorption in silicon nanocrystals with an optical microcavity," Nano Lett. **8**, 3787–3793 (2008). (Cited on pages 11, 94 and 95.)

[55] K. Kůsová, O. Cibulka, K. Dohnalová, I. Pelant, J. Valenta, A. Fučíková, K. Žídek, J. Lang, J. Englich, P. Matějka, P. Štěpánek, and S. Bakardjieva, "Brightly luminescent organically capped silicon nanocrystals fabricated at room temperature and atmospheric pressure," ACS Nano **4**, 4495–4504 (2010). (Cited on pages 11, 96 and 98.)

[56] K. Dohnalová, L. Ondič, K. Kůsová, I. Pelant, J. L. Rehspringer, and R.-R. Mafouana, "White-emitting oxidized silicon nanocrystals: Discontinuity in spectral development with reducing size," J. Appl. Phys. **107**, 053102 (2010). (Cited on pages 11, 34 and 37.)

[57] X. Wang, X. Ren, K. Kahen, M. A. Hahn, M. Rajeswaran, S. Maccagnano-Zacher, J. Silcox, G. E. Cragg, A. L. Efros, and T. D. Krauss, "Non-blinking semiconductor nanocrystals," Nature **459**, 686–689 (2009). (Cited on page 11.)

[58] F. García-Santamaría, Y. Chen, J. Vela, R. D. Schaller, J. A. Hollingsworth, and V. I. Klimov, "Suppressed Auger recombination in "giant" nanocrystals boosts optical gain performance," Nano Lett. **9**, 3482–3488 (2009). (Cited on page 11.)

[59] S. Fan, J. N. Winn, A. Devenyi, J. C. Chen, R. D. Meade, and J. D. Joannopoulos, "Guided and defect modes in periodic dielectric waveguides," J. Opt. Soc. Am. B. **12**, 1267–1272 (1995). (Cited on page 14.)

[60] E. M. Purcell, "Spontaneous emission probabilities at radio frequencies," Phys. Rev. **69**, 681 (1946). (Cited on pages 14 and 30.)

[61] J. D. Joannopoulous, S. G. Johnson, J. N. Winn, and R. D. Meade, *Photonic Crystals: Molding the Flow of Light* (Princeton University Press, Princeton, 2008). (Cited on pages 14, 15 and 16.)

[62] W. M. Robertson, G. Arjavalingam, R. D. Meade, K. D. Brommer, A. M. Rappe, and J. D. Joannopoulos, "Measurement of photonic band structure in a two-dimensional periodic dielectric array," Phys. Rev. Lett. **68**, 2023–2026 (1992). (Cited on page 17.)

[63] L. Ondič and I. Pelant, "Efficient light amplification in low gain materials due to a photonic band edge effect," Opt. Express **20**, 7071–7080 (2012). (Cited on pages 18, 29, 101 and 176.)

[64] S. G. Johnson and J. D. Joannopoulos, "Block-iterative frequency-domain methods for Maxwell's equations in a planewave basis," Opt. Express **8**, 173–190 (2001). (Cited on pages 19 and 123.)

[65] L. Sapienza, H. Thyrrestrup, S. Stobbe, P. D. Garcia, S. Smolka, and P. Lodahl, "Cavity quantum electrodynamics with Anderson-localized modes," Science **327**, 1352–1355 (2010). (Cited on page 19.)

[66] M. Nomura, S. Iwamoto, A. Tandaechanurat, Y. Ota, N. Kumagai, and Y. Arakawa, "Photonic band-edge micro lasers with quantum dot gain," Opt. Express **17**, 640–648 (2009). (Cited on pages 19 and 30.)

[67] S. Fan and J. D. Joannopoulos, "Analysis of guided resonances in photonic crystal slabs," Phys. Rev. B **65**, 235112 (2002). (Cited on page 21.)

[68] E. Yablonovitch, "Inhibited spontaneous emission in solid-state physics and electronics," Phys. Rev. Lett. **58**, 2059–2062 (1987). (Cited on page 21.)

[69] T. Fujii, Y. Gao, R. Sharma, E. L. Hu, S. P. DenBaars, and S. Nakamura, "Increase in the extraction efficiency of GaN-based light-emitting diodes via surface roughening," Appl. Phys. Lett. **84**, 855–857 (2004). (Cited on page 21.)

[70] J. J. Wierer, D. A. Steigerwald, M. R. Krames, J. J. O'Shea, M. J. Ludowise, G. Christenson, Y.-C. Shen, C. Lowery, P. S. Martin, S. Subramanya, W. Gotz, N. F. Gardner, R. S. Kern, and S. A. Stockman, "High-power AlGaInN flip-chip light-emitting diodes," Appl. Phys. Lett. **78**, 3379 (2001). (Cited on page 21.)

[71] C. Wiesmann, K. Bergenek, and U. T. Schwarz, "Photonic crystal LEDs – designing light extraction," Laser Photon. Rev. **3**, 262–286 (2009). (Cited on pages 21, 24, 27 and 123.)

[72] E. Matioli and C. Weisbuch, "Impact of photonic crystals on LED light extraction efficiency: approaches and limits to vertical structure designs," J. Phys. D: Appl. Phys. **43** (2010). (Cited on pages 21 and 27.)

[73] S. Fan, P. R. Villeneuve, J. D. Joannopoulos, and E. F. Schubert, "High extraction efficiency of spontaneous emission from slabs of photonic crystals," Phys. Rev. Lett. **78**, 3294–3297 (1997). (Cited on page 21.)

[74] M. Fujita, S. Takahashi, Y. Tanaka, T. Asano, and S. Noda, "Simultaneous inhibition and redistribution of spontaneous light emission in photonic crystals," Science **308**, 1296–1298 (2005). (Cited on page 21.)

[75] J. J. Wierer, A. David, and M. M. Megens, "III-nitride photonic-crystal light-emitting diodes with high extraction efficiency," Nature Photon. **3**, 163–169 (2009). (Cited on pages 21, 25 and 26.)

[76] K. Bergenek, C. Wiesmann, R. Wirth, L. O'Faolain, N. Lindner, K. Streubel, and T. F. Krauss, "Enhanced light extraction efficiency from AlGaInP thin-film light-emitting diodes with photonic crystals," Appl. Phys. Lett. **93** (2008). (Cited on page 21.)

[77] A. F. Oskooi, D. Roundy, M. Ibanescu, P. Bermel, J. D. Joannopoulos, and S. G. Johnson, "Meep: A flexible free-software package for electromagnetic simulations by the FDTD method," Comput. Phys. Commun. **181**, 687–702 (2010). (Cited on pages 24, 124, 181 and 183.)

[78] L. Ondič, K. Kůsová, O. Cibulka, I. Pelant, K. Dohnalová, B. Rezek, A. Kromka, O. Babchenko, and N. Ganesh, "Enhanced photoluminescence extraction efficiency from a diamond photonic crystal via leaky modes," New J. Phys. **13**, 063005 (2011). (Cited on pages 25, 122, 126 and 176.)

[79] J.-Y. Kim, M.-K. Kwon, K.-S. Lee, S.-J. Park, S. H. Kim, and K.-D. Lee, "Enhanced light extraction from GaN-based green light-emitting diode with photonic crystal," Appl. Phys. Lett. **91**, 181109 (2007). (Cited on page 27.)

[80] B. Cluzel, V. Calvo, T. Charvolin, E. Picard, P. Noé, and E. Hadji, "Single-mode room-temperature emission with a silicon rod lattice," Appl. Phys. Lett. **89**, 201111 (2006). (Cited on page 27.)

[81] H. Y. Ryu, Y. H. Lee, R. L. Sellin, and D. Bimberg, "Over 30-fold enhancement of light extraction from free-standing photonic crystal slabs with InGaAs quantum dots at low temperature," Appl. Phys. Lett. **79**, 3573–3575 (2001). (Cited on page 27.)

[82] A. A. Erchak, D. J. Ripin, S. Fan, P. Rakich, J. D. Joannopoulos, E. P. Ippen, G. S. Petrich, and L. A. Kolodziejski, "Enhanced coupling to vertical radiation using a two-dimensional photonic crystal in a semiconductor light-emitting diode," Appl. Phys. Lett. **78**, 563–565 (2001). (Cited on page 27.)

[83] C. D. Presti, A. Irrera, G. Franzò, I. Crupi, F. Priolo, F. Iacona, G. D. Stefano, A. Piana, D. Sanfilippo, and P. G. Fallica, "Photonic-crystal silicon-nanocluster light-emitting device," Appl. Phys. Lett. **88**, 033501 (2006). (Cited on page 27.)

[84] J. Carrol, J. Whiteaway, and D. Plumb, *Distributed feedback semiconductor lasers*, vol. 10 (The Institution of Electrical Engineers, London, 1998). (Cited on page 28.)

[85] J. P. Dowling, M. Scalora, M. J. Bloemer, and C. M. Bowden, "Group index limitations in slow-light photonic crystals," J. Appl. Phys. **75**, 1896–1899 (1994). (Cited on pages 28 and 29.)

[86] M. Lu, B. Cunningham, S.-J. Park, and J. Eden, "Vertically emitting, dye-doped polymer laser in the green ($\lambda \sim 536$ nm) with a second order distributed feedback grating fabricated by replica molding," Opt. Commun. **281**, 3159 – 3162 (2008). (Cited on page 30.)

[87] Y. H. Lee, D. H. Jang, H. K. Park, I. Y. Han, H. Y. R. D. S. Song, and J. K. Hwang, "Continuous room-temperature operation of optically pumped two-dimensional photonic crystal lasers at 1.6 μm," IEEE Photon. Technol. Lett. **12**, 1295–1297 (2000). (Cited on page 30.)

[88] G. Vecchi, F. Raineri, I. Sagnes, A. Yacomotti, P. Monnier, T. J. Karle, K.-H. Lee, R. Braive, L. L. Gratiet, S. Guilet, G. Beaudoin, A. Taneau, S. Bouchoule, A. Levenson, and R. Raj, "Continuous-wave operation of photonic band-edge laser near 1.55 μm on silicon wafer," Opt. Express **15**, 7551–7556 (2007). (Cited on page 30.)

[89] Y. Park, S. Kim, C. Moon, H. Jeon, and H. J. Kim, "Butt-end fiber coupling to a surface-emitting Gamma-point photonic crystal band edge laser," Appl. Phys. Lett. **90**, 171115 (2007). (Cited on page 30.)

[90] G. Xu, R. Colombelli, S. P. Khanna, A. Belarouci, X. Letartre, L. Li, E. H. Linfield, A. G. Davies, H. E. Beere, and D. A. Ritchie, "Efficient power extraction in surface-emitting semiconductor lasers using graded photonic heterostructures," Nat. Commun. **3**, 952 (2007). (Cited on page 30.)

[91] L. J. Martínez, B. Alén, I. Prieto, J. F. Galisteo-López, M. Galli, L. C. Andreani, C. Seassal, P. Viktorovitch, and P. A. Postigo, "Two-dimensional surface emitting photonic crystal laser with hybrid triangular-graphite structure," Opt. Express **17**, 15043–15051 (2009). (Cited on page 30.)

[92] K. Nozaki, S. Kita, and T. Baba, "Room temperature continuous wave operation and controlled spontaneous emission in ultrasmall photonic crystal nanolaser," Opt. Express **15**, 7506–7514 (2007). (Cited on page 30.)

[93] M. Lončar, T. Yoshie, A. Scherer, P. Gogna, and Y. Qiu, "Low-threshold photonic crystal laser," Appl. Phys. Lett. **81**, 2680–2682 (2002). (Cited on page 30.)

[94] S. Matsuo, A. Shinya, T. Kakitsuka, K. Nozaki, T. Segawa, T. Sato, Y. Kawaguchi, and M. Notomi, "High-speed ultracompact buried heterostructure photonic-crystal laser with 13 fJ of energy consumed per bit transmitted," Nature Photon. **4**, 645–654 (2010). (Cited on page 30.)

[95] O. Painter, R. K. Lee, A. Scherer, A. Yariv, J. D. O'Brien, P. D. Dapkus, and I. Kim, "Two-dimensional photonic band-gap defect mode laser," Science **284**, 1819–1821 (1999). (Cited on page 30.)

[96] A. M. Hartel, D. Hiller, S. Gutsch, P. Löper, S. Estradé, F. Peiró, B. Garrido, and M. Zacharias, "Formation of size-controlled silicon nanocrystals in plasma enhanced chemical vapor deposition grown SiO_xN_y/SiO_2 superlattices," Thin Solid Films **520**, 121 – 125 (2011). (Cited on pages 34 and 93.)

[97] L. Ruizendaal, S. P. Pujari, V. Gevaerts, J. M. J. Paulusse, and H. Zuilhof, "Biofunctional silicon nanoparticles by means of thiol-ene click chemistry," Chem. Asian J. **6**, 2776–2786 (2011). (Cited on page 34.)

[98] V. Svrček, D. Mariotti, and M. Kondo, "Ambient-stable blue luminescent silicon nanocrystals prepared by nanosecond-pulsed laser ablation in water," Opt. Express **17**, 520 (2009). (Cited on page 34.)

[99] L. Ondič, K. Dohnalová, I. Pelant, K. Žídek, and W. D. A. M. de Boer, "Data processing correction of the irising effect of a fast-gating intensified charge-coupled device on laser-pulse-excited luminescence spectra," Rev. Sci. Instrum. **81**, 063104 (2010). (Cited on page 36.)

[100] L. Ondič, K. Kůsová, M. Ziegler, O. Cibulka, K. Herynková, M. Gallart, P. Gilliot, B. Hönerlage, and I. Pelant, "Complex study of fast blue luminescence of oxidized silicon nanocrystals: the role of the core," submitted to Nanoscale (2013). (Cited on pages 38 and 176.)

[101] A. S. Moskalenko, J. Berakdar, A. N. Poddubny, A. A. Prokofiev, I. N. Yassievich, and S. V. Goupalov, "Multiphonon relaxation of moderately excited carriers in Si/SiO_2 nanocrystals," Phys. Rev. B **85**, 085432 (2012). (Cited on page 39.)

[102] K. Kůsová, L. Ondič, E. Klimešová, K. Herynková, I. Pelant, S. Daniš, J. Valenta, M. Gallart, M. Ziegler, B. Hönerlage, and P. Gilliot, "Luminescence of free-standing versus matrix-embedded oxide-passivated silicon nanocrystals: The role of matrix-induced strain," Appl. Phys. Lett. **101**, 143101 (2012). (Cited on pages 39 and 176.)

[103] K. L. Shaklee and R. F. Leheny, "Direct determination of optical gain in semiconductor crystals," Appl. Phys. Lett. **18**, 475 (1971). (Cited on page 86.)

[104] J. Valenta, I. Pelant, and J. Linnros, "Waveguiding effects in the measurement of optical gain in a layer of Si nanocrystals," Appl. Phys. Lett. **81**, 1396 (2002). (Cited on pages 86 and 87.)

[105] N. N. Ha, K. Dohnalová, T. Gregorkiewicz, and J. Valenta, "Optical gain of the 1.54 μm emission in MBE-grown Si:Er nanolayers," Phys. Rev. B **81**, 195206 (2010). (Cited on pages 86, 87, 89 and 90.)

[106] K. Kůsová, "Silicon nanocrystals: Narrowing down size distribution, organic passivation and novel optical properties," Ph.D. thesis, Charles University in Prague, Czech Republic (2009). (Cited on page 99.)

[107] L. D. Negro, M. Cazzanelli, N. Daldosso, Z. Gaburro, L. Pavesi, F. Priolo, D. Pacifci, G. Franzo, and F. Iacona, "Stimulated emission in plasma-enhanced chemical vapour deposited silicon nanocrystals," Physica E **16**, 297 (2003). (Cited on page 99.)

[108] K. Dohnalová, K. Kůsová, O. Cibulka, L. Ondič, and I. Pelant, "Time-resolved measurements of optical gain and photoluminescence in silicon nanocrystals," Phys. Scr. **T141**, 014011 (2010). (Cited on pages 100 and 176.)

[109] K. Luterová, I. Pelant, I. Mikulskas, R. Tomasiunas, D. Muller, J.-J. Grob, J.-L. Rehspringer, and B. Hönerlage, "Stimulated emission in blue-emitting Si$^+$-implanted SiO$_2$ films?" J. Appl. Phys. **91**, 2896 (2002). (Cited on page 100.)

[110] M. Cazzanelli, D. Kovalev, L. Dal Negro, Z. Gaburro, and L. Pavesi, "Polarized optical gain and polarization-narrowing of heavily oxidized porous silicon," Phys. Rev. Lett. **93**, 207402 (2004). (Cited on page 100.)

[111] I. Aharonovich, A. D. Greentree, and S. Prawer, "Diamond photonics," Nat. Photon. **5**, 397–405 (2011). (Cited on page 122.)

[112] B. J. M. Hausmann, I. B. Bulu, P. B. Deotare, M. McCutcheon, V. Venkataraman, M. L. Markham, D. J. Twitchen, and M. Lončar, "Integrated high-quality factor optical resonators in diamond," Nano Lett. **13**, 1898–1902 (2013). (Cited on page 122.)

[113] T. van der Sar, Z. H. Wang, M. S. Blok, H. Bernien, T. H. Taminiau, D. M. Toyli, D. A. Lidar, D. D. Awschalom, R. Hanson, and V. V. Dobrovitski, "Decoherence-protected quantum gates for a hybrid solid-state spin register," Nature **484**, 82–86 (2012). (Cited on page 122.)

[114] A. Gruber, A. Dräbenstedt, C. Tietz, L. Fleury, J. Wrachtrup, and C. von Borczyskowski, "Scanning confocal optical microscopy and magnetic resonance on single defect centers," Science **276**, 2012–2014 (1997). (Cited on page 122.)

[115] A. M. Zaitsev, *Optical Properties of Diamond: A Data Handbook* (Springer-Verlag, Berlin, 2001). (Cited on page 122.)

[116] L. S. Pan, ed., *Diamond: Electronic Properties and Applications* (Kluwer Academic Publishers, Dordrecht, 1995). (Cited on page 122.)

[117] J. E. Field, ed., *The Properties of Natural and Synthetic Diamond* (Academic Press, London, 1992). (Cited on page 122.)

[118] L. Ondič, K. Dohnalová, M. Ledinský, A. Kromka, O. Babchenko, and B. Rezek, "Effective extraction of photoluminescence from a diamond layer with a photonic crystal," ACS Nano **5**, 346–350 (2011). (Cited on pages 122, 125, 126 and 176.)

[119] A. Kromka, B. Rezek, Z. Remes, M. Michalka, M. Ledinsky, J. Zemek, J. Potmesil, and M. Vanecek, "Formation of continuous nanocrystalline diamond layers on glass and silicon at low temperatures," Chem. Vap. Deposition **14**, 181–186 (2008). (Cited on page 122.)

[120] Z. Remes, A. Kromka, and M. Vanecek, "Towards optical-quality nanocrystalline diamond with reduced non-diamond content," Phys. Status Solidi (a) **206**, 2004–2008 (2009). (Cited on page 122.)

[121] A. David, H. Benisty, and C. Weisbuch, "Optimization of light-diffracting photonic-crystals for high extraction efficiency LEDs," J. Disp. Technol. **3**, 133–148 (2007). (Cited on page 123.)

[122] N. Ganesh, W. Zhang, P. C. Mathias, E. Chow, J. A. N. T. Soares, V. Malyarchuk, A. D. Smith, and B. T. Cunningham, "Enhanced fluorescence emission from quantum dots on a photonic crystal surface," Nat. Nanotechnol. **2**, 515–520 (2007). (Cited on page 124.)

[123] N. Ganesh, I. D. Block, P. C. Mathias, W. Zhang, E. Chow, V. Malyarchuk, and B. T. Cunningham, "Leaky-mode assisted fluorescence extraction: application to fluorescence enhancement biosensors," Opt. Express **16**, 21626 (2008). (Cited on page 124.)

[124] L. Ondič, O. Babchenko, M. Varga, A. Kromka, J. Čtyroký, and I. Pelant, "Diamond photonic crystal slab: Leaky modes and modified photoluminescence emission of surface-deposited quantum dots," Scientific Reports **2**, 914 (2012). (Cited on pages 152, 153 and 176.)

[125] L. Ondič, M. Varga, K. Hruška, A. Kromka, K. Herynková, B. Hönerlage, and I. Pelant, "Two-dimensional photonic crystal slab with embedded silicon nanocrystals: Efficient photoluminescence extraction," Appl. Phys. Lett. **102**, 251111 (2013). (Cited on pages 152, 154, 155 and 176.)

[126] T. Ostatnický, J. Valenta, I. Pelant, K. Luterová, R. Elliman, S. Cheylan, and B. Hönerlage, "Photoluminescence from an active planar optical waveguide made of silicon nanocrystals: dominance of leaky substrate modes in dissipative structures," Opt. Mater. **27**, 781 – 786 (2005). (Cited on page 154.)

Curriculum Vitae

Personal data

Name: RNDr. Lukáš Ondič
Date and place of birth: 22nd January 1985, Košice, Slovak Republic
Nationality: Slovak

Address: Academy of Sciences, Institute of Physics
                               Department of Thin Films
                               Cukrovarnická 10, Prague 6 - 162 53, Czech Republic
                               Email: ondic@fzu.cz
                               Phone: +420 220 318 414

Education

2010–2014   Post-graduate "doctorat cotutelle" studies
             Université de Strasbourg (France) and
             Charles University in Prague (Czech Republic), Faculty of Mathematics
             and Physics (specialization: Quantum optics and optoelectronics)
             PhD thesis on *Silicon nanocrystals, photonic structures and optical gain.*

2009–2014   Doctorate Programme at the Faculty of Mathematics and Physics,
             Charles University in Prague, Czech Republic
             Doctoral degree 'RNDr.'. (specialization: Optics and optoelectronics)

2007–2009   Master studies at the Faculty of Mathematics and Physics, Charles University in Prague (Czech Republic)
             Master degree 'Mgr.'. (specialization: Optics and optoelectronics)
             Master thesis on *Time-resolved measurement of optical gain in silicon based nanostructures*

2004–2007   Bachelor studies at the Faculty of Mathematics and Physics, Charles University in Prague (Czech Republic)
             Bachelor degree 'Bc.'. (specialization: General physics)
             Bachelor thesis on *Newtonian limit of the Schwarzschild-de Sitter solution*

Research interests

- optical properties of semiconductors, semiconductor nanostructures (optical properties and preparation methods), temporally and temperature resolved photoluminescence, optical gain, light amplification, laser oscillators and generators, optical feedback, integrated optoelectronics, silicon photonics

- experimental (photoluminescence, transmission) and theoretical (FDTD technique, RCWA method) study of photonic properties of photonic crystals prepared from different materials.

Work experience

since 2009   Part time research position at the Institute of Physics, Academy of Sciences of the Czech Republic, Prague.

Professional research activities

Author or co-author of 10 scientific publications that were published in high-impact international scientific journals. Number of total citations: 60. H-factor: 5.

Experience with leading research projects

2008-2012   Project KJB No. 100100903 of the Grant Agency of the Academy of Sciences of the Czech Republic
Title *Nanocomposites from silicon and diamond nanocrystals for optoelectronic applications*

2009-2012   Project GAUK No. 73910 of the Grant Agency of the Charles University in Prague
Title *Time-resolved spectroscopy of optical gain in silicon nanocrystals.*

Scholarships and scientific awards

2013   Josef Hlávka Award for the best students and graduates of Czech universities
2012   1st prize of the Milan Odehnal's Award organized by Czech Physical Society, Union of Czech Mathematicians and Physicists

2009   French government scholarship "doctorat cotutelle"

Interests, other skills:

Language skills: Slovak, Czech, English (advanced, active), French (basic, passive)
Computer skills: MS Windows, MS Office, Origin, Matlab, Corel Draw, Adobe Photoshop, LaTeX, MEEP (FDTD method), MPB, RSoft DiffractMOD (RCWA method)
Other skills and interests: driving license B, photography, guitar-playing, sports, family

List of publications in high-impact journals:

1. L. Ondič, K. Kůsová, M. Ziegler, O. Cibulka, K. Herynková, M. Gallart, P. Gilliot, B. Hönerlage, and I. Pelant, "Complex study of fast blue luminescence of oxidized silicon nanocrystals: the role of the core," submitted to Nanoscale (2013).

2. K. Kůsová, P. Hapala, J. Valenta, P. Jelínek, O. Cibulka, L. Ondič, and I. Pelant, "Direct Bandgap Silicon: Tensile-Strained Silicon Nanocrystals," Advanced Materials Interfaces (2013), accepted.

3. L. Ondič, M. Varga, K. Hruška, A. Kromka, K. Herynková, B. Hönerlage, and I. Pelant, "Two-dimensional photonic crystal slab with embedded silicon nanocrystals: Efficient photoluminescence extraction," Applied Physics Letters **102**, 251111 (2013).

4. L. Ondič, O. Babchenko, M. Varga, A. Kromka, J. Čtyroký, and I. Pelant, "Diamond photonic crystal slab: Leaky modes and modified photoluminescence emission of surface-deposited quantum dots," Scientific Reports **2**, 914 (2012).

5. K. Kůsová, L. Ondič, E. Klimešová, K. Herynková, I. Pelant, S. Daniš, J. Valenta, M. Gallart, M. Ziegler, B. Hönerlage, and P. Gilliot, "Luminescence of free-standing versus matrix-embedded oxide-passivated silicon nanocrystals: The role of matrix-induced strain," Applied Physics Letters **101**, 143101 (2012).

6. L. Ondič and I. Pelant, "Efficient light amplification in low gain materials due to a photonic band edge effect," Optics Express **20**, 7071–7080 (2012).

7. L. Ondič, K. Kůsová, O. Cibulka, I. Pelant, K. Dohnalová, B. Rezek, A. Kromka, O. Babchenko, and N. Ganesh, "Enhanced photoluminescence extraction efficiency from a diamond photonic crystal via leaky modes," New Journal of Physics **13**, 063005 (2011).

8. L. Ondič, K. Dohnalová, M. Ledinský, A. Kromka, O. Babchenko, and B. Rezek, "Effective extraction of photoluminescence from a diamond layer with a photonic crystal," ACS Nano **5**, 346–350 (2011).

9. L. Ondič, K. Dohnalová, I. Pelant, K. Žídek, and W. D. A. M. de Boer, "Data processing correction of the irising effect of a fast-gating intensified charge-coupled device on laser-pulse-excited luminescence spectra," Review of Scientific Instruments **81**, 063104 (2010).

10. K. Dohnalová, K. Kůsová, O. Cibulka, L. Ondič, and I. Pelant, "Time-resolved measurements of optical gain and photoluminescence in silicon nanocrystals," Physica Scripta **T141**, 014011 (2010).

11. K. Dohnalová, L. Ondič, K. Kůsová, I. Pelant, J. L. Rehspringer, and R.-R. Mafouana, "White-emitting oxidized silicon nanocrystals: Discontinuity in spectral development with reducing size," Journal of Applied Physics **107**, 053102 (2010).

12. K. Dohnalová, K. Žídek, L. Ondič, K. Kůsová, O. Cibulka, and I. Pelant, "Optical gain at the F-band of oxidized silicon nanocrystals," Journal of Physics D: Applied Physics **42**, 135102 (2009).

Internationally established conferences:

1. L. Ondič, K. Kůsová, K. Herynková, I. Pelant, M. Gallart, M. Ziegler, B. Hönerlage and P. Gilliot, "On the origin of fast radiative processes in silicon nanocrystals," E-MRS Spring Meeting 2013, Strasbourg, France, May 2013 (oral presentation).

2. L. Ondič, K. Dohnalová, A. Kromka, B. Rezek, M. Ledinský, K. Kůsová, O. Cibulka, and I. Pelant, "Light control employing a diamond-based photonic crystal slab," E-MRS Spring Meeting 2012, Strasbourg, France, May 2012 (poster presentation).

3. L. Ondič, K. Dohnalová, A. Kromka, B. Rezek, M. Ledinský, K. Kůsová, O. Cibulka, and I. Pelant, "Enhanced extraction efficiency of intrinsic photoluminescence from a diamond photonic crystal," Diamond 2011, Garmisch-Partenkirchen, Germany, September 2011 (poster presentation).

4. L. Ondič, K. Dohnalová, and I. Pelant, "Silicon nanocrystals embedded in a two-dimensional diamond photonic structure," PECX IX, Granada, Spain, September 2010 (poster presentation).

5. L. Ondič, K. Dohnalová, A. Kromka, B. Rezek, M. Ledinský, K. Hruška, K. Kůsová, O. Cibulka, and I. Pelant, "Optical properties of silicon nanocrystals in two-dimensional diamond photonic crystal," E-MRS Spring Meeting 2010, Strasbourg, France, June 2010 (poster presentation).

6. K. Kůsová, O. Cibulka, K. Dohnalová, L. Ondič, and I. Pelant, "Surface of silicon nanocrystals and spectral tunability of their photoluminescence," E-MRS Spring Meeting 2010, Strasbourg, France, June 2010 (oral presentation).

7. K. Kůsová, O. Cibulka, L. Ondič, and I. Pelant, "Effect of laser irradiation on suspensions of silicon nanocrystals," 7th Porous Semiconductors – Science and Technology, Valencia, Spain, May 2010 (poster presentation).

8. K. Dohnalová, A. Kromka, Z. Remeš, B. Rezek, M. Ledinský, and L. Ondič, "Diamond thin films and silicon nanocomposites for optical and electrical applications," Diamond Nanotechnology and Science, Czech Republic and Sweden, 2010 (oral presentation).

9. K. Dohnalová, K. Kůsová, O. Cibulka, L. Ondič, and I. Pelant, "Time-resolved measurements of optical gain and photoluminescence in silicon nanocrystals," Nordic Semiconductor Meeting 2009, Reykjavik, Iceland, June 2009 (poster presentation).

10. L. Ondič, K. Dohnalová, K. Žídek, O. Cibulka, I. Pelant, B. Hönerlage, O. Cregut, and P. Gilliot, "Time-resolved optical gain spectroscopy of small silicon nanocrystals," E-MRS Spring Meeting 2009, Strasbourg, France, June 2009 (poster presentation).

International advanced schools:

1. Ettore Majorana Foundation And Center For Scientific Culture International School Of Atomic And Molecular Spectroscopy, "28th Course – NANO-OPTICS: Plasmonics, Photonic Crystals, Metamaterials and Sub-Wavelength Resolution," Erice, Sicily (Italy), July 2011 (poster presentation)

2. First International Education Forum on Environment and Energy Science organized by Tokyo Institute of Technology, Hawaii (USA), December 2012 (oral presentation)

3. Second International Education Forum on Environment and Energy Science organized by Tokyo Institute of Technology, California (USA): December, 2013 (oral presentation)

Lukáš Ondič

Silicon nanocrystals, photonic structures and optical gain

Résumé

Les nanocristaux de Silicium (SiNCs) de taille inférieure à 5 nm sont des matériaux qui présentent une intense photoluminescence (PL) et capables d'amplification optique. Cette dernière propriété est un pré-requis à l'obtention d' émission stimulée sous pompage optique. Atteindre l' émission stimulé (et l'effet laser) à partir de nanostructures basées sur Si est d'un interêt particulier dans le domaine de la photonique à base de silicium. Dans ce travail nous avons (i) étudié les propriétés optiques fondamentales de SiNCs – la bande d' émission bleue-verte de recombinaison rapide a été attribuée à la recombinaison quasi-directe des électrons et trous chauds autour du point Γ; (ii) fabriqué un cristal photonique présentant une efficacité d'extraction augmentée – une augmentation de l'intensité d'un facteur 7 a été obtenue – et (iii) exploré la possibilité d'améliorer le gain optique des émetteurs de lumière à base de SiNCs en les combinant avec un cristal photonique à deux dimensions. Des simulations numériques par „Finite-difference time-domain computer simulation technique" ont montré qu'une émission stimulée pouvait être obtenue dans un milieu à faible gain si celui-ci est incorporé dans un cristal photonique à deux dimensions spécialement conçcu.

MOTS-CLÉS:

NANOCRISTAUX DE SILICIUM, PHOTOLUMINESCENCE, AMPLIFICATION OPTIQUE, INCORPORATION DANS UN CRISTAL PHOTONIQUE

Résumé en anglais

Silicon nanocrystals (SiNCs) of sizes below approximately 5 nm are a material with an efficient room-temperature photoluminescence (PL) and optical gain. Optical gain is a prerequisite for obtaining stimulated emission from a pumped material, and the achievement of stimulated emission (and lasing) from Si-based nanostructures is of particular interest of the field of silicon photonics. In this work, we (i) investigated fundamental optical properties of SiNCs – the fast blue-green emission band of these SiNCs was linked with the quasi-direct recombination of hot electrons and holes in the vicinity of the Γ-point, (ii) designed and fabricated photonic crystal structures with up to 7-fold enhanced light extraction efficiency and (iii) explored a possibility of enhancing optical gain of light-emitting SiNCs by combining them with a two-dimensional photonic crystal. By employing Finite-difference time-domain computer simulations, it was shown that stimulated emission from a low-gain medium can be achieved by embedding it into a two-dimensional photonic crystal with well-designed dimensions. We also proposed some further steps for future sample improvement.

KEYWORDS:

SILICON NANOCRYSTALS, PHOTOLUMINESCENCE, OPTICAL AMPLIFICATION, PHOTONIC CRYSTALS